Gas mixing in anaerobic digestion

Davide Dapelo

First supervisor: Prof J. Bridgeman

Second supervisor: Prof M. Sterling

June, 2016

"Merely seeing each other's face would in itself be insignificant. It is the heart that is important. Someday let us meet at Eagle Peak, where Shakyamuni Buddha dwells. Nam-myoho-renge-kyo, Nam-myoho-renge-kyo."

Nichiren Daishonin (1278).
The Drum at The Gate of Thunder

To my mentor, Daisaku Ikeda
and to all my comrades in faith

Abstract

Mesophilic anaerobic digestion is one of the most used and successful technologies to treat the sludges resulting from wastewater treatment. However, traditional approaches to digester design are firmly rooted in empiricism and rule of thumb rather than science. In particular, whilst mixing has been recognised to be a key element for the success of the digestion process, the degree of mixing necessary for a stable process, as well as a clear picture of its effect on biogas production are still unclear. In particular, the literature on gas mixing is still particularly poor. Mixing is an energy-intensive operation, and therefore the need to lower the wastewater process carbon footprint requires searching how to lower the input mixing energy without compromising—and indeed enhancing—biogas production.

Computational Fluid Dynamics was used to produce recommendations on how to enhance mixing in the specific case of gas-mixed anaerobic digesters. For the first time, an Euler-Lagrangian multiphase model was developed to simulate gas mixing in anaerobic digestion. The model was validated against laboratory experiments with the Particle Image Velocimetry and the Positron Emission Particle Tracking techniques, and gave predictions in agreement with the experimental results.

Full-scale simulations reproducing a real digester were performed with the validated model, and scenarios with different mixing input power, bubble size and sludge rheologies were reproduced. In all the scenarios, it was possible to show that input mixing power can be lowered by the same, significant amount, while maintaining the degree of mixing unaltered. The simulations also showed the formation of low-viscosity flow patterns localized in the zones where the liquid phase velocity magnitude was higher. This phenomenon is intrinsically linked to the non-Newtonian nature of the sludge, and is problematic as it

leads to short-circuited mixing.

Finally, recommendations on how to mitigate the issue of the low-viscosity flow patterns were given. Explanations on how to understand the mixing in laboratory and full-scale vessels, in particular the respective roles of diffusion, advection and turbulence, were traced, as well as on how to develop a more comprehensive criterion for defining and assessing a satisfactory degree of mixing. Recommendations for further works comprise experimental research on biogas bubble size inside a gas-mixed industrial digester, further validation conducted on pilot-scale vessels, computational simulations on different geometries, coupling computational fluid dynamics with a biochemical model, and research on the effect of different sources of nutrients uniformization (e.g., turbulence or diffusion) on biogas production.

A journal paper published in Water Research and a conference paper presented at the Fifteenth International Conference on Civil, Structural and Environmental Engineering Computing (Civil-Comp) were produced as a result of this work. They are both reported in Appendix F. Two other papers are currently in preparation.

Acknowledgements

I would like to thank my first supervisor, Professor John Bridgeman. His support has not been limited solely to the field of research, as he has been also—and especially—a reference point for the human aspect. Additionally, I am grateful to my second supervisor, Professor Mark Sterling: his insight has been invaluable. I owe a debt of gratitude towards both for the trust they granted to me.

A PhD is quite a wide job, and it would have not been possible without the invaluable help of many and many people working with, supporting and advising. I am grateful to the BlueBear high performance computing facility, in particular with Paul Hatton, for their fundamental support. I also wish to thank Severn Trent Water, Inc., in particular Pete Vale, for the precious information they shared with me. The experimental part of this work would not have been possible without the knowledge, the support and the capabilities of Federico Alberini and Mark Simmons for the PIV part, and of Thomas Leadbeater and David Parker for the PEPT. I am deeply grateful to all of them. Mark Carter's help was also determinant to realising the experimental apparatus; his contribution is deeply appreciated. The support and the knowledge of my Postgraduate and research fellows colleagues has been invaluable. I wish to thank Rebecca Sindall, my "predecessor", for all her advice and the work we undertook together; Nainesh, Dominic and Justin for their insight in CFD; Roger, Sally, Ashley, Simon, Giulio, Valeria, Carlo, Martin, Marianna, Michaela, Anna, Aryan and Mehran for their warm support. Outside the University, I would like to deeply acknowledge Doctor Massimo d'Elia and Doctor Andrea Mazzino for the constant support through these years. Without Euroforma and the European Social Fund, I would ignore even what anaerobic digestion means. Thank you to Mladen Ciglar and Luca Marigo,

among the others.

My family—it is impossible to express in words how I am grateful for your constant support. Thank you to my wife, Cinzia, for your love and support. I am deeply honoured to be your husband, Thank you to Michele, as you are making our lives much busier and full of joy and bliss as well—especially now that you have finally decided to get out of your mother's belly! Still I am convinced that some fundamental principles such as the mass conservation do not hold for children, especially as regards what they leave in the nappy. Thank you to my parents, Gabry and Guido. It is said that the debt of gratitude towards one's parents is higher than the heaven and deeper than the earth: I hope to become able to repay my debt towards you. Thank you to my parents in law, Luisa and Franco: I am deeply honoured to be part of your family, even though I have not had the opportunity to personally meet you, Luisa, if we do not consider the mirror of your daughter. Thank you to my brothers in law, Daniele and Claudia, your spouses Giulia and Daniele, and your children Pietro and Veronica. Thank you to my grandparents, who is still in live, Silvia, and who is not, Mari, Luisito and Mino. You have all been a reference point and a model, in particular you, Mino: I cannot wait for meeting you again!

Contents

3 Fluid Dynamics Modelling **29**

List of Figures

List of Tables

1

Introduction

> *"But I don't want to go among mad people," Alice Remarked.*
>
> *"Oh, you can't help that," said the Cat: "we're all mad here. I'm mad. You're mad."*
>
> *"How do you know I'm mad?" said Alice.*
>
> *"You must be," said the Cat, "or you wouldn't have come here."*
>
> Lewis Carroll (1865).
> Alice in Wonderland
> (Suggested by my wife—hey, wait for a moment. . . !)

EVERY DAY, OVER 10 billion litres of wastewater are treated in UK in more than 9,000 wastewater plants (WaterUK, 2012). Wastewater is treated through a chain of different processes that includes debris screening, sedimentation, aerobic treatment and eventually disinfection (Tchobanoglous et al., 2010), and finally returned to the environment.

A number of stages in the wastewater process result in sludge production: in 2010—2011, the wastewater plants in the UK produced about 1.5 million tonnes of sewage sludge (WaterUK, 2012). Sludge can be thermally destructed, landfilled, or recycled to land. The latter, which includes agricultural use, is the most common option in UK, covering about 71% of the overall sludge disposal. Recycling as a land fertilizer is also considered as one of the most sustainable options for sludge disposal, as it allows a reduction of artificial fertiliser needs (WaterUK, 2012). The EU Directive on the protection of the environment (86/278/EEC) states that sludge must have "undergone biological, chemical or heat treatment, long-term storage or any other appropriate process so as to significantly reduce its fermentability and the health hazards resulting from its use” before it can be applied to land (Sindall, 2014).

The whole wastewater treatment process, including sludge treatment and disposal, is an energy-intensive operation. Data returned by the EU Member States suggest energy consumption exceeds 23,800 GWh per annum, and further increases of 60% are forecast in the next 10-15 years, primarily due to tightened regulation of effluent discharges. Predictions show that by 2030 the world will have to produce 50% more food and energy and provide 30% more water, while mitigating and adapting to climate change. Therefore, the “explicit link between wastewater and energy” must be addressed.

Mesophilic anaerobic digestion is the most widespread technology for sludge treatment (Bridgeman, 2012). Sludge is mixed with anaerobic bacteria at temperatures between 22 and 41 °C, and biodegradable material is broken down into more stable compounds. One of the most interesting aspects of anaerobic digestion is that biogas, which is prevalently methane, is produced during the process. Biogas, in turn, is increasingly harnessed as a renewable energy by means of combined heat and power technology (Bridgeman, 2012)

Energy is required to maintain a stable digestion process within the digester, mainly in the form of heat and mixing energy. The current need to maximise energy recovery drives toward the need to improve the balance between input energy and biogas yield. It is well known (Chae et al., 2008; Agler et al., 2010) that mesophilic process efficiency increases with increasing temperature up to 41 °C, after which efficiency drops. For this reason, it is not feasible to decrease the operating temperature in the attempt of reducing the operational costs of a digester. As regards mixing, according to Owen (1982), it is responsible for about 17—73% of the total energy consumpion of an industrial digester. Therefore, the only strategy feasible to reduce the energy consumption of a digester consists of reducing the level of mixing without compromising, and indeed enhancing, biogas production.

In order to understand how to enhance digester mixing, it is important to determine to what extent biogas output is influenced by flow patterns in a digester; flow patterns which are determined by physical parameters of the digesters, inflow mode, sludge rheology and, crucially, mixing regimes (Bridgeman, 2012; Sindall et al., 2013). However, research is still lacking in this area. Traditional approaches to digester design are firmly rooted in empiricism and rule of thumb rather than science, and design standards focus only on treated sludge quality, not quality and gas yield/energy consumption.

Although the importance of thorough mixing has been recognized, recent studies e.g. Stroot et al. (2001); McMahon et al. (2001); Ong et al. (2002); Gómez et al. (2006); Ward et al. (2008), have questioned traditional approaches. Preliminary studies conducted by Bridgeman and others (Bridgeman 2012; Sindall et al. 2013; Wu 2010a) on sludge mixing have shown that computational fluid dynamics (CFD) offers significant potential for understanding flow patterns of the non-Newtonian sewage sludge within digesters. However, there are clear limitations with the work undertaken to date; for example, while much work has been done to understand mechanical mixing, gas mixing remains poorly studied.

1.1 Research Relevance

The research reported in this thesis is aimed at filling the knowledge gap on gas mixing in anaerobic digestion. A novel CFD model specifically designed to reproduce a multiphase system with the characteristics of the gas-mixed sludge was developed. The named model was validated against experimental work carried on with the PIV and PEPT techniques, and then, applied to a full-scale setup. Recommendations were given to improve the mixing efficiency of real gas-mixed anaerobic digesters.

A journal paper published in Water Research and a conference paper presented at the Fifteenth International Conference on Civil, Structural and Environmental Engineering Computing (Civil-Comp) were produced as a result of this work. They are both reported in Appendix F. Two other papers are currently in preparation.

1.2 Layout of This Work

After this introduction Chapter, a literature review of anaerobic digestion and the fluid mechanics theory involved in mixing is exposeddiscussed in Chapters 2 and 3 respectively. Following the literature review, the aim and objectives of this thesis are listed in Chapter 4. All the materials and methods—both experimental and numerical—used to pursue the named objectives are outlined in Chapter 5. The results of the experiments follow in Chapter 6. The details of the settings for the numerical simulations are reported in Chapter 7. The results of the numerical simulations are then compared with the outcome of the simulations in Chapter 8, and then a series of full-scale CFD simulations is reported in Chapter 9. A discussion is performed in Chapter 10. Finally, conclusions and recommendations for further research are reported in Chapters 11 and 12 respectively.

2

Anaerobic Digestion and Mixing

“Dai diamanti non nasce niente

Dal letame nascono i fior.”[a]

---

[a] From diamonds nothing rises
From manure the flowers rise.

Fabrizio de André (1967).

Via del Campo

MESOPHILIC ANAEROBIC DIGESTION involves the decomposition of organic and inorganic matter in the absence of molecular oxygen due to bacteria, at a temperature range of 30—40 °C (Tchobanoglous et al., 2010). Anaerobic digestion offers the following contribution to lower the overall carbon footprint of wastewater treatment.

(*i*) Sludge stabilization—Sludge is degraded into a safer end-product with less organic content and a reduced presence of pathoges (van Haandel and van der Lubbe, 2007), which is therefore suitable to be used as a valuable fertilizer.

(*ii*) Sludge volume reduction—During anaerobic digestion, sludge undergoes a volume reduction (van Haandel and van der Lubbe, 2007). Sludge must be transported from the wastewater plant to the place where disposal occurs, thus increasing the overall wastewater process cost and carbon footprint. The volume reduction due to the anaerobic digestion process allows both to be reduced.

(*iii*) Energy recovery—Methane-rich biogas is produced during anaerobic digestion.

Biogas can be harnessed via combined heat and power technology, thus reducing the need for energy in the whole wastewater process.

(*iv*) Reduced methane emissions—Anaerobic digestion reduces the methane emissions to atmosphere (WaterUK, 2012).

In Sections 2.1 and 2.2, the main aspects of the biochemistry of anaerobic digestion are reviewed. Then, a description of mixing is introduced in Section 2.3. Finally, the literature on mixing in anaerobic digestion is reviewed in Section 2.4, and the knowledge gaps are identified in Section 2.5.

2.1 Anaerobic Digestion

Cells take the carbon they need to thrive and the energy to live through respiration (Gerardi, 2003). During this process, large high-energy compounds (substrate) are broken down into smaller low-energy compounds. Cells withhold a part of energy and carbon to live (Gerardi, 2003). Energy is obtained from the electrons that are released by breaking the substrate chemical bounds. The electrons are then transferred through a series of electron carrier molecules. As they are transferred from one carrier molecule to another, a part of their energy is used to build adenosine triphosphate (Gerardi, 2003) which, in turn, is directly used in the cell metabolic processes as an energy source. Finally, electrons are removed from the cell by a final electron carrier molecule that is discharged into the surrounding environment (Gerardi, 2003).

The final electron carrier employed by a given bacteria group determines the specific form of respiration (Gerardi, 2003). The highest energy yield is achieved with oxygen (aerobic, or oxic respiration), which leads to full transfer of carbon to carbon dioxide and new bacterial cells and therefore is called complete respiration (Gerardi, 2003). Other final electron carriers are typical of different forms of respiration (anaerobic, or anoxic). They lead to lesser energy yields and, depending on the particular type of molecule, also to incomplete respiration, that is: carbon is transferred to carbon dioxide, new bacterial cells and organic products such as simple acids and alcohols (Gerardi, 2003). A summary is depicted in Table 2.1.

Anaerobic digestion is a complex pattern of respiration processes that occur in the absence of free molecular oxygen (Gerardi, 2003). Several bacteria groups work in syntrophy, each bacteria group degrading a given substrate and producing compounds that in turn are used as a substrate by other groups (Gerardi, 2003; Schink and Stams, 2006). In addition, some bacteria groups produce suitable environmental conditions for other groups, e.g. by consuming molecular hydrogen or sulphate (Gerardi, 2003). The final products of the food chain are carbon dioxide and methane.

2.1.1 Biochemical Reactions

As the reaction chain depends strongly on the type of nourishment, the environmental conditions and the bacteria groups involved, each digester has its particular behaviour—and, also, a character—depending on the substrate, the climatic conditions and the history. For instance, digesters with a history of unstable operation tend to be much more resistant against failure in case of sudden overloading (Stroot et al., 2001; McMahon et al., 2001). Nevertheless, as illustrated in Gerardi (2003), the reaction chain can be schematically represented in all the cases as a succession of three stages: hydrolysis, acidogenesis and methanogenesis (Figure 2.1).

(*i*) *Hydrolysis*. In this stage, particulate (e.g., cellulose) and colloidal organic compounds (e.g., proteins) are broken down into monomers and solubilized, as schematically

RedOx potential (mV)	Final e^- carrier	Biochemical reaction	Respiration occurring	Complete / incomplete
$> +50$	O_2	$CH_2O + O_2 \rightarrow CO_2 + H_2O + \text{cells}$	Aerobic (oxic)	Complete
$+50$ to -50	NO_3^-	$CH_2O + NO_3^- \rightarrow CO_2 + H_2O + N_2 + N_2O + \text{cells}$	Denitrification	Complete
< -50	SO_4^{2-}	$CH_2O + SO_4^{2-} \rightarrow CO_2 + H_2O + H_2S + \text{acids} + \text{alcohols} + \text{cells}$	Sulfate reduction	Complete with exceptions
< -100	Organic molecules (CH_2O)	$CH_2O \rightarrow CO_2 + \text{acids} + \text{alcohols} + \text{cells}$	Fermentation	Incomplete
< -300	CO_2 as carbonate	$CH_2O + CO_2 \rightarrow H_2O + CH_4 + \text{cells}$	Methane production	Incomplete

Table 2.1 *Forms of respiration. From Gerardi (2003).*

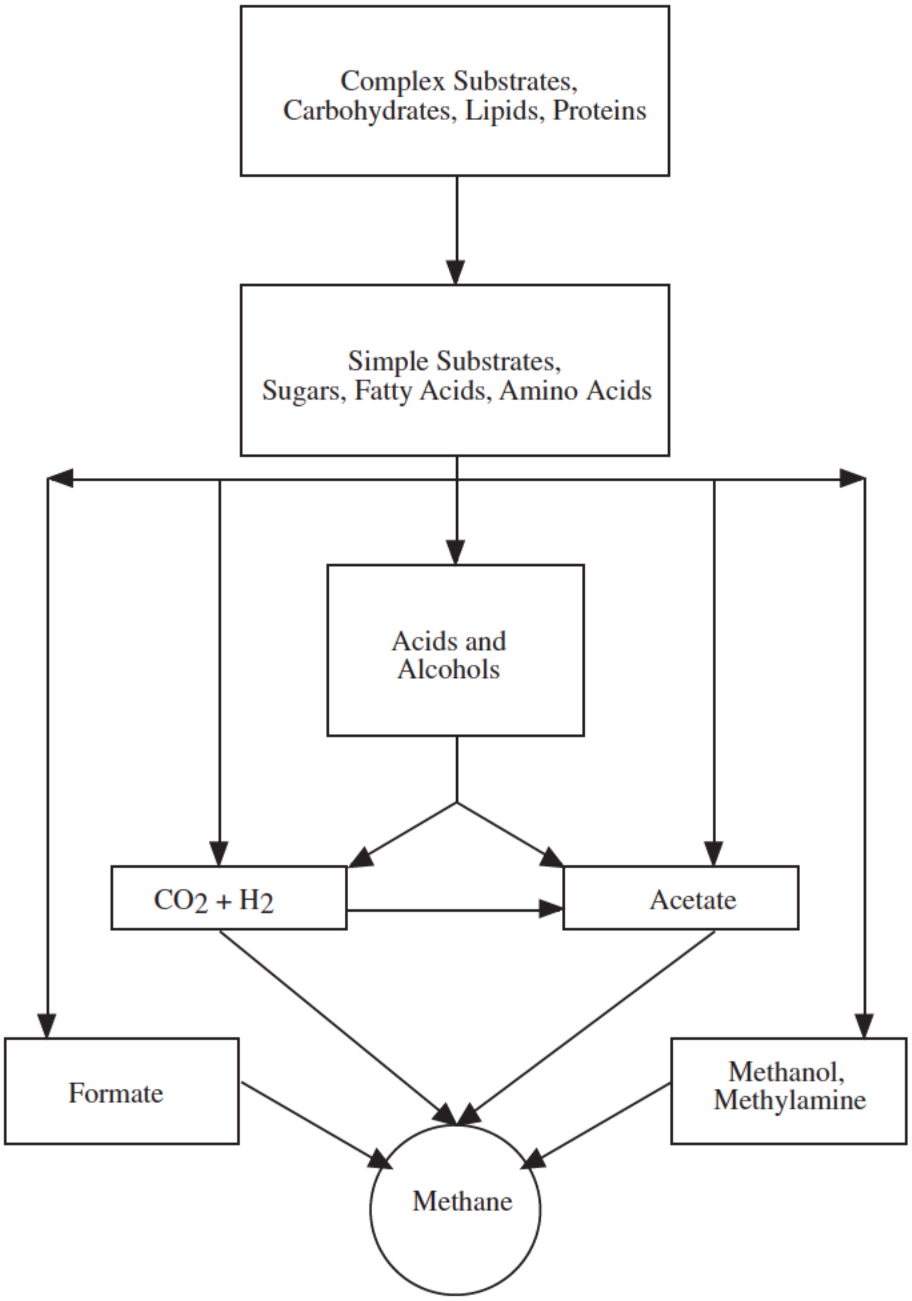

Figure 2.1 *Anaerobic digestion reaction chain (Gerardi, 2003).*

illustrated in Equation 2.1 (Gerardi, 2003):

$$\begin{aligned} \text{Complex carbohydrates} &\longrightarrow \text{Simple sugars,} \\ \text{Complex lipids} &\longrightarrow \text{Fatty acids,} \\ \text{Complex proteins} &\longrightarrow \text{Amino acids.} \end{aligned} \tag{2.1}$$

Hydrolysis is catalysed by enzymes released by specific bacteria groups into the substrate (exoenzymes). Some examples are reported in Table 2.2. Since each bacteria group produces only a small group of exoenzymes and each exoenzyme degrades only a specific group of substrates, a large and diverse bacteria community is required for optimal digestion (Gerardi, 2003).

(*ii*) *Acidogenesis*. In this stage, soluble compounds produced by hydrolysis or directly discharged into the digester are absorbed and degraded by a large diversity of bacteria groups through many fermentative processes (Gerardi, 2003). Figure 2.2 illustrates some example of fermentative processes. The outcome of acidogenesis consists of carbon dioxide, hydrogen gas, alcohols, organic acids, some nitrogen and sulphur compounds (Gerardi, 2003).

Bacteria groups involved in acidogenesis include facultative anaerobes, aero tolerant and strict anaerobes (Gerardi, 2003). Some bacteria produce a large variety of products: for instance, *Clostridia* produce acetate, acetone, butanol, butyrate, ethanol, lactate and also carbon dioxide and hydrogen gas; *Escherichia coli* acetate, 2,3-butanediol, ethanol, formate, lactate, succinate and also carbon dioxide and hydrogen gas (Gerardi, 2003). On the other hand, some bacteria groups perform only specific fermentations (Gerardi, 2003). For instance, *Erwinia*, *Sarcina* and *Zymomonas* perform ethanol fermentation:

$$1\text{glucose} \rightarrow 2\text{ethanol} + 2\mathrm{H_2O} \tag{2.2}$$

(Gerardi, 2003). *Clostridium* and *Butyrivibrio* perform butyrate fermentation:

$$\text{hexose} \rightarrow \text{butyrate} \tag{2.3}$$

(Gerardi, 2003). *Bifidobacterium*, *Lactobacillus*, *Leuconostoc*, *Pediococcus*, *Sporolacto-*

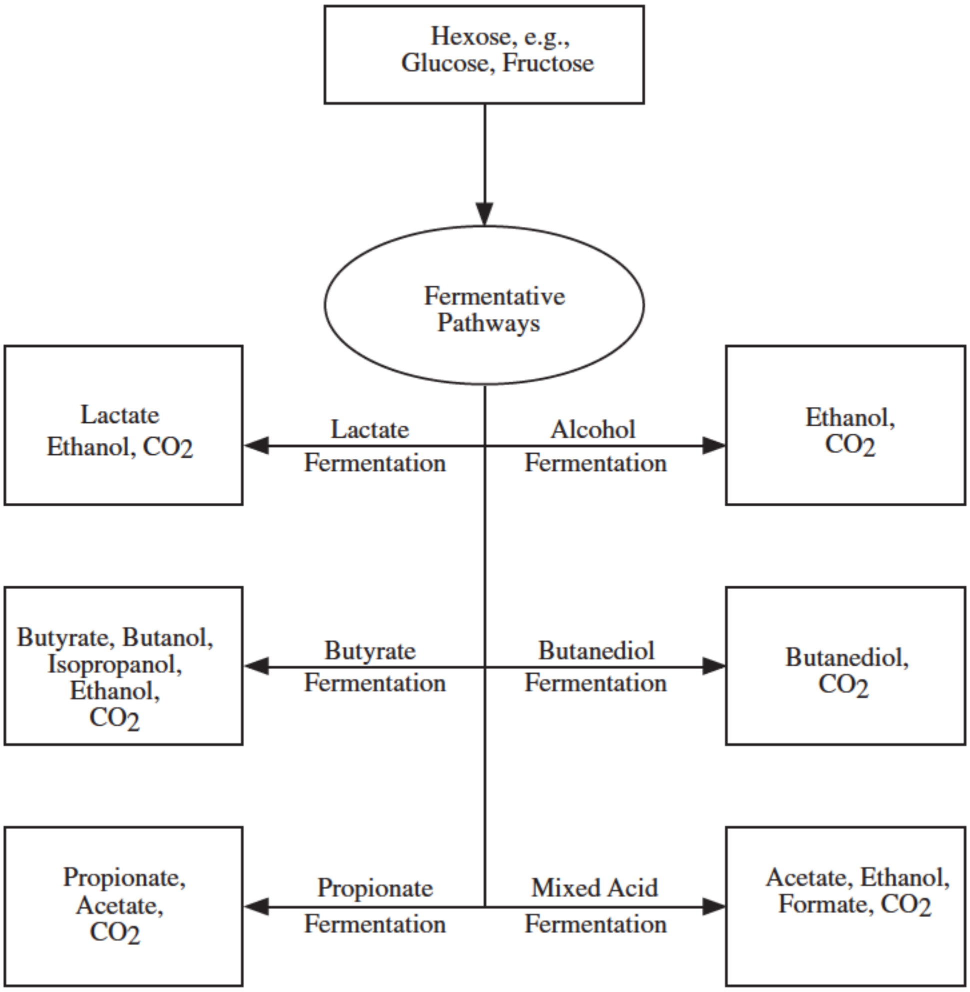

Figure 2.2 *Examples of simple sugar fermentation (Gerardi, 2003).*

Substances to be degraded	Exoenzyme needed	Example	Bacteria	Product
Polysaccharides	Saccharolytic	Cellulase	*Cellulomonas*	Simple sugar
Proteins	Proteolytic	Protease	*Bacillus*	Amino acids
Lipids	Lipolytic	Lipase	*Mycobacterium*	Fatty acids

Table 2.2 *Examples of hydrolysis exoenzymes, bacteria and substrates (Gerardi, 2003).*

bacillus and *Streptococcus* perform lactate fermentation:

$$\begin{aligned} \text{glucose} &\rightarrow 2\text{lactate}, \\ \text{glucose} &\rightarrow \text{lactate} + \text{ethanol} + CO_2\,, \\ 2\text{glucose} &\rightarrow 2\text{lactate} + 3\text{acetate} \end{aligned} \tag{2.4}$$

(Gerardi, 2003). *Bacteroides*, *Clostridium*, *Peptostreptococcus*, *Ruminococcus*, *Selenomonas*, *Succinivibrio* and *Veillonella* perform propionate fermentation:

$$\begin{aligned} 1.5\text{glucose} &\rightarrow 2\text{propionate} + \text{acetate} + \mathrm{CO_2}\ , \\ 3\text{lactate} &\rightarrow 2\text{propionate} + \text{acetate} + \mathrm{CO_2} \end{aligned} \tag{2.5}$$

(Gerardi, 2003). A large bacteria group, known as acetogenic bacteria, produce a very small number of products, mainly acetate. This group includes *Acetobacterium* and *Sporomusa* (Gerardi, 2003). The reactions involved (Gerardi, 2003) are reported below. Among them, a predominant part is played by acetate production from hydrogen gas (Gerardi, 2003).

$$\begin{aligned} \mathrm{4H_2 + 2CO_2} &\rightarrow \mathrm{CH_3COOH + 2H_2O}\ , \\ \mathrm{4CO + 2H_2O} &\rightarrow \mathrm{CH_3COOH + 2CO_2}\ , \\ \mathrm{4CH_3OH + CO_2} &\rightarrow \mathrm{3CH_3COOH + 2H_2O}\ , \\ \mathrm{C_6H_{12}O_6} &\rightarrow \mathrm{3CH_3COOH}\ . \end{aligned} \tag{2.6}$$

Some products of acidogenesis can serve directly as a substrate for methane-forming bacteria: this is the case for acetate, the principal substrate for methanogenesis, but also for formate, methanol and methylamine (Gerardi, 2003). Other products, such as ethanol, butyrate and propionate, can be used indirectly by methane-forming bacteria once converted into acetate or formate (Gerardi, 2003). Finally, many products cannot be used by methane-forming bacteria and need to be converted into acetate during a re-fermentation. This is the case for butanol, caproic acid lactate, propanol and succinate (Gerardi, 2003).

(*iii*) *Methanogenesis*. This is the final conversion of the products of the previous reactions into methane. There are three groups of methane-forming bacteria: hydrogenotrophic, acetotrophic and methylotrophic (Gerardi, 2003). A summary of involved bacteria is depicted in Table 2.3.

Hydrogenotropyc methanogens use hydrogen to convert carbon dioxide into methane.

Species	Substrate	Behaviour
Methanosarcima bakerii	Acetate, carbon dioxide, hydrogen, methanol, methylamine	Generalist acetotroph
Methanosaeta concilii	Acetate	Specialist acetotroph
Methanobacterium formicium	Carbon dioxide, formate, hydrogen	Hydrogenotrophic
Methanobacterium thermoantotrophicum	hydrogen, carbon dioxide, carbon monoxide	Hydrogenotrophic
Methanosarcina frisius	Hydrogen, methanol, methylamine	Methylotrophic
Methanosarcina mazei	Acetate, methanol, methylamine	Methylotrophic

Table 2.3 *Exmples of methanogenesis bacteria and substrates. From Gerardi (2003); McMahon et al. (2001).*

Some of them can also use carbon monoxide:

$$\begin{gathered} CO_2 + 4H_2 \rightarrow CH_4 + 2H_2O \ , \\ 4CO + 2H_2O \rightarrow CH_4 + 3CO_2 \end{gathered} \tag{2.7}$$

Gerardi (2003). Acetotrophic methanogens split acetate into methane and carbon dioxide:

$$CH_3COOH \rightarrow CH_4 + CO_2 \tag{2.8}$$

Gerardi (2003). Methylotrophic methanogens use substrates that contain the methyl group (CH_3), for example methanol (CH_3OH) or methylamines ($(CH_3)_3{-}N$):

$$\begin{gathered} 3CH_3OH + 6H \rightarrow 3CH_4 + 3H_2O \ , \\ 4\,(CH_3)_3{-}N + 6H_2O \rightarrow 9CH_4 + 3CO_2 + 4NH_3 \end{gathered} \tag{2.9}$$

Gerardi (2003). Hydrogen-consuming methanogenesis (the first of the Equations 2.7) is the most energetically convenient, but it is not the most common (it contributes for about 30% of the methane yield) due to the limited hydrogen supply inside an anaerobic digester (Gerardi, 2003). However, it is important because it reduces the partial hydrogen pressure, and high hydrogen levels affect adversely both acetotrophic methanogens and some groups of acetate-forming bacteria (Gerardi, 2003; De Bok et al., 2004). The role of hydrogenotrophic methanogens has been recognized as important during the initial phases, but they are in general outperformed by acetoclastics when the digestion process becomes stable (Monteiro, 1997). According to Gerardi (2003), at steady state the maximum methane yield (about 70%) is obtained from acetotrophic methanogenesis (Equation 2.8).

2.1.2 Bacteria Consortia and Syntrophic Relationships

Anaerobic digestion can occur only if the different bacteria groups coexist in a mutually beneficial, or syntrophic relationship, where the products of a group serve as substrate for another (Schink and Stams, 2006). For instance, as already mentioned above, some acetogenic bacteria are adversely affected by the presence of the compounds they produce—acetate, formate (De Bok et al., 2004) and hydrogen (Schmidt and Ahring, 1995)—and therefore benefit of the presence of methanogens. Moreover, the methanogenic bacteria cell wall is sensitive to toxicity from several fatty acids, and therefore can thrive only if such acids are removed by acetogenic bacteria (Gerardi, 2003).

The metabolic efficiency of this cooperation depends on an efficient metabolites transfer between the partners involved (De Bok et al., 2004; Schink and Stams, 2006), and this requires that the distance between the partners is short. For instance, the flux of hydrogen between the hydrogen-forming fermenters and the hydrogen-consuming methanogens is inversely proportional to the distance between the two groups (Schmidt and Ahring, 1995; Schink and Stams, 2006). It has been observed that optimal cooperation is achieved when bacteria form granules in which the partner organisms are evenly distributed (Schink and Stams, 2006), as shown in Figure 2.3. Schmidt and Ahring (1995) verified that the

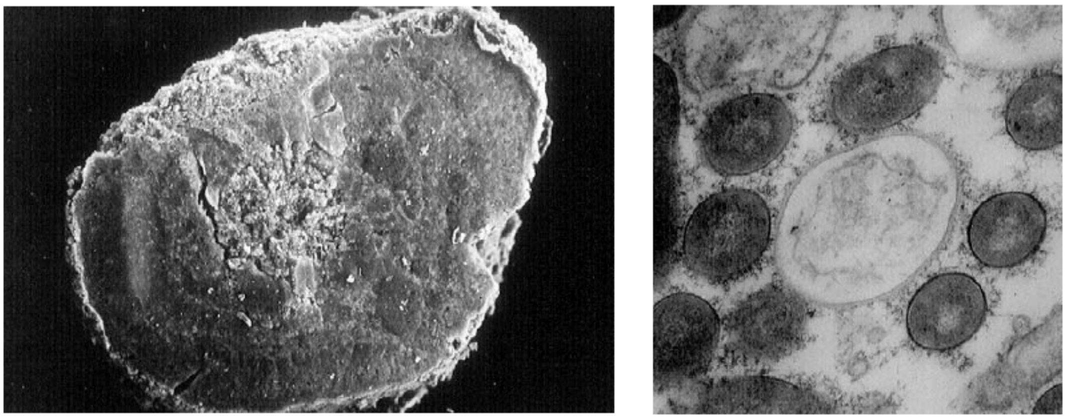
(a) (b)

Figure 2.3 *(a) Scanning electron micrograph image of a granule from an up-flow anaerobic sludge bed reactor (UASB). (b) Transmission electron micrograph image of an ultrathin section of a granule from an UASB-reactor. A syntrophic acetogen is in the middle, surrounded by methanogenic bacteria. De Bok et al. (2004).*

disintegration of granules in a bacteria culture leads to a decrease of the propionate and butyrate degradation by 20% and 34% respectively.

2.2 Factors Affecting Anaerobic Digestion

Anaerobic digestion is sensitive to a large number of factors. The most important are: mixing intensity, temperature, retention time, nutrients concentration, pH and inhibitors concentration. The mixing intensity is described in Section 2.3; all the others are described below.

Temperature. Depending on the temperature range, anaerobic digestion can be psychrophilic (below 20 °C), mesophilic (30—40 °C) and thermophilic (50—60 °C). Psycrophilic, mesophilic and thermophilic digestions involve different bacteria communities, and a change between one to another is in general not possible: change in temperature of 2 °C have been reported to have a negative impact on biogas production (Chae et al., 2008). The psychrophylic rate of digestion is lower than mesophilic, which in turn is slower than thermophilic. However, thermophilic digestion is less favourable due to higher operational costs of heating and a higher sensitivity of bacteria to toxic substances (Gerardi, 2003), and therefore mesophilic digestion is the most preferrable (Sindall, 2014).

Changes in temperature affect the bacteria groups in different ways. Hydrolics and acidogens do not suffer from changes in temperature, while acetate producers and methanogens are more vulnerable, with temperature fluctuations having a stronger impact on the methanogens activity than the absolute value of the temperature (Ward et al., 2008). Each bacteria group has its specific ideal range of temperatures, and therefore fluctuations in temperature can have a negative effect to some groups, and at the same time a positive effect to others (Ward et al., 2008). Consequently, the activity of the different bacteria groups change when the temperature fluctluates; as a consequence of this, volatile fatty acids, alcohols and other intermediary products can undergo a change of concentration, eventually impairing the global digester performance (Gerardi, 2003). For this reason, even slights temperature variations can lead to process failure, and accordingly, Appels et al. (2008) recommend that changes in temperature are less than 0.6 °C per day.

Retention times. It is possible to define the solids retention time and the hydraulic retention time. The former indicates the average time that solids, and the bacteria living on them, spend inside the digester, while the latter refers to the liquid fraction. In a digester with recycle, the solids and hydraulic retention times are decoupled, contrarily to a digester without recycle (Gerardi, 2003).

Methanogens are slow-growing bacteria, and therefore the solids retention time is generally not less than 12 days and often much longer in order to prevent methanogens washout. It is also recognised (Sindall, 2014) that high solids retention times provide the digester a protective buffering against the effects of shock or toxic loadings. However, higher retention times require larger digesters and, consequently, larger capital costs (Gerardi, 2003). Conversely, the volatile solids rely on the hydraulic retention time to be degraded to methane and carbon dioxide. However, increases greater than 12 days do not lead to a significantly increased removal of volatile solids (Gerardi, 2003).

Nutrients. The nutrients required by the bacteria to thrive consist of macronutrients and micronutrients. Macronutrients are nutrients required in relatively high quantities from all the bacteria groups, and consist of nitrogen (in the form of ammonical nitrogen, $\mathrm{NH_4^+}$–N) and phosphorus (ortophosphate-phosphorus, $\mathrm{HPO_4^-}$–P). The nutrient requirements vary considerably depending on the organic loading rate, but a rule of thumb, based on an empirical formula for cellular material, $\mathrm{C_5H_7O_2NP_{0.1}}$, can be introduced. It consists of a COD:N:P ratio of 1000:7:1 for high strength wastes, and a ratio of 350:7:1 for low loadings (Gerardi, 2003; Sindall, 2014). Alternatively, a check of the $\mathrm{NH_4^+{-}N}$ and $\mathrm{HPO_4^-{-}P}$ concentration in the effluent can be performed in order to prevent a lack of these elements (Gerardi, 2003). Gerardi (2003) also recommends a minimum concentration of the former of 5 $\mathrm{mg}\,\ell^{-1}$, and of the latter of 1—2 $\mathrm{mg}\,\ell^{-1}$.

Micronutrients are required in relatively small quantities. For acetotrophic methanogens, elements like cobalt, iron, nickel and sulphur are needed in traces. In general, also barium, calcium, magnesium, molybdenum, selenium, sodium and tungsten are to be considered essential micronutrients for the methanogens (Gerardi, 2003). In general, these micronutrients are present in sufficient concentrations in municipal wastewaters, but it is often necessary for industrial wastewaters to dose digesters with additional specific micronutrients (Gerardi, 2003).

pH. Most fermentative bacteria can thrive in a wide range of pH, between 4.0 and 8.5; however, what they produce as by-product does depend on pH, with acetic and butyric acid being produced at low pH, and acetic and propionic acid at high pH. On the other hand, methanogens can be more affected by pH, with an ideal value between 6.8 and 7.2 (Appels et al., 2008). Because of this difference of pH ranges, the industrial anaerobic process is often designed as in two separate stages. In this way, a lower pH is present in the first stage in order to enhance hydrolysis and acidogenesis, and conversely methanogenesis is optimised in the second stage by maintaining a more basic pH. In one-stage digesters (or in the second stage of two-stages digesters), is common to set a pH of 6.8—7.2, as a lower pH would result to too high levels of acidogens, and this condition could generate an increase of volatile fatty acids, which in turn would further lower the pH and, finally, bring to the failure of the digestion process (Rajeshwari et al., 2000).

During a normal digestion process, a balance exists between the production of volatile fatty acids due to acidogens activity, and the production of alkaline compounds such as carbon dioxide, ammonia and bicarbonate, due to the activity of methanogens (Ward et al., 2008). Appels et al. (2008) recommend a molar ratio of bicarbonate to volatile fatty acids of at least 1.4:1 in order to guarantee process stability. However, it has been shown that the stability of such ratio is more important than its absolute value (Appels et al., 2008).

Inhibitors. Literature reports a broad variety of chemicals which are toxic or inhibitory for microbial growth. The inhibitory effect is generally detected from a decrease in biogas production and the accumulation of volatile fatty acids (Sindall, 2014). According to Chen et al. (2008), the literature, the concentrations at which the inhibitory effect take place vary considerably.

The presence of ammonia is due to the degradation of proteins, urea and other nitrogenous molecules, and as nitrogen is an essential nutrient, an ammonia concentration of about 200 $\mathrm{mg}\,\ell^{-1}$ is beneficial for anaerobic digestion. However, ammonia is also considered to be an inhibitor for methanogens, and literature reports a 50$\%$ reduction of methane production for concentrations between 1.7 and 14 $\mathrm{g}\,\ell^{-1}$ (Chen et al., 2008).

Salt concentrations, especially cations, cause bacterial cells dehydration due to osmosis. Many substances reported as inhibitors are also essential micronutrients, but act as inhibitors when their concentration exceeds a critical value. However, there is no universal agreement on such critical values; and in fact, the conclusions reported in the literature diverge considerably with one another, as evident from Table 2.4.

Table 2.4 *Inhibitory effects of cations on anaerobic digestion. Sindall (2014)*

Cation	$\mathrm{mg}\,\ell^{-1}$	Result	Reference
Al^{3+}	1000 $\mathrm{Al\,(OH)_3}$ for 59 days	Specific activity of methanogens and acetogens decreased by 50% and 72% respectively	Cabirol et al. (2003)
	2500	Tolerated after acclimation	Jackson-Moss and Duncan (1991)
Ca^{2+}	< 7000	No inhibitory effect	Jackson-Moss et al. (1989)
	200	Optimal for methanation of acetic acid	McCarty and Kugelman (1964)
	2500—4000	Moderately inhibitory	”
	8000	Strongly inhibitory	”
Mg^{2+}	720	Optimal	Ahring et al. (1991)
	400	Growth ceases	Schmidt and Ahring (1993)
K^{+}	< 400	Enhance performance	McCarty and Kugelman (1964)
	> 400	Inhibitory	”
Na^{2+}	100—200	Beneficial	McCarty and Kugelman (1964)
	230	Optimal for aceticlastic methanogens	Kugelman and Chin (1971)
	350	Optimal for hydrogenotrophic methanogens	Patel and Roth (1977)
	3500—5500	Moderately inhibitory	McCarty and Kugelman (1964)
	8000	Strongly inhibitory	”

2.3 Mixing

Mixing can be defined as: “The reduction of inhomogeneity in order to achieve a desired process result. The inhomogeneity can be one of concentration, phase, or temperature. Secondary effects, such as mass transfer, reaction, and product properties are usually the critical objectives” (Amanullah et al., 2003). Mixing is of critical importance for anaerobic digestion for the following reasons:

(*i*) mixing brings bacteria and nutrients together (Zickefoose and Hayes, 1976);

(*ii*) mixing contributes to create a homogeneous environment for anaerobic digestion by reducing temperature, pH, and concentration gradients (Appels et al., 2008; Sindall, 2014);

(*iii*) mixing minimises the formation of grit and scum, and contributes to reducing the extent of the dead zones (Zickefoose and Hayes, 1976).

2.3.1 Methods of Mixing

Mixing for industrial anaerobic digesters can be mechanical, gas and recirculating. Mechanical mixing is the most efficient in terms of mixing input power per unit of volume (Brade and Noone, 1981), but is prone to problems such as wear and expensive maintenance due to the presence of mobile devices (e.g., impellers, shafts, ball bearings) inside the digester. Recirculation mixing uses pumps to channel sludge out of the digester through external pipes and again into the digester, but in another location.

Gas mixing can be unconfined or confined. In unconfined mixing, biogas is collected from the top of the digester and pumped at the bottom through nozzles. The bubbles rise in columns via buoyancy and transfer momentum to the surrounding sludge. This momentum transfer takes place due to the push force that the bubbles exert to the surrounding liquid, and the riptide effect arising from the low-pressure region created by the motion of the bubbles. In confined mixing, biogas is collected and injected in the same way, but the discharge takes place inside confined tubes within the digester. This generates a forced sludge flux throughout the tubes, which in turn creates convective currents out of them (Tchobanoglous et al., 2010).

As explained in Section 3.8, Wu (2010a) confirmed that mechanical mixing is the most efficient method, and also showed that recirculating mixing is the least efficient.

2.3.2 Industrial Mixing

The importance of an efficient mixing for an efficient anaerobic digestion and gas production in industry is generally recognised, but universal consensus on what efficient mixing means is still lacking (Appels et al., 2008), and digester design is still based on empiricism and rule of thumb rather than science. This is reflected, for instance, in Auty and Marquet (2009), where a huge variation in how anaerobic digesters are designed and operated across the UK is described: some digesters use continuous mixing, while others use an alternated setup with five minutes mixing is active only five minutes through one hour, yet without any apparent difference in terms of biogas production. This can be due to the wide range of design variables reported by Auty and Marquet (2009), which change depending, for instance, on the particular digester depending on total solids, temperature, biological loading and treatment that the sludge underwent before being injected into the digester. Such variables include sludge rheology, digester geometry, method of mixing, mixing energy input and mixing and retention times.

Sindall (2014) reports a trial carried out with digesters in Loughborough, UK, which concluded that continuous mixing of mesophilic anaerobic digesters produced more gas than periodic mixing. However, a balance between the energy cost of continuous mixing against the benefit of the increased biogas production was not mentioned.

2.4 Previous Studies on the Effects of Mixing

There is a body of literature which suggests that anaerobic digestion may work more efficiently with minimal mixing. However, there is no definitive conclusion as to what constitutes minimal mixing and what constitutes an efficient mixing regime (Sindall, 2014). Even more importantly, it is difficult to compare results from different works in which different gas measurement methods have been employed, and quantitative measurements of mixing have often not been reported. Shear rate is a generally recognised parameter to classify mixing in a vessel (Tchobanoglous et al., 2010), but only few works provided some information about it: Hoffmann et al. (2008a) through a radioactive particle tracking technique (CARPT); and Bridgeman (2012); Sindall et al. (2013) through a comparison with computational fluid dynamics (CFD). The CFD framework is treated extensively in Chapter 3; Bridgeman (2012); Sindall et al. (2013) confirmed that a lower level of mixing does not hinder, and indeed can increase, the biogas production. Bridgeman (2012) observed that biogas production did not fall if the average shear rate inside a laboratory-scale digester fell from 22 to 0 s^{-1}. Sindall et al. (2013) showed that biogas production in similar digesters increased when average shear rate decreased from 9.7 to 7.2 s^{-1}, and conversely decreased when shear rate increased from 9.7 to 14.3 s^{-1}, so implying a threshold of biogas production performance at 9.7 s^{-1}.

2.4.1 Effects of Mixing Intensity

Stroot et al. (2001) performed experiments on laboratory-scale digesters. Continuous and minimal mixing were applied, and it was showed that minimal mixed digesters were more stable. It was also observed that digesters with a history of unstable operation respond to overloading with greater resilience compared to a stable digester. Finally, unstable digester running under continuous mixing were reported to be stabilised by switching to minimal mixing.

Ong et al. (2002) performed experiments with impeller-mixed laboratory-scale digesters filled with cow manure. Continuous and intermittent mixing were tested. It was shown that the two mixing regimes led to comparable biogas yields over 70 days, but the produced biogas experienced difficulty in escaping from the manure in the absence of mixing. In the same work, it was also observed that a lower level of mixing around the bottom of the tank, achieved by lifting the paddles, produced an increase of biogas production. This was attributed to the formation of a solid layer at the bottom, resulting in a lower methanogens washout. Finally, a comparison between mixed and unmixed setup was undertaken. In the latter case, the biogas production was higher, and also a higher concentration of extracellular polymeric substances was found. Extracellular polymeric substances, according to Lin et al. (2014), increase adhesion of bacteria thereby preventing washout, and help bacteria to form aggregates.

Similar results were fond in thermophilic laboratory and pilot scale digester by Kaparaju et al. (2008). Furthermore, it was shown that the higher methane generation potential resided in the floating solids at the top (with an abundance of *Methanobacteria*) and in the settled solids at the bottom (rich in *Methanosarcina*) present in the intermittently mixed digesters. This stratification was not observed in the continuously mixed digester, where biogas production dropped. A description of the effects of mixing on bacteria is reported in Section 2.4.3.

Vavilin and Angelidaki (2005) performed experiments on mesophilic batch laboratory-scale digesters, and compared the results with a simplified computer model of the anaerobic digestion process. Similar results were obtained. In particular, a comparison of the experimental data with the results of the numerical model showed that the methanogen bacteria clusters could thrive properly without being negatively influenced by high volatile fatty acid concentrations only under low mixing levels. However, in special cases in which the methanogens population was high, hydrolysis became the rate-limiting process, and in such cases, mixing might improve hydrolysis and, consequently, increase the overall digestion rate.

Gómez et al. (2006) studied the mesophilic digestion, with the influent being a mixture of sludge (22% of influent) and a vegetable and fruit waste (78%) in laboratory-scale digesters. Despite the problems affecting the measurements listed in Sindall (2014), it was shown that biogas production from co-digestion was higher due to the increased volatile solids in the feed. The authors also showed that a reduction in the level of mixing (from high to low in their work) did not affect biogas production. On the other hand, both the biogas production and the methane concentration were reported to be low in unmixed conditions if compared with low mixing conditions.

2.4.2 Effects of Mixing Method

In a series of articles (Karim et al. 2005a,b,c), the operation of laboratory-scale digesters with different methods of mixing (impeller, confined gas and recirculation mixing), different biogas mixing intensities and different Total Solids (TS) concentration (5%, 10% and 15%) was studied. As regards the biogas mixing, no effect on gas production was observed for changes of mixing intensity and clearance height of the draft tube and, accordingly, it was concluded that changes in the "mixing conditions" (meaning, for the authors, mixing intensity and clearance height of the draft tube) do affect biogas production. As regards the effect of the "methods of mixing" (meaning, for the authors, impeller, gas and recirculated mixing), the digesters fed with 5% TS sludge behave similarly regardless of the mixing method. At 10% TS, the gas-mixed digester was reported to produce less biogas than the impeller and recirculated-mixed digester, and the unmixed digester was observed to behave even worse. At 15% TS, recirculated mixing was impossible due to the high viscosity of the sludge, and the gas-mixed digester showed severe sedimentation problems. Finally, mixing was reported to be beneficial in stabilising a digester after undergoing a shock consisting of a change in feed, irrespective of the method of mixing, if compared with the non-mixed case.

2.4.3 Effects of Mixing on Bacteria

As discussed in Section 2.1.1, the largest contribution to biogas production arises from acetothopic methanogens activity, that is *Methanosarcina* and *Methanosaeta* (Miyamoto, 1997). Bacteria belonging to these two genera display different behaviour: in particular, from the kinetic coefficients reported in Conklin et al. (2006), it is possible to imply that the *Methanosaeta* populations are favoured under conditions of low acetate concentrations or of high solids retention, and that *Methanosarcina* dominate in the opposite case.

Mixing has different impacts on *Methanosarcina* and *Methanosaeta* because of their different community structures. *Methanosarcina* populations consist of single, 2 μm diameter coccoidal cells (Ni et al., 1994), or in groups of up to 3 mm diameter shaped as blackberries (Schmidt and Ahring, 1999). Conversely, *Methanosaeta* are straight rod-shaped cells with flat ends in stiff chains, or filaments, of 8 to 100 μm length, which form flocs of diameter of up to 20—30 mm (Janssen, 2003). *Methanosarcina* and *Methanosaeta* cultures are shown in Figure 2.4. It is reasonable to consider cells as potentially affected by turbulence if their size is comparable or larger than the scale of the smallest turbulent eddies, or Kolmogorov dissipation range (see Section 3.3.1), inside the vessel (Amanullah et al., 2003). According to Amanullah et al. (2003), such the linear dimension of such eddies is around 10-100 μm, and therefore it is reasonable to assume that the filaments formed by *Methanosaeta* are more likely to be adversely affected by mixing than *Methanosarcina* (Sindall, 2014). According to Joshi et al. (1996), under the effect of turbulent shear stress the filamentous cells, such as *Methanosaeta*, undergo effects such as filemant breakage,

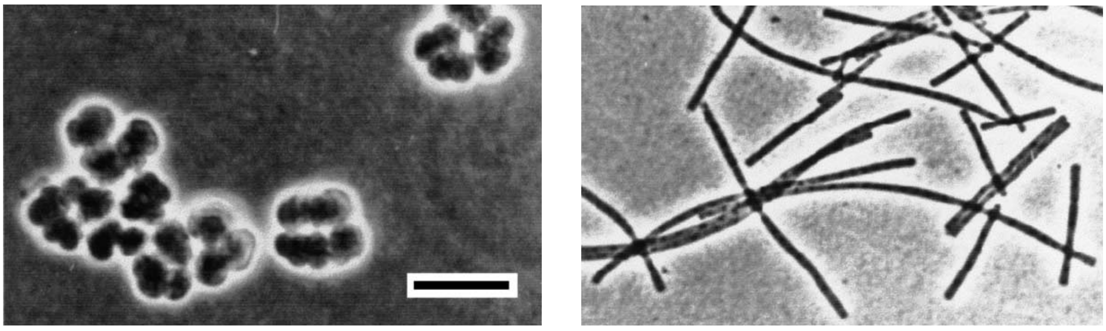

(a) (b)

Figure 2.4 *Phase contrast photomicrograph of methanogen bacteria, Janssen (2003). Bar = 10* μm *for all panels. (a)* Methanosarcina. *(b)* Methanosaeta.

or changes of development, and changes of cell morphology leading to a reducted mass transfer into the cells. It is therefore reasonable to conclude that *Methanosaeta* are likely to be more adversely affected when the level of mixing is increased, and consequently that they are outperformed by *Methanosarcina* when the mixing intensity increases.

Hoffmann et al. (2008a) showed that the intensity of mixing did not affect the overall number of bacteria but, conversely, influenced the relative metanogens' relative abundance. In particular, a drop in the *Methanobacteriaceae* population at higher mixing levels was observed, and constant levels of *Methanobacteriaceae* and low populations of *Methanococcaceae* were observed at lower levels of mixing.

McMahon et al. (2001)'s work is the continuation of Stroot et al. (2001)'s. While Stroot et al. (2001) analyzed the biogas yield and the stability of laboratory-scale digesters, McMahon et al. (2001) focussed on the bacteria group present and their relative abundance. As regards the relative abundance of *Methnosarcina* and *Methanosaeta*, the formers were found to predominate with high acetate values and consequently in unstable digester, while the converse held for *Methanosaeta*. As regards the mixing intensity, the overall density of methanogens was found to be much higher in digesters under minimal mixing conditions if compared with digesters under continuous mixing. Furthermore, the density of methanoges was found to increase when the mixing was changed from continuous to minimal, with *Methanosarcina* being the most populous group. Conversely, the methanogens density decreased when the mixing was changed from minimal to continuous.

2.5 Summary of the Previous Works and Research Gaps

The biochemistry of anaerobic digestion has been briefly described, and many factors that affect it have been reviewed. The biochemical processes involved are undoubtely complex, but they have been understood well. The factors that affect the process are well documented, but the understanding of their role varies depending on the given factor taken into consideration For instance, the effects of temperature have been clarified with accuracy, while the concentrations of inhibitory or required compounds are more contentious.

Mixing has been recognised to bring bacteria and substrate into contact, so that the digestion process can proceed efficiently, and other benefits, such as reducing temperature, pH and concentration gradients, and in general, creating an environment suitable for anaerobic digestion to take place, are recognised. However, a general consensus as regards what constitutes an efficient mixing regime is still to be reached (Bridgeman, 2012; Sindall et al., 2013). Anyway, it has been recognised that mixed vessels perform better in terms of both biogas production and process stability, when compared with unmixed. However, higher levels of mixing result to be detrimental both to production and stability, and therefore lower levels are preferable. Similarly, intermittent mixing is preferable to continuous. Finally, the impact of mixing is less pronounced at low TS concentrations.

This being the situation, it is evident that the knowledge of mixing is fundamental, but we still have far from a comprehensive understanding. In particular, a quantitative understanding on mixing based on unambiguous parameters such as average shear rate is still in its infancy. Furthermore, an understanding of the mechanisms that drive the mixing—i.e., how the nutrients are brought in contact with the bacteria, and how the internal gradients are uniformed—are still lacking.

Finally, all the research reported in this review considers only laboratory and pilot-scale setups, with the sole exception of the trial cited in Sindall (2014). The behaviour of a full scale digester may be very different, especially as regards the flow patterns, and therefore research on full-scale anaerobic digesters is surely desirable.

3

Fluid Dynamics Modelling

"When I meet God, I am going to ask him two questions: Why relativity? And why turbulence? I really believe he will have an answer for the first."

Werner Heisenberg (1976).

COMPUTATIONAL FLUID mechanics (CFD) has proved to be effective in deepening the knowledge of anaerobic digestion, in particular in mixing. Several works have proposed CFD models of sludge with the ultimate goal of improving mixing in anaerobic digestion, which is known to be an energy-intensive operation. In this chapter, a description of the CFD framework and of the relevant literature on CFD modelling for anaerobic digestion is given, and then the research gaps are analysed.

First, a general description of fluid mechanics is given. The Navier-Stokes equations and the underlying hypotheses are explained in Section 3.1, and then a more detailed dissertation on rheology, turbulence and turbulence modelling are reported in Sections 3.2 and 3.3. Then, computational fluid mechanics is introduced in Section 3.4, and particular attention is given to multiphase modelling in Section 3.5. A literature review of sludge and CFD modelling of anaerobic digestion is reported in Sections 3.6 and 3.7 respectively, and a particular focus is given to the relevant literature on multiphase CFD modelling for anaerobic digestion in Section 3.8. Finally, a summary of the existing literature is reported in Section 3.9, together with the knowledge gaps.

3.1 Navier-Stokes Equations

A fluid can be identified by the property of "deforming continuously under the action of a shear force, however small" (Kundu and Cohen, 2008). A fluid is described as a continuum when its molecules are considered much smaller than any small ("infinitesimal") volume element (Landau and Lifshitz, 1987). Under this approximation, there are two approaches to describe a fluid as a continuum. One consists of dividing it into infinitesimal elements of constant mass and following their trajectory—this is called Lagrangian description. The other one, called Eulerian description, consists of considering immobile infinitesimal control volumes, and building up the velocity field.

A simple way to provide a description for a fluid is to derive a set of equations for the velocity field $\mathbf{u}(\mathbf{x},\, t)$. The assumptions are conservation of mass, Galilean invariance and isotropy in the local rest frame, the latter being defined as the rest frame of an infinitesimal element of fluid. Two additional, but not general, hypotheses are constant density and constant viscosity. The former does not hold for gases but reproduces well the behaviour of liquids such as water or sludge. The latter is necessary to derive the Navier-Stokes equations, but it is understood that does not hold for a large variety of liquids, including sludge. Later on, in Section 3.2 an explanation of how to remove this constraint is provided.

With the hypotheses above, a system of four differential equations can be derived for the velocity field $\mathbf{u}$ and the pressure field p:

$$\nabla \cdot \mathbf{u} = 0 \,, \tag{3.1}$$

$$\rho\, \partial_t \mathbf{u} + \rho \nabla \cdot (\mathbf{u} \otimes \mathbf{u}) = -\nabla p + \nabla \cdot \tau + \mathbf{b} \,. \tag{3.2}$$

The term $\mathbf{b}$ takes into account eventual non-gravitational body forces. The shear stress tensor τ can be composed by any combination of spatial derivatives of $\mathbf{u}$ that form a symmetric second-rank tensor. The Newtonian hypothesis consists of considering only linear first order derivatives:

$$\tau_{ij} = \mu \left(\partial_i u_j + \partial_j u_i \right) \,, \tag{3.3}$$

where μ is the dynamic viscosity. Equation 3.3 is often written in the equivalent form:

$$\tau_{ij} = \mu \, \dot{\gamma}_{ij} \,, \tag{3.4}$$

where the shear rate $\dot{\gamma}$ is defined in terms of derivatives of $\mathbf{u}$:

$$\dot{\gamma}_{ij} = \partial_i u_j + \partial_j u_i \,. \tag{3.5}$$

Equations 3.1 and 3.2 are called the Navier-Stokes Equations and, together with the equations 3.4 and 3.5, provide a closed set of equations for the Eulerian velocity and pressure fields. A derivation of these equations is reported in Appendix A.

A result of the Equations 3.1 and 3.2 is the following. If we take the divergence of Equation 3.2 (we do not consider body forces now) and consider Equation 3.4, we obtain:

$$\left(\rho \, \partial_t + \rho \, \mathbf{u} \cdot \nabla - \mu \nabla^2 \right) \nabla \cdot \mathbf{u} = - \left(\nabla^2 p + \rho \, \partial_i u_j \, \partial_j u_i \right) \tag{3.6}$$

that is, the condition of zero-divergence (Equation 3.1) is equivalent to the Poisson equation for the pressure:

$$\frac{1}{\rho} \nabla^2 p = - \partial_i u_j \, \partial_j u_i \,. \tag{3.7}$$

3.2 Fluid Rheology

The Newtonian approximation depicted in Equation 3.3 is valid for a wide variety of problems. Nevertheless, it fails with many types of fluids—in particular, it fails with sludge. In these cases, the shape of τ depends of the particular molecular characteristics of the liquid in study, and therefore needs modelling. In many models, τ is still assumed to depend symmetrically on the first derivatives of $\mathbf{u}$ only, but the dependence is not linear. Rather than changing the formulation of Equation 3.4, it is preferred to include the non-linear dependence on $\dot{\gamma}$ into μ. Therefore, instead of a constant viscosity, an effective, or apparent, viscosity, dependant on a number of parameters and the shear rate magnitude $|\dot{\gamma}|$ is provided. $|\dot{\gamma}|$ is defined as follows:

$$|\dot{\gamma}| = \frac{1}{\sqrt{2}}\sqrt{\dot{\gamma}_{ij}\,\dot{\gamma}_{ij}}\ . \tag{3.8}$$

A variety of models has been provided in the literature (Kennedy and Zheng, 2013; Eshtiaghi et al., 2012):

Power-law model:

$$\mu = K\,|\dot{\gamma}|^{n-1}\ , \tag{3.9}$$

where n is the power-law index, and K the consistency coefficient. Depending of the value of n, a power-law fluid can be pseudoplastic ($0 < n < 1$) or dilatant ($n > 1$). In the former, the effective viscosity decreases when the shear rates increase; the contrary in the latter. Equation 3.9 holds only for an interval $\left(|\dot{\gamma}|_{\mathrm{min}}\,, |\dot{\gamma}|_{\mathrm{max}}\right)$. Out of that interval, the viscosity takes a constant maximum or minimum value.

Bird-Carreau model:

$$\frac{\mu - \mu_\infty}{\mu_0 - \mu_\infty} = \left(1 + \lambda^2\,|\dot{\gamma}|^2\right)^{\frac{n-1}{2}}\ . \tag{3.10}$$

Here, in addition to the power-law index n, three other consistency coefficients, μ_0, μ_∞ and λ, are present.

Cross model:

$$\mu = \frac{\mu_0}{1 + (\lambda\,|\dot{\gamma}|)^{1-n}}\;. \tag{3.11}$$

Some models require a minimum non-zero shear stress ("yield stress") τ_0 before the fluid is displaced. Strictly speaking, materials with this behaviour are not fluids as they fail to display infinitesimal deformation under an infinitesimal shear force, and they are better described as plastics (Kundu and Cohen, 2008). The literature describes some models of plastics (Eshtiaghi et al., 2012):

Bingham model:

$$\tau_{ij} = \tau_0\,\frac{\dot{\gamma}_{ij}}{|\dot{\gamma}|} + \mu\,\dot{\gamma}_{ij}\;. \tag{3.12}$$

The Bingham model describes a material that does not experience deformation for shear stress less than τ_0 , and then behaves like a Newtonian fluid when the shear stress exceeds τ_0 .

Casson model:

$$\tau_{ij} = \left(\sqrt{\mu} + \sqrt{\frac{\tau_0}{|\dot{\gamma}|}}\right)^2 \dot{\gamma}_{ij}\;. \tag{3.13}$$

The Casson (1959) model is similar to the Bingham, but the transition occurs smoothly.

Herschel-Bulkley model:

$$\tau_{ij} = \tau_0\,\frac{\dot{\gamma}_{ij}}{|\dot{\gamma}|} + K\,|\dot{\gamma}|^{n-1}\,\dot{\gamma}_{ij}\;. \tag{3.14}$$

The Herschel-Bulkley model describes a material that does not experience deformation for shear stress less than τ_0 , and then behaves like a power-law fluid when the shear stress exceeds τ_0 .

A particular class of fluid consists of *thixotropic* fluids. Their peculiarity consists of the fact that they retain memory of the stress they undergo. The molecules of a thixotropic fluid are bound together by weak bonds that are easily broken by shear force. Therefore, when subjected to a constant shear, they oppose a higher resistance when the shear starts. Then the inter-molecules bonds are gradually broken by the shear force and the viscosity falls gradually accordingly (breakdown phase) until a regime value, corresponding to a complete breakdown, is reached. When the fluid is at rest again, the inter-molecule bonds are gradually rebuilt, and the viscosity gradually increases (build-up phase), until the original value is reached if a sufficient rest time is provided (Barnes, 1997). If subjected to a step-wise stress, according to Barnes (1997) the typical response of a thixotropic material is:

$$\frac{\mu - \mu_\infty}{\mu_0 - \mu_\infty} = 1 - e^{(-t/\tau)^r} \ . \tag{3.15}$$

Viscosity depends on temperature, and different models are proposed in several books (e.g., Kennedy and Zheng 2013). In general, the viscosity μ is multiplied by a correction factor a dependant on the temperature T and a number of parameters. The first model that incorporated the effect of temperature into the viscosity was Reynolds model (Reynolds, 1886):

$$a = \exp\left(-bT\right) \ , \tag{3.16}$$

where b is an empirical parameter. A more accurate model, widely employed in the polymers industry (Kennedy and Zheng, 2013), is the Williams-Landel-Ferry model (Williams et al., 1955):

$$a = \exp\left[\frac{-C_1^g\left(T - T_g\right)}{C_2^g + T - T_g}\right] \ , \tag{3.17}$$

where C_1^g and C_2^g are constant coefficients and T_g is the glass transition temperature. According to Kennedy and Zheng (2013), this model is generally appliable to amorphous polymers in the temperature range $T_g < T < T_g + 100$ °C. For higher temperatures, or where T_g is irrelevant (or not definible), the Arrhenius equation (Arrhenius, 1889) is more appropriate (Kennedy and Zheng, 2013):

$$a = \exp\left(\frac{-E_a}{RT}\right) \, . \tag{3.18}$$

Here, E_a is the activation energy per mole, and R is the universal gas constant. The latter model is the one which has commonly been employed in sludge viscosity (e.g., Wu and Chen 2008; Bridgeman 2012) because T_g is not defined for the sludge.

3.3 Turbulence

Velocity, pressure, coordinates, time and spatial derivative and body force can be made dimensionless by rescaling them by the characteristic length of the system $\mathcal{L}$ and the characteristic velocity $\mathcal{U}$:

$$\begin{aligned} \hat{\mathbf{u}} &\equiv \frac{1}{\mathcal{U}}\mathbf{u}\,, \quad \hat{p} \equiv \frac{1}{\rho\mathcal{U}^2}p\,, \quad \hat{\mathbf{x}} \equiv \frac{1}{\mathcal{L}}\mathbf{x}\,, \\ \hat{\partial}_t &\equiv \frac{\mathcal{L}}{\mathcal{U}}\partial_t\,, \quad \hat{\nabla} \equiv \mathcal{L}\nabla\,, \quad \hat{\mathbf{b}} \equiv \frac{\mathcal{L}}{\mathcal{U}^2}\mathbf{b}\,. \end{aligned} \tag{3.19}$$

With these redefinitions, the Navier-Stokes equations 3.2 can be cast into a dimensionless form:

$$\hat{\partial}_t\hat{\mathbf{u}} + \hat{\nabla}\cdot(\hat{\mathbf{u}}\otimes\hat{\mathbf{u}}) = -\hat{\nabla}\hat{p} + \frac{1}{\mathrm{Re}}\hat{\nabla}\cdot\hat{\dot{\gamma}} + \hat{\mathbf{b}}\,. \tag{3.20}$$

The dimensionless Reynolds number, Re, is defined as:

$$\mathrm{Re} \equiv \frac{\rho\mathcal{L}\mathcal{U}}{\mu} = \frac{\mathcal{L}\mathcal{U}}{\nu}\,, \tag{3.21}$$

where $\nu \equiv \mu\rho$ is the kinematic viscosity. When the Reynolds number is small, the viscous dissipation term in Equation 3.20 is much larger than the inertial one, and the equations become linear. Conversely, when the Reynolds number grows, the inertial term becomes more and more marked, and the non-linear behaviour more and more important. Therefore, the Reynolds number can be interpreted as the ratio of inertial to viscous forces. When the Reynolds number is larger than a given limit value[1], the flow starts displaying an acute sensitivity to small perturbation, that is called chaotic behaviour, and the velocity field becomes a random variable (Pope, 2000).

3.3.1 The Kolmogorov Description of Turbulence

A beautiful description of turbulence was provided by Richardson (1922) with the concept of energy cascade, and by the work carried out by Kolmogorov in 1941 (Kolmogorov, 1991c,a,b). Both are reported by Pope (2000). According to Richardson's idea, a turbulent flow is composed of eddies of different sizes, an eddy being a region of size ℓ, average velocity u_ℓ and timescale $\tau_\ell \equiv \ell/u_\ell$, in which the flow motion is "at least moderately coherent" (Pope, 2000). The largest eddies have size ℓ_0 of the order of magnitude of $\mathcal{L}$ and velocity u_0 of the same order of $\mathcal{U}$, and take the energy from the mean flow; they break up into smaller eddies that yet break up into even smaller eddies. In this way, the energy is transferred from the main flow to smaller and smaller eddies. The process continues until the eddy Reynolds number $\mathrm{Re}_\ell \equiv u_\ell\,\ell/\nu$ is small enough for the dissipative term of Equation 3.20 to dissipate the energy (Pope, 2000). From dimensional considerations, the energy dissipation rate is of the order of magnitude of (Pope, 2000):

$$\varepsilon \sim \frac{u_0^2}{\tau_0} = \frac{u_0^3}{\ell_0}\,. \tag{3.22}$$

Kolmogorov's theory enriches Richardson's description by introducing the following hypotheses (Pope, 2000).

---

[1] This limit value depends on the particular system taken into consideration. For instance, in pipe flow the limit value is $\mathrm{Re} = 2000$ while for a body falling into a viscous medium it is $\mathrm{Re} = 10$ (Kundu and Cohen, 2008).

1. Kolmogorov's hypothesis of local isotropy: at a sufficiently high Reynolds number, the small-scale turbulent motions are statistically isotropic.
2. Kolmogorov's first similarity hypothesis: at a sufficiently high Reynolds number, the small-scale motions have a universal form that is uniquely determined by the kinematic viscosity ν and the energy dissipation rate ε.
3. Kolmogorov's second similarity hypothesis: at a sufficiently high Reynolds number, the small-scale motions have a universal form that is uniquely determined by ε, independent of ν.

Kolmogorov's description cannot provide an accurate description of any turbulent flow. In this regard, there is a famous objection by Landau pointing out that the dissipation ε can depend on large-scale structures, that in turn are dependant on the particular problem addressed, and therefore a universal form for small-scale motions (Kolmogorov hypotheses 2 and 3) cannot exist (Frisch, 1995). Moreover, backscatter phenomena in which energy is transferred from smaller to larger eddies, can be present, even though the backscatter energy transfer is generally much lower than the energy cascade transfer rate (Pope, 2000). Nevertheless, this description still provides a useful insight of turbulent phenomena.

As a consequence of the Kolmogorov hypotheses, there are length, velocity and time scales, known as Kolmogorov scales, that identify the smallest possible eddies:

$$\begin{aligned} \eta &\equiv \left(\nu^3/\varepsilon\right)^{1/4} \sim \mathrm{Re}^{-3/4}\,\ell_0 \ , \\ u_\eta &\equiv (\nu\varepsilon)^{1/4} \ \sim \mathrm{Re}^{-1/4}\,u_0 \ , \\ \tau_\eta &\equiv (\nu/\varepsilon)^{1/2} \sim \mathrm{Re}^{-1/2}\,\tau_0 \ . \end{aligned} \tag{3.23}$$

According with the Kolmogorov hypotheses, the eddy length ℓ range can be split into different ranges and subranges (Figure 3.1). The main division consists of the energy-containing range ($\ell_{\mathrm{EI}} < \ell < \ell_0$), and the universal equilibrium range ($\ell < \ell_{\mathrm{EI}}$). Arguments propend to set $\ell_{\mathrm{EI}} \sim \ell_0/6$ (Pope, 2000). The Kolmogorov hypotheses 1 and 2 are assumed to hold in the universal equilibrium range, while the energy production range is dominated by large, anisotropic and problem-dependant eddies that take the energy directly from the main flow. Arguments show that approximately the 80% of the energy is contained in the energy-containing range (Pope, 2000). Next, the universal equilibrium range can be split into two subranges: the dissipation subrange ($\ell < \ell_{\mathrm{DI}}$), and the inertial subrange ($\ell_{\mathrm{DI}} < \ell < \ell_{\mathrm{EI}}$). Arguments propend to set $\ell_{\mathrm{DI}} \sim 60\eta$ (Pope, 2000). In the inertial subrange, the Reynolds number is high enough to make the dissipation term of Equation 3.20 negligible, and therefore the Kolmogorov hypothesis 3 holds. On the contrary, the dissipation term is important in the dissipation range, and viscous dissipation occurs. In conclusion, the Kolmogorov hypotheses, together with Richardson's concept of energy cascade, build up a model in which energy is extracted from the main flow by eddies in the energy-containing range, is passed down to smaller and smaller eddies in the inertial subrange and is finally dissipated by the smallest eddies in the dissipation range (Pope, 2000).

The turbulence energy E can be decomposed into Fourier modes $E(\kappa)$ dependant on the eddy wavenumber $\kappa \equiv 2\pi/\ell$. A general form for the energy spectrum can be deduced from the Kolmogorov hypotheses, and respects the following characteristics (Pope, 2000): *(i)* in the inertial subrange, $E(\kappa)$ exhibits a power-law behaviour with exponent $-5/3$; *(ii)* in the energy-containing range, the power-law exponent is 2; *(iii)* in the dissipation range,

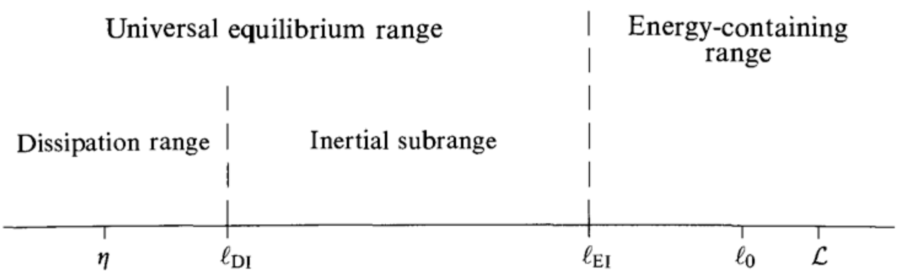

Figure 3.1 *Kolmogorov length scales and ranges (Pope, 2000).*

$E(\kappa)$ decays exponentially. An example of energy spectrum is depicted in Figure 3.2, and a model for the energy spectrum function can be built as follows (Pope, 2000):

$$E(\kappa) = C\,\varepsilon^{2/3}\kappa^{-5/3}\,f_{\ell_0}(\kappa\ell_0)\ f_\eta(\kappa\eta)\ . \tag{3.24}$$

The functions f_{ℓ_0} and f_η design the energy-containing and dissipation ranges, and are expected to tend to unity respectively for large $\kappa\ell_0$ and small $\kappa\eta$. They can be specified as follows (Pope, 2000):

$$f_{\ell_0}(\xi) = \left(\frac{\xi}{\sqrt{\xi^2 + c_{\ell_0}^2}}\right)^{5/3+p_0}\ , \tag{3.25}$$

$$f_\eta(\xi) = \exp\left\{-\beta\left[\left(\xi^4 + c_\eta^4\right)^{1/4} - c_\eta\right]\right\}\ . \tag{3.26}$$

The parameters in Equation 3.24, 3.25 and 3.26 can be selected as follows: $p_0 = 2$, $C = 1.5$, $\beta = 5.2$, $c_{\ell_0} \approx 6.78$ and $c_\eta \approx 0.40$ (Pope, 2000).

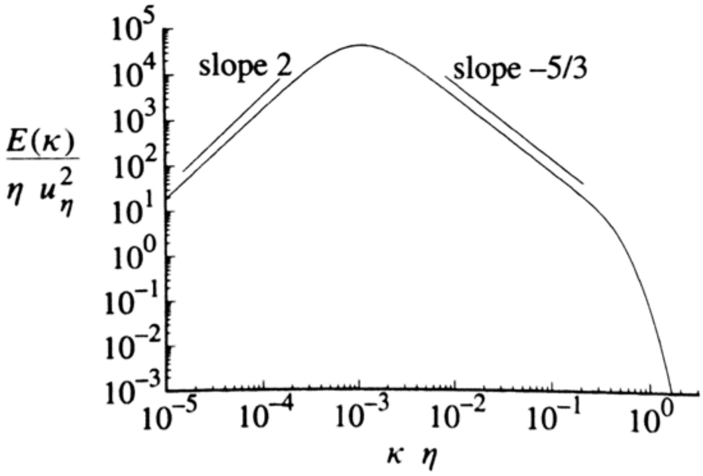

Figure 3.2 *Kolmogorov energy spectrum for* $\mathrm{Re}_{\ell_0} \simeq$ 30,000 *(Pope, 2000).*

3.3.2 Reynolds Equations

The extremely wide range of length scales involved in a turbulent flow (for instance Figure 3.2) makes the numerical reproduction of a real turublent flow extremily numerically expensive: according to Pope (2000), the number of floating-point operations necessary for a simulation of the duration of four times the turbulence time scale τ_0 is Re^6. For this reason, the numerical reproduction of the full turbulence spectrum, or direct numerical simulation, is limited to foundational studies involving low Reynolds numbers, simple geometries and small volumes. However, in industrial application, an averaged solution is sufficient for practical purposes. The Reynolds decomposition consists of separating the Eulerian velocity field $\mathbf{u}(\mathbf{x},\, t)$ into a constant $\langle \mathbf{u}(\mathbf{x},\, t) \rangle$ and a fluctuating component $\tilde{\mathbf{u}}(\mathbf{x},\, t)$:

$$\mathbf{u}(\mathbf{x},\, t) = \langle \mathbf{u}(\mathbf{x},\, t) \rangle + \tilde{\mathbf{u}}(\mathbf{x},\, t) \ . \tag{3.27}$$

It is evident that $\langle \tilde{\mathbf{u}} \rangle = 0$. In the case of stationary flow, the average is intended to be performed over the whole time span of the problem taken into consideration. In case of variable flow, the average is taken over a time period Δt much larger than the timescale of the eddies responsible of the turbulence (Versteeg and Malalasekera, 1995):

$$\langle \mathbf{u}(\mathbf{x},\, t) \rangle \equiv \frac{1}{\Delta t} \int_t^{t+\Delta t} \mathbf{u}(\mathbf{x},\, \tau) \ \mathrm{d}\tau \ . \tag{3.28}$$

It should be noted that the space and time partial derivative commute with the averaging procedure described in Equation 3.28, but not the substantial derivative. The same averaging procedure is carried out for the pressure field.

The averaging procedure of Equation 3.28 can be applied to the Navier-Stokes equations 3.1 and 3.2. The resulting equations are called Reynolds equations:

$$\nabla \cdot \langle \mathbf{u} \rangle = 0 \ , \tag{3.29}$$

$$\rho\,\partial_t \langle \mathbf{u} \rangle + \rho\nabla \cdot (\langle \mathbf{u} \rangle \otimes \langle \mathbf{u} \rangle) = -\nabla \langle p \rangle + \nabla \cdot (\langle \tau \rangle + R) + \langle \mathbf{b} \rangle \ . \tag{3.30}$$

The averaging of the shear stress tensor is straightforward as it depends only on the spatial derivatives of the velocity field; also the averaging of the body forces does not cause complications. On the contrary, the averaging of the inertial transport term gives rise to the extra term $\nabla \cdot R$ at the second member, where R is the Reynolds tensor and is defined as:

$$R_{ij} \equiv -\rho \, \langle \tilde{u}_i \tilde{u}_j \rangle \ . \tag{3.31}$$

The Reynolds tensor is built from the fluctuating velocity, and contains the whole information about the turbulence. As it cannot be deduced from the averaged flow, a (turbulence) model that reproduces R must be introduced in order to provide a closure to the Reynolds equations 3.29 and 3.30.

3.3.3 Boundary Layer

Turbulent flow near a solid surface behaves differently from the bulk fluid. The zero velocity condition at the wall, in fact, has as a consequence that near-wall flow is dominated by viscous effects even in high Reynolds number bulk flow.

Let us consider a near-wall flow with transverse length scale D. The flow main direction is parallel to the wall surface. Let the x coordinate indicate the direction parallel to the wall, and y the direction normal the wall. Let u and v be respectively the velocity components parallel and normal to the wall. If the flow is fully developed, u does not depend on x. The main component of the shear stress tensor τ is τ_{xy} , and can be written in terms of viscous and turbulent contributions:

$$\tau \equiv \tau_{xy} = \mu \frac{\mathrm{d}\langle u \rangle}{\mathrm{d}y} - \rho \, \langle \tilde{u}\tilde{v} \rangle \ . \tag{3.32}$$

At the wall, the turbulent contribution vanishes due to the zero velocity condition:

$$\tau_\mathrm{w} \equiv \mu \left(\frac{\mathrm{d}\langle u \rangle}{\mathrm{d}y} \right)_{y=0} \quad . \tag{3.33}$$

From dimensional considerations, the following velocity and length scales can be derived. Friction velocity:

$$u_\tau \equiv \sqrt{\frac{\tau_\mathrm{w}}{\rho}} \ ; \tag{3.34}$$

viscous length scale:

$$\delta_\nu \equiv \frac{\nu}{u_\tau} \ . \tag{3.35}$$

A dimensionless wall coordinate y^+ and a dimensionless wall velocity u^+ can be defined as:

$$y^+ \equiv \frac{y}{\delta_\nu} \ , \tag{3.36}$$

$$u^+ \equiv \frac{u}{u_\tau} \ . \tag{3.37}$$

The relative contributions of viscous and turbulent shear stressed are shown in Figure 3.3. There is a strong dominance of viscous stress for $y^+ < 5$ and, conversely, a strong turbulent dominance for $y^+ > 35$. The two terms are both present in-between.

It is noticeworthy that the profiles in Figure 3.3 are the same for both the Reynolds numbers considered (Re = 5,600 and 13,750). Accordingly, the Prandtl hypothesis (Prandtl, 1925) states that there exists an inner layer $y/D \ll 1$ (say $y/D < 0.1$), where the average velocity profile is determined by a universal function independent of D and the inlet velocity. The average velocity along the x direction can be written as a function of the friction velocity and the two non-dimensional groups y/D and y/δ_ν:

$$\langle u \rangle = u_\tau \, F\!\left(\frac{y}{D}, \frac{y}{\delta_\nu} \right) \ , \tag{3.38}$$

or, equivalently:

$$\frac{\mathrm{d}\langle u\rangle}{\mathrm{d}y} = \frac{u_\tau}{y}\,\Phi\left(\frac{y}{D}, \frac{y}{\delta_\nu}\right) \; . \tag{3.39}$$

Due to the Prandtl hypothesis, Equation 3.39 becomes in the limit $y/D \ll 1$:

$$\frac{\mathrm{d}\langle u\rangle}{\mathrm{d}y} \simeq \frac{u_\tau}{y}\,\Phi_1\left(\frac{y}{\delta_\nu}\right) \; . \tag{3.40}$$

The importance of Equation 3.40 lies in the fact that it states that the velocity in the inner layer depends only on one variable, and assumes the universal form:

$$u^+ = f_\mathrm{w}\big(y^+\big) \; . \tag{3.41}$$

Equation 3.41 is called law of the wall. Applying a non-slip condition and dimensional considerations yields:

$$f_\mathrm{w}(0) = 0 \; ; \qquad f'_\mathrm{w}(0) = 1 \; . \tag{3.42}$$

As discussed above, for $y^+ < 5$ the viscous contribution in Equation 3.32 is dominant. This domain is called the viscous sublayer. According to Equations 3.41 and 3.42, u^+ can

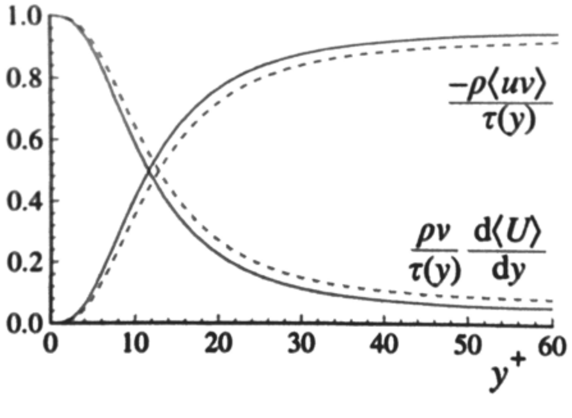

Figure 3.3 *Viscous and turbulent near-wall shear stress in a channel flow. Figure from Pope (2000), data from direct numerical simulations performed by Kim et al. (1987). Dashed line:* $\mathrm{Re} = 5{,}600$. *Solid line:* $\mathrm{Re} = 13{,}750$.

be written as:

$$u^+\big(y^+\big) = y^+ \ . \tag{3.43}$$

On the contrary, for $y^+ > 35$ the turbulent contribution is dominant and consequently the dependence on the viscosity vanishes. Therefore, Equation 3.40 reduces to:

$$\frac{\mathrm{d}\langle u\rangle}{\mathrm{d}y} \simeq \frac{u_\tau}{y}\frac{1}{\kappa} \ . \tag{3.44}$$

Consequently:

$$u^+\big(y^+\big) = \frac{1}{\kappa}\ln y^+ + B \ . \tag{3.45}$$

The generally accepted values for κ and B are 0.41 and 5.2 respectively. The domain $y^+ > 35$ is called the log-law region and is extended to the limit of the viscous layer. An upper limit for y^+ can be set to 300. Beyond this value, the flow can be considered as in the bulk region.

The layer intermediate to the viscous sublayer and the log-law region is called the buffer region. Here, the profile of y^+ varies from Equation 3.43 to Equation 3.45.

3.3.4 Turbulence Models

The first attempts to model the Reynolds tensor are based on the turbulent viscosity hypothesis, or Boussinesq hypothesis. A parallel is traced with the relationship between laminar shear stress and shear rate; more specifically, the deviatoric part of the Reynolds tensor is assumed to be proportional to the main shear rate:

$$\frac{1}{\rho}R_{ij} + \frac{2}{3}k\,\delta_{ij} = \nu_\mathrm{T}\,\langle\dot\gamma_{ij}\rangle \ . \tag{3.46}$$

The coefficient ν_T is called turbulence viscosity. The models based on this hypothesis are called “turbulence viscosity models”. The apparently natural assumption of constant

ν_T works only in a very limited number of cases and it is strongly model-dependant, and therefore is of no practical use.

One of the most common approaches consists of closing the Reynolds equations 3.29 and 3.30 with two additional equations for the turbulent kinetic energy k and the turbulence energy dissipation rate ε, and calculate ν_T from k and ε. This is called the standard k–ε model, and was proposed by Jones and Launder (1972). A more detailed description of the standard k-ε model is given in Appendix B. The standard k–ε model provides reliable results for many flows at a low computational cost, and therefore is extensively used. However, it gives inaccurate results for a large category of flows, including jets, rotating or swirling flow, and low-Reynolds numbers.

In order to improve the performance of the standard k–ε model, a number of improvements have been proposed. The realisable k–ε model proposed by Shih et al. (1995) addresses part of the standard k–ε shortcomings, even though yields unphysical results in domains composed of both rotating and stationary domains. In this model, the dissipation rate equation is reformulated on the base of the dynamic equation of the mean-square vorticity fluctuation at large turbulent Reynolds number and does not involve a Reynolds tensor production term. In the k–ω model (Wilcox, 2006), an equation for the specific dissipation rate $\omega \equiv \varepsilon/k$ is provided in place of the one for ε. This model behaves better than the k–ε models, especially for low-Reynolds flows, but is problematic for non-turbulent free-stream boundaries. A blend of the k–ε and k–ω models, called SST k–ω, has was proposed by Menter (1994) and is aimed at using the respective strength points of the k–ε and k–ω models.

An alternative to the Boussinesq hypothesis consists of directly solving all the six independent components of the Reynolds stress tensor, plus one scalar involving dissipation. The models that follow this idea are known as Reynolds stress models. A more detailed description of the Reynolds stress models is given in Appendix C. Due to the absence of the Boussinesq hypothesis, Reynolds stress models generally give slightly better results when compared with turbulent viscosity models, but at the price of a generally higher computational expense due to the higher number of equations to be solved. Therefore, Reynolds stress models are usually confined to problems in which the turbulence is manifestly non-isotropic, and generally a cost/benefits analysis is advisable before applying them.

Large-eddy simulations are another method to model turbulence, alternative to the Reynolds decomposition described in Section 3.3.2. Instead of being averaged over time, the velocity field $\mathbf{u}(\mathbf{x},\, t)$ undergoes a filtering operation aimed at decomposing it into low-wavenumbers, higher-scale motions $\bar{\mathbf{u}}(\mathbf{x},\, t)$, and high-wavenumbers, smaller-scale fluctuations $\mathbf{u}'(\mathbf{x},\, t)$ (Pope, 2000). The higher-scale motions are affected by the geometry and are not universal, while the smaller fluctuations can be considered to have a universal character according with the Kolmogorov hypotheses. The Navier-Stokes equations are solved for $\bar{\mathbf{u}}(\mathbf{x},\, t)$. The small-scale fluctuations are addressed by considering an additional "residual stress tensor" in the equations (Pope, 2000). The closure is obtained by modelling the residual stress tensor, most simply by an eddy-viscosity model (Pope, 2000). According to Pope (2000), large eddy simulations require a finer mesh than the Reynolds-averaged models, partly due to the need of resolving the near-wall flow. Large eddy simulations are expected to provide improved accuracy compared to the Reynolds-averaged methods, but at the cost of a much higher computational expense.

3.4 Computational Fluid Dynamics (CFD)

Very few problems allow analytical solutions of the Navier-Stokes equations 3.1 and 3.2. For this reason, a numerical approach is desirable. Computational fluid dynamics is a framework in which the equations of motion are discretized and solved with numerical algorithms. In the case of this work, the equations of motion consist of the Navier-Stokes equations 3.2 and the Poisson equation 3.7 for the pressure.

3.4.1 Pre-Processing

First of all, the physical domain in which the fluid dynamics phenomena of interest must be identified. The physical domain is a continuum, and therefore a complete knowledge of the solution would require computation of the value of the fields at an infinite number of points. As this is impossible, a finite set of points, called the computational domain, is extracted from the physical domain, and it is assumed that the knowledge of the fields at these points gives a satisfactory representation of the solution. This also implies that the (continuous) differential equations 3.2 and 3.7 must be rewritten as algebraic equations defined at the point of the computational domain. The process of extracting a finite set of points from the physical domain and rewriting the equations of motion in an algebraic form is called discretization.

There are many discretization methods. In this work, the finite volume method has been employed. This consists of dividing the physical domain into a set of cells; for each cell, the values of the fields are considered as constant and equal to the value of the fields at the cell centre. The set of the cells is called the mesh.

The discretization of the Navier-Stokes equations is carried out by integrating them over a cell, and then enforcing the divergence theorem. In this way, the spatial derivatives are reduced to the differences of the field values at the face centres. A number of interpolation methods, called discretization schemes, use the field values at the neighbouring cells to calculate the field values at the face centres. A number of time discretization schemes make use of the field values at different timesteps to discretize the time derivatives.

3.4.2 Processing

Once the boundary and initial conditions are set, an iterative procedure to solve the discretized equations takes place. The equations 3.2 and 3.7 are solved with a "segregated" algorithm that splits the problem of finding the solution of the two equations into two sub-problems. An initial guess for the pressure field is used to solve the Navier-Stokes equation 3.2 for the velocity. The velocity field obtained in this way is used as an initial guess to solve the Poisson equation 3.7 for the pressure. The procedure is repeated until the relative difference from the previous iteration falls below a given value, and the solution is deemed to be "converged".

When convergence is achieved, the fields values are used as initial conditions for the next timestep, and the procedure is repeated until the difference between the fields values at two timesteps falls below a given value (in the case of steady state simulations), or a given total amount of timesteps has been simulated (transient simulations).

3.4.3 Post-Processing

Once the simulation has been carried out, the data files are analysed and physical data are extracted according to the particular problem being studied. The problem of assessing the reliability of the output data arises as errors due to modelling or discretization can be present. In order to accomplish this and to estimate the error, two complementary approaches of "verification" and "validation" are available (Roache, 1998).

Verification consists of addressing the error arising from discretization. When the physical domain is discretized, an approximation of the problem is performed. Consequently, the final result is expected to depend on the number of cells N or, equivalently, on a length scale h typical of the cell size. The exact (continuum) case is represented by the limit $N \to \infty$ or, equivalently, $h \to 0$. The discretization error is considered to be under control when the simulation converges with order $p > 0$. That is, given a variable ϕ critical to the conclusions of the work, we have:

$$|\phi - \phi_{\text{exact}}| \sim h^p \, . \tag{3.47}$$

The (theoretical) order of convergence is determined by the discretization schemes employed. Each scheme has a proper order of convergence, and the global order of convergence is equal to the lowest order of convergence among the discretization schemes employed. However, due to mesh skewness and local variations of the grid size, the actual order of convergence (Equation 3.47) is generally lower than the theoretical order of convergence. The simulation is considered as satisfactory when the mesh is fine enough to reproduce the behaviour described in Equation 3.47; that is, when the asymptotic range of convergence is achieved. Roache (1994, 1998) proposed the Grid Convergence Index (GCI) method to assess the asymptotic range of convergence and give an estimation of the discretization error. According to Celik et al. (2008), the variable ϕ is determined from three sets of grids, say a, b and c from the finest to the coarsest. The underlying hypothesis is that the value of ϕ determined by the simulation can be written as a Taylor polynomial of h:

$$\phi = \phi_{\text{exact}} + g_1 h + g_2 h^2 + g_3 h^3 + \dots \tag{3.48}$$

p is calculated recursively in the following way:

$$\begin{aligned} p &= \frac{1}{\ln r_{ba}} \left| \ln |\epsilon_{cb}/\epsilon_{ba}| + p(q) \right| \\ q(p) &= \ln \frac{r_{ba}^p - s}{r_{cb}^p - s} \\ s &= \operatorname{sign}\left(\epsilon_{cb}/\epsilon_{ba}\right) \end{aligned} \tag{3.49}$$

where r_{cb} and r_{ba} are the linear refinement factors from mesh c to b and from mesh b to mesh a respectively, and:

$$\epsilon_{cb} \equiv \phi_c - \phi_b \ , \qquad \epsilon_{ba} \equiv \phi_b - \phi_a \ . \tag{3.50}$$

The grid convergence index (GCI) is defined as:

$$\mathrm{GCI}_{cb} \equiv \frac{1.25\,|\epsilon_{cb}/\phi_b|}{r_{cb}-1} \ , \qquad \mathrm{GCI}_{ba} \equiv \frac{1.25\,|\epsilon_{ba}/\phi_b|}{r_{ba}-1} \ . \tag{3.51}$$

The simulations are in the asymptotic range of convergence (and hence mesh independence is achieved) when

$$\frac{\mathrm{GCI}_{cb}}{r_{ba}^{p}\,\mathrm{GCI}_{ba}} \simeq 1 \ . \tag{3.52}$$

Under these circumstances, the value of GCI_{ba} can be used as a (conservative) estimation of the relative error on the finest mesh.

Validation is the comparison of the verified output of a simulation with experimental data. The comparison with nature facilitates the assessment of whether the modelling is correct, i.e. the equations discretized and solved in the simulation correctly represent the physical laws involved in the phenomenon under study.

3.5 Multiphase Models

Multiphase flow occurs when different immiscible fluids, or fluids with different phases, are simultaneously present in the domain. The phenomenology of multiphase flows is extremely wide—it is not surprising, then, that a unified model does not exist. A number of different models depending on the particular problem taken in analysis has been developed. However, the question of the empirical closure models is still open and debated (Andersson et al., 2012).

In the CFD framework, three models have been a wide field of applicability: Euler-

Euler, Euler-Lagrange and Volume-of-fluid (van Wachem and Almstedt, 2003; Andersson et al., 2012).

3.5.1 Euler-Lagrange Model

In the Euler-Lagrange model, one (or more) “dispersed phase” is treated as an ensemble of discrete particles moving inside a continuous phase. If the dispersed phase senses the continuous phase but the latter is unaffected, then the phase coupling is called “one-way coupling”, and the problem can be simply treated as a single-phase problem with post-processing particle tracking (Andersson et al., 2012). In contrast, the case of the continuous phase being affected by the dispersed phase is called “two-way coupling”. In this case, the continuous phase is described by the Navier-Stokes equations 3.1 and 3.2 with an additional momentum exchange term $\mathbf{F}$ between fluid and particles (van Wachem and Almstedt, 2003):

$$\nabla \cdot \mathbf{u} = 0 \; , \tag{3.53}$$

$$\rho \, \partial_t \mathbf{u} + \rho \nabla \cdot (\mathbf{u} \otimes \mathbf{u}) = -\nabla p + \nabla \cdot \tau + \mathbf{b} + \mathbf{F} \; . \tag{3.54}$$

The momentum transfer can be expressed as:

$$\mathbf{F}(\mathbf{x}) = \sum_p \mathbf{F}_p \, \delta(\mathbf{x} - \mathbf{x}_p) \;\; , \tag{3.55}$$

where $\mathbf{F}_p$ is the resultant of the forces acting on the p-th bubble. The Dirac delta, after discretization, states that the contribution of the p-th bubble to Equation 3.54 is $\mathbf{F}_p$ in the cell in which the bubble is present, and zero elsewhere. The equation of motion for each bubble is Newton’s second law:

$$m_p \dot{\mathbf{u}}_p = \mathbf{F}_p \; , \tag{3.56}$$

where $\mathbf{u}_p \equiv \dot{\mathbf{x}}_p$ is the instantaneous velocity of the bubble. The resultant for the p-th bubble $\mathbf{F}_p$ is usually modelled as the sum of components arising from the effect of pressure gradient, buoyancy, drag and lift. A number of models are available for expressing these effects depending on the particular characteristics of the problem studied. The case of particles interacting with each other is called "four-way coupling" (Andersson et al., 2012). In this case, Equation 3.56 becomes:

$$m_p \dot{\mathbf{u}}_p = \mathbf{F}_p + \hat{\mathbf{F}}_p \ , \tag{3.57}$$

where $\hat{\mathbf{F}}_p$ is the resultant of all the particle-particle forces acting on the p-th particle.

The Euler-Lagrange model is particularly effective when the dispersed phase is diluted, i.e. when the dispersed over continuum phase volume ratio is "small" (van Wachem and Almstedt, 2003; Andersson et al., 2012). Although neither van Wachem and Almstedt (2003) nor Andersson et al. (2012) provide a more precise definition of "small", it is reasonable to assume that the volume of the dispersed phase should be meant to be as negligible if compared to the continuum phase volume; this being the case, the dispersed phase volume should be one at least one order of magnitude smaller than the continuum phase. In other words, it is reasonable to assume that "smaller" in van Wachem and Almstedt (2003); Andersson et al. (2012) means "smaller than 10^{-1}". As the computational expense is proportional to the number of particles, this method can become unaffordable when the number of particles increases too much. This is especially true in the case of four-way coupling because the addition of the particle-particle interactions makes the problem numerically stiff (van Wachem and Almstedt, 2003).

Finally, it should be noted that the underlying hypothesis in the Navier-Stokes equation 3.54 is that the particle volume is negligible when compared to the cell size (van Wachem and Almstedt, 2003). Therefore, the validity of the model is not guaranteed if the particles have non-negligible volume compared with the cell size.

3.5.2 Volume-Of-Fluid Model

The volume-of-fluid model is usually employed to model a system in which two phases with a well distinct interphase surface coexist. Let the two phases be labelled as phase 1 and phase 2. First, the interphase surface is tracked with a volume-of-fluid function, or colour function field $\xi(\mathbf{x})$, defined to be as 1 at the points in which the phase 1 is present, and 0 elsewhere (van Wachem and Almstedt, 2003). The colour function must obey a continuity equation:

$$(\partial_t + \mathbf{u} \cdot \nabla)\, \xi = 0 \; . \tag{3.58}$$

In the continuum, ξ is a step function, but after discretization it is expected that cells crossed by the interphase surface experience a colour function value between 0 and 1 as they are expected to contain a non-zero fraction of each phase. In this way, the gradient of ξ is zero everywhere except for the cells crossed by the interphase surface. Therefore, the surface is tracked by identifying the cells with non-zero ξ gradient.

Once the interphase surface is tracked, the Navier-Stokes equations 3.1 and 3.2 are solved with the appropriate density and viscosity depending on which phase is present at a given cell:

$$\nabla \cdot \mathbf{u} = 0 \; , \tag{3.59}$$

$$\rho_f\, \partial_t \mathbf{u} + \rho_f \nabla \cdot (\mathbf{u} \otimes \mathbf{u}) = -\nabla p + \nabla \cdot \tau_f + \mathbf{b}_f + \sigma \; , \tag{3.60}$$

where σ is the surface tension vector. Here the subscript $\cdot_f$ indicates that the quantity is referred to the phase 1 or the phase 2 depending on which phase is present at the given point. The velocity and pressure fields are intended as referred to the phase present at the given point.

The volume-of-fluid model is particularly effective when the two phases are well separated, i.e. when the interphase surface cuts a large number of cells smoothly: according with Andersson et al. (2012), about 20 cells/diameter are needed to satisfactorily resolve a spherical bubble or drop. Conversely, the model works as long as there are enough cells to properly describe the geometry of the interphase surface, and therefore the model can become inaccurate and eventually fail to track the surface in cases of complex geometries, for example in the extreme case of bubbles of volume smaller than the cell size, or where vorticity occurs.

3.5.3 Euler-Euler Model

In the Euler-Euler model, the phases are modelled as immiscible, interpenetrating continua. The information about the (perhaps complex) geometry of the interphase surface is averaged out by introducing the volume fraction field $\alpha_n(\mathbf{x})$, that defines the ratio of the volume occupied by the n-th phase over the total volume at a given cell. The Navier-Stokes equations 3.1 and 3.2 are solved for each phase after being weighted by the volume fraction α_n . Additional terms consist of the mass transfer $\dot{M}_{mn}$ from phase m to phase n and the momentum transfer I_{mn} (van Wachem and Almstedt, 2003):

$$\sum_n \alpha_n = 1 \ , \tag{3.61}$$

$$\rho_n \left(\partial_t + \nabla\right) \left(\alpha_n \mathbf{u}_n\right) = \sum_m \left(\dot{M}_{mn} - \dot{M}_{nm}\right) \ , \tag{3.62}$$

$$\begin{split}\rho_n \, \partial_t \left(\alpha_n \mathbf{u_n}\right) + \rho_n \nabla \cdot \left(\alpha_n \mathbf{u}_n \otimes \mathbf{u}_n\right) = \\ - \alpha_n \nabla p + \nabla \cdot \left(\alpha_n \tau_n\right) + \alpha_n \mathbf{b}_n + \sum_m I_{mn} \ .\end{split} \tag{3.63}$$

The momentum transfer coefficients are subject to global momentum conservation:

$$\sum_{m,n} I_{mn} = 0 \ . \tag{3.64}$$

In theory, the Euler-Euler model is quite flexible and can address problems that cannot be treated with the other models, for example a dispersed phase with high dispersed to continuous volume ratio, or two-phase flows with a complicated interphase surface geometry. However, the mass transfer terms I_{nm} require a larger amount of empirical modelling compared with the Euler-Lagrange and the volume-of-fluid models. Moreover, the simplifications performed by introducing α_n must be accounted for in the turbulence model by adding additional terms describing the additional turbulence energy arising from the fluctuations of the interphase surface (Andersson et al., 2012). For these reasons, Andersson et al. (2012) suggest using the Euler-Euler model only when other models are not available.

3.6 Literature Review on Sludge Viscosity

Sludge rheology is complex. It has been well known for a long time (Allen and Robinson, 1990) that filamentous fermentation broths display non-Newtonian characteristics such as pseudoplasticity and yield stress, and that non-Newtonian behaviour increases with TS content. Achkari-Begdouri and Goodrich (1992) investigated dairy cattle manure and stated that the rheological characteristics depend on the temperature. Moeller and Torres (1997) investigated raw primary, raw secondary, and aerobically and anaerobically digested sludges from biologically-treated combined municipal and industrial wastewaters and recorded very different rheological properties. They also showed that in batch fermenters, the sludge rheological characteristics change drastically, the apparent viscosity and non-Newtonian behaviour decreasing when digestion progresses. More recently, Baudez et al.

(2013) showed that sludge displays a wide set of non-Newtonian behaviours such as pseudoplasticity, yield stress and shear banding. Thixotropic behaviour was also recorded (Eshtiaghi et al., 2012).

From a modelling point of view, Achkari-Begdouri and Goodrich (1992) proposed a simple power-law model, with the coefficients depending on TS and temperature. Sindall (2014) reports that the following models were used in the literature: Bingham (Guibaud et al., 2004; Pevere et al., 2009), Herschel-Bulkley (Mori et al., 2008; Yang et al., 2009) and Casson (Yang et al., 2009). Eshtiaghi et al. (2012) proposed different models for different ranges of shear rate.

Wu and Chen (2008) performed series of CFD simulations with sludge modelled as a Newtonian fluid, and another one using a power-law model with the parameters chosen according with the work of Achkari-Begdouri and Goodrich (1992), and demonstrated that the outcomes are completely different. The validation was performed by comparing the simulated data with the experimental results of Pinho and Whitelaw (1990), which were obtained from an aqueous solution of carboxymethyl cellulose (CMC). CMC solutions were chosen because they display power-law indices and densities similar to the sludge considered in Achkari-Begdouri and Goodrich (1992). The first approximation of considering sludge as a power-law fluid was adopted by a number of authors, e.g. Terashima et al. (2009); Bridgeman (2012); Wu (2014). Craig et al. (2013), on the contrary, adopted a Herschel-Bulkley model.

3.7 Previous CFD Studies of Anaerobic Digestion

Thanks to the progress of computer performance, computational fluid dynamics has become an invaluable resource in the simulation of processes involving fluid flow, and it is not a surprise that it has been widely used to study mixing in anaerobic digestion. Sludge is opaque: this makes experiments difficult to perform and therefore makes the use of

CFD more valuable, but for the same reason it makes also the process of validation more difficult.

The only experiments—and, consequently, validations—reported in the literature on full-scale anaerobic digesters consist of the introduction of a tracer fluid at the inlet and its detection at the outlet. They are costly experiments and only give a "black box" representation of the flow through the digester (Sindall, 2014). Other approaches consist of comparing dimensionless groups calculated from specifications such as the power absorbed by the impeller (Wu, 2011, 2012a).

The scarcity of full-scale experimental evidence is due to the difficulties in performing experiments on sludge explained above, together with the logistical impediments on performing experiments on a plant that operates on corrosive and biochemically hazardous matter. Therefore, it is laboratory-scale experiments that usually provide the benchmark for CFD models aimed at describing mixing in anaerobic digestion. They are also the tools for choosing the most appropriate rheological and turbulence models, as well as informing modelling strategies involved in the simulations, such as bubble injection methods, boundary conditions or multiphase momentum transfers. Moreover, they are the ones that allow a thorough validation of the CFD models. It is not surprising, then, that the majority of the published work makes use of CFD simulations to predict the flow behaviour of full-scale plant, while the validation of CFD models is mostly limited to laboratory-scale setups.

For the sake of simplicity, the literature on mixing in anaerobic digestion can be split into laboratory-scale, pilot-scale and full-scale.

3.7.1 Laboratory-Scale Literature

Wu and Chen (2008) were the first authors to simulate mixing in anaerobic digestion using a non-Newtonian fluid model. A computational model equipped with a standard k-ε

turbulence model was first validated against the experimental data of Pinho and Whitelaw (1990) for a non-Newtonian liquid flowing through a pipe, and then applied it to a 4-litre digester. As explained before, they showed that Newtonian and non-Newtonian flow patterns are largely different.

Bridgeman (2012) modelled a 6-litre impelled-mixed tank. The capacity of Standard k-ε, Resizable k-ε, Renormalised Group k-ε, Standard k-ω, and Reynolds Stress turbulence models of reproducing the experimental results was assessed in the following way: the simulated dissipated power resulting from the simulations was integrated over the computational domain, and then compared with the result of the experimentally measured power input. The Reynolds stress model was considered to perform best, while the standard k-ε model was the worst. This result was to be expected, as the hydrodynamics of a closed digester are characterised by rotating and swirling flow, and it is well-known that the standard k-ε model fails to reproduce such flows accurately (cfr. Section 3.3.4). On the other hand, it is accepted that the Boussinesq hypotheses may not hold in a constrained domain such as a vessel, the Reynolds tensor's component normal to the wall being attenuated near the wall. For this reason, it is understandable that the Reynolds stress model might perform better than the models based on the isotropic eddy viscosity. The dependence of flow patterns on the total solids was assessed by comparing simulations with different TS and the same impeller rotational speed (100 rpm). The digester volume was divided into zones with low velocity magnitude ($< 0.02\ \mathrm{m\,s^{-1}}$), medium (0.02—$0.1\ \mathrm{m\,s^{-1}}$), and high ($> 0.1\ \mathrm{m\,s^{-1}}$). It was shown that the mean velocity fell and the volume of the dead zones increased when TS increased. The dependence of the flow patterns on the rotational speed was assessed by comparing simulations with different rotational speed and the same TS (5.4%). It was shown that, while the volume of the zones in which the mean velocity is relatively high does not change much, the volume of the dead zones decreases when rotational speed increases. Nevertheless, it was not possible to eliminate the dead zones.

In all the cases, the average shear rate was well below the value of 50-80 s^{-1} suggested by literature for anaerobic digestion plants (Tchobanoglous et al., 2010). Nevertheless, this was shown to have no effect on experimental biogas production; furthermore, increasing speed from zero to 100 rpm was shown to have no effect on biogas yield.

Wu (2010c) used twelve turbulence models, including low-Reynolds number models to simulate the pressure loss of power-law sludge through a pipe. The outcome of the simulations was compared to empirical correlations. However, according with Sindall (2014), such correlations are referred to fully developed turbulence, while the simulations displayed relevant developing zones. Moreover, no mesh independence test was performed. It was found that the Chang-Hsieh-Chen low Reynolds model using 52,800 cells reproduced the correlations best. However, the results did not differ greatly from the outcome of the standard k-ω model using 18,000 cells, and the latter was judged as a better quality/computational cost compromise. Then, the standard k-ω model was employed to simulate a 790 m^3 digester. The shear rate was calculated locally, and a division of the domain into zones as in Bridgeman (2012), but with the shear rate magnitude in the place of the velocity, was performed. The results were compared with the average shear rate calculated from an estimation of the average shear rate taken from the power input proposed by Coufort et al. (2005), and were found to be sensibly lower. The author attributed the discrepancy to the non-Newtonian nature of the sludge and concluded that the study of the local shear rate is more reasonable than the traditional definition of the G value that characterizes a complex flow field with a single number.

Wu (2012c) compared the relative performance of large eddy simulations (LES) and RANS turbulence models applied to a 4.3 litre mechanically mixed digester filled with power-law sludge. The results were validated against the experimental work of Hoffmann et al. (2008b). Due to the issues concerning energy conservation in the experimental data pointed out in the article of Wu (2012c), a further comparison was carried out with the experimental data of Bugay et al. (2002). It was found that LES models gave slightly better predictions albeit with a much higher computational cost. According to Sindall (2014), however, the results of the work of Wu (2012c) are affected by issues deriving from a too small number of cells for the LES simulations and the lack of a grid-independence test.

3.7.2 Pilot-Scale Literature

Wu (2011) reproduced a 0.57 m^3 tank filled with a power-law sludge and used six turbulence models (standard k-ε, realisable k-ε, RNG k-ε, standard k-ω, SST k-ω, Reynolds stress). Two dimensionless groups were calculated from the simulated data, and then compared to the lab specifications of the impellers. It was shown that the standard k-ω model predicted dimensionless numbers values better for water and 2.5% TS, while realisable k-ε behave better for higher TS values. In all cases, the Reynolds stress model was more computationally expensive than the turbulent viscosity models.

Wu (2012a) reproduced a tank of about 18 m^3 filled with a power-law sludge and stirred with impellers of different designs. Two dimensionless groups were calculated from the simulated data, and then compared to the outcome of experimental measurements performed on an apparatus of the same design filled with a xanthan gum solution. It was shown that the choice of the impeller significantly influences the flow patterns. The simulations were performed under a laminar flow hypothesis: however, according to Sindall (2014), this can be detrimental for the reliability of the results as the Reynolds numbers fall in the transition range.

3.7.3 Full-Scale Literature

Meroney and Colorado (2009) modelled the injection of a tracer into four full-scale digesters of different sizes and recirculation-driven mixing with different draft tube configurations, and then compared the outcome with the experimental work of Cholette and

Cloutier (1959). They modelled turbulence with the standard k-ε model, and the sludge rheology as a Newtonian fluid with the same density and viscosity of water. As explained before, however, the standard k-ε model gives inaccurate results in rotating flows, that are known to occur in closed vessels. Moreover, the flow patterns of Newtonian and non-Newtonian fluids differ greatly (Wu and Chen, 2008).

Wu (2010b) simulated an egg-shaped digester with mechanical draft tube mixing. Newtonian (water) and power-law (sludge) fluids with the same characteristics of Wu and Chen (2008) were modelled. The work investigated the optimal propeller position and performed a comparison between mechanical draft tube and recirculated mixing, concluding that the former is more efficient. The simulations also showed that the amount of dead zones increases with increasing apparent viscosity. The CFD results were validated against a digester at the San Mateo Wastewater Treatment Facility in Arizona filled with water, and two global dimensionless groups were compared with the lab specifications of the impellers.

Terashima et al. (2009) modelled a full-scale digester mixed by an impeller confined inside a draft tube. A power-law model was used to assess the sludge viscosity. The numerical results were compared with an experimental tracer response curve. The coefficients of the power-law model were determined experimentally by studying the pressure drop through a pipe. In spite of the clear limitations of the model, such as impeller modelled as an applied force to the sludge with a try-and-fail setup, small number of cells and laminar flow model, the simulations were in good agreement with the experimental tracer curve. The outcome of the simulations was that an increase of mixing lead to a more uniform tracer concentration, and that uniformity was achieved more quickly in less viscous solutions.

Craig et al. (2013) simulated a full-scale draft-tube impeller filled with water and Herschel-Bulkley sludge with different coefficient in order to take the differences between raw and digested sludge into account. The SST k-ω turbulence model was adopted. An attempt to reproduce the surface profile due to the bell-mouth exit was performed with a two-dimensional volume-of-fluid model, and the output surface profile as an input to the full-scale simulations. However, the outcome of the latter behaved worse than simulations performed with a flat, free surface. It was shown that the flow patterns of water and sludge differ significantly, the latter displaying more dead zones. Also, they showed that mixing digested sludge takes less energy than mixing raw sludge. A GCI test was performed, and it was found that, although the value of the parameters adopted for the grid independence verification expressed only a weak grid dependence, the flow patterns showed larger variations. Therefore, a GCI test is advisable when performing CFD simulations of sludge mixing.

3.8 Previous Multiphase CFD Studies of Anaerobic Digestion

In contrast to the quantity of work carried out to understand mechanical and recirculation mixing, gas mixing still remains poorly studied. During the gas-mixing process, a complex pattern of momentum exchange between bubbles and liquid phase takes place, and therefore a genuine multiphase model is required to reproduce the liquid phase mixing robustly and with fidelity. However, only Vesvikar and Al-Dahhan (2005); Wu (2010a, 2012b) have investigated this subject with a robust multiphase model. Karim et al. (2007) investigated gas mixing, but they carried out broad simplifications in their analysis, as their model works only on a specific case of draft tube-driven mixing. Furthermore, the effect of gas injection was modelled by specifying the outlet velocity at the exit of the draft tube, while the inside the draft tube was not studied. As can be seen, their analysis was actually carried out with a single-phase model: even though their model was able to reproduce the experimental data satisfactorily, it was specific for a very definite problem.

Vesvikar and Al-Dahhan (2005) investigated draft-tube confined gas mixing in a 7.2 litre digester filled with a Newtonian sludge. An Euler-Euler two-way-coupling model was chosen. A standard k-ε model for the liquid fraction, and a zero-equation mixing-length turbulence model for the gas fraction were chosen. According to Sindall (2014), the simulated flow patterns were qualitatively similar to experiment, but the axial velocity showed a discrepancy of about 20%. The authors discussed the effects of changing the geometry and the gas flow rate, and concluded that a change of the gas flow rate did not affect the flow patterns outside the draft tube, while increasing the tube diameter led to a decrease of dead zones. According to Sindall (2014), it is likely that the results are negatively affected by the choice of a Newtonian viscosity model, the use of the standard k-ε turbulence model and the adoption of first-order upwind discretization schemes for the convection terms.

Wu (2010a) investigated gas-mixed power-law sludge with an Euler-Euler two-way-coupling model. The gas phase was approximated as an ensemble of non-interacting spherical bubbles. Twelve turbulence models for the continuous phase were tested by simulating a bubbly pipe flow and comparing the pressure drop with empirical correlations. It was shown that the model underpredicts the pressure drop when the bubble size increases. However, these simulations were hindered by the same issues for pipe flow simulations described for the work of Wu (2010c), and by the choice of a first-order upwind discretization scheme for the convection terms. The SST k-ω model was used to model a laboratory-scale confined gas mixed digester, and the results were compared with the experimental data of Karim et al. (2004), which was carried out using the computer automated radioactive particle tracking (CARPT) and computed tomography (CT) techniques, and showed that a relevant part of the digester was occupied by dead zones despite the increasing of gas flow rate. The simulations were reported to predict the axial velocity well except for near the surface and the draft tube: in these zones, the axial velocity resulted to be underpredicted by a factor of 1/2. The model developed in Wu (2010a) was then used to simulate a full-scale 791 m^3 digester and confined and unconfined gas mixing were compared. It was reported that the extension of the dead zones increases and the average velocity decreases when the total solid content increases. It was shown that unconfined gas mixing displays higher average velocities but larger dead zones if compared with confined mixing, and it was concluded that the latter achieved a better mixing for 5.4% TS. Furthermore, confined gas mixing was compared to recirculated mixing and draft tube impeller mixing, and it was concluded that, in terms of efficiency, gas mixing lied between recirculation mixing and mechanical mixing, with mechanical mixing being the most effective.

No Euler-Lagrange finite volume-based model has been proposed in the literature to simulate gas mixing in anaerobic digestion. Sungkorn et al. (2011) studied highly turbulent constant-viscosity column bubbly flow, while Sungkorn et al. (2012) modelled a generic shear-thinning aerated stirred tank. However, they did not attempt to reproduce the rheological characteristics of sludge and, most significantly, they adopted a Lattice-Boltzmann scheme, that is a completely different framework from finite volume. In the Lattice-Boltzmann scheme, the fluid is modelled as an ensemble of particles to be treated statistically, and is described by the probability density function $f(\mathbf{x},\, \mathbf{v},\, t)$ of finding a particle of velocity comprised between $\mathbf{v}$ and $\mathbf{v} + \mathrm{d}\mathbf{v}$ inside the volume element $(\mathbf{x},\, \mathbf{x} + \mathrm{d}\mathbf{x})$ and the time interval $(t,\, t + \mathrm{d}t)$. The probability density function obeys the Boltzmann equation, which relates its total derivative with a collision operator. Density, velocity and pressure fields calculated out from the probability density function. The discretization is carried out by defining a lattice in which the grid points are linked with unitary velocity vectors. The probability density function is defined at the grid points. Each grid point is linked to its neighbours via velocity direction vectors. In order to obtain a physically meaningful solution, it is crucial to define a grid with a sufficiently rich symmetry group. For each lattice velocity direction, the corresponding probability density function is obtained by evolving it from the previous timestep by using the Boltzmann equation according with the scattering matrix and the deviation of the probability density function from the Maxwell (equilibrium) function. The interested reader can consult literature on finite volume CFD such as Versteeg and Malalasekera (1995); Andersson et al. (2012) and on lattice-Boltzmann via Succi (2001); Wolf-Gladrow (2005).

3.9 Summary of the Previous Works and Research Gaps

A considerable amount of CFD research has been performed to model mixing in anaerobic digestion. Laboratory, pilot and full-scale setups have been considerated. Due to the inherent difficulties in performing experiments on full-scale plants, only black-box data with limited utility are available. For this reason, the majority of the work undertaken is related to laboratory-scale setups. The latter allow a more complete validation and also an understanding of the impact of different factors such as rheology, turbulence and geometry. The tendency is to develop a model in a laboratory-scale setup, and then use it to give predictions of the full-scale behaviour.

The rheological characteristics of sludge have been studied extensively, and the importance of correct modelling has been stressed. In particular, it is evident that the Newtonian approximation is unsuitable for CFD simulations of sludge mixing. The choice of the turbulence model is also another critical aspect. Simple models, such as standard k-ε, have been proved to be ineffective. On the other hand, large eddy simulations and Reynolds stress are very computationally expensive and the progress in terms of accuracy may not justify the increased expense.

The understanding of mixing in anaerobic digestion has undoubtedly benefitted from the application of CFD modelling. The minimum shear rate values recommended from the literature for appropriate mixing have been proved to be excessively high: this means that there is space to reduce the mixing input energy with an unquestionable benefit as mixing is an energy-intensive operation. However, the persistent presence of dead zones has been widely observed regardless of the efforts undertaken for improving the mixing efficiency. It has been shown that a correct choice of the tank geometry has a direct impact in reducing the dead zones, but a conclusion has not been found yet. Therefore, there are both space and motivation to carry forward the research in this field.

The vast majority of the research carried out so far has considered mechanical mixing: in comparison, the research on gas mixing is rather scarce. Some works in the literature (e.g. Wu 2010a) suggest that gas mixing is less effective than mechanical mixing, but the inherent advantage of not having moving parts inside the digester was not taken into consideration. Moreover, the issue of enhancing the performance of existing gas-mixed digesters is yet to be solved. Therefore, a conclusion is yet to be found, and this alone is a motivation to carry forward the research.

In the limited amount of research carried out so far in gas mixing for anaerobic digestion, only the Euler-Euler model has been employed. Different factors should be taken into consideration in multiphase CFD modelling, and there is not a universal multiphase model, as explained in Section 3.5. Moreover, the inherent issues of this model have been addressed in Section 3.5.3. It is therefore evident that research employing multiphase models other than the Euler-Euler is more than beneficial in understanding gas mixing in anaerobic digestion.

4

Aim and Objectives

> *"The lion king is said to advance three steps, then gather himself to spring, unleashing the same power whether he traps a tiny ant or attacks a fierce animal."*
>
> Nichiren Daishonin (1273).
> Reply to Kyo'o

THE AIM of this research is to produce recommendations to enhance the performance of gas-mixed anaerobic digesters by improving the mixing efficiency. The enhancement is to be achieved by obtaining a satisfactory balance between energy input for sludge mixing and the resultant biogas yield.

This aim is underpinned by a series of objectives:

1. Develop a CFD-based numerical model to simulate air bubble injection and motion inside a non-Newtonian fluid with rheological characteristics set to mimic those of municipal sewage sludge.

2. Write the computer code to implement the model described in Objective 1. Test its behaviour against different rheologies, Reynolds-averaged turbulence models and grid refinement/coarsening.

3. Build a lab-scale apparatus to mimic sludge under unconfined gas mixing conditions and perform measurements using high speed camera, particle image velocimetry and positron emission particle tracking for different air flow rates and rheologies.

4. Apply the numerical model developed in Objective 2 to the geometry and operating conditions of the apparatus of Objective 3. Compare the numerical results with the experimental data of Objective 3 in order to validate the numerical model under lab-scale conditions.
5. Apply the numerical model developed in Objective 2 to a full-scale case. Reproduce the geometry and operating conditions of the digesters of a real, operating municipal sewage sludge treatment plant. Investigate the influence of different biogas flow rates and mixing intensity and find the minimum gas flow rate that ensures a satisfactory mixing intensity.

5

Materials and Methods

> *"Per vedere quale acqua del vaso è quella che si muove all'uscita del fondo d'esso vaso, piglierai due piastre di vetro quadre d'un quarto di braccio, e falle vicine l'una all'altra 2 coste di coltello con uniforme spazio, e salda li stremi da 3 lati colla cera. Poi pel quarto lato l'empi d'acqua chiara nella quale sia sparso piccole semenze le quali sien notanti per tutta l'altezza di tale acqua. Di poi farai un piccolo buso nel fondo e dà l'uscita a tale acqua e tieni l'occhio fermo nella faccia del vase e 'l moto delle dette simenze ti darà notizia quale è quell'acqua che con più velocità corre all'uscita e di qual sito si move."*[a]

---

[a] To see how water flows from a hole at the bottom of a vase, take two square glass plates of a quarter of an arm side, place them at a uniform distance of two knife blades and seal three sides with wax. Then, fill with water with small floating seeds from the forth side. And then, make a small hole at the bottom to make the water flow, and keep a firm eye to the vase, and the motion of the seeds will tell you where water flows faster, and to what direction.

> Leonardo da Vinci (c. 1508-10).
> Codex Atlanticus, f. 219 recto

IN THIS CHAPTER, the main materials and methods are described. First, a description of the viscosity model chosen for describing sludge rheology is given in Section 5.1. Then, a description of the laboratory setup is given in Section 5.2. A description of the experimental rig is given (Section 5.2.1, and instructions about the preparation of the liquid phase for the laboratory experiment are reported. Carboxymethyl cellulose (CMC) was used as a transparent substitute of sludge. The apparatus used for the rheological measurements is also described. The bubble size was assessed as explained in Section 5.2.3. The Particle Image Velocimetry (PIV) and the Positron Emission Particle Tracking (PEPT) techniques were used for the experimental measurements, and are described in Sections 5.3 and 5.4 respectively. Finally, the data processing procedures for establishing the velocity field and the shear rate from both experimental and simulated data are reported in Section 5.5 and 8.5 respectively.

5.1 Sludge Rheology

The research performed by Achkari-Begdouri and Goodrich (1992) on dairy cattle manure was used as a basis for modelling the rheological characteristics of sludge in Wu and Chen (2008); Terashima et al. (2009); Bridgeman (2012); Wu (2014). The first approximation of considering the sludge as a power-law fluid as in Equation 3.9 (and thus ignoring yield stress, shear banding and thixotropy) proved to work well in the work cited above, and therefore was adopted also in the work reported here. The data of Achkari-Begdouri and Goodrich (1992) are reported in Table 5.1 where the sludge densities for different TS are shown. All the values of density differ by less than 1% from water density at 35 degrees (994 kg/m3). For the sake of simplicity, in the CFD simulations a constant density of 1,000 $\mathrm{kg\,m^{-3}}$ was assumed.

Table 5.1 *Rheological properties of sludge at T=35 $^\circ\mathrm{C}$. From Achkari-Begdouri and Goodrich (1992).*

TS ($\%$)	K ($\mathrm{Pa\,s}^n$)	n (–)	$\lvert\dot{\gamma}\rvert$ range (s^{-1})	$\mu_{\min}$ ($\mathrm{Pa\,s}$)	$\mu_{\max}$ ($\mathrm{Pa\,s}$)	Density ($\mathrm{kg\,m^{-3}}$)
2.5	0.042	0.710	226—702	0.006	0.008	1,000.36
5.4	0.192	0.562	50—702	0.01	0.03	1,000.78
7.5	0.525	0.533	11—399	0.03	0.17	1,001.00
9.1	1.052	0.467	11—156	0.07	0.29	1,001.31
12.1	5.885	0.367	3—149	0.25	2.93	1,001.73

5.2 Laboratory Experiment Setup

Validation of CFD models requires an assessment of model performance in comparison to experimental data. This is considered as a fundamental step in any CFD work to ensure that the numerical results have a strong foundation in reality. The CFD work reported here was underpinned by comparing full-scale operational and design scenarios, and therefore a validation of the full-scale case should be the first, natural step. However, the difficulties of performing full-scale validations in anaerobic digestion have been described extensively in Section 3.7, and hence it is unsurprising that satisfactory full-scale validations have not yet been reported in the literature. For this reason, the approach adopted in the work reported here followed that of Wu (2010a) (Section 3.7), which consisted of a first phase of laboratory-scale simulations aimed at proving the concept of the modelling approach, and a second phase in which the same modelling approach was applied to full-scale cases.

The proof of the concept of the modelling approach offered by the laboratory-scale validation is deemed satisfactory when the experimental setup reproduces the conditions of sludge inside a mixed full-scale digester as faithfully as possible. “As faithfully as possible” may be interpreted in different ways. One way is to define a dimensionless group Φ as a product of quantities such as gas flow rate, volume and constants. A laboratory-scale design can be chosen in such a way that the corresponding Φ assumes the same value of the full-scale digester: quantities such as volume and gas flow rate will scale accordingly. This approach leads to a laboratory-scale rig design which is in theory equivalent to a full-scale digester. However, it inevitable that several elements of modelling cannot be incorporated within dimensionless analysis; in particular, the number, size and behaviour of the bubbles. This issue is exacerbated in the case of CFD-based work, where the elements of modelling described above interfere with numerical aspects, such as discretization techniques. For this reason, it is important to stress the fact that the validation of a laboratory-scale case

Table 5.2 *Details of the digester geometry. Courtesy of Peter Vale and Severn Trent Water Inc.*

External diameter	D_{ext}	14.63 m
Diameter at the bottom of the frustum	D_{int}	1.09 m
Cylinder height	h	14 m
Frustum height	h_0	3.94 m
Distance of the nozzle from the axis	R_{noz}	1.75 m
Distance of the nozzle from the bottom	h_{noz}	0.3 m
Maximum gas flow rate per nozzle	Q_{max}	$4.717\ 10^{-3}\ \mathrm{m^3 s^{-1}}$

does in no way ensure that the full-scale case will result to be validated automatically, even in the case of a correctly scaled Φ and flow patterns correctly reproduced. For this reason, an approach based on a dimensionless group can of course be considered as an obvious choice, but in reality, it does not offer a significant advantage over other possible approaches.

An alternative way to interpret “as faithfully as possible” can be to reproduce in the laboratory-scale setup the values of some physical quantities which are important in the full-scale digester. For the problem of gas mixing in anaerobic digestion, it is natural to consider liquid phase rheology, and input mixing power. Even though such approach might be considered less rigorous from the point of view of modelling, it is reasonable to expect that similar conditions of rheology and input mixing power produce similar interaction between number, size and behaviour of the bubbles, even in the case of different setups. Such interactions play a fundamental role in the robustness of the numerical model, and therefore this latter approach was adopted here.

A transparent artificial sludge that matched the rheological properties of the sludge as modelled in Section 5.1 was prepared (Section 5.2.2) and assessed.

To address the input energy mixing, some previous work (for instance Stroot et al. 2001) was driven by practical utility, while many others (Karim et al. 2004, 2005b for instance) chose a maximum mixing power input of 5—8 $\mathrm{W\,m^{-3}}$ in order to meet the US EPA recommendations for proper mixing (U.S. EPA, 1979). In contrast, the approach in this work was to reproduce the mixing input power representative of a real anaerobic digestion plant, or slightly less, in a volume of approximately 4 litres. A typical digester design, provided by Severn Trent Water Ltd, was used as the basis for modelling. More details are reported in Table 5.2. The geometry represented a cylindrical digester with inclined bottom; i.e. a cylinder above an inverted cone, with twelve nozzles positioned in a circular array towards the the bottom of the tank.

The power input for a single nozzle is Wu (2010a):

$$E = P_1 Q \, \ln\left(P_2 / P_1\right) \ , \tag{5.1}$$

where Q is the volumetric flow rate, P_1 is the absolute pressure at the surface (that is, the atmospheric pressure), and P_2 is the absolute pressure at the nozzle (that is, $P_2 = P_1 + \rho g H$). Considering the value of Q_{max} in Table 5.2, the value of the total power per volume unit corresponding to the maximum flow rate is around 2.16 $\mathrm{W\,m^{-3}}$. It is noteworthy that this value is considerably lower than that recommended in U.S. EPA (1979).

Adopting the dimensionless group approach, one could define $\Phi \equiv q^2 g^{-1} \mathcal{V}^{-5/3}$, where q is the total gas flow rate, g the acceleration of gravity and $\mathcal{V}$ the volume. For a volume of 4 litre, this would yield $q = 0.81 \ \mathrm{ml\,s^{-1}}$, for a mixing power per volume unit of 0.26 $\mathrm{W\,m^{-3}}$, one order of magnitude less than the value of a full-scale digester, and consequently, one order of magnitude less than the approach of reproducing relevant physical quantities.

Given that it is impossible to validate the full-scale case through laboratory-scale experiments, it is interesting to prove the concept of modelling though a (laboratory-scale) case which runs in conditions that are more numerically demanding than the full-scale case. Higher input mixing energies means higher flow rates, which in turn means more and larger bubbles. Hence, it is evident that simulating higher input mixing energies, as in the approach of reproducing relevant physical quantities, puts the numerical modelling approach under more adverse circumstances. If the numerical results correspond to the experimental measures in spite of this added difficulty, then it is easier to assume that the modelling approach will be robust even in the full-case case. This aspect is particularly meaningful in the work reported here, as a novel modelling approach, with no analogue in the literature, was developed. In such conditions, it was particularly important to test the numerical validity of the modelling approach.

5.2.1 Experimental Rig

The experimental apparatus (Figure 5.1) consisted of a small tank of about 4 litre capacity, with a simple air nozzle at the bottom. This was assembled by gluing a 20 cm diameter, 20 cm long, 3 mm thick plexiglass pipe onto a square support of side 25.5 cm. Care was taken in order to make sure that the plexiglass pipe axis passed through the support centre. The junction was sealed with silicon. Once filled with the liquid phase, the wet height of the tank was 13 cm.

A simple nozzle arrangement was effected by drilling a 1 mm diameter hole through the axis of a plastic bolt of 10 mm head diameter, 5 mm internal diameter, 25 mm length. A hole with the same diameter of the bolt and a compatible threading was drilled at the centre of the squared support. The bolt was screwed through it such that its head remained at the inner side of the support. The bolt head was neglected in the simulations as its size is negligible when compared with the plexiglass pipe. The air flow was generated by a Nitto Kohki Co., LTD LA-28B air compressor and flow rate was controlled between 0 and 65 $\mathrm{ml\,s^{-1}}$ using a Cole-Parmer EW-03216-14 correlated flowmeter with valve. Flexible plastic 5 mm diameter PVC pipes connected the pump to the flowmeter and the flowmeter to the bolt at the back of the square support. With flow rates of 2.05, 5.30 and 8.63 $\mathrm{ml\,s^{-1}}$, the mixing power per unit of volume, according with Equation 5.1 and the dimensions of the tank reported above, is 0.64, 1.64 and 2.68 $\mathrm{W\,m^{-3}}$ respectively. These value are of the order of magnitude of the input power of the digester described above or slightly less, as

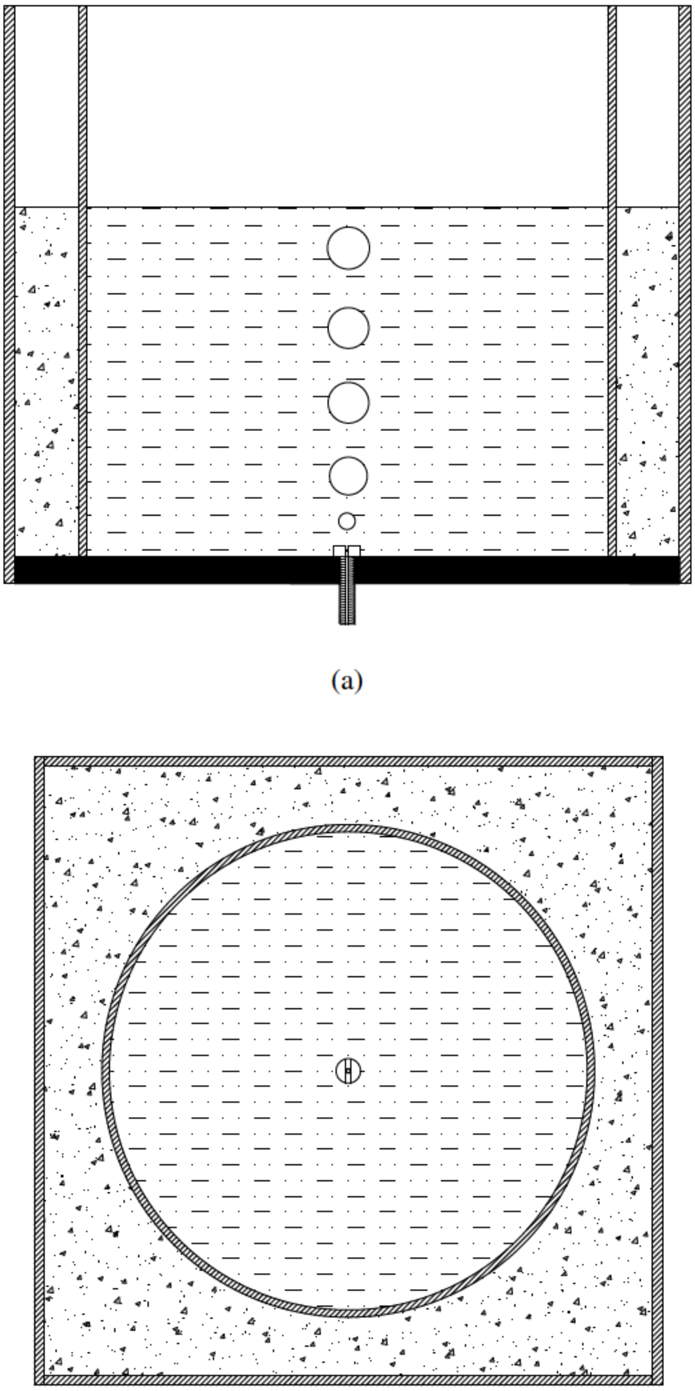
(a)

(b)

Figure 5.1 *Experimental rig top and front view. Pump, flowmeter, pipes and fittings not shown.*

required.

The PIV measurement involved laser beams, and refraction was expected to occur at the curved plexiglass surface of the cylinder. As this could potentially alter the results, a mitigation strategy was implemented by encasing the cylindrical tank within a plexiglass tank fixed to the square support which was subsequently filled with water. This ensured that the refraction coefficient through the plexiglass surface was minimised. The glass layer was set orthogonal to the PIV camera such that refraction through the water-glass and glass-air interfaces might be neglected. According to the Snell law, the difference Δ between the incident angle θ and the refracted θ' can be expressed as a function of the respective refractive indices n and n':

$$\Delta \equiv \left| \frac{\theta - \theta'}{\theta} \right| \simeq \left| 1 - \frac{n'}{n} \right| \ . \tag{5.2}$$

Assuming the refractive indices to be 1.333 for water at 20 degrees, 1.488 for plexiglass and 1.000 for air, Δ assumes the value of 0.33 for plexiglass-air interface and 0.12 for plexiglass-air interface. Thus, the gain in precision of the strategy described above is evident.

5.2.2 Preparation of the Liquid Phase

In the work reported here, water solutions of Sigma-Aldrich 419338 sodium carboxymethyl cellulose (CMC) with average molar weight of 700,000 were used in order to reproduce the behaviour of sludge. CMC is a polymeric cellulose derivative that is widely used for reproducing pseudoplastic fluids, and, in particular, sludges (e.g. Wu and Chen (2008)). It consists of a white powder that can be dissolved into water and gives rise to a transparent solution. Three CMC solutions were employed, namely 2, 4 and 8 $\mathrm{g\,l^{-1}}$.

Each solution was prepared as follows. (*i*) 5 litres of room temperature, tap water were poured into a bucket. (*ii*) A 20 cm width, 4 cm height rectangular impeller was used to stir the water. The impeller angular velocity was set in order to guarantee a sufficient degree of mixing, but to minimise the inclusion of air bubbles into the water. (*iii*) The CMC powder was added to the water at a rate not greater than 5 g min^{-1}. (*iv*) The impeller mixed the solutions for between one and two hours, whereupon it was removed and the bucket sealed. The solution was left standing at room temperature for at least 24 hours.

Sludge rheology was assessed using a TA Instruments AR1000 rheometer fitted with a 40 mm diameter 2° steel cone.

5.2.3 Bubble Size Assessment

Evaluations of bubble diameters and regime velocity were obtained from visual examination of the outcome of the High Speed Camera experiment. If N is the number of bubbles crossing a given ideal horizontal plane in a time t and Q is the volume flow rate, then the average bubble volume can be evaluated by:

$$V_p = \frac{Qt}{N}\,, \tag{5.3}$$

and the diameter as:

$$d = \left(\frac{6}{\pi}V_p\right)^{1/3}\,. \tag{5.4}$$

5.3 Particle-Image Velocimetry (PIV)

PIV is a non-invasive flow-visualization technique that allows quantitative measurements of the velocity field in 2D or 3D. Reflective microparticles are seeded within the fluid and then are illuminated in a plane of the flow at least twice within a short time interval (Raffel et al., 2007). The illumination is due to a pulsating laser beam spread in a plane by an appropriate optical system. The light scattered by the particles is recorded with a CCD camera (Raffel et al., 2007). The displacement of the particle images between the light pulses is determined by a post-processing software through evaluation of the PIV recordings (Raffel et al., 2007). Figure 5.2 shows a generic PIV schematic diagram.

The idea of using seeding particles to study flow patterns was implemented qualitatively by Leonardo Da Vinci in 1508-1510 and, later, by Ludwig Prandtl in 1904. However, it was in the 1980s that the technological advance allowed to perform quantitative measurements with PIV (Raffel et al., 2007).

The PIV measurements described in this work were performed using a TSI PIV system (TSI Inc, USA). The system comprised a 532 nm (green) Nd-Yag laser (New Wave Solo III) pulsing at 7 Hz, synchronized to a single TSI Power view 4MP (2048 x 2048 pixels) 12 bit CCD camera using a synchronizer (TSI 610035) attached to a personal computer. The PIV system was controlled using TSI Insight 4G software. The spatial resolution of the measurements was 977 $\mu\mathrm{m}\,\mathrm{pixel}^{-1}$. Insight software was used to process the sets of pair raw images and convert them in a $n \times 4$ matrix, where n is the number of cell of the grid and the four columns are x position, y position, x velocity and y velocity. Each experiment

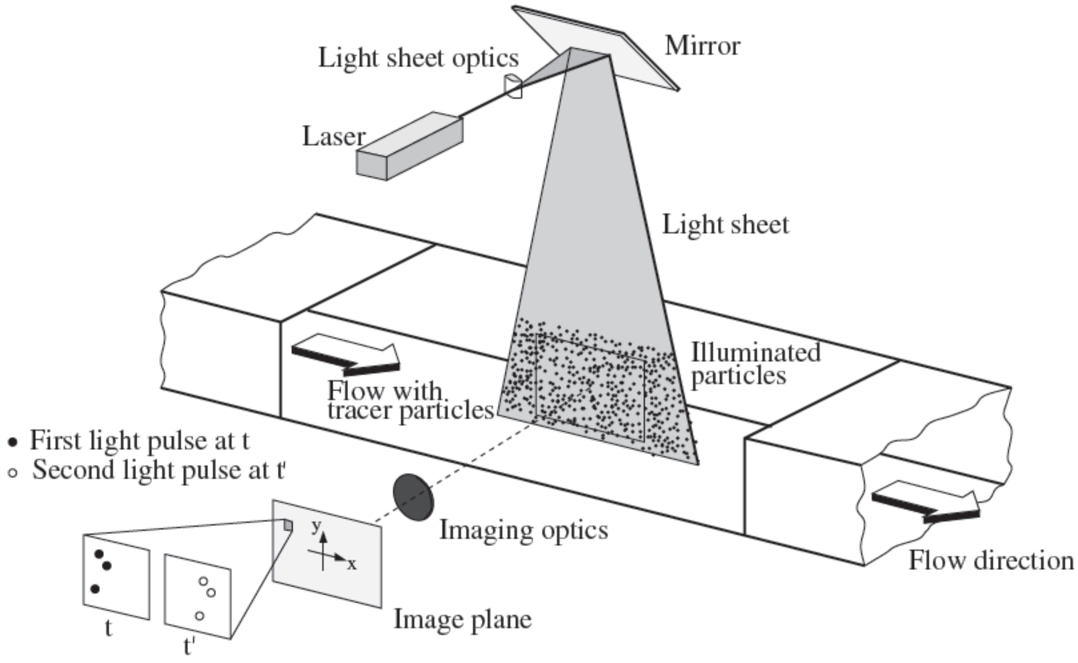

Figure 5.2 *Schematic of a PIV experimental setup. Raffel et al. (2007)*

captured 300 images which were used to determine the average flow field of the system. The cell size selected for these experiments was 64×64 pixels.

5.4 Positron-Emission Particle Tracking (PEPT)

The technique of Positron Emission Particle Tracking (PEPT) was developed at the University of Birmingham (Parker et al., 1993). This technique employs radioactivity to track the flow patterns, and therefore has the benefit of being unaffected by the fluid optical properties. For this reason, it can be successfully applied to opaque fluids such as sludge. The PEPT technique is based around the medical imaging modality of Positron Emission Tomography (PET) where the spatial distribution of radioactive material is measured based upon detecting the gamma emissions produced by radioactive decay of the material. In PEPT however, rather than a volume of activity which is traditionally imaged, just a single particle labelled with radioactive ^{18}F is tracked. According to Fan et al. (2006), ^{18}F is used because does not produce any γ-rays other than the 511 keV annihilation photons, thus giving a high accuracy of detected locations, and because of its convenient half-life (109 minutes).

The tracer particles were prepared as explained in Fan et al. (2006). A ^{18}F aqueous solution was produced by exposing ultrapurified water to a 35 MeV ^{3}He beam from the Birmingham Radial Ridge Cyclotron. ^{18}F is produced from oxygen due to the following nuclear reactions:

$$^{16}_{8}\mathrm{O} + ^{3}_{2}\mathrm{He} \longrightarrow ^{18}_{9}\mathrm{F} + p\ ; \tag{5.5}$$

$$\begin{aligned} ^{16}_{8}\mathrm{O} + ^{3}_{2}\mathrm{He} &\longrightarrow ^{18}_{10}\mathrm{Ne} + n\ , \\ ^{18}_{10}\mathrm{Ne} + e^{-} &\longrightarrow ^{18}_{9}\mathrm{F} + \nu_e\ . \end{aligned} \tag{5.6}$$

The tracer particle consisted of strong base anion exchange neutrally-buoyant resin beads which were immersed into the ^{18}F aqueous solution and then dried and fixed under a heated and dry nitrogen gas steam and an infrared lamp, following the same procedure as in Sindall (2014). In order to ensure long-term survival of the tracking particles and prevent loss of activity to the surrounding media (which could potentially introduce additional noise to the measurement), the beads were sealed with a thin layer of lacquer coating. The details of the tracer particles are summarised in Table 5.3.

The ^{18}F nuclei undergo a β^+ decay:

$$^{18}_{9}\mathrm{F} \longrightarrow {}^{18}_{8}\mathrm{O} + e^+ + \nu_e \ . \tag{5.7}$$

$^{18}_{8}$O is stable. The positron produced in Reaction 5.7 quickly annihilate with local electrons in the surrounding media. Advantageously, this annihilation results in a pair of gamma photons which are constrained to have equal and opposite momenta and a fixed energy of 511 KeV. Provided both photons are detected by the PEPT photomultiplier and scintillator arrays, the line along which they travelled can be reconstructed, with the annihilation site placed somewhere along this Line of Response (LoR). In PEPT a set of consecutive LoRs are recorded on a rapid timescale, and a triangulation technique is applied to locate the centroid of the LoR ensemble. This is assumed to be the instantaneous particle position. This technique has been shown to locate particles through significant amounts of dense and opaque materials and is relatively insensitive to the effects of gamma ray scatter and attenuation. Typically at the University of Birmingham LoRs can be acquired at rates up to

Table 5.3 *Details of the tracer particle.*

Label	Diameter (μm)	Type	Activity (μCi)	Avg. count rate (kHz)	Location rate (Hz)
cmc02	425—500	Sealed resin	340—650	83	55
cmc04 no. 1	180—250	Resin	340—650	78	52
cmc04 no. 2	425—500	Sealed resin	340—650	14	9.5

100kHz, giving particle location rates of around 1kHz which are accurate to approximately 0.5mm in 3 dimensions.

The ADAC positron camera which consists of 2 large area position sensitive gamma detectors (Parker et al. (2002)) was used to record the pairs of gamma photons emitted by the particle. The PEPT algorithm was used to determine the instantaneous location of the particle in 3 dimensions and hence its velocity distribution. The algorithm parameters were optimised and pertinent data calculated using the standard methods outlined by Leadbeater et al. (2012).

5.5 Computation of Velocity Field

5.5.1 PIV-Averaged Velocity Field

In the arrangement described in this work, the PIV technique detected the components of the Eulerian velocity field lying on a given planar section of the fluid domain. A vertical plane, 3 cm away from the cylinder axis and parallel to the x axis was chosen for the scope.

$$\begin{cases} x \in (-X_{\max},\, X_{\max}) \\ y \in (0,\, H) \\ z = Z_{\mathrm{PIV}} \end{cases} \tag{5.8}$$

Z_{PIV} is the (constant) z coordinate at the PIV plane, $X_{\max} = (R^2 - Z_{\mathrm{PIV}}^2)^{1/2}$, where R is the tank radius, and H is the tank height. This plane is referred to as the PIV plane hereafter.

The “PIV-averaged” velocity field is defined as a two-component field defined thorough the PIV plane, built up by the x and y components of the liquid phase velocity field, each one separately averaged over time. The PIV-averaged velocity field is what the PIV technique produced as an output. In order to compare the PIV experimental measurements with the simulated predictions, the PIV-averaged velocity field was calculated also from the simulated data.

5.5.2 PEPT-Averaged Experimental Velocity Field

The output of a PEPT run is a succession:

$$\left(\mathbf{x}_n^{\mathrm{tr}},\, t_n\right) , \qquad n = 1, \ldots , N , \tag{5.9}$$

where $\mathbf{x}_n^{\mathrm{tr}} \equiv (x_n^{\mathrm{tr}},\, y_n^{\mathrm{tr}},\, z_n^{\mathrm{tr}})$ are the measured Cartesian coordinates of the tracer particle at the time t_n, and the integer n labels the timestep. What is required is to work out an estimation of the stationary Eulerian liquid velocity field $\mathbf{u}(\mathbf{x})$ from the PEPT measurements (Equation 5.9).

First of all, a succession for the velocities:

$$\left(\mathbf{u}_n^{\mathrm{tr}},\, t_n\right) , \qquad n = 1, \ldots , N - 1 , \tag{5.10}$$

can be calculated from the PEPT output (Equation 5.9) by applying an upward differencing scheme:

$$\mathbf{u}_n^{\mathrm{tr}} \approx \frac{\mathbf{x}_{n+1}^{\mathrm{tr}} - \mathbf{x}_n^{\mathrm{tr}}}{t_{n+1} - t_n} . \tag{5.11}$$

As explained later on, the Eulerian velocity field was found to be axis-symmetric. Therefore, the information about $\mathbf{u}(\mathbf{x})$ reduces to the knowledge of $\mathbf{u}(r,\, y)$. The domain $(0,\, R) \times (0,\, H)$ can be decomposed into small rectangles, each labelled by the couple of integers $(\alpha,\, \beta)$, by dividing the interval $(0,\, R)$ into N_r parts, and $(0,\, H)$ into N_y parts. Therefore we have $\alpha = 1, \ldots , N_r$ and $\beta = 1, \ldots , N_y$. $\mathbf{u}(r,\, y)$ is then approximated by $\mathbf{u}_{\alpha\beta}$, that takes a constant value inside the rectangle $(\alpha,\, \beta)$.

The PEPT output (Equation 5.9) can therefore be converted into a discretized form:

$$(\alpha_n,\, \beta_n,\, t_n)\ , \qquad n = 1, \ldots, N \tag{5.12}$$

by using the following expressions:

$$\begin{aligned} \alpha_n &= \text{ int}\left[r_n^{\text{tr}} \frac{N_r}{R} - \varepsilon \right] + 1 \\ \beta_n &= \text{ int}\left[y_n^{\text{tr}} \frac{N_y}{H} - \varepsilon \right] + 1\,, \end{aligned} \tag{5.13}$$

where:

$$r_n^{\text{tr}} = \sqrt{\left(x_n^{\text{tr}}\right)^2 + \left(z_n^{\text{tr}}\right)^2}\ . \tag{5.14}$$

Here $\text{int}\,[\xi]$ means “integer part of ξ”, and rounds ξ to the nearest smaller integer and ε is a small correction, in this work 10^{-6}.

The field $\mathbf{u}_{\alpha\beta}$ is constructed in this way: for every couple $(\alpha^*,\, \beta^*)$ inside the domain, the value of $\mathbf{u}_{\alpha^*\beta^*}$ is evaluated by averaging over all the $\mathbf{u}_n^{\text{tr}}$ such that $\alpha_n = \alpha^*$ and $\beta_n = \beta^*$. If there are no such $(\alpha_n,\, \beta_n)$, then the value $\mathbf{u}_{\alpha^*\beta^*}$ is left undefined. This can be done in a computationally effective way by initializing all the $\mathbf{u}_{\alpha\beta}$ and a matrix of integer counters $C_{\alpha\beta}$ to zero, cycle over the n and, inside the cycle, add the value of $\mathbf{u}_n^{\text{tr}}$ to the corresponding $\mathbf{u}_{\alpha^*\beta^*}$ and increase $C_{\alpha^*\beta^*}$ by one. After the cycle ends, every $\mathbf{u}_{\alpha^*\beta^*}$ is divided by its corresponding$C_{\alpha^*\beta^*}$ if the latter is not zero, otherwise it is set to `NaN` (“not-a-number”) value. The velocity field calculated in this way is called “PEPT-averaged” experimental velocity field.

As an estimation of the measurement uncertainty, the standard error calculated from the adapted standard deviation was employed for the rectangles the tracer passed through at least three times. For the rectangles it passed through once, the maximum value for the standard error over the domain as described above was used.

5.5.3 PEPT-Averaged Simulated Velocity Field

In order to compare the PEPT outcome with simulated data, a PEPT-averaged velocity field was calculated from the simulated data in the following way. Passive parcels of 5 $\mu\mathrm{m}$ diameter and 1,000 g m^{-3} density were generated and used as a tracer. The parcels were introduced after a simulation time of 10 s from the start of the main runs at predetermined sites, and then left evolving. The sites were chosen at the vertices of a cubic lattice of 1 cm side that spans the whole computational domain, with the exception of the lattice vertices with x or z coordinate magnitude of 0 or 1 cm. A total of 1,968 passive parcels was generated.

The positions and velocities of the tracer parcels were recorded at integer seconds. The resulting output consists of a succession of points coordinates and velocities:

$$\left(\mathbf{x}_n^{\mathrm{tr}}, \mathbf{u}_n^{\mathrm{tr}}\right) , \qquad n = 1, \ldots, N , \tag{5.15}$$

where N is the product of the tracer parcels times the timesteps at which the positions and velocities were recorded. From the succession above, a radial discretized velocity field $\mathbf{u}_{\alpha\beta}$ was build out of radial symmetry considerations in the same way as described in Section 5.5.2.

5.6 Average Shear Rate

Following the seminal work presented in Camp and Stein (1943), average shear rate has become a fundamental process characteristic to classify mixing in vessels (Bridgeman, 2012), and a parameter of interest in environmental engineering design (Tchobanoglous et al., 2010). This approach is still in use, even if it has been pointed out (Clark, 1985) that a single number cannot represent a complex turbulent flow, where areas of high input power coexist with dead zones (Sindall et al., 2013). Bridgeman (2012) performed CFD simulations on an impelled-stirred laboratory-scale digester and divided the domain into high, medium and low-velocity zones depending on the pointwise value of the velocity magnitude, and showed that a change in the impeller angular velocity does not have a relevant effect on the low-velocity zone. Bridgeman (2012) also divided the domain into bulk, bottom impeller, top impeller and vessel zones, and showed that each zone has a different value of average shear rate.

In this work, the shear rate value is expected to encompass several orders of magnitude due to the coexistence of turbulent (around the bubbles) and relatively quiescent zones. It is then appropriate to divide the domain into fixed, concentric zones and compute the average shear rate therein. In this way, a single number can be associated to a relatively homogeneous zone, and then compared with an analogous number calculated from the experimental data. This approach is simple as it uses only single numbers, but it is more meaningful than assessing simulated and experimental shear rate values averaged over the whole domain. This is because, if the datum of the shear rate averaged is over the whole domain, an element of granularity would be lost.

5.6.1 PIV-Averaged Shear Rate

An expression for the average shear rate can be worked out from the two components of the PIV-averaged velocity field. Assuming axis symmetry, Equation 3.8 reduces to:

$$|\dot{\gamma}(r,\, y)| = \left| \frac{\partial u_r}{\partial y} + \frac{\partial u_y}{\partial r} \right| \,, \tag{5.16}$$

where r is the radial coordinate, and the tangential components of the shear stress are eliminated due to the radial symmetry. Equation 5.16 can be rewritten in terms of x and y, and thus evaluated on the PIV plane:

$$|\dot{\gamma}(x,\, y)| = \sqrt{1 + \frac{Z_{\mathrm{PIV}}^2}{x^2}} \left| \frac{\partial u_x}{\partial y} + \frac{\partial u_y}{\partial x} \right| \, . \tag{5.17}$$

The equation above can be discretized with a central differencing scheme. The intervals $(-X_{\max},\, X_{\max})$ and $(0,\, H)$ can be decomposed into $2N_x$ and N_y parts:

$$\begin{aligned} -X_{\max} \equiv x_{-N_x},\, x_{-N_x+1},\, \ldots,\, x_\alpha,\, \ldots,\, x_{N_x-1},\, x_{N_x} \equiv X_{\max} \\ 0,\, \ldots,\, y_\beta,\, \ldots,\, y_{N_y} \equiv H \end{aligned} \tag{5.18}$$

Then we have:

$$\begin{aligned} |\dot{\gamma}|_{\alpha\beta} \approx \sqrt{1 + \frac{Z_{\mathrm{PIV}}^2}{x_\alpha^2}} & \left| \frac{u_{x,\,\alpha,\,\beta+1} - u_{x,\,\alpha,\,\beta-1}}{y_{\beta+1} - y_{\beta-1}} \right. \\ & + \left. \frac{u_{y,\,\alpha+1,\,\beta} - u_{y,\,\alpha-1,\,\beta}}{x_{\alpha+1} - x_{\alpha-1}} \right| \, . \end{aligned} \tag{5.19}$$

The shear rate can be integrated over a volume domain comprised between two radii r_a and r_b and height equal to the cylinder wet height, and divided by the volume of the domain. This gives the average shear rate over that domain. r_a and r_b can be rewritten as $(x_a^2 + z^2)^{1/2}$ and $(x_b^2 + z^2)^{1/2}$ respectively, where x_a and x_b are the x components of r_a and r_b respectively. A change of integration variables from r to x thus allows us to express the average shear rate in tems of x and y, and to evaluate it by integrating over the PIV plane. x_a and x_b can be rewritten as $aX_{\max}$ and $bX_{\max}$:

$$\begin{aligned} \langle\dot{\gamma}\rangle_a^b = \frac{2}{X_{\max}^2 H \left(b^2 - a^2\right)} \int_0^H \mathrm{d}y \\ \frac{1}{2} \left(\int_{-bX_{\max}}^{-aX_{\max}} + \int_{aX_{\max}}^{bX_{\max}} \right) \mathrm{d}x \, \sqrt{x^2 + Z_{\mathrm{PIV}}^2} \; |\dot{\gamma}(x,\, y)| \, . \end{aligned} \tag{5.20}$$

The expression above can be evaluated numerically with the rectangle rule method:

$$\langle\dot{\gamma}\rangle_a^b \approx \frac{2}{X_{\mathrm{max}}^2 H\left(b^2-a^2\right)} \sum_{\beta=0}^{N_y} \frac{1}{2}\left(\sum_{\alpha=-b}^{-a} + \sum_{\alpha=a}^{b}\right) \frac{x_{\alpha+1}-x_{\alpha-1}}{2}\,\frac{y_{\beta+1}-y_{\beta-1}}{2}\sqrt{x_\alpha^2+Z_{\mathrm{PIV}}^2}\;|\dot{\gamma}|_{\alpha\beta}\ , \tag{5.21}$$

5.6.2 PEPT-Averaged Shear Rate

Analogous with Section 5.6.1, another expression for the average shear rate can be calculated, this time from the PEPT-averaged velocity field. Again, axial symmetry is directly exploited, and the starting point is the expression of the shear rate reported in Equation 5.16:

$$|\dot{\gamma}(r,\,y)| = \left|\frac{\partial u_r}{\partial y} + \frac{\partial u_y}{\partial r}\right|\ . \tag{5.22}$$

This expression can be averaged over a volume domain comprised between two radii $r_a \equiv aR$ and $r_b \equiv bR$, $0 \le a < b \le 1$, as:

$$\langle\dot{\gamma}\rangle_a^b = \frac{\int_0^H \mathrm{d}y \int_a^b \mathrm{d}r\; r\;|\dot{\gamma}(r,\,y)|}{\int_0^H \mathrm{d}y \int_a^b \mathrm{d}r\; r}\ . \tag{5.23}$$

Equation 5.22 can be discretized with a central differencing scheme using the same discretization of Section 5.5.3:

$$|\dot{\gamma}|_{\alpha\beta} \approx \left|\frac{u_{r,\,\alpha,\,\beta+1}-u_{r,\,\alpha,\,\beta-1}}{y_{\beta+1}-y_{\beta-1}} + \frac{u_{y,\,\alpha+1,\,\beta}-u_{y,\,\alpha-1,\,\beta}}{r_{\alpha+1}-r_{\alpha-1}}\right|\ . \tag{5.24}$$

Equation 5.23 can then be approximated with the rectangle rule method. Let $\xi_{\alpha\beta}$ be 0 if the rectangle $(\alpha\,\beta)$ has never been occupied by a tracer particle; 1 elsewhere. Then we have:

$$\langle\dot{\gamma}\rangle_a^b \approx \frac{\sum_{\beta=0}^{N_y}\sum_{\alpha=a}^{b} \frac{x_{\alpha+1}-x_{\alpha-1}}{2}\,\frac{y_{\beta+1}-y_{\beta-1}}{2}\; r_\alpha\;\xi_{\alpha\beta}\;|\dot{\gamma}|_{\alpha\beta}}{\sum_{\beta=0}^{N_y}\sum_{\alpha=a}^{b} \frac{x_{\alpha+1}-x_{\alpha-1}}{2}\,\frac{y_{\beta+1}-y_{\beta-1}}{2}\; r_\alpha\;\xi_{\alpha\beta}}\ . \tag{5.25}$$

6

Experimental Results

> *"No amount of experimentation can ever prove me right; a single experiment can prove me wrong."*
>
> Albert Einstein (4th December 1926).
> Letter to Max Born

THE LABORATORY-SCALE experimental results are described in this chapter. First of all, the results of the experimental measurements as well as the outcome of the high speed camera for measuring the bubble size are presented in Sections 6.1 and 6.2 respectively. Then, the outcome of the PIV measurements is described in Section 6.3. Finally, the results of the PEPT experiment are shown in Section 6.4.

6.1 Rheological Measurements

Viscosity measurements were performed in the shear rate interval 100—500 s^{-1} and fitted to the power-law relation of Equation 3.9. The results are shown in Figure 6.1, and rheological data are reported in Table 6.1. The power-law assumption is clearly verified.

6.2 Bubble Size Measurement

Three CMC solutions were used (Section 6.1, Table 6.1) and for each of them, three different air flow rates were assessed. An example of the high speed camera output is

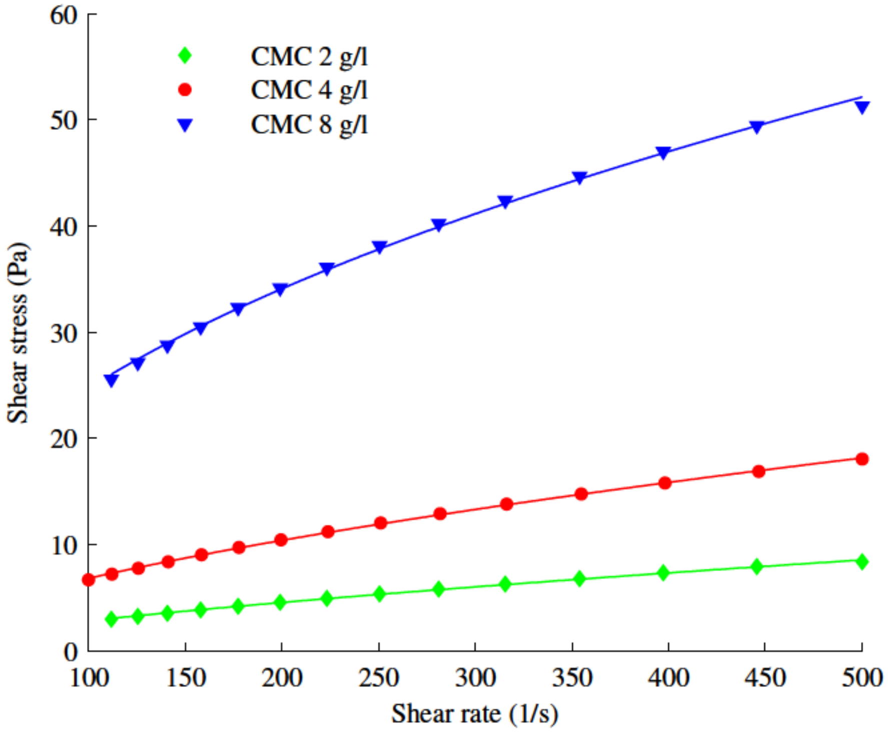

Figure 6.1 *Shear rate-shear stress dependence. Points: measured values. Lines: best fits.*

depicted in Figure 6.2. The values of Q, together with the measured quantities t and N and the resulting d are displayed in Table 6.2.

6.3 PIV

Experiments were performed for each of the CMC solutions shown in Table 6.1, and each of the air flow rates shown in Table 6.2. Once the regime conditions for the flow

Table 6.1 *Fitted parameters for the shear rate-shear stress dependance.*

Label (–)	Concentration ($\mathrm{g\,l^{-1}}$)	K ($\mathrm{Pa\,s}^n$)	n (–)
cmc02-*	2	0.054	0.805
cmc04-*	4	0.209	0.730
cmc08-*	8	1.336	0.619

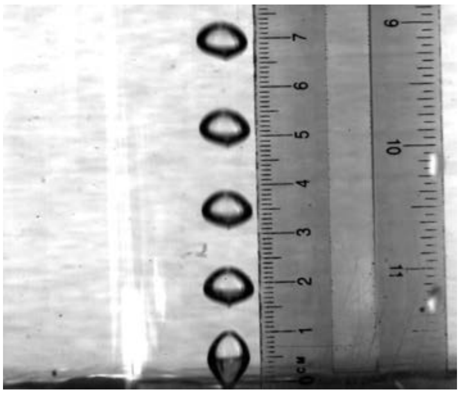

Figure 6.2 *High speed camera photo of the bubble plume. The cmc04-2 solution was used.*

and the bubbly motion had been reached (at least 2 minutes after the air flow rate had been set), the average field was measured over a time period of approximately 3 s (being approximately the time between one bubble reaching the surface and the next one to do the same). The maximum experiment timescale was observed to be 0.34 s, which is one order of magnitude smaller than the PIV averaging time.

6.3.1 PIV Velocity Field

The PIV technique was employed to measure the x and y components of the velocity field throuough the PIV plane defined in Equation 5.8. In Figure 6.3, the resulting PIV-averaged

Table 6.2 *High speed camera outcome.*

Label (–)	Q $(\mathrm{ml\,s^{-1}})$	d (mm)
cmc02-1	2.05	7.01
cmc02-2	5.30	7.01
cmc02-3	8.63	7.01
cmc04-1	2.05	7.94
cmc04-2	5.30	7.94
cmc04-3	8.63	7.94
cmc08-1	2.05	11.0
cmc08-2	5.30	12.8
cmc08-3	8.63	13.8

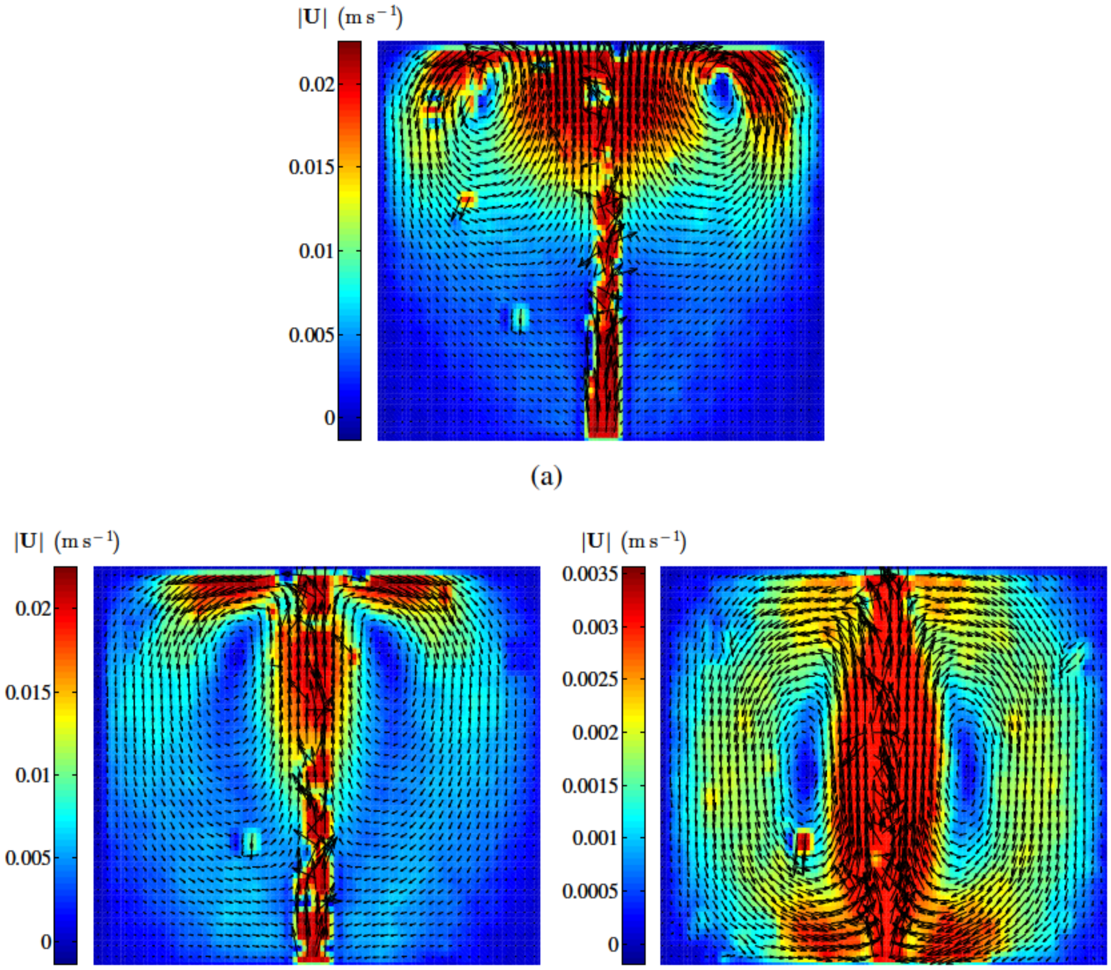

(a)

(b)

(c)

Figure 6.3 *PIV-averaged experimental velocity field, measured with the PIV technique. (a) cmc02-2 run. (b) cmc04-2 run. (c) cmc08-2 run. Note change in scale on vertical axis from (b) to (c).*

velocity field (see Section 5.5.1) is depicted for the cmc02-2, cmc04-2 and cmc08-2 runs.

The flow patterns structure is broadly the same for all the runs. The liquid phase first rises fast in a narrow central region due to the push of the bubble column; then, it moves laterally towards the walls once the surface is reached, and finally it sinks towards the bulk and forms a toroidal vortex. Two circular dead zones, corresponding to the intersection of the PIV plane and the toroidal vortex, are clearly visible at mid-distance between the rising column and the wall, both left and right to the column.

The most evident effect of the increase of the quantity of CMC in the solution consists of a decrease of the average velocity, but also some changes on the flow patterns occur. The central vertical column increases in width. In addition, the lateral motion below the surface is proportionally less intense, and the liquid phase sinks earlier, thus resulting in the toroidal vortex being displaced below and more near the rising column. Finally, the higher-velocity zones in the higher half of the tank that can be seen in the cmc02-2 solution become less and less intense, until the velocity magnitude is approximately the same in both the higher and lower parts of the tank. This effect can be explained as follows. In the cmc02-2 solution, the bubbles are accelerated through the whole height of the tank due to buoyancy; therefore, their velocity near the surface is higher than at the bottom of the tank, and consequently the momentum transferred to the liquid phase is higher. However, when the CMC concentration rises, the viscous friction becomes large enough to counter the buoyancy, and the bubbles reach a lower regime velocity in progressively lower parts of the tank. Figure 6.3c indicates that the regime velocity is probably reached shortly after the bubble is released by the nozzle. This explains the relatively uniform velocity distribution for higher CMC concentrations.

6.4 PEPT

Three PEPT runs were preformed. One was performed with the 2 g ℓ^{-1} solution and the air flow rate labelled as cmc-2-2 in Table 6.2. Two were also performed with the 4 g ℓ^{-1} solution and the air flow rate labelled as cmc-4-2 in Table 6.2. Data were collected for approximately 30 minutes for the 2 g ℓ^{-1} run, and 50 minutes for the 4 g ℓ^{-1} ones. Care was taken to change the tracer position between the first and the second 4 g ℓ^{-1} run.

6.4.1 Time Evolution

The time evolution of the x, y and z coordinates of the tracer during each run are shown in Figure 6.4. The time evolutions of the coordinates are correlated with one another in each run. Each coordinate generally evolves following a main oscillatory mode of about 0.1 Hz for the 2 g l-1 run, and between 0.1 (first run) and 0.01 Hz (second run) for the 4 g l-1 runs.

The main oscillatory mode is modulated by modes of period comparable with the time span of the runs. These secondary modes do not have a large impact on the two 4 g ℓ^{-1} runs; on the contrary. they give rise to a chaotic pattern on the 2 g ℓ^{-1} run.

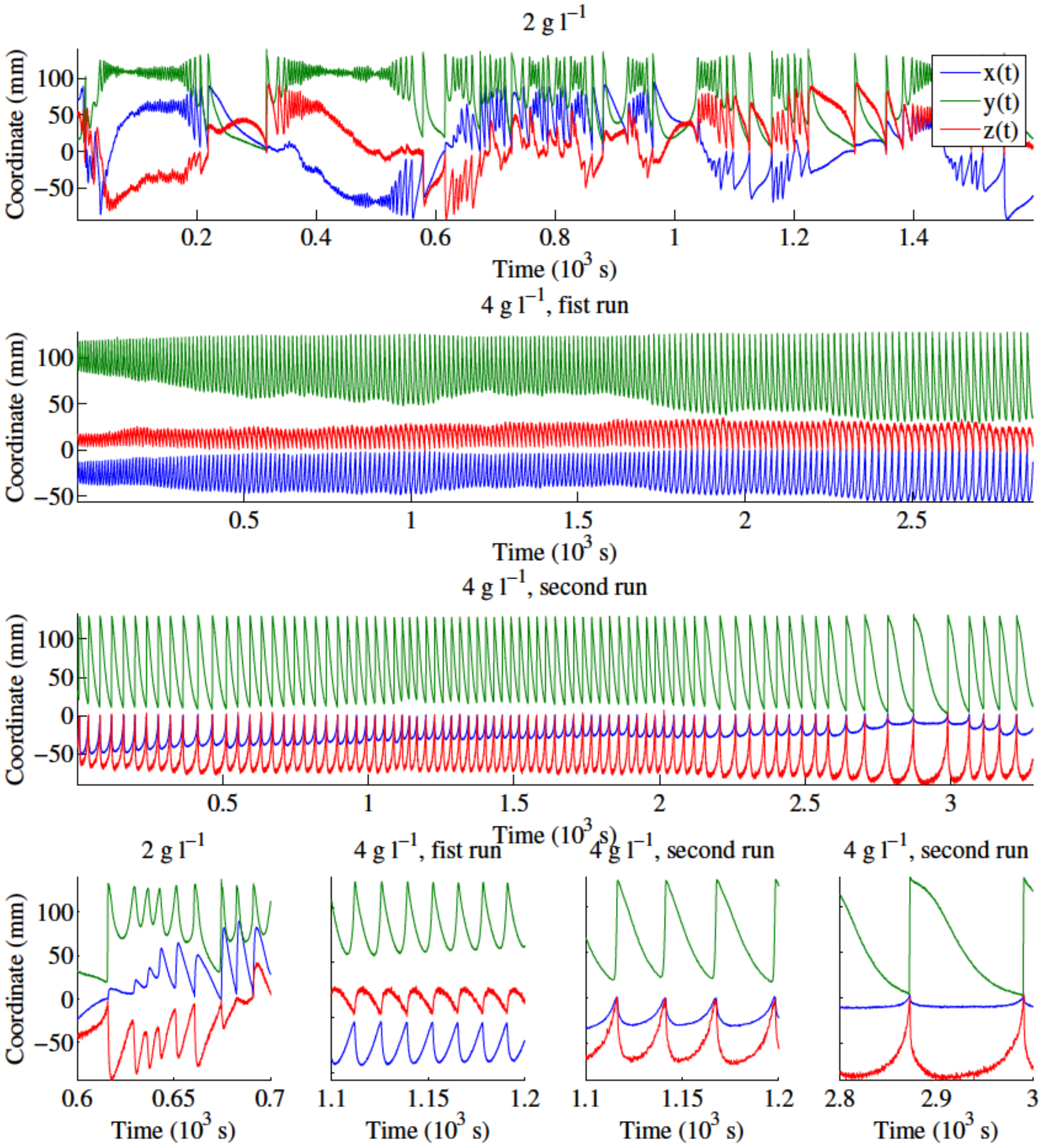

Figure 6.4 *Time evolution of the tracer position during the PEPT runs.*

6.4.2 Trajectories

In Figure 6.5, the trajectories of the tracer are shown. It is evident that the main motion consists of a quasi-cyclical trajectory in which the tracer is swiftly dragged upwards by the central bubble plume, and then revolves around a toroidal vortex approximately 100 mm

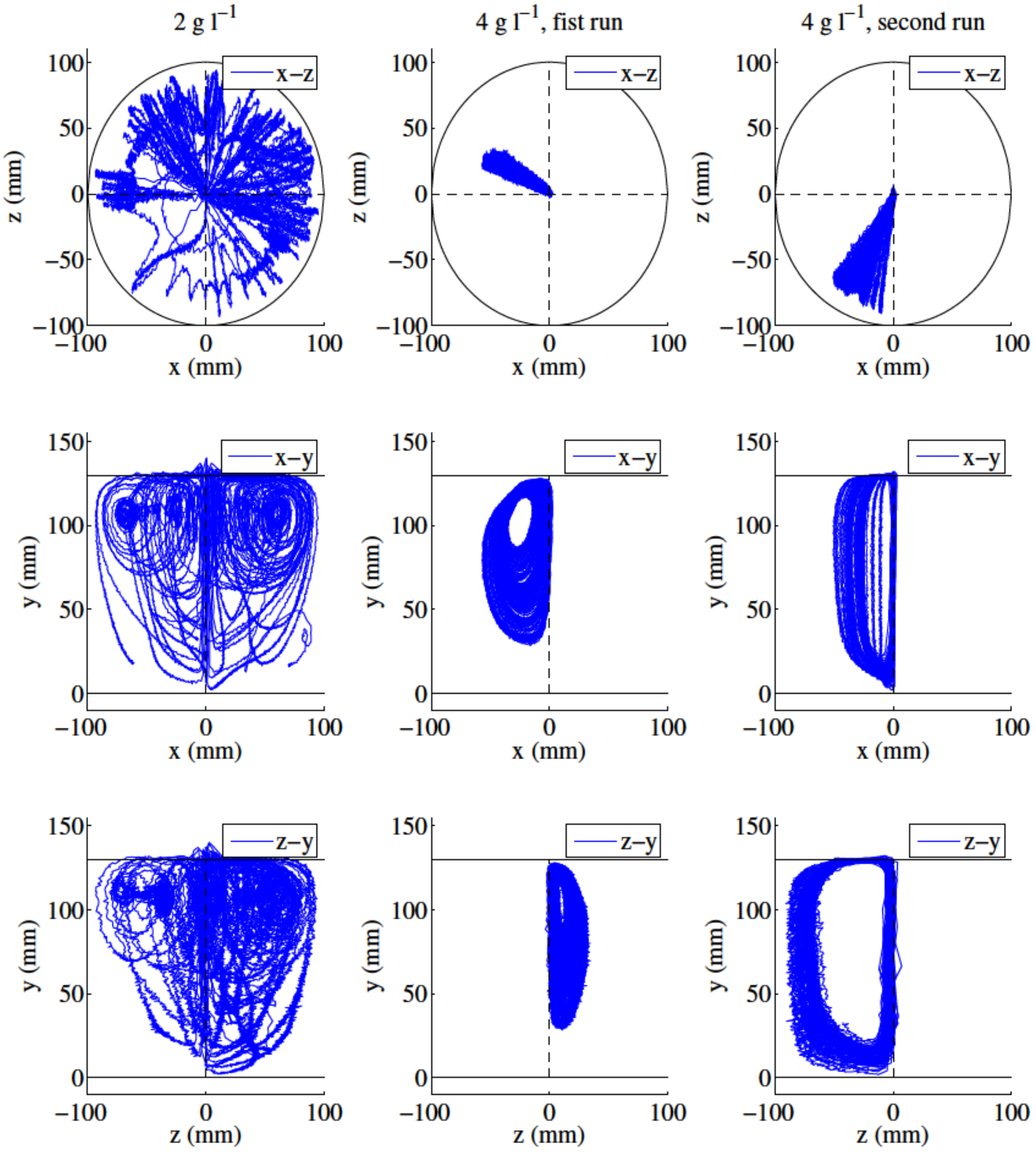

Figure 6.5 *Trajectory of the tracer. Projections over the x-z, x-y and x-z plane.*

above the bottom of the tank. The trajectory of a single revolution lies onto a radial plane, and the radial symmetry of the flow is evident. This cyclical pattern corresponds to the main oscillatory motion observed in Figure 6.4.

The trajectory is not perfectly cyclical as a precession of the radial plane on with the particle revolves is evident. Moreover, the radius of the cycles varies considerably. Deviations from a uniform cyclical motion occur smoothly in the 4 $\mathrm{g}\,\ell^{-1}$ runs, in contrast to the 2 $\mathrm{g}\,\ell^{-1}$ runs where frequent and abrupt changes occur. The deviations from the uniform cyclical motion can be attributed to the disturbance due to the pulsating nature of the bubble column. In fact, even though the air is injected at a constant flow rate, it arranges itself into discontinuous bubbles once inside the system. The momentum transfer from air to liquid is therefore pulsating, and this forces the tracer to change trajectory smoothly (as in the 4 $\mathrm{g}\,\ell^{-1}$ runs) or abruptly (as in the 2 $\mathrm{g}\,\ell^{-1}$ runs).

In both the 4 $\mathrm{g}\,\ell^{-1}$ runs, the tracer spans a narrow zone of the domain—closer to the vortex in the first, away from it and closer to the border in the second. This implies that the degree of mixing is poorer in thicker solutions, and that the trajectory depends more strongly on the initial conditions (in the case reported in this work, the starting point in which the tracer particle was dropped).

6.4.3 Average Occupancy

In Figure 6.6, the azimuthally-averaged occupancy (see Section 5.5.2) is displayed. In the 4 $\mathrm{g}\,\ell^{-1}$ solution, the particle gets trapped into a circular revolution with approximately constant radius. This has already been noticed in the discussion about trajectories (Section 6.4.2).

In comparison, in the 2 $\mathrm{g}\,\ell^{-1}$ solution, the particle spans a wider area, but spends a large amount of time at the centre of the toroidal vortex. This is in agreement with the time evolution described in Section 6.4.1. Figure 6.4, in fact, shows that the particle undergoes a sequence in which first spans a large part of the domain, then gets trapped inside the vortex and oscillates there for long time before eventually escaping and repeating the whole sequence.

6.4.4 PEPT Velocity Field

The PEPT-averaged velocity field is shown in Figure 6.7. The two runs performed with the 4 g ℓ^{-1} solution are joined together. Flow phenomena identified in the PIV measurements (Section 6.3.1) are confirmed by PEPT. The rapidly-rising column in the proximity of the

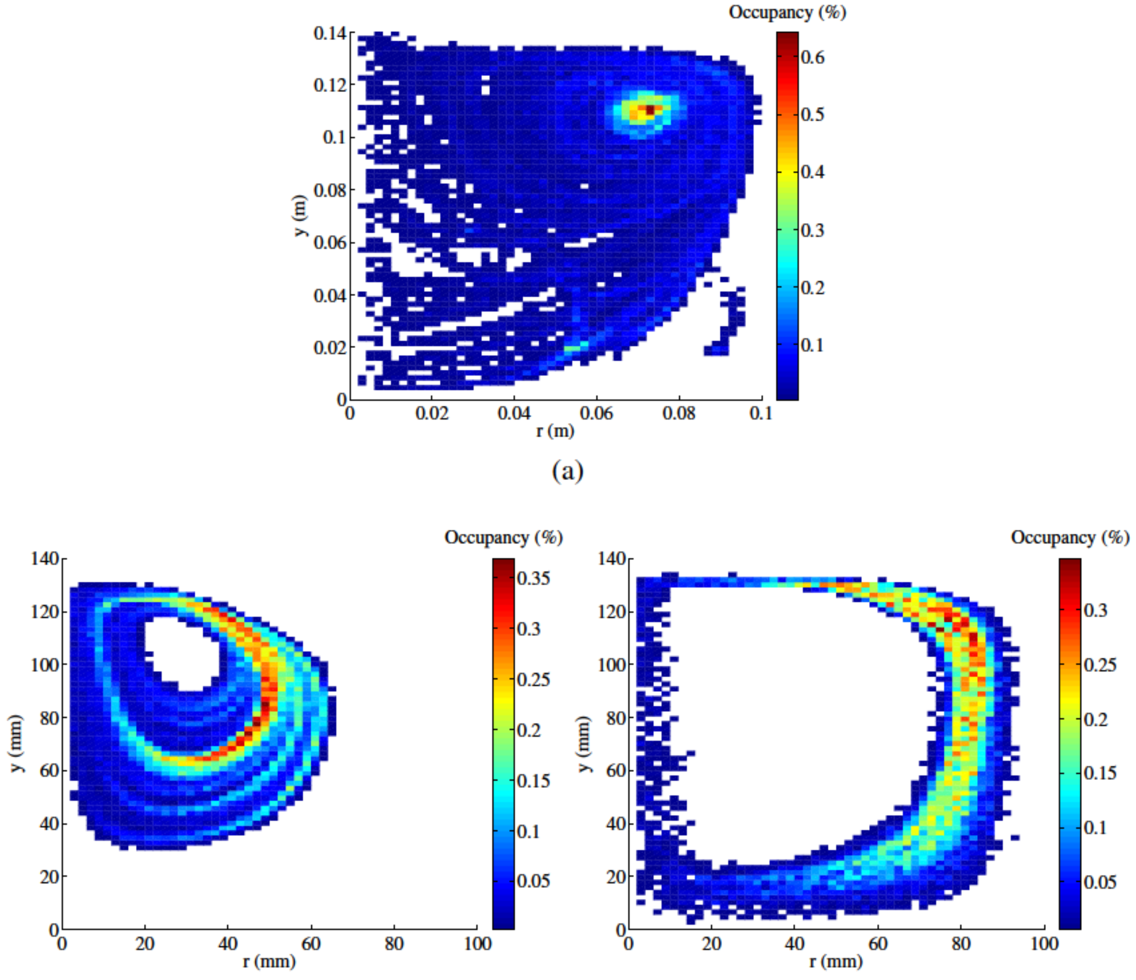

(a)

(b) (c)

Figure 6.6 *Average occupancy. (a) 2 g ℓ^{-1}. (b) 4 g ℓ^{-1}, first run. (c) 4 g ℓ^{-1}, second run.*

central bubble column, the horizontal displacement once the flow reaches the surface, the toroidal vortex and the velocity decrease in the lower part of the tank are all clearly visible. For both the solutions, the vortex can be identified as a relatively quiet zone surrounded by a circular crown in which the velocity is higher. Unfortunately, in the 4 g ℓ^{-1} solution, the particle was trapped in circular trajectories larger than the vortex, and the latter could not be tracked directly. However, the structure of the flow patterns in the surrounding area is similar to the surrounding of the vortex in the 2 g ℓ^{-1} solution.

When the concentration increases, the central column appears to be less affected when compared to the PIV measurements (Figure 6.3). Conversely, the average velocity diminishes and the size of the low-velocity areas increases, especially in the external zones, as in the PIV measurements. In both of the tested solutions, the vortex is formed by the sinking of the rapidly-flowing surface liquid phase. In the 2 g ℓ^{-1} solution, the liquid phase sinks almost adjacent to the tank wall, while in the 4 g ℓ^{-1} it sinks at approximately 1/3 of the radius, as already seen from the PIV measurements. As a consequence, in the 4 g ℓ^{-1} solution, the vortex is placed much more centrally, again in agreement with the PIV measurements. This causes an attenuation of the velocity in the most external zones.

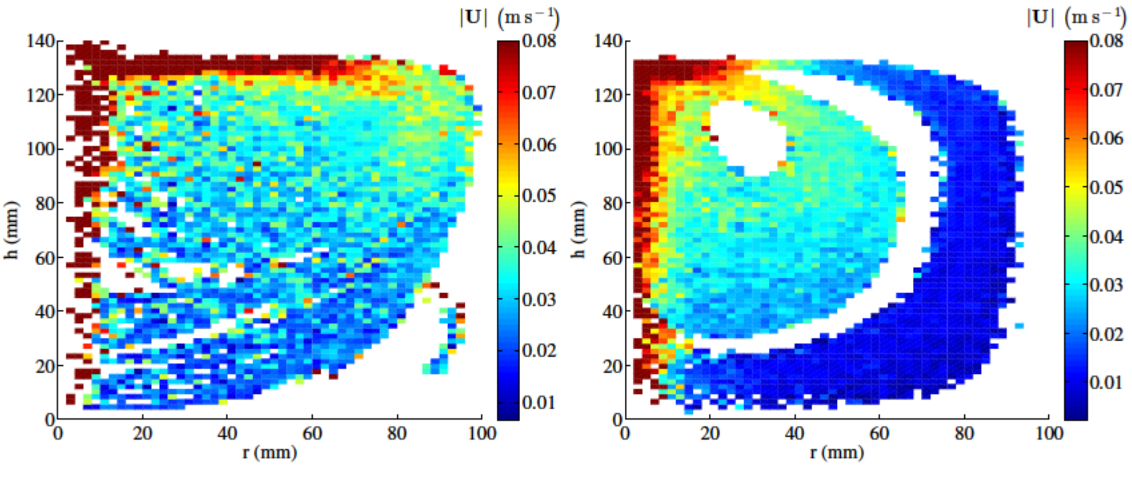

(a)

(b)

Figure 6.7 *PEPT-averaged velocity field, measured with the PEPT technique. (a) 2 g ℓ^{-1} run. (b) 4 g ℓ^{-1} runs.*

7

CFD Modelling

> *"I remember my friend Johnny von Neumann used to say, with four parameters I can fit an elephant, and with five I can make him wiggle his trunk."*
>
> Enrico Fermi (1953).
> Conversation with Freeman Dyson

WITHIN THIS CHAPTER, a CFD-based numerical model to simulate gas mixing in anaerobic digestion was developed and described. The model was first applied to a laboratory-scale case for validation purposes. Once validated, the model was then applied to a full-scale case to reproduce the flow patterns of a real digester. For the validation to be meaningful, it is crucial that all the characteristics of the laboratory-scale case—type of model, source code, boundary and initial conditions, turbulence model, discretization schemes—are correctly reproduced in the full-scale simulations.

In a multiphase flow, the choice of the model is far from straightforward. In section 7.1, the rationale for choosing a particular model is discussed. Then, the theoretical features of the chosen model, together with the closure relations, are reported in Section 7.2. The characteristics of the mesh, both for the laboratory and the full-scale cases, are described in Section 7.3. The choices for the simulation parameters and the turbulence model are illustrated in Section 7.4 and 7.5 respectively. Finally, the simulation strategy for both cases is described in Section 7.6. Details on the implementation of the code for the CFD simulations are reported in Appendix D.

The computational work was undertaken using the BlueBEAR high performance computing facility at the University of Birmingham. Each simulation was run in parallel on three dual-processor 8-core 64-bit 2.2 GHz Intel Sandy Bridge E5-2660 worker nodes with 32 GB of memory, for a total of 48 nodes.

7.1 Choice of the Multiphase Model

As described in Section 3.5, several multiphase models exist, and each has its specific range of applications. Consequently, in order to choose a model properly, it is important to address the nature of the multiphase flow taken into consideration as well as the results that are expected to be produced.

In gas-mixed anaerobic digestion, a liquid sludge coexists with a bubble-dispersed gas phase. The significant of the modelling challenge here was to reproduce the flow patterns of the liquid phase, as it is flow patterns that give the indication of the degree of mixing inside a digester. Consequently, the simulation of the bubbles' motion was only functional to obtaining a correct reproduction of the flow patterns, and was not interesting in itself.

In the laboratory-scale case, the bubble diameter was measured experimentally (Section 6.2), was found to be between 7 and 14 mm. The bubbles were reported to be arranged in vertical lines (Figure 6.2). As regards the full-scale, no data in the literature about the dimension of the bubbles inside a digester are available, and therefore the bubble size must be estimated. It is reasonable to estimate the typical full-scale bubble size as between 10 and 100 mm diameter. It is also reasonable to suppose that the bubbles are arranged in narrow vertical plumes, as in the laboratory-scale case.

As a consequence of what is explained above, the bubbles are small (one order of magnitude smaller than the laboratory-scale linear dimension; two orders smaller than the full-scale), and the bubble plume occupies a volume that is small compared with the entire computational domain. According with the 20 cells/diameter requirement described in Section 3.5.2, the application of the volume-of-fluid method would result in high computational expense (at least 10^9 cells would be required for full-scale simulations). As explained above, the local dynamics of single bubbles is not of interest for the purpose of studying the liquid-phase flow patterns, and therefore the benefits of the computationally-expensive volume-of-fluid approach are questionable.

According to Andersson et al. (2012) and what explained in Section 3.5, the Euler-Lagrange method is preferable when the number of particles is not so high as to render the computational cost prohibitive and the particle size remains negligible, while the Euler-Euler model is suggested to be used only when other models are not available. The two requirements of low bubbles number and negligible bubble size are easily met in the full-scale simulations, but in the laboratory-scale, only the former is verified. However, Sungkorn et al. (2011, 2012) demonstrated that, within the lattice-Boltzmann framework, the requirement of negligible particle size can be relaxed if the number of bubbles remains "small". In their research, the number of bubbles present in the system was of the order of $\mathcal{O}(10^4)$ and therefore, the term "small" can be interpreted as "smaller than 10^4". This relaxed requirement would be met in the laboratory-scale simulations.

In the light of the above, the Euler-Lagrange method appeared more suitable for modelling gas mixing in anaerobic digestion. In addition, adopting the Euler-Lagrange method appears even more interesting because: (*i*) as explained in Section 3.5, there is a lack of literature on Euler-Lagrange modelling applied to gas mixing in anaerobic digestion; (*ii*) applying the Euler-Lagrange model to the laboratory-scale case provides an opportunity to test the Sungkorn et al. (2011, 2012)'s hypothesis (that has been proved to be valid for the lattice-Boltzmann framework) also in the finite-volume framework. For the purpose of validation, it is interesting to (laboratory-scale) validate a model under more adverse circumstances (that is, non-zero bubble size) than the (full-scale) effective application (where the zero bubble size approximation is verified with higher accuracy).

As explained above, the focus of the work reported here was on resolving the flow patterns away from the bubble plume rather than describing the bubble motion in detail. For this reason, it was possible to adopt the following approximations: (*i*) bubble-bubble interactions were neglected, and a two-way coupling was adopted; (*ii*) effects on fluid motion due to deformations of the bubble surface were neglected, and bubbles were considered as spherical; (*iii*) bubbles were considered to be pointwise. These approximations did not allow a detailed description of the flow in close proximity to the bubbles, but did reproduce an interphase momentum transfer sufficiently accurate to reproduce the flow patterns away from the bubble column satisfactorily.

7.2 Theoretical Model

The two-way coupling Euler-Lagrange model is described by the Navier-Stokes equations with the momentum exchange term, Equation 3.53, 3.54 and 3.55. According with the discussion in Section 5.1, the shear stress tensor τ was modelled using the power law (Equation 3.9).

The resultant of the forces acting on the p-th particle $\mathbf{F}_p$ can be described as:

$$\mathbf{F}(\mathbf{x}) = \sum_p \mathbf{F}_p \, \delta(\mathbf{x} - \mathbf{x}_p) \ , \tag{7.1}$$

where $\mathbf{F}_p$ is the resultant of the forces acting on the p-th bubble. The Dirac delta, after discretization, states that the contribution of the p-th bubble to Equation 3.54 is $\mathbf{F}_p$ in the cell in which the bubble is present, and zero elsewhere. The equation of motion for each bubble is Newton's second law:

$$m_p \dot{\mathbf{u}}_p = \mathbf{F}_p \ , \tag{7.2}$$

where $\mathbf{u}_p \equiv \dot{\mathbf{x}}_p$ is the instantaneous velocity of the bubble. The resultant for the p-th bubble can be expressed as in Deen et al. (2004)

$$\mathbf{F}_p = \mathbf{F}_p^{\mathrm{a}} + \mathbf{F}_p^{\mathrm{b}} + \mathbf{F}_p^{\mathrm{d}} + \mathbf{F}_p^{\ell} \ , \tag{7.3}$$

that is: added mass, pressure gradient, buoyancy, drag, lift. We have:

$$\mathbf{F}_p^{\mathrm{a}} = C_{\mathrm{a}}\, \rho V_p \left(D_t \mathbf{u} - \mathrm{d}_t \mathbf{u}_p \right) \ , \tag{7.4}$$

$$\mathbf{F}_p^{\mathrm{b}} = V_p \left(\rho_p - \rho \right) \mathbf{g} \ , \tag{7.5}$$

$$\mathbf{F}_p^{\mathrm{d}} = \frac{1}{2} C_{\mathrm{d}}\, \rho\, \pi \frac{{d_p}^2}{4} \left| \mathbf{u} - \mathbf{u}_p \right| \left(\mathbf{u} - \mathbf{u}_p \right) \ , \tag{7.6}$$

$$\mathbf{F}_p^{\ell} = C_{\ell}\, \rho V_p \left(\mathbf{u} - \mathbf{u}_p \right) \wedge \nabla \wedge \mathbf{u} \ . \tag{7.7}$$

Here D_t indicates the total temporal derivative and reads $D_t \equiv \partial_t + \mathbf{u} \cdot \nabla$. The coefficients C_{a} and C_{ℓ} can be expressed as in the model proposed by Dewsbury et al. (1999), that is specific for gas bubbles and light solid particles rising in pseudoplastic liquids, and Tomiyama et al. (2002):

$$C_{\mathrm{a}} = \frac{1}{2} \ , \tag{7.8}$$

$$C_\ell = \begin{cases} \min\left[0.288\tanh\left(0.121\mathrm{Re}_p\right)\,,\; f(\mathrm{Eo}_d)\right]\,, & \mathrm{Re}_p \leq 4\,, \\ f(\mathrm{Eo}_d)\,, & 4 < \mathrm{Re}_p \leq 10\,, \\ -0.29\,, & \mathrm{Re}_p > 10\,, \end{cases} \tag{7.9}$$

where:

$$\begin{aligned} f(\mathrm{Eo}_d) =& 0.00105{\mathrm{Eo}_d}^3 - 0.0159{\mathrm{Eo}_d}^2 \\ & - 0.0204\mathrm{Eo}_d + 0.474\,. \end{aligned} \tag{7.10}$$

Eo_d is the modified Eötvös number and is defined as $(\rho_p - \rho)\, {d_{d,p}}^2/\sigma$, where $d_{d,p}$ is the maximum horizontal dimension of the p-th bubble. Since here the bubbles are considered to be spherical, $d_{d,p}$ is the bubble diameter. C_d is a function of the bubble Reynolds number (Dewsbury et al., 1999):

$$C_\mathrm{d} = \begin{cases} \dfrac{16}{\mathrm{Re}_p}\left(1 + 0.173{\mathrm{Re}_p}^{0.657}\right) + \dfrac{0.413}{1 + 16,300{\mathrm{Re}_p}^{-1.09}}\,, & \mathrm{Re}_p \leq 195\,, \\ 0.95\,, & \mathrm{Re}_p > 195\,. \end{cases} \tag{7.11}$$

The bubble Reynolds number Re_p is defined as:

$$\mathrm{Re}_p = \frac{\rho\, d\, U_t}{\mu}\,, \tag{7.12}$$

where U_t is the velocity scale and is evaluated as the modulus of the difference between the bubble velocity and the fluid velocity in the bubble surroundings. During the simulation runs, the value of Re_p is evaluated from Equation 7.12 and the value of μ calculated according with the rheology model chosen, for every point $\mathbf{r}$ and time t. The field $\mathrm{Re}_p(\mathbf{r},\, t)$ thus obtained is used as an input to compute the velocity field.

7.3 Meshing

7.3.1 Laboratory-scale Meshing

The purpose of the laboratory-scale modelling was to reproduce the flow patterns of the experimental rig described in Section 5.2.1.

Six grids were generated for this study all with different cell numbers, but with the same structure. Details of the grids are summarised in Table 7.1, and an example is shown in Figure 7.2. The presence of a central column of bigger cells in Figure 7.2 is explained as follows. In order to successfully reproduce the liquid phase flow patterns, it was necessary to generate a grid in which the cells were much smaller than a single bubble. As verified by Sungkorn et al. (2011, 2012) and reported in Section 7.1, the zero bubble size requirement for Euler-Lagrange models can be relaxed, but nevertheless, it was observed that the flow patterns depend strongly on the grid size when cells are much smaller than the bubbles. And in fact, the works of Sungkorn et al. (2011, 2012) referred to bubbles not larger than the order of magnitude of a single cell. For this reason, larger cells, of the order of magnitude of the bubbles' volumes or slightly larger, were placed along the bubbles'

Table 7.1 *Details of the laboratory-scale grids.*

Grid Id.	Cells no.	Central cells size	Central cells no.	Cells over circle
1	2,348,787	9.19 mm	10	72
2	1,361,367	9.19 mm	10	60
3	230,410	9.19 mm	10	48
4a	121,240	7.66 mm	12	36
4	97,210	9.19 mm	10	36
4b	77,992	11.0 mm	8	36

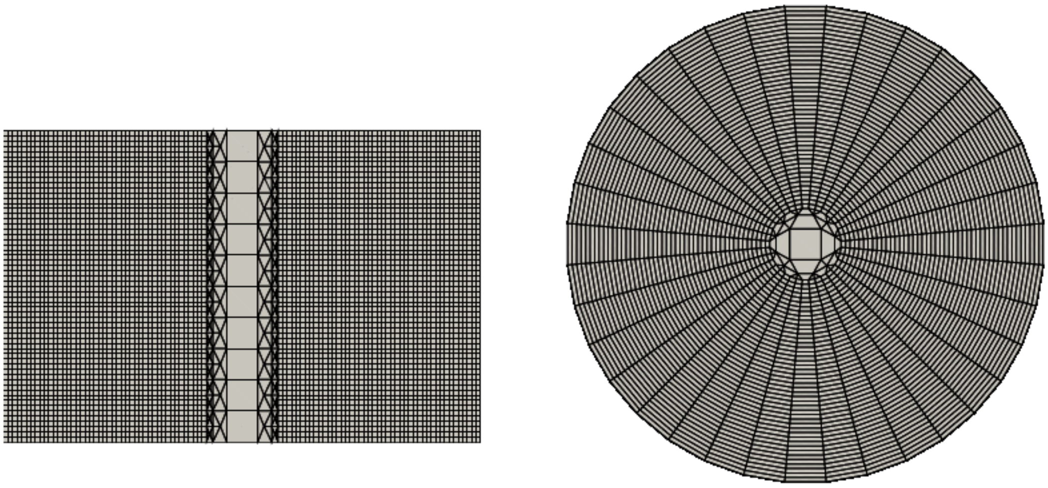

(a) (b)

Figure 7.1 *Example of laboratory-scale grid.*

expected trajectory.

7.3.2 Full-scale Meshing

The purpose of the full-scale modelling was to reproduce the flow patterns of a real digester.

The reference for modelling the full-scale mesh was taken from the projects of a typical digester realized by Severn Trent Water Inc., similar to the ones built for the Spernal Wastewater plant, UK, described in in Section 5.2. The details of the digester have been already reported in Table 5.2.

The CFD domain consisted of a wedge comprising an angle of $\pi/6$ radians. A single nozzle lay on the symmetry plane of the wedge. Four grids with cells number of 394,400 (grid1), 98,420 (grid2), 47,422 (grid3) and 18,760 (grid4) respectively were generated. An example is shown in Figure 7.2.

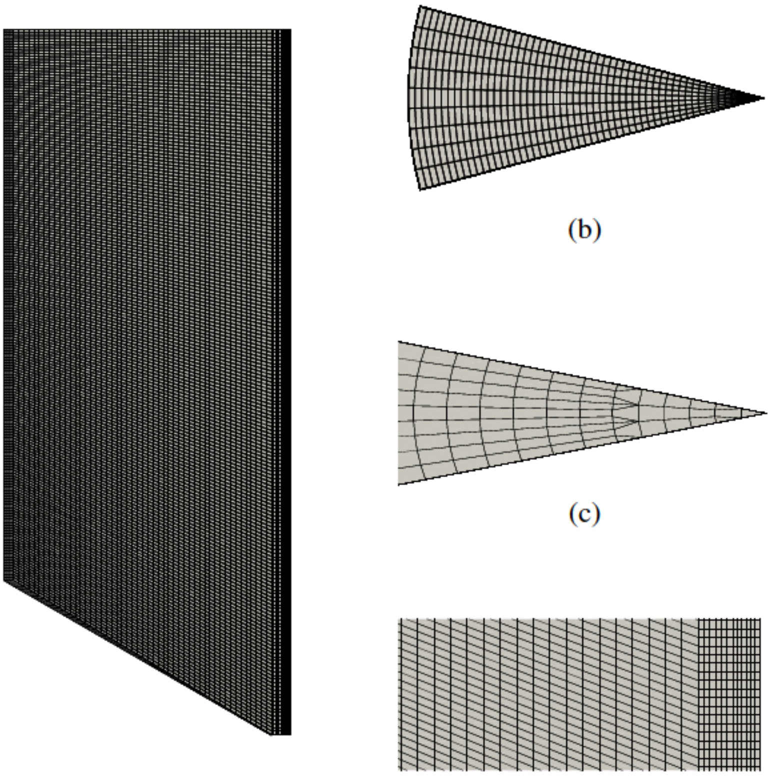

(b)

(c)

(a) (d)

Figure 7.2 *Grid example. (a): Side view. (b): Top view. (c): Wedge apex. (d): Side detail.*

7.4 Simulations Parameters

The injection of a bubble into the system is simulated as follows. During a simulation, a bubble is “created” at certain times, in a place near the nozzle’s coordinates, such that its centre lies along the vertical line passing through the nozzle’s coordinates, at about 5 to 11 mm above it and completely inside the computational domain, with its velocity set to zero. The reality is somewhat different in both laboratory and full scales. In the former, a bubble takes non-zero time to expand out of the nozzle and then detaches with a non-zero velocity. In the latter, gas expands out of the nozzle and then collides against the leaf spring diffuser. In both cases, the gas expansion pushes upwards the water column above it. This may give rise to a liquid recall from the external zones near the bottom towards the centre in the lower part of the tank, and to an increase of the velocity of the liquid phase around the

Table 7.2 *Initial conditions (preliminary runs only) and boundary conditions (both preliminary and main runs).*

Place	Quantity	Condition
Top	p	Constant zero
	$\mathbf{u}$	Slip
	ε	Slip
	R_{ij}	Slip
Wall / bottom	p	Adjusted such that the velocity flux is zero
	$\mathbf{u}$	Constant zero
	ε	Zero gradient
	R_{ij}	Zero gradient

column above it. Both these possible effects are neglected in the model.

The timestep was defined indirectly and dynamically by an algorithm aimed at keeping the maximum Courant number just below a specified limit of 0.2. The Courant number is a quantity defined for every cell such that given a cell labelled i, let $|\mathbf{u}_i|$ be the velocity magnitude, L_i the length dimension along $\mathbf{u}_i$ and Δt the timestep, then the Courant number for the cell i is:

$$\mathrm{Co}_i = \frac{|\mathbf{u}_i|\ \Delta t}{L_i}\ . \tag{7.13}$$

The maximum Courant number, Co, is the maximum value of Co_i over i. Starting from a small initial timestep (in this work, 10^{-5} s) the timestep was assessed in order to keep the maximum Courant number as near as possible to, but smaller than, the limit value of 0.2.

Initially, a series of (transient) first-order runs was performed to simulate the development of the bubble column from a state in which no liquid phase motion and no bubbles were present in the system. As the object of study in this work is the liquid phase motion in presence of a fully-developed bubble column, the sole use of these first series of runs was to provide the initial conditions for the main (transient) second-order runs. The latter provided the data relative to the behaviour of the system in the presence of the fully-developed bubble column, and were compared with the experimental data.

The initial and boundary conditions are shown in Table 7.2. The initial conditions for the preliminary runs were: 4.95 $10^{-4}\,\mathrm{m}^2\,\mathrm{s}^{-3}$ for the ε field; zero for the other fields (p, u, R). The wall function was found to be within the viscous sublayer at the centre of the cells adjacent to the walls, and then no wall function was necessary. The differencing schemes were: linear for interpolations, limited central differencing for the Gradient operator, linear for the Laplacian, Van Leer for all the other spatial operators. For the preliminary runs, the first-order Eulerian scheme for the time derivative was used; however, for the main runs, the second-order backward scheme was used.

The output of the simulations consisted of a series of binary files arranged into directories, one for each timestep recorded. Binary files were collected for times corresponding to integer seconds after the initial conditions. The preliminary runs were performed for a simulation time of 10 s for the laboratory-scale runs and 60 seconds for the full-scale; then, their final timesteps were used as initial conditions for the main simulations, which were run for an additional simulation time of 50 s for the laboratory-scale runs and 240 s for the full-scale, for a total time of 60 s for the laboratory-scale and 300 s for the full-scale.

7.5 Turbulence Model

It is well known that vortices arise behind a sphere moving through a liquid already at $\mathrm{Re}_p > 4$ (Kundu and Cohen, 2008). According with the high speed camera results (Section 6.2, Table 6.2), Re_p was found to vary between 1.1 (cmc08-1) and 185 (cmc02-3), and it is reasonable to suppose that even higher values occur in full-scale plants. Therefore, it is most likely that such vortices play an important part in the turbulence energy cascade. As they cannot be resolved because the bubbles (and thus such vortices themselves) are approximated as pointwise, their effect is included in the turbulence model. As the bubbles are expected to form a vertical plume, it is reasonable to suppose that the contribution of the vortices behind the bubbles to the turbulent Reynolds stress tensor R is not isotropic. Consequently, it is natural to take the Reynolds stress models into account to model turbulence.

As explained in Appendix C, the Launder-Reece-Rodi model takes into account both slow and rapid pressure strain terms of the Reynolds tensor, and it is the first that has been widely used (Pope, 2000). The Launder-Gibson model (Gibson and Launder, 1978), in addition to the former, takes into account the redistribution of normal stresses near the walls (ANSYS, 2012). It was considered that the wall effects may be of interest in the present study, and therefore the Launder-Gibson model was used. The modification suggested in ANSYS (2012) were adopted: the isotropic diffusivity proposed by Daly and Harlow (1970) (Equation C.18) was used in place of the anisotropic transport term (Equation C.17); and the isotropic dissipation rate of the standard k-ε model (equations B.7, B.1 and B.8) was used in place of the anisotropic (Equation C.10).

A series of laboratory-scale preliminary simulations was run in order to compare the performance of the Launder-Gibson model (modified as described above), the SST k-ω model that is generally recommended in the literature (Section 3.7), and laminar simulations. For the Launder-Gibson model, the runtime remained below 30 hours per run, and the timestep was observed to be between 0.0004 to 0.02 s. For the SST k-ω and the laminar simulations, at least double the runtime was necessary, and the timestep was approximately one order of magnitude smaller, thus indicating a much poorer convergence when compared with the Launder-Gibson runs. This is likely to be due to the difficulty in the SST k-ω model, and the impossibility in the laminar simulations, to reproduce the anisotropic vortices behind the bubbles. For this reason, the modified Launder-Gibson model was adopted for all the simulations.

7.6 Simulation Strategy

The model requires the following data as input parameters: liquid phase rheology (that is, K and n of Equation 3.9), gas flow rate and bubble diameter.

For the laboratory-scale case, simulations were performed for each of the CMC solutions as in Table 6.1 and each of the air flow rates of Table 6.2. The binary files were processed to extract data to be compared with the PIV data. The Eulerian velocity field was interpolated onto the PIV plane described in Section 5.3. Then, the components parallel to the plane were averaged over time. As only the flow pattern originating from a fully-developed bubble column is of interest, the preliminary times were not included into the average. Also the first ten seconds of the main runs were disregarded in order to avoid the artificial transience from first-order to second-order solutions. Thus, only the last (second-ordered) 40 seconds of each run were included in the average.

As regards the full-scale case, the rheology was taken from Table 5.1, and in particular, the parameters corresponding to 2.5, 5.4 and 7.5% TS were employed. Different values of gas flow rate corresponding to fractions of $Q_{\max}$ were used, namely $q \equiv Q/Q_{\max}$ = 0.1, 0.2, 0.3, 0.5, 0.7 and 1.0. The choice of the bubble diameter needs particular attention as there are no data in the literature about the dimension of the bubbles inside a digester, and therefore bubble size must be estimated. The approach followed in this work was to run a series of simulations, each of these with a fixed bubble size. Simulations were run for value of d of 2, 6 and 10 cm.

8

Laboratory-Scale Validation

"Stop swearing at the computer!"

My colleagues (2015).

IN THIS AND IN THE next chapter, the results of the CFD simulations described in Chapter 7 are presented and compared with the outcome of the experimental measurements (Chapter 6). In particular, in this chapter a comparison is traced between the outcome of the laboratory experiments and the laboratory-scale simulations. The scope of this comparison is to provide a validation for the computational model, so that it can be confidently applied to full-scale design.

First, a grid independency test is performed (Section 8.1). Then, a comparison is carried out between computational and experimental data, both from PIV and PEPT. The velocity field (Sections 8.3 and 8.4) and the average shear rate (Section 8.5) are assessed.

8.1 Impact of Central Cells Size

A preliminary series of runs was performed to verify that the flow patterns were stable under variations of the central cells size. The configuration labelled as cmc04-2 in Table 6.2 was tested with the Grids 4a, 4 and 4b described in Table 7.1 and the outcome is shown in Figure 8.1. The graphs show the magnitude of the velocity along three vertical lines lying on the PIV plane, respectively at 0.4, 0.6 and 0.8 half-widths from the central axis projection. There is a general good agreement between the three grids: small differences

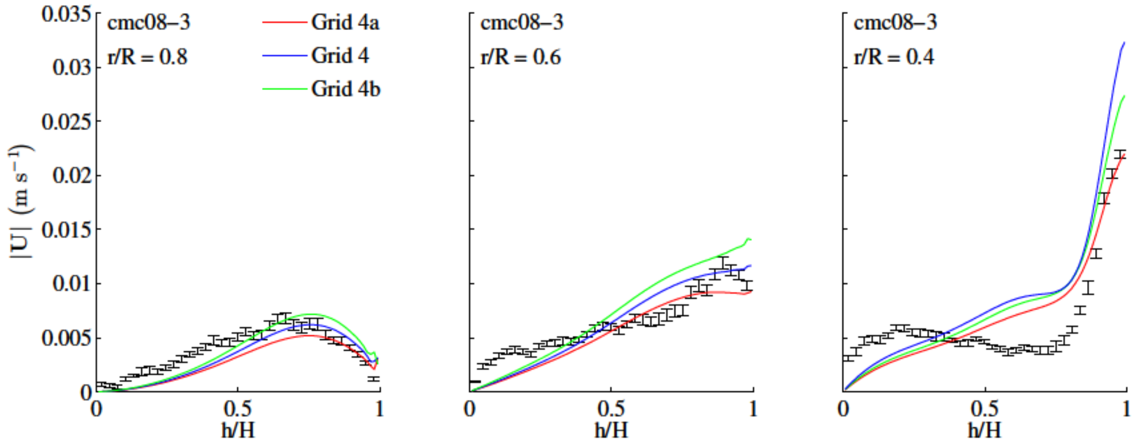

Figure 8.1 *Preliminary series along a vertical axis against PIV outcome. Red: Grid 4a. Blue: Grid 4. Green: Grid 4b.*

are either inside experimental errors (r/R=0.8 and r/R=0.6), or are confined to limited domain zones, such as near the surface, around the central axis (r/R-0.4 and, less, r/R=0.6).

8.2 Assessment of the Mesh Dependence

A GCI analysis was carried out as described in Section 3.4.3. The PIV-averaged shear rate (see Section 5.6.1) over the whole computational domain was chosen as the critical variable. Two tests were performed for each run series, one involving grids 1,2 and 3, and another one involving grids 2, 3 and 4. The results are shown in Tables 8.1, 8.2 and 8.3. The asymptotic convergence is generally reached for grid 2, but lost in grid 1. Oscillations are reported in the run series cmc02-2 and cmc04-2, with grid 1 behaving slightly better than grid 2 for the former series, and the converse for the latter. For the runs cmc04-1 and cmc04-3 the situation is less clear.

This behaviour is to be expected because, as explained in Section 7.3.1, there is a lower limit for the mesh size, dependant on the bubble size. Therefore, the GCI underlying hypothesis Equation 3.48 can not hold. Consequently, it is expected that the critical variable converges to, or oscillates around, a limit value for decreasing values of h, but still larger

Table 8.1 *GCI analysis. 2 g* l^{-1}.

	cmc02-1	cmc02-2	cmc02-3
$\langle\dot{\gamma}\rangle_4$ (s^{-1})	0.9662	1.7051	1.9331
$\langle\dot{\gamma}\rangle_3$ (s^{-1})	0.8757	1.6717	1.4556
$\langle\dot{\gamma}\rangle_2$ (s^{-1})	0.8357	1.0916	1.2244
$\langle\dot{\gamma}\rangle_1$ (s^{-1})	0.6446	1.2838	1.5850
p_2	3.855	2.755	3.605
p_1	—	2.337	—
$\mathrm{GCI2}_{43}$	$6.360\ 10^{-2}$	$2.065\ 10^{-2}$	$2.252\ 10^{-1}$
$\mathrm{GCI2}_{32}$	$6.799\ 10^{-3}$	$1.616\ 10^{-1}$	$3.167\ 10^{-2}$
$\mathrm{GCI1}_{32}$	—	$2.222\ 10^{-1}$	—
$\mathrm{GCI1}_{21}$	—	$3.536\ 10^{-1}$	—
Asymp.2	0.954	0.025	0.841
Asymp.1	—	0.411	—

than the lower limit. Below this limit, the simulation is expected to produce unphysical results, and therefore the asymptotic convergence is lost.

The GCI test was introduced to give an indication whether the mesh is fine enough to achieve the asymptotic convergence range. However, in this context, it gives additional information about whether the mesh is too fine compared with the bubble size. It can be concluded that the asymptotic range of convergence is reached for grid2. In general, grid

Table 8.2 *GCI analysis. 4 g* l^{-1}.

	cmc04-1	cmc04-2	cmc04-3
$\langle\dot{\gamma}\rangle_4$ (s^{-1})	0.2125	0.5358	0.8568
$\langle\dot{\gamma}\rangle_3$ (s^{-1})	0.2144	0.6393	0.8829
$\langle\dot{\gamma}\rangle_2$ (s^{-1})	0.2249	0.4586	0.9994
$\langle\dot{\gamma}\rangle_1$ (s^{-1})	0.2076	0.5866	1.3548
p_2	1.314	0.725	1.028
p_1	—	2.809	—
$\mathrm{GCI2}_{43}$	$2.397\ 10^{-2}$	$8.729\ 10^{-1}$	$1.071\ 10^{-1}$
$\mathrm{GCI2}_{32}$	$4.974\ 10^{-2}$	$9.185\ 10^{-1}$	$1.739\ 10^{-1}$
$\mathrm{GCI1}_{32}$	—	$1.152\ 10^{-1}$	—
$\mathrm{GCI1}_{21}$	—	$4.091\ 10^{-1}$	—
Asymp.2	0.221	0.619	0.335
Asymp.1	—	0.169	—

Table 8.3 *GCI analysis. 8 g* l^{-1}.

	cmc08-1	cmc08-2	cmc08-3
$\langle\dot{\gamma}\rangle_4$ (s^{-1})	0.0273	0.0549	0.0841
$\langle\dot{\gamma}\rangle_3$ (s^{-1})	0.0282	0.0570	0.0848
$\langle\dot{\gamma}\rangle_2$ (s^{-1})	0.0283	0.0573	0.0851
$\langle\dot{\gamma}\rangle_1$ (s^{-1})	0.0285	0.0582	0.0864
p_2	8.134	7.458	3.258
p_1	—	—	—
$\mathrm{GCI2}_{43}$	$4.272\ 10^{-3}$	$6.124\ 10^{-3}$	$6.089\ 10^{-3}$
$\mathrm{GCI2}_{32}$	$3.447\ 10^{-5}$	$7.365\ 10^{-5}$	$8.811\ 10^{-4}$
$\mathrm{GCI1}_{32}$	—	—	—
$\mathrm{GCI1}_{21}$	—	—	—
Asymp.2	1.003	1.005	1.004
Asymp.1	—	—	—

1 is too fine, and that the grid 2 is optimal for all the runs except for the series cmc02-2, where the grid 1 is superior. For these reasons, all the simulations were performed on grid 2.

8.3 Qualitative Analysis of the Velocity Field

Figure 8.2 depicts the PIV-averaged simulated velocity field projected onto the PIV plane for the cmc02-2, cmc04-2 and cmc08-2 runs. Grid 2 was used in all the cases, calculated as explained in Secion 5.5.1. A comparison can be traced between Figure 8.2 and its experimental analogue, Figure 6.3. The simulations reproduce well the measured flow both in magnitude and in flow shape. Also the position of the centre of the vortices correlates well with the PIV outcome. The principal differences between simulation and PIV consist of: (*i*) under-estimated velocity magnitude around the bubble column, especially at the bottom; (*ii*) slightly over-estimated velocity in the upper part of the tank; and (*iii*) slightly under-estimated velocity in the lower part of the tank.

The point (*i*) is the most significant difference. In this regard, however, it should be noted that the bubble column was interposed between the PIV plane and the camera.

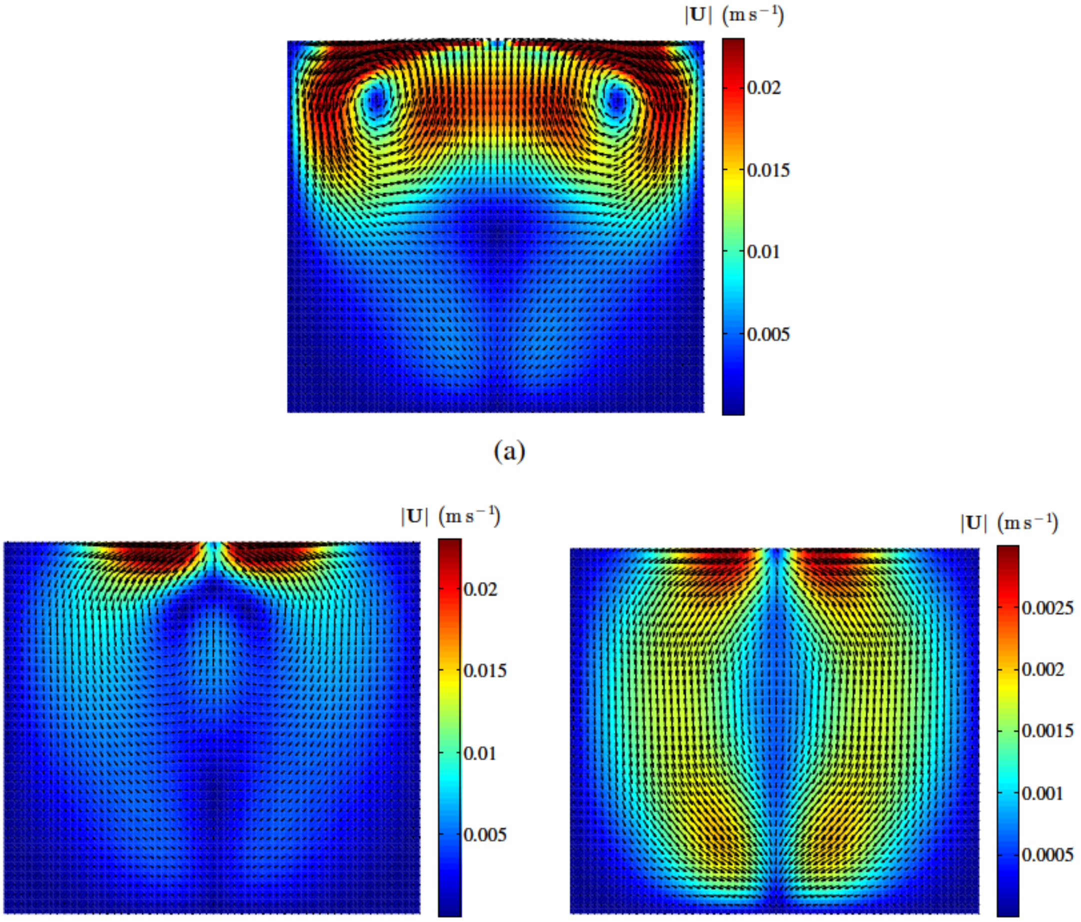

(a)

(b) (c)

Figure 8.2 *PIV-averaged simulated velocity field through the PIV plane. (a) cmc02-2 run. (b) cmc04-2 run. (c) cmc08-2 run.*

Therefore, there is a refraction effect of the laser rays through the bubbles and thus the PIV data may be less robust in the inner parts of the domain. As an example of this, by a simple application of the Snell's law with standard values for the refraction coefficients of air (1.000) and water (1.333), it can be noted that a laser beam scattering into a bubble with an impact parameter of half the bubble radius is deflected of an angle of 20.5°. Nevertheless, explanations concerning the nature and the approximations of the theoretical model can be elaborated. In particular:

(*i*) For under-estimation of velocity magnitude there are three possible causes. First, the cells along the central column are much larger than any other cell, and there are only

10 to 12 along the whole tank height (see Table 7.1). Thus, there may be too few cells to expect an accurate description of the flow near the central axis. The second source of error may be related to the way the parcels are introduced into the system. The implications of this simplification, in particular regarding the possible increase of liquid phase velocity in the central column, have been discussed in Section 7.4. A final cause for this difference may be the fact that, due to the model assumption (Section 7.1), the model may simply be unable to reproduce the flow in the immediate surroundings of a bubble.

(ii) The cause of over-estimation of velocity in the upper part of the tanks may lie in the description of the liquid-atmosphere interface. In reality, as shown in Figure 8.3, the bubbles approaching the surface give rise to a water hump just above it, with vertical oscillations along the whole interface that are larger when the viscosity decreases. The fraction of the bubbles' kinetic energy that is transferred to the liquid phase is then redistributed as kinetic energy and potential energy of the mass displaced into the hump, and also to the air above due to the interface oscillations. In the simulations, however, the

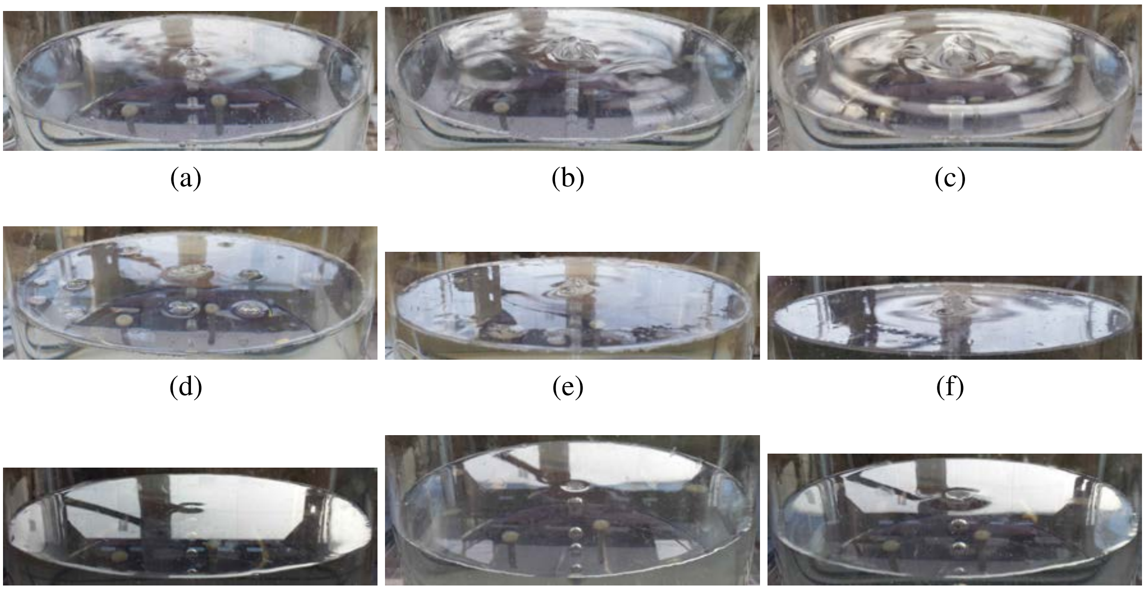
(a) (b) (c)
(d) (e) (f)
(g) (h) (i)

Figure 8.3 *Liquid-air interface.* (a)*: cmc02-1.* (b)*: cmc02-2.* (c)*: cmc02-3.* (d)*: cmc04-1.* (e)*: cmc04-2.* (f)*: cmc04-3.* (g)*: cmc08-1.* (h)*: cmc08-2.* (i)*: cmc08-3.*

interface is modelled as a rigid free-slip surface, and no liquid displacement is possible, nor is any energy transfer to the air. The transferred energy is therefore not redistributed, and remains in the form of liquid kinetic energy. Thus, the simulations are expected to over-estimate the velocity field magnitude especially in the regions where the energy redistribution should (but does not) take place, i.e. near the interface or just below it.

(*iii*) As before, the velocity under-estimation in the lower part of the tank may once again be due to the way the bubbles are introduced into the system. The implications of this simplification, in particular with regard to the possible liquid recall from the external zones, have been discussed in Section 7.4.

Figure 8.4 depicts the PEPT-averaged velocity field calculated according with Section 5.5.3. There is a general qualitative agreement between PEPT and CFD runs. In particular, the position of the vortex is clearly defined in the 2 g ℓ^{-1} runs, and there is good agreement even in the 4 g $1^{-\ell}$ ones. The strong velocity field due to the central bubble plume is well resolved and corresponds to what observed in the experiment (Figure 6.7). This is different to the PIV case (Figure 6.3 for the experiment, and 8.2 for the simulations), where the difficulties mentioned above due to refraction through the bubbles prevented

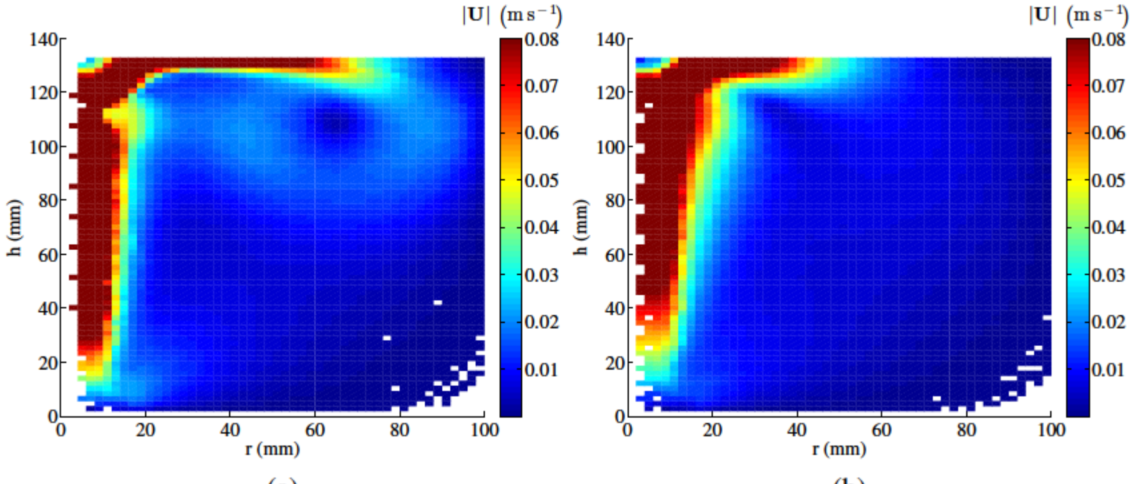

(a) (b)

Figure 8.4 *PEPT-averaged simulated velocity field. (a) 2 g ℓ^{-1} run. (b) 4 g ℓ^{-1} runs.*

from having reliable measurements in the central zone. This is an example of how a visualization technique unaffected by the optical properties of the continuous phase (such the PEPT is) can yield improvements in flow patterns visualization. Also, the horizontal displacement at the surface is well reproduced.

Of course, there are some differences between the PEPT outcome and the simulations. For instance, the CFD runs slightly underestimate the magnitude of the velocity field at the bottom of the plume, and overestimate the span of the horizontal displacement at the surface. The simulated velocity magnitude field differs from the experimental inthe zone around the lower part of the domain. Such differences have already been reported above, in the comparison with the PIV experiments. Such differences can be synthetically explained in the following ways.

8.4 Quantitative Analysis of the Velocity Field

In Figures 8.5, 8.6 and 8.7, the velocity magnitude along a vertical axis was plotted for the 2 $\mathrm{g}\,\ell^{-1}$, the 4 $\mathrm{g}\,\ell^{-1}$ and the 8 $\mathrm{g}\,\ell^{-1}$ respectively. The graphs show the magnitude of the projected velocity along three vertical lines lying on the PIV plane, respectively at 0.4, 0.6 and 0.8 half-widths from the central axis projection. There is a good general agreement between the different grids. In particular, the differences are smaller when the CMC concentration increases. The runs with larger mesh size (especially grid 4) sporadically differ in the lower concentrations, in particular in the 2 $\mathrm{g}\,\ell^{-1}$ solution. In general, the experimental data are well reproduced by the computational runs. Only the local minima on the r/R=0.4 runs are not very well reproduced. This corresponds to a slight misplacement of the main vortices towards the central axis, as can also be noted in the comparison with the qualitative PIV outcome. The effect is more marked when the CMC concentration increases. Nevertheless, the agreement, even quantitatively, is good.

A quantitative comparison between simulations and PEPT outcome is shown in Fig-

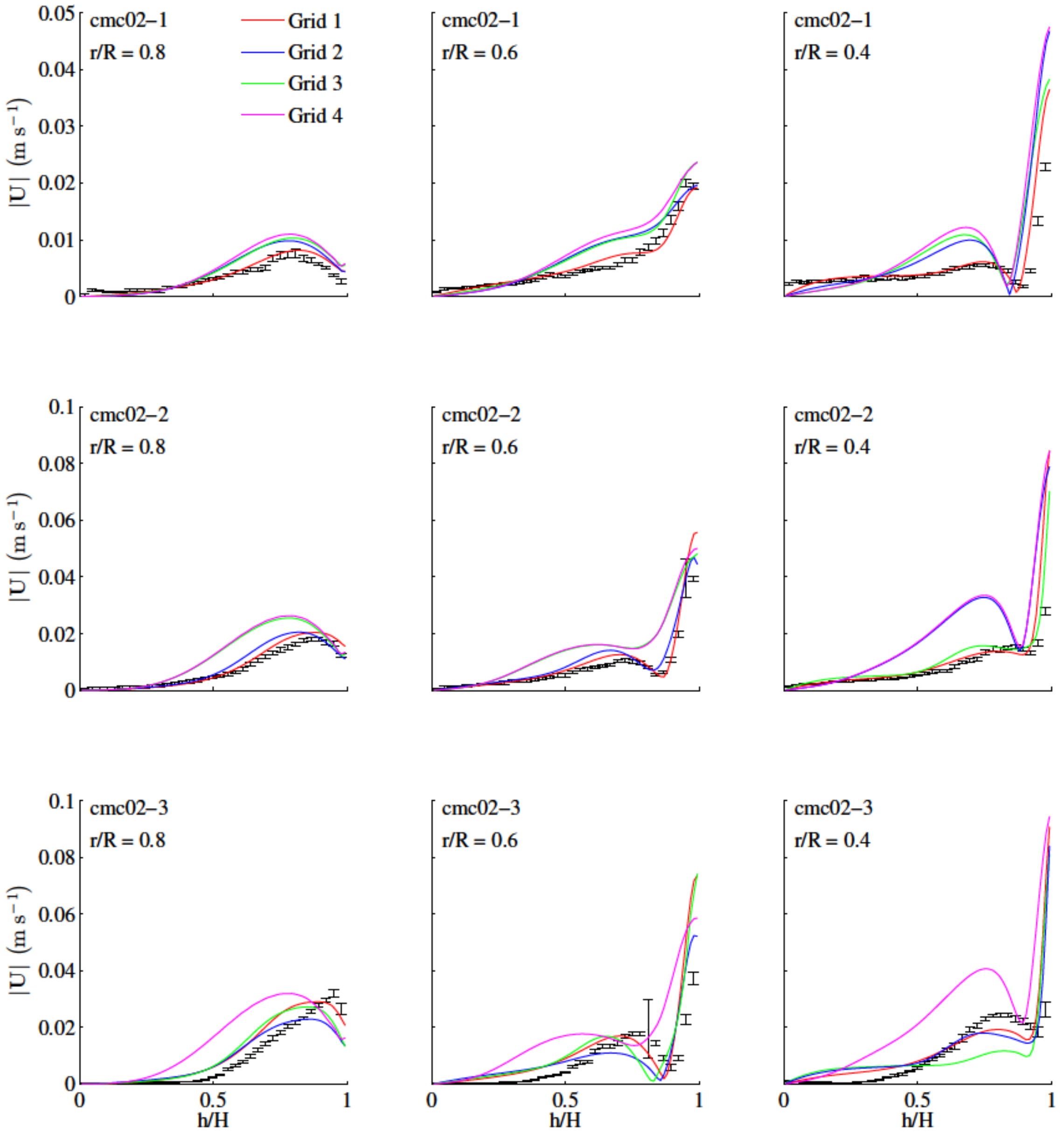

Figure 8.5 *PIV-averaged velocity magnitude along a vertical axis. Simulated data against PIV outcome.* $2\,\mathrm{g}\,\ell^{-1}$.

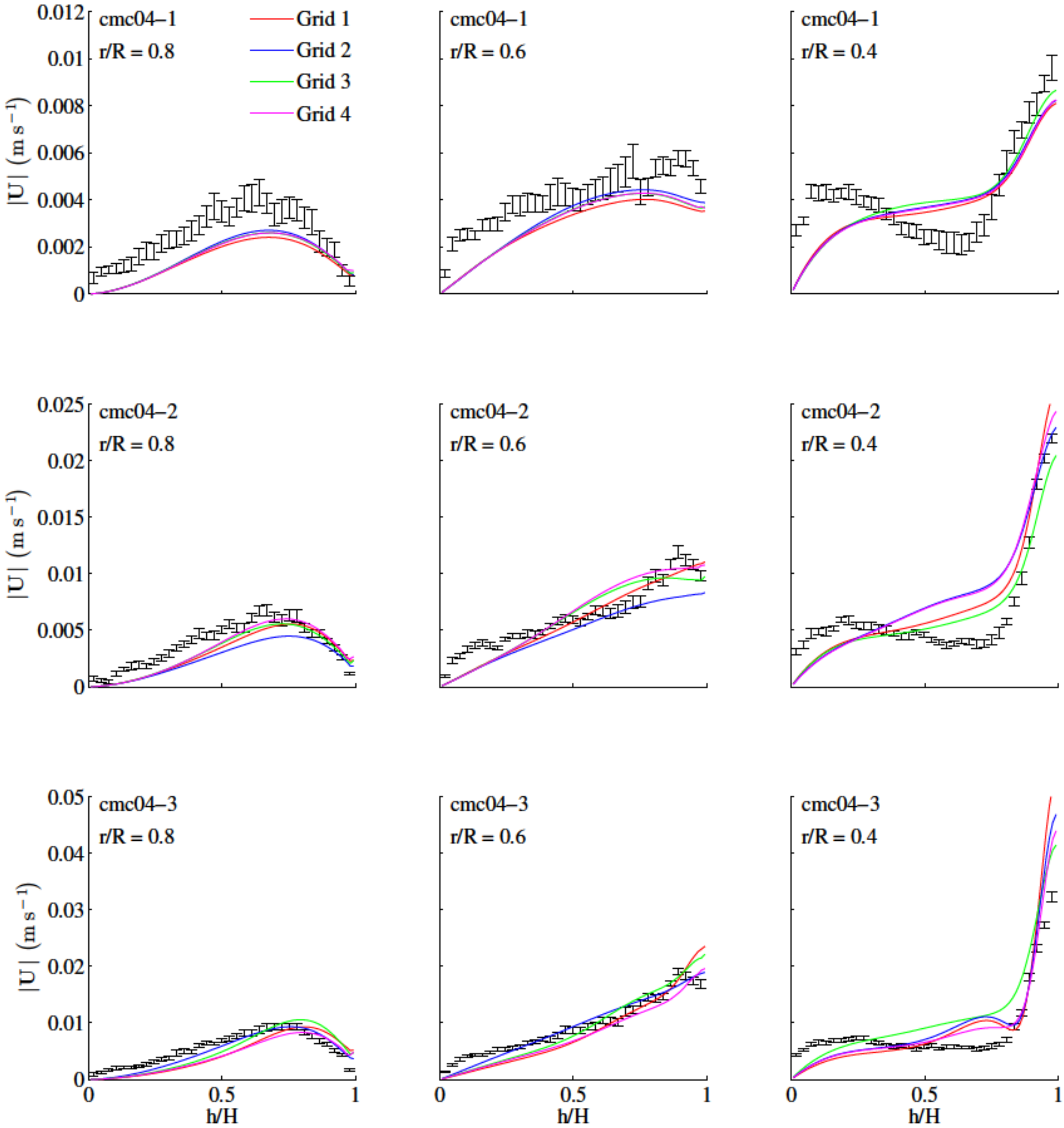

Figure 8.6 *PIV-averaged velocity magnitude along a vertical axis. Simulated data against PIV outcome. 4* g ℓ^{-1}.

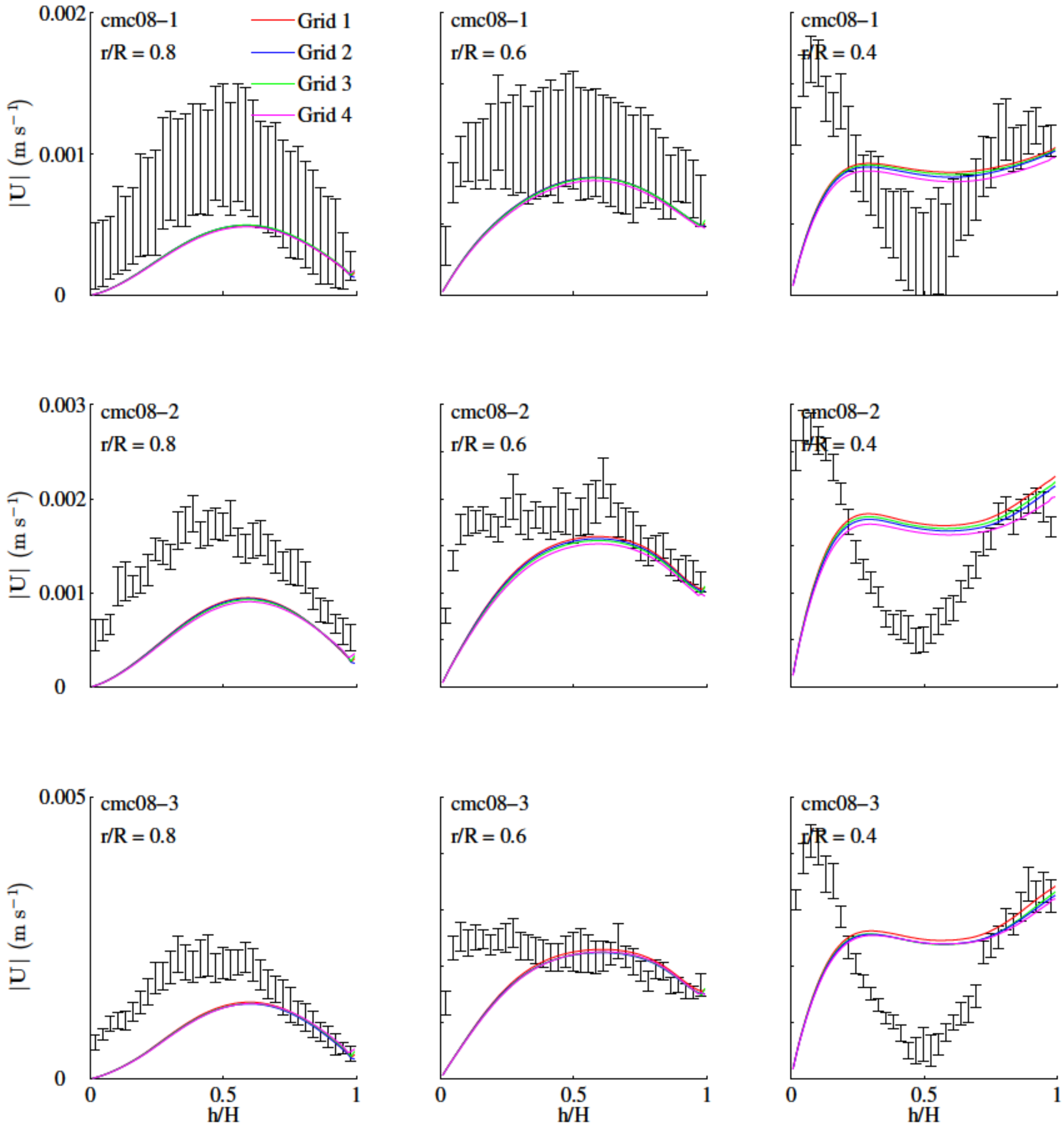

Figure 8.7 *PIV-averaged velocity magnitude along a vertical axis. Simulated data against PIV outcome. 8* g ℓ^{-1}.

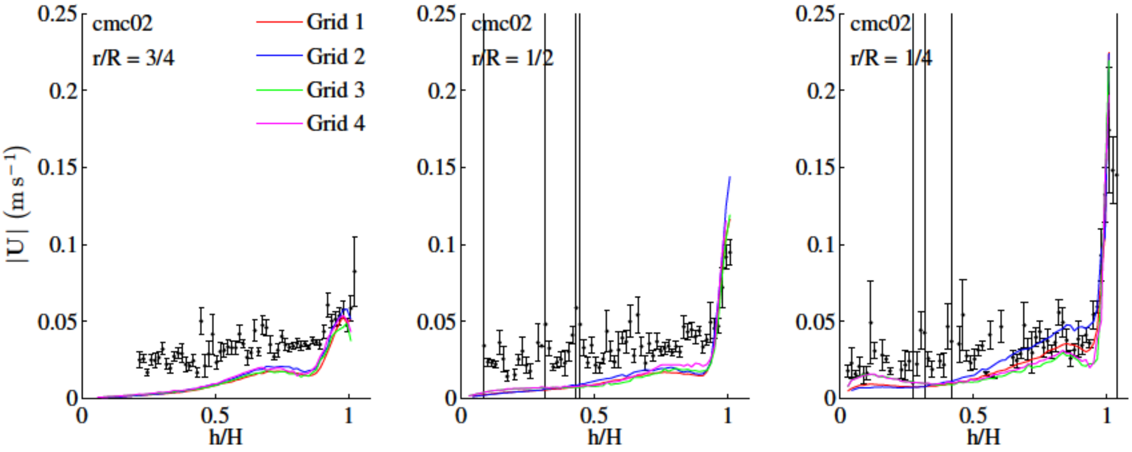

Figure 8.8 *PEPT-averaged velocity magnitude along a vertical axis. Simulated data against PEPT outcome. 2* g ℓ^{-1}.

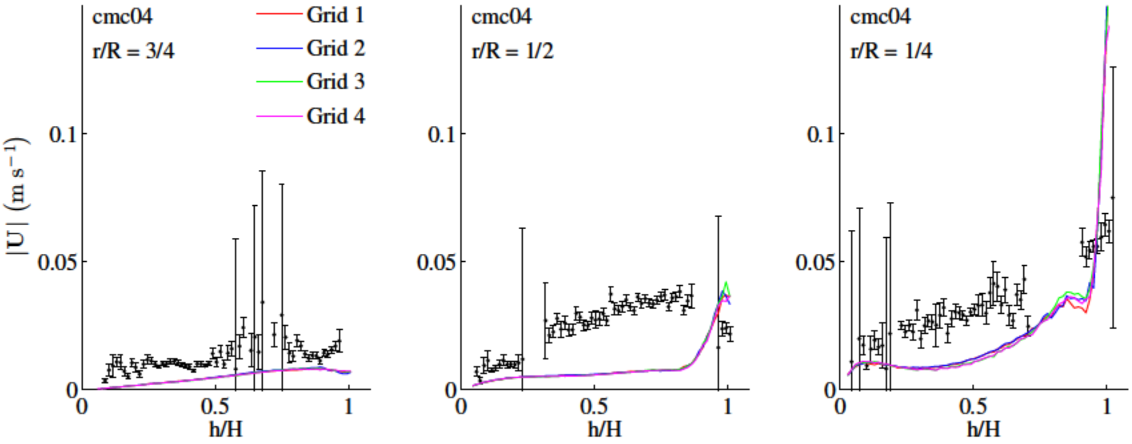

Figure 8.9 *PEPT-averaged velocity magnitude along a vertical axis. Simulated data against PEPT outcome. 4* g ℓ^{-1}.

ures 8.8 (2 $\mathrm{g}\,\ell^{-1}$) and 8.9 (4 $\mathrm{g}\,\ell^{-1}$). Each graph depicts the velocity magnitude around a vertical line at 1/4, 1/2 and 3/4 the radius from the cylinder axis. The behaviour of the PEPT points is well reproduced in all the graphs, and also the numerical values of the CFD simulations approach the experimental data. There are differences only in the 4 $\mathrm{g}\,\mathrm{l}^{-1}$ run along the axis at half radial distance (Figure 8.9), but in general the agreement is satisfactory.

The experimental uncertainty of the PEPT data is high compared to the PIV. This is due to the fact that the statistics of the PEPT measures is much scarcer than the PIV, as many points can have very few records, if not only one or none.

8.5 Average Shear Rate

As explained in Section 8.5, Bridgeman (2012) divided the computational domain for CFD simulations on an impelled-stirred laboratory-scale digester into high, medium and low-velocity zones, and drew conclusions about the mixing. The purpose of the laboratory-scale simulations and experiments is to provide numerical validation for a CFD model, and therefore an analysis as in Bridgeman (2012) is out of scope. Nevertheless, it is fruitful to divide the domain into fixed, concentric zones as explained in Section 8.5, thus taking advantage of the axial symmetry, and compute the average shear rate therein.

Figure 8.10 depicts the PIV-averaged shear rate over different subdomains, calculated as indicated in Section 5.6.1. The largest discrepancies between experimental and simulated data are concentrated in the inner part of the domain—between 0 and $0.2X_{\max}$, and, to a lesser extent, between $0.2X_{\max}$ and $0.5X_{\max}$. This was expected due to the aforementioned issue concerning the PIV technique in the inner part of the domain due to refraction through the bubbles. Nevertheless, the agreement is good in the external part of the domain, between $0.5X_{\max}$ and $X_{\max}$. This result can be considered satisfactory, as it provides a further confirmation that the CFD model is able to reproduce the real flow in the zone of interest

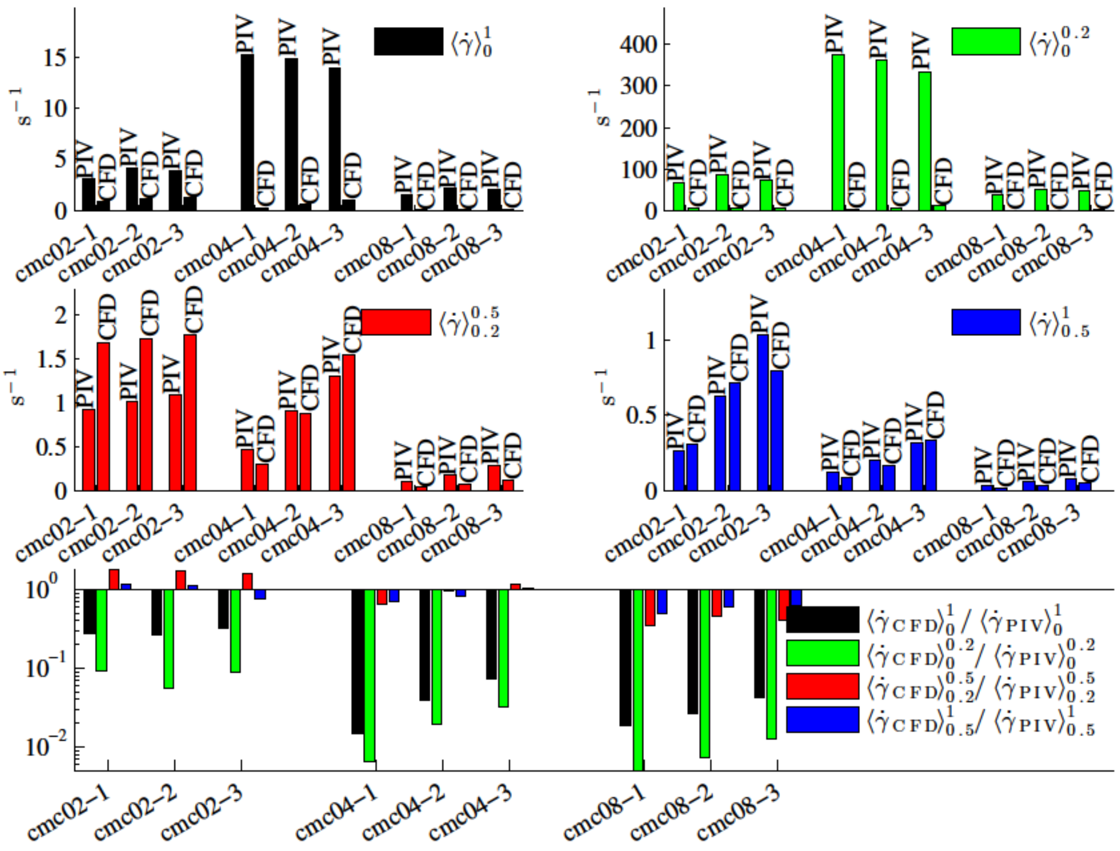

Figure 8.10 *PIV-averaged shear rate over different subdomains: comparison between experimental and simulated data. Below: ratio between simulated and experimental data.*

for the anaerobic digestion design, that is, away from the bubble column.

The shear rate values lie between 0.1 and 1 s^{-1}, well below the value of 50-80 s^{-1} suggested by literature for anaerobic digestion plants (Tchobanoglous et al., 2010). Similarly, low values of shear rate magnitude compared with the literature were found also in Bridgeman (2012), where it was observed that the presence of dead or low-mixed zones in an impeller-mixed laboratory-scale digester could not be avoided even by increasing the power input, and that this did not affect the biogas production.

In Figure 8.11, the PEPT-averaged shear rate over different subdomains is depicted. The shear rate was calculated in line with Section 5.6.2. A comparison can be made between Figure 8.10 and Figure 8.11. The PIV data approach represents the CFD simulations in the

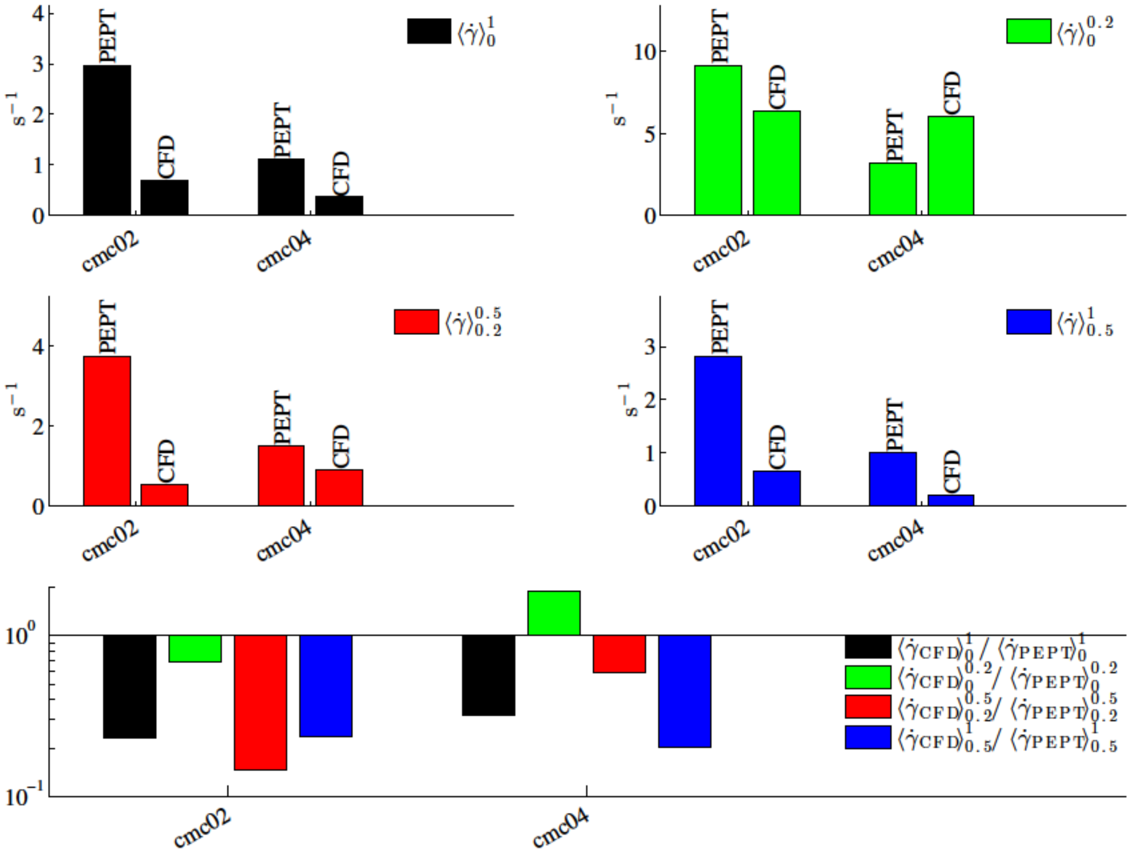

Figure 8.11 *PEPT-averaged shear rate over different subdomains: comparison between experimental and simulated data. Below: ratio between simulated and experimental data.*

outer region of the domain better than PEPT, probably also due to the problem, inherent to the PEPT, of scarce statistics and large uncertainty. However, PIV measurements differed from the simulated data in the centre by at least one order of magnitude, while the PEPT data appear to be in much better agreement. This confirms that the discrepancy between PIV and simulated data are attributable to the refraction of the laser beams through the bubbles, and not to inaccuracies of the theoretical model, nor to the effect of the large bubble size through the central column. On the contrary, the relatively good agreement between PEPT and simulated data shows that the theoretical model is able to reproduce the motion satisfactorily even in the bubble region, despite the potentially limitating assumptions.

9

Full-Scale Scenarios

> *"Anything found to be true of E. coli must also be true of elephants."*
>
> Jacques Monod (1954).

AFTER BEING VALIDATED as shown in Chapter 8, the CFD model described in Chapter 7 was applied to the full-scale setup described in Section 7.3.2. After assessing the mesh dependence (Section 9.1), the velocity flow patterns are described (Section 9.2), and the effect of the change in viscosity due to the non-Newtonian nature of sludge discussed (Section 9.3). Then, the shear rate magnitude is assessed in Section 9.4. In particular, the computational domain is divided into very low, low, average and high shear rate magnitude zones.

9.1 Assessment of the Mesh Dependence

The mesh dependence was assessed in the same way as in Section 8.2. The results are shown in Tables 9.1, 9.2 and 9.3. Behaviour similar to the laboratory-scale case was observed, with convergence being lost as the grid becomes too refined (2.5% TS, 6 and 10 cm; 7.5% TS, 10 cm). However, this effect is much less important than in the laboratory-scale case (Section 8.2) due to the relative smaller dimension of the bubbles compared to the cell size. In this aspect, the full scale simulations are more accurate than the laboratory scale, and thus the model (that was successfully validated with less precise numerical data) can be confidently applied.

Table 9.1 *GCI analysis. 2.5% TS.*

	$d = 2$ cm	$d = 6$ cm	$d = 10$ cm
$\langle\dot{\gamma}\rangle_4$ (s^{-1})	0.7551	0.6623	0.5927
$\langle\dot{\gamma}\rangle_3$ (s^{-1})	0.7576	0.7827	0.7353
$\langle\dot{\gamma}\rangle_2$ (s^{-1})	0.7496	0.7414	0.7224
$\langle\dot{\gamma}\rangle_1$ (s^{-1})	1.1029	0.9585	0,9947
p_2	6.196	3.668	7.937
p_1	5.772	2.676	4.715
GCI2$_{43}$	$7.1506\ 10^{-04}$	$9.1190\ 10^{-02}$	$2.2806\ 10^{-02}$
GCI2$_{32}$	$3.8067\ 10^{-03}$	$4.8282\ 10^{-02}$	$3.7909\ 10^{-03}$
GCI1$_{32}$	$4.3551\ 10^{-03}$	$7.5829\ 10^{-02}$	$1.0403\ 10^{-02}$
GCI1$_{21}$	$2.9770\ 10^{-02}$	$1.1561\ 10^{-01}$	$4.3522\ 10^{-02}$
Asymp.2	0.042	0.773	0.872
Asymp.1	0.010	0.190	0.027

Conversely, problems arise with grid3 and grid4, that are out of the convergence range in many runs (2.5% TS, 6 cm; 5.4% TS, 5 and 10 cm; 7.5% TS, 2 and 5 cm). This indicates that grid3 and grid4 are probably too coarse to reproduce the flow patterns properly. For this reason, grid2 was chosen for all the full scale simulations.

In all the tests, the GCI index shows higher values for smaller bubble sizes, indicating that the uncertainty related to the simulations increases with decreasing bubble size. The

Table 9.2 *GCI analysis. 5.4% TS.*

	$d = 2$ cm	$d = 6$ cm	$d = 10$ cm
$\langle\dot{\gamma}\rangle_4$ (s^{-1})	0.6160	0.6096	0.5605
$\langle\dot{\gamma}\rangle_3$ (s^{-1})	0.6724	0.5926	0.5817
$\langle\dot{\gamma}\rangle_2$ (s^{-1})	0.7558	0.6501	0.6314
$\langle\dot{\gamma}\rangle_1$ (s^{-1})	0.9021	0.8057	0.8796
p_2	3.059	6.498	5.385
p_1	0.231	0.612	1.657
GCI2$_{43}$	$6.6645\ 10^{-02}$	$5.5732\ 10^{-03}$	$1.0628\ 10^{-02}$
GCI2$_{32}$	$1.2482\ 10^{-01}$	$2.8625\ 10^{-02}$	$3.6311\ 10^{-02}$
GCI1$_{32}$	$2.3858\ 10^{+00}$	$6.8833\ 10^{-01}$	$1.9799\ 10^{-01}$
GCI1$_{21}$	$1.7965\ 10^{+00}$	$7.3744\ 10^{-01}$	$3.0606\ 10^{-01}$
Asymp.2	0.254	0.040	0.079
Asymp.1	1.193	0.703	0.301

Table 9.3 *GCI analysis. 7.5% TS.*

	$d = 2$ cm	$d = 6$ cm	$d = 10$ cm
$\langle\dot{\gamma}\rangle_4$ (s^{-1})	0.6556	0.5910	0.5344
$\langle\dot{\gamma}\rangle_3$ (s^{-1})	0.6421	0.5942	0.6034
$\langle\dot{\gamma}\rangle_2$ (s^{-1})	0.7399	0.6264	0.6092
$\langle\dot{\gamma}\rangle_1$ (s^{-1})	0.9021	0.7674	0.7729
p_2	10.97	13.25	7.757
p_1	0.390	1.432	4.481
$\mathrm{GCI2}_{43}$	$9.1367\ 10^{-04}$	$1.1162\ 10^{-04}$	$1.4284\ 10^{-02}$
$\mathrm{GCI2}_{32}$	$1.2299\ 10^{-02}$	$2.6651\ 10^{-03}$	$2.1418\ 10^{-03}$
$\mathrm{GCI1}_{32}$	$1.6600\ 10^{+00}$	$1.5436\ 10^{-01}$	$6.0757\ 10^{-03}$
$\mathrm{GCI1}_{21}$	$1.1366\ 10^{+00}$	$2.4435\ 10^{-01}$	$3{,}8080\ 10^{-02}$
Asymp.2	0.005	0.002	1.010
Asymp.1	1.219	0.326	0.020

average number of bubbles inside the system at a given time is reported in Table 9.4. It is clear that this number approaches and eventually overcomes the value of $\sim 10^4$ suggested previously in Section 7.1. Under these conditions, the approximation (*iii*) of pointwise bubbles introduced in Section 7.1 may be no longer valid. Therefore, care must be adopted in interpreting the results from simulations with smaller bubble sizes, in particular d = 2 cm.

Another test can be performed by comparing the averaged velocity magnitude field along a vertical line lying onto the symmetry plane, placed at a distance of half of the external radius from the wedge vertex. The result is shown in Figure 9.1, and confirms what was observed in the GCI analysis.

Table 9.4 *Average number of bubbles inside the system at a given time.*

TS	$d = 2$ cm	$d = 6$ cm	$d = 10$ cm
2.5%	10,900	330	73
5.4%	10,900	340	78
7.5%	10,900	330	70

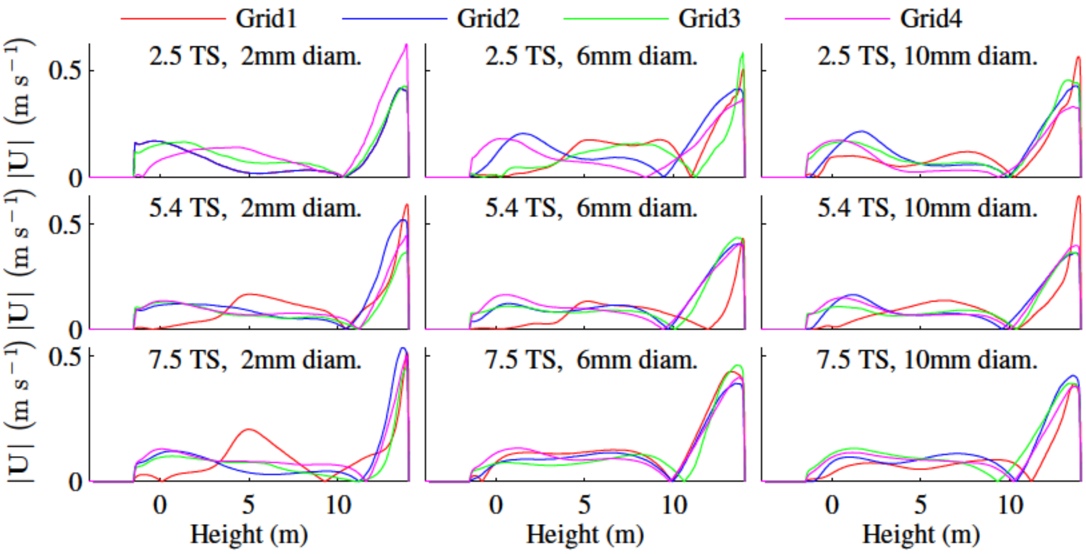

Figure 9.1 *Mesh independence test,* $q = 1$.

9.2 Velocity Flow Patterns

Figures 9.2, 9.3 and 9.4 show the velocity field at the last timestep (300 s) for $q = 1.0$, 0.5 and 0.2 respectively. All the values of TS and bubble diameter are shown. The general structure of the flow patterns is the same for all the runs: the rising bubbles create a column of liquid phase rapidly moving upwards from above the nozzle to the surface. Once it reaches the surface, the liquid phase is displaced horizontally towards the wall, and then forms a large vortex that moves slightly downwards and then occupies almost all of the remaining part of the domain. The centre of the vortex is mid-way in the upper part of the domain. Once inside the vortex, the liquid phase slowly descends beside the external boundary of the domain, follows the slope of the bottom of the tank and finally approaches the zone around the nozzle. A small stagnant zone can be seen in the upper part of the domain, between the rising column and the symmetry axis.

Beyond the general similarities, effects arising as a result of changes to the gas flow rate, the rheology (that is, total solids content) and the bubble size can be observed.

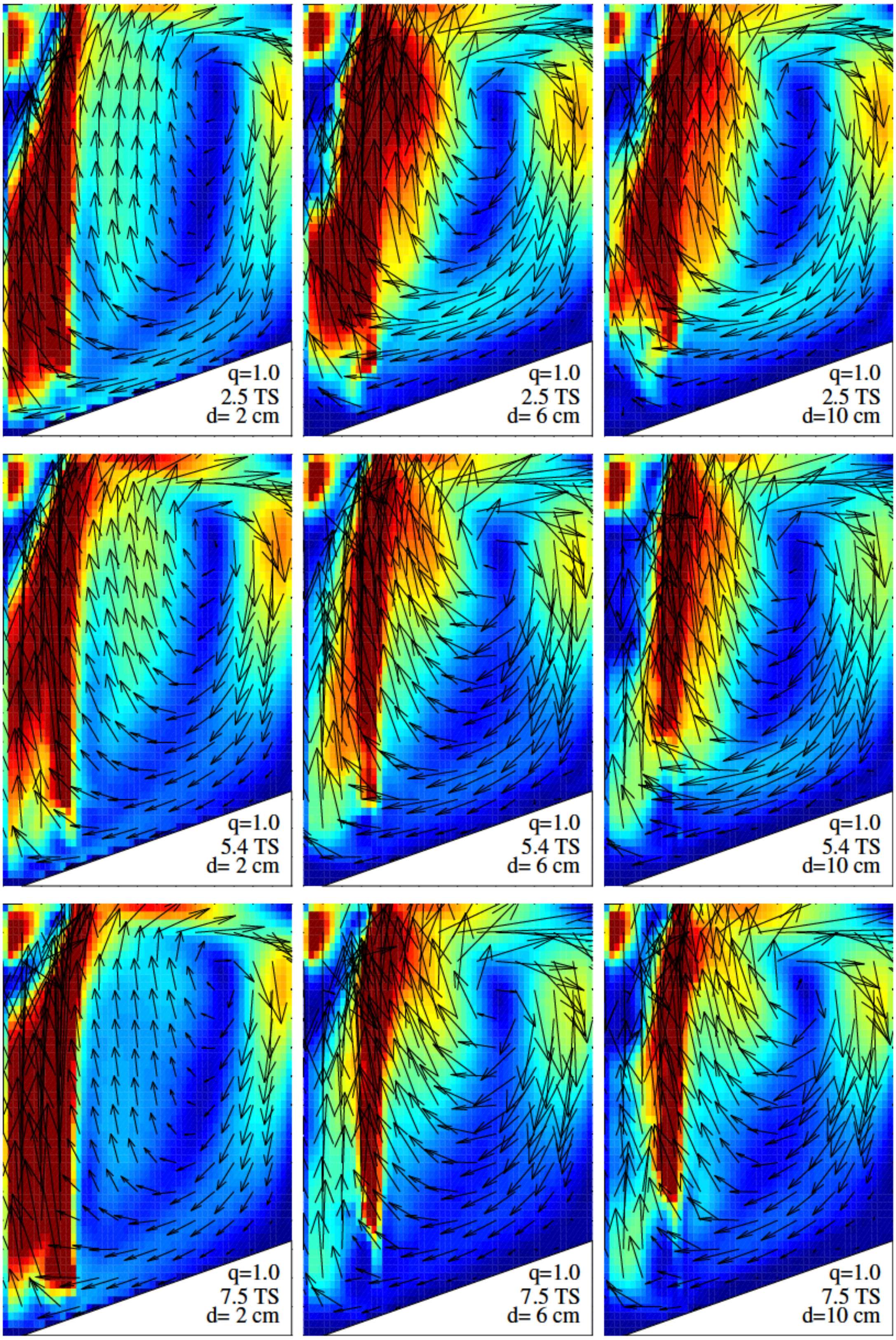

Figure 9.2 *Flow patterns for* $q = 1.0$ *with* $|\mathbf{u}| \in (0\,, 0.5)\ \mathrm{m\,s^{-1}}$.

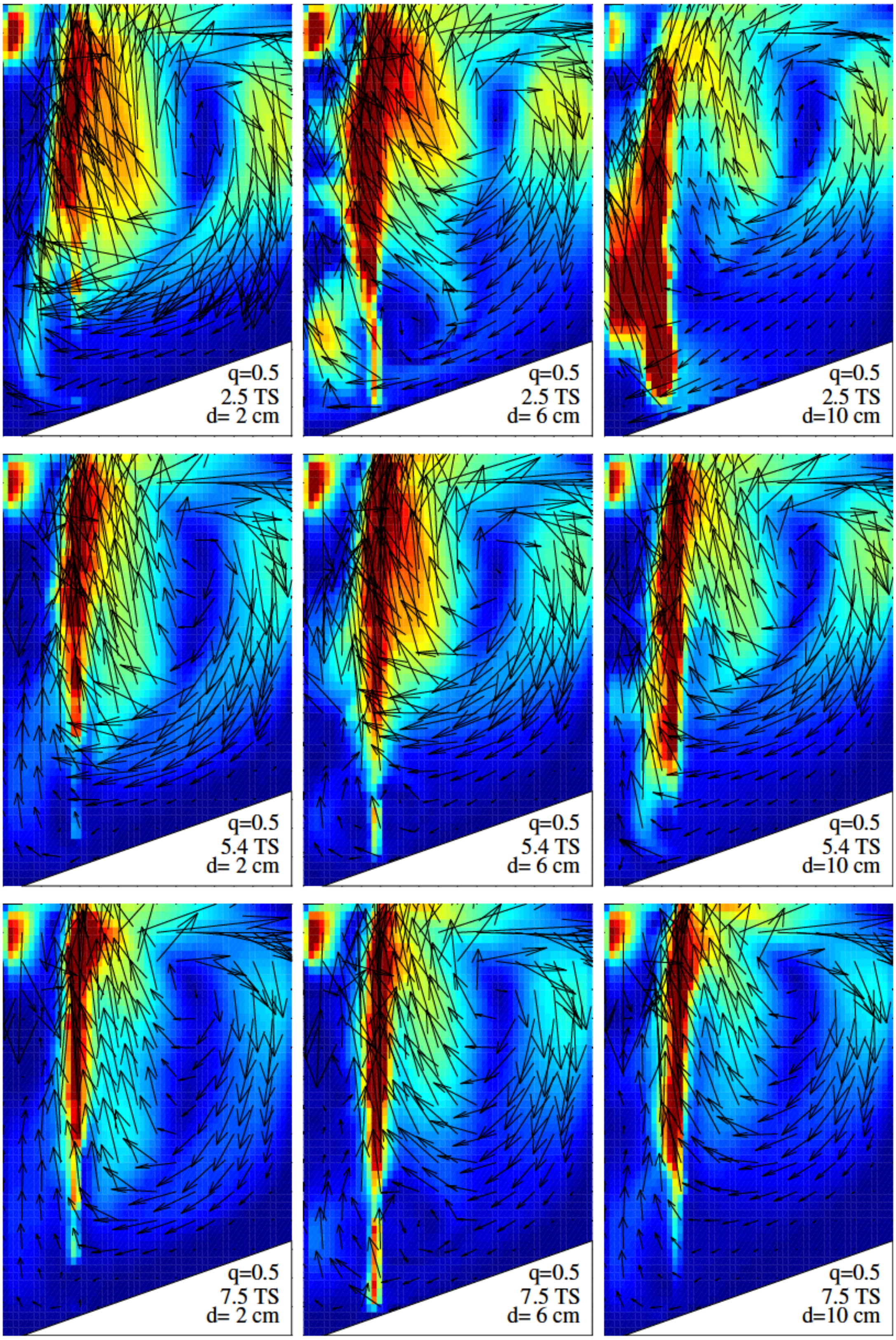

Figure 9.3 *Flow patterns for* $q = 0.5$ *with* $|\mathbf{u}| \in (0\,, 0.5)\ \mathrm{m\,s^{-1}}$.

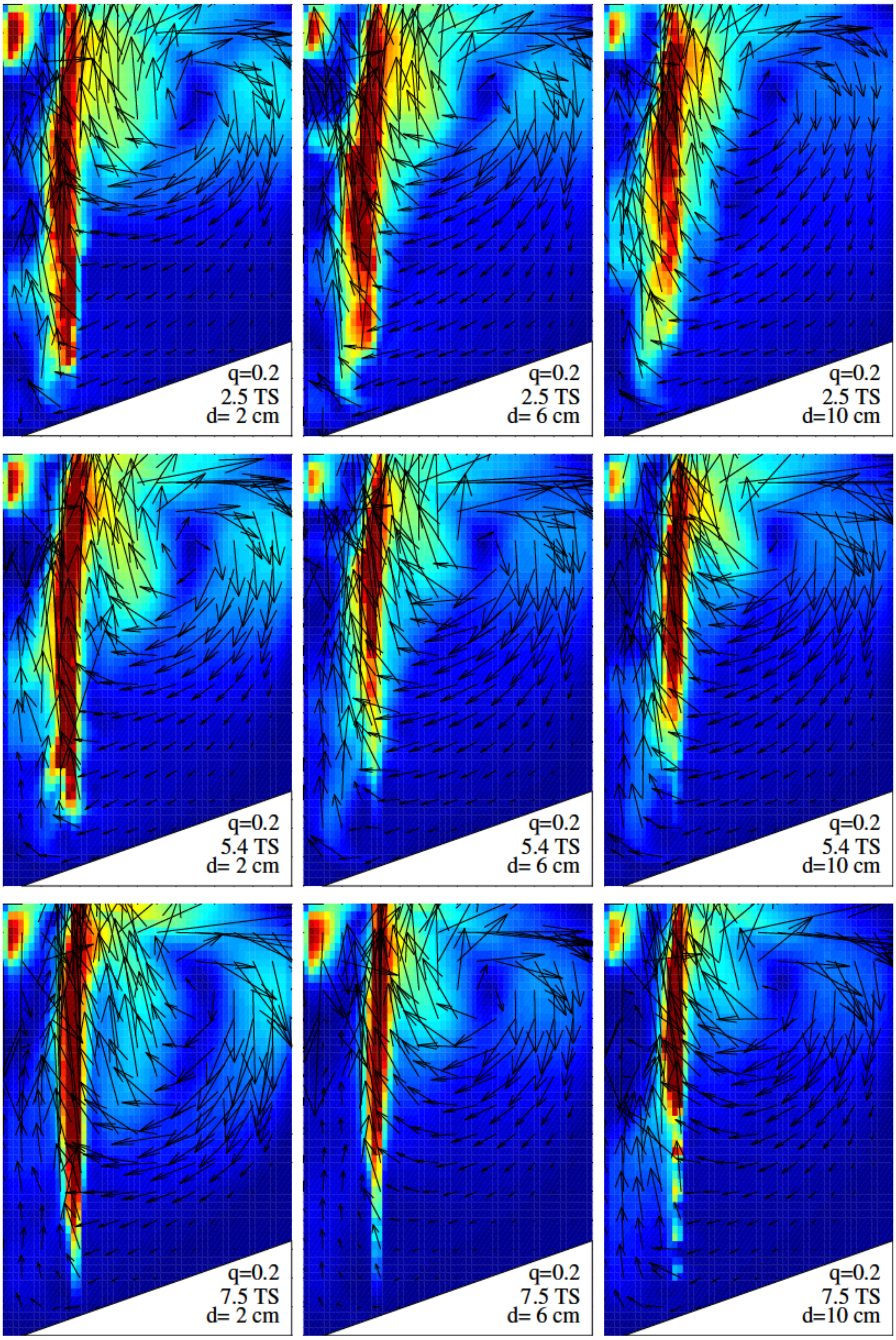

Figure 9.4 *Flow patterns for* $q = 0.2$ *with* $|\mathbf{u}| \in (0\,,0.5)\ \mathrm{m\,s^{-1}}$.

(*i*) from the gas flow rate: the velocity magnitude increases and the vortex becomes more and more developed when q rises; in particular, the vortex does not reach the lower part of the domain for small values of q. Interestingly, the intermediate flow rate shows velocity intensities not too different from the maximum flow rate, while the velocity magnitude falls considerably in the lowest flow rate. As expected, the flow rate has the highest effect on the flow patterns.

(*ii*) from the rheology: the vortex becomes less compact and the velocity patterns more dispersed as TS rises. The effect of the total solids variation is to attenuate the flow pattern as it rises.

(*iii*) from the bubble size: the shape of the vortex changes slightly; in particular, the vortex is more extended downwards when the bubble diameter is small, even though the general behaviour of the flow patterns does not change.

9.3 Viscosity Patterns

An analysis of viscosity under different flow regimes was undertaken. and depicted in Figure 9.5, 9.6 and 9.7. The non-Newtonian behaviour is evident, with viscosity decreasing when shear rate increases. In particular, it can be seen that viscosity increases in the stagnant zones and, conversely, drops along the vertical column and, more interestingly, along the descending branch of the vortex. As a consequence of this, flow patterns in which the viscosity is considerably lower than in the surroundings arise inside the domain. Such patterns can be readily identified in the flow patterns (Figures 9.2, 9.3 and 9.4), as the rising column and the vortex descending branch.

Areas of flow with lower viscosity than the surrounding offer less resistance against incoming liquid and, consequently, circulation is expected to be enhanced within the lower viscosity areas. Conversely, areas with higher viscosity oppose a higher resistance to the flow and, consequently, are expected to undergo a reduced circulation. This is expected to

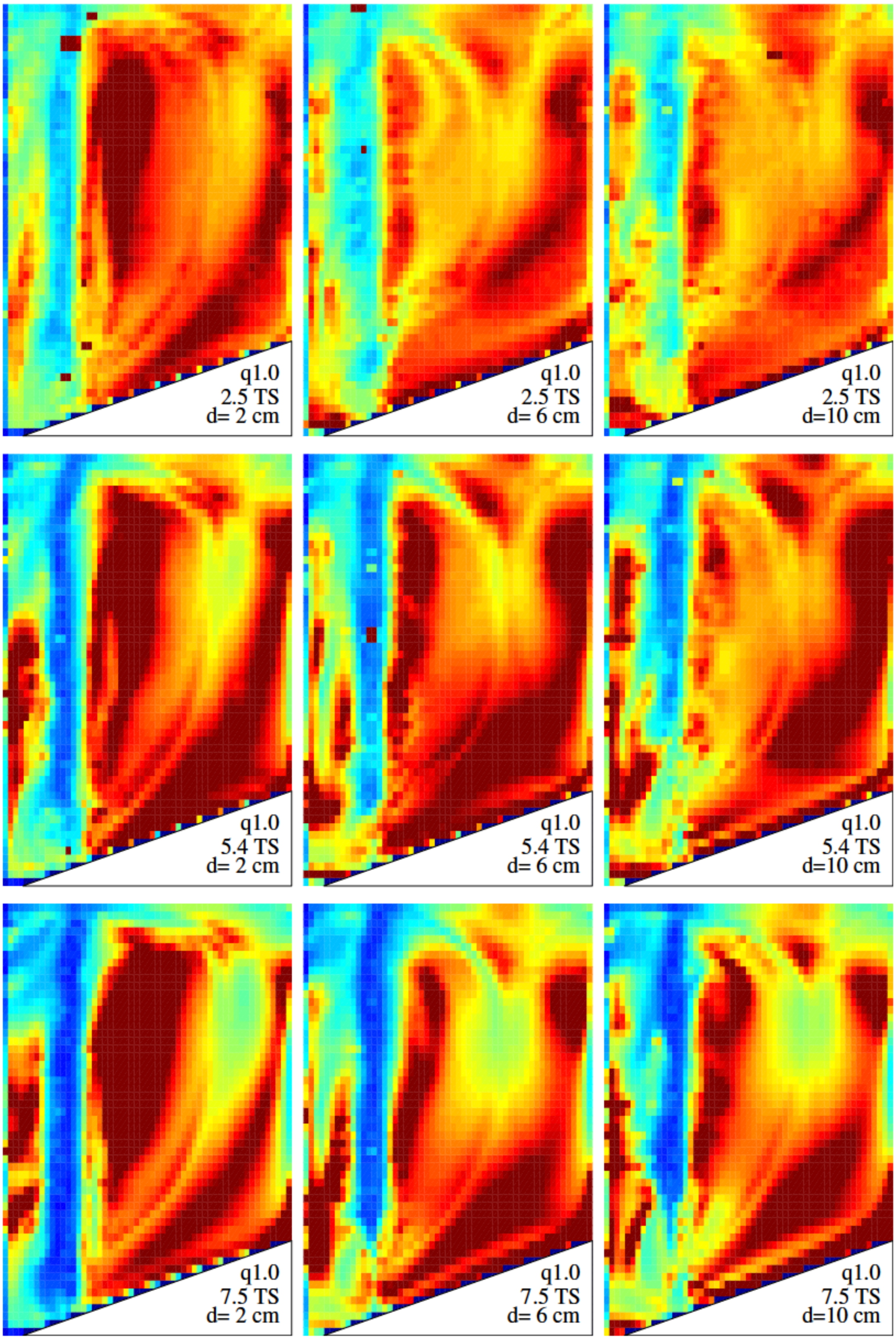

Figure 9.5 *Viscosity for* $q = 1.0$ *with* $\mu \in (0\,, 0.1)$ *Pa s for the 2.5 TS runs,* $(0\,, 0.6)$ *Pa s for the 5.4 TS runs,* $(0\,, 2.0)$ *Pa s for the 7.5 TS runs.*

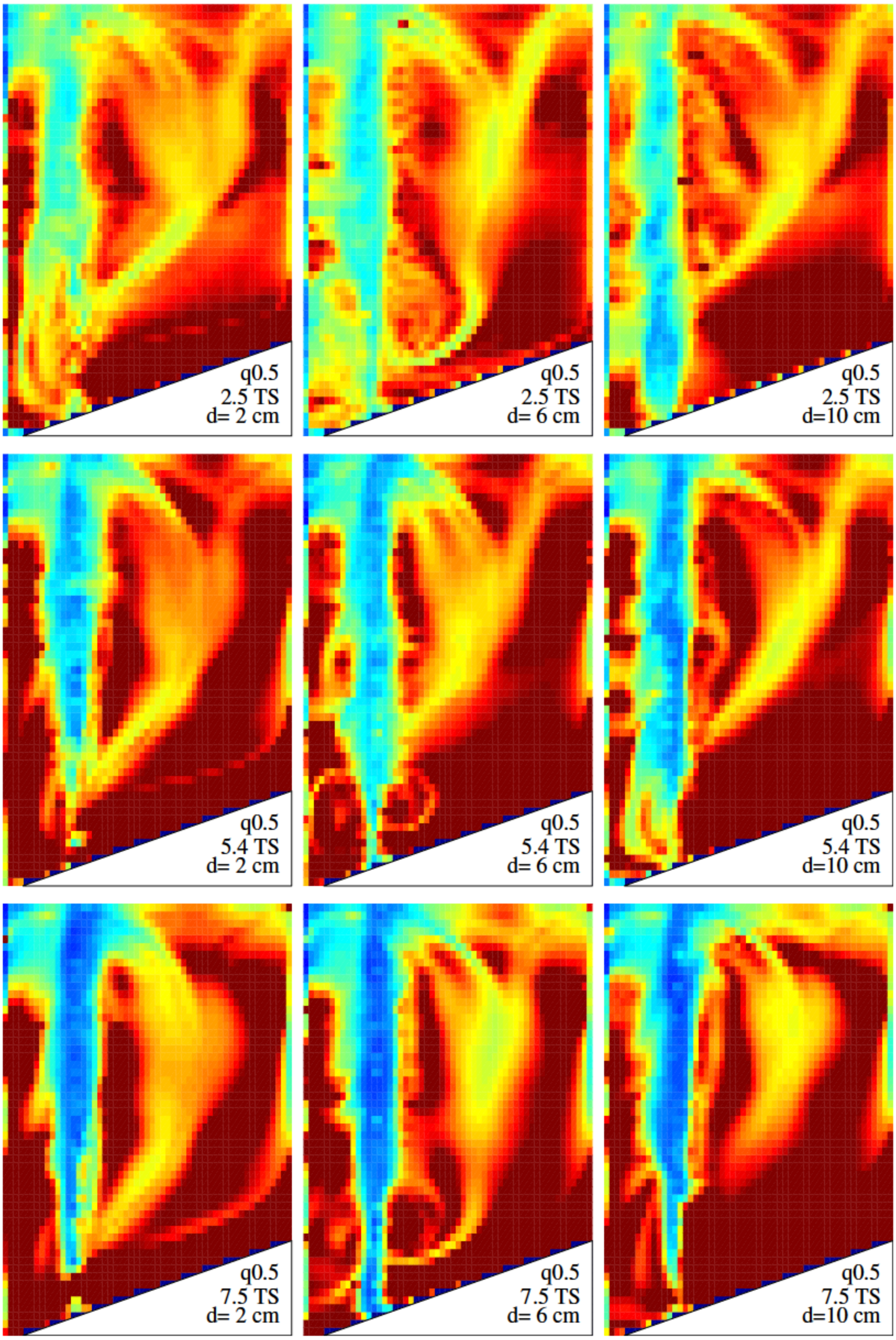

Figure 9.6 *Viscosity for* $q = 0.5$ *with* $\mu \in (0\,,0.1)$ *Pa s for the 2.5 TS runs,* $(0\,,0.6)$ *Pa s for the 5.4 TS runs,* $(0\,,2.0)$ *Pa s for the 7.5 TS runs.*

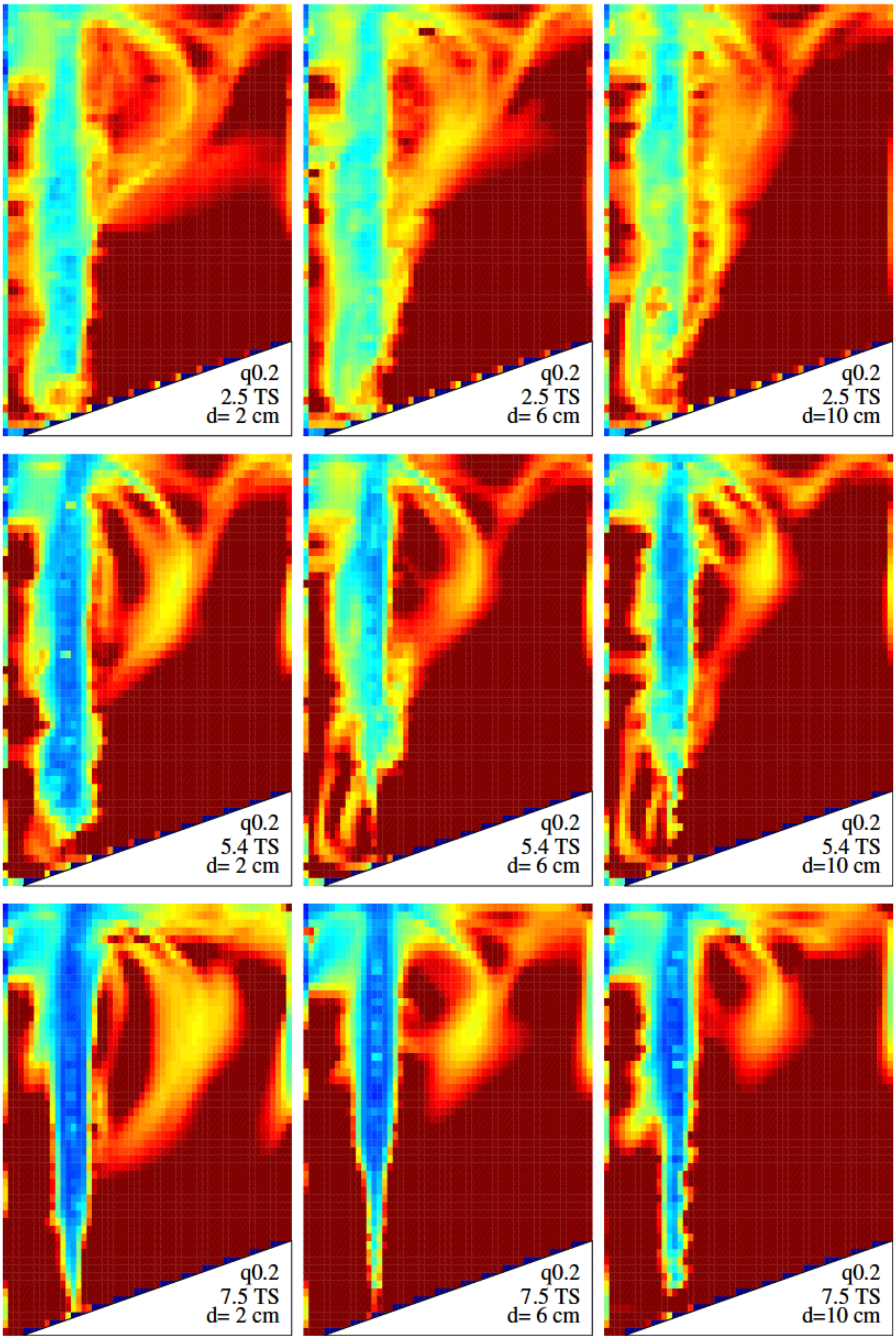

Figure 9.7 *Viscosity for* $q = 0.2$ *with* $\mu \in (0\,, 0.1)$ *Pa s for the 2.5 TS runs,* $(0\,, 0.6)$ *Pa s for the 5.4 TS runs,* $(0\,, 2.0)$ *Pa s for the 7.5 TS runs.*

have a detrimental effect in the uniform distribution of nutrients throughout the digester because creates short circuits in the flow patterns.

This issue can be mitigated by amending the geometry of the digester. Specifically, this can be accomplished quite simply, for instance, by arranging a second series of nozzles at a different distance from the tank symmetry axis. Biogas can be injected alternately from the original or the additional nozzles series, at intervals of approximately ten minutes. As a result, the low viscosity flow patterns that arise when injecting biogas through the original nozzles series will be destroyed when biogas is injected via the new nozzles series, and vice versa. This hypothesis of flow patterns with less short-circuited mixing being generated by switching biogas injection between two nozzles series has been investigated and reported later on, in Section 9.5.

9.4 Average Shear Rate

As mentioned in Section 8.5, Bridgeman (2012) reported an analysis of an impeller-stirred laboratory-scale digester with different TS values and rotational regimes: high, medium and low-velocity zones depending on the pointwise value of the velocity field were identified, and the average shear rate was calculated. The conclusions of that work can be summarized as:

(*i*) an increase of TS raises the volume of low-mixed zones, but does not have significant effects on the volume of the high-mixed zones;

(*ii*) a change of the impeller angular velocity scarcely affects the average shear rate in the bulk of the domain;

(*iii*) in all the cases taken into consideration, the average shear rate was well below (up to an order of magnitude) of the suggested value Tchobanoglous et al. (2010) for optimum mixing, and yet biogas production was still achieved.

The observations listed above suggest that an analysis of the average shear rate can

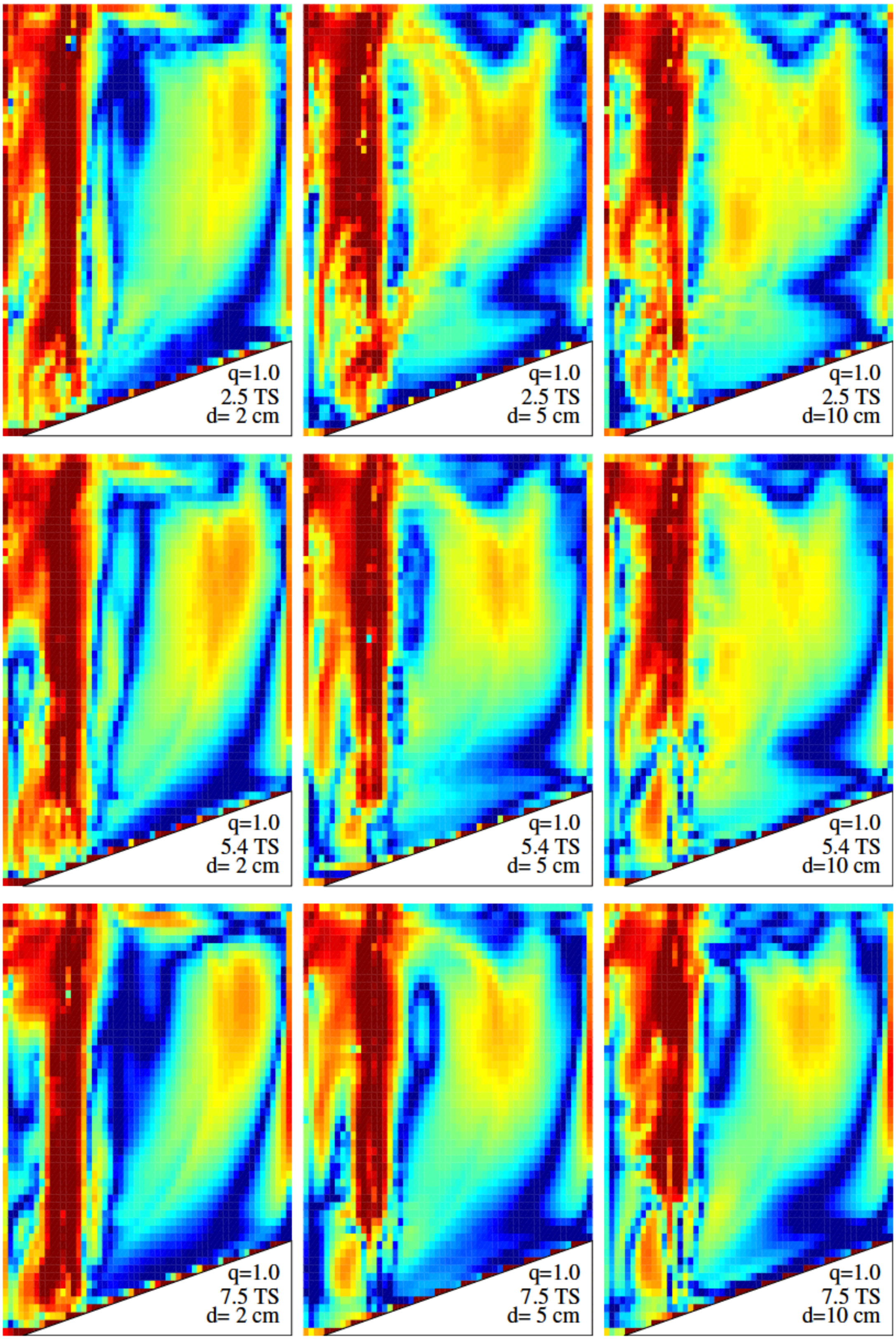

Figure 9.8 *Shear rate in logarithmic plot for* $q = 1.0$ *with* $\langle \dot{\gamma} \rangle \in \left(10^{-2}, 10^{0}\right)\ \mathrm{s}^{-1}$.

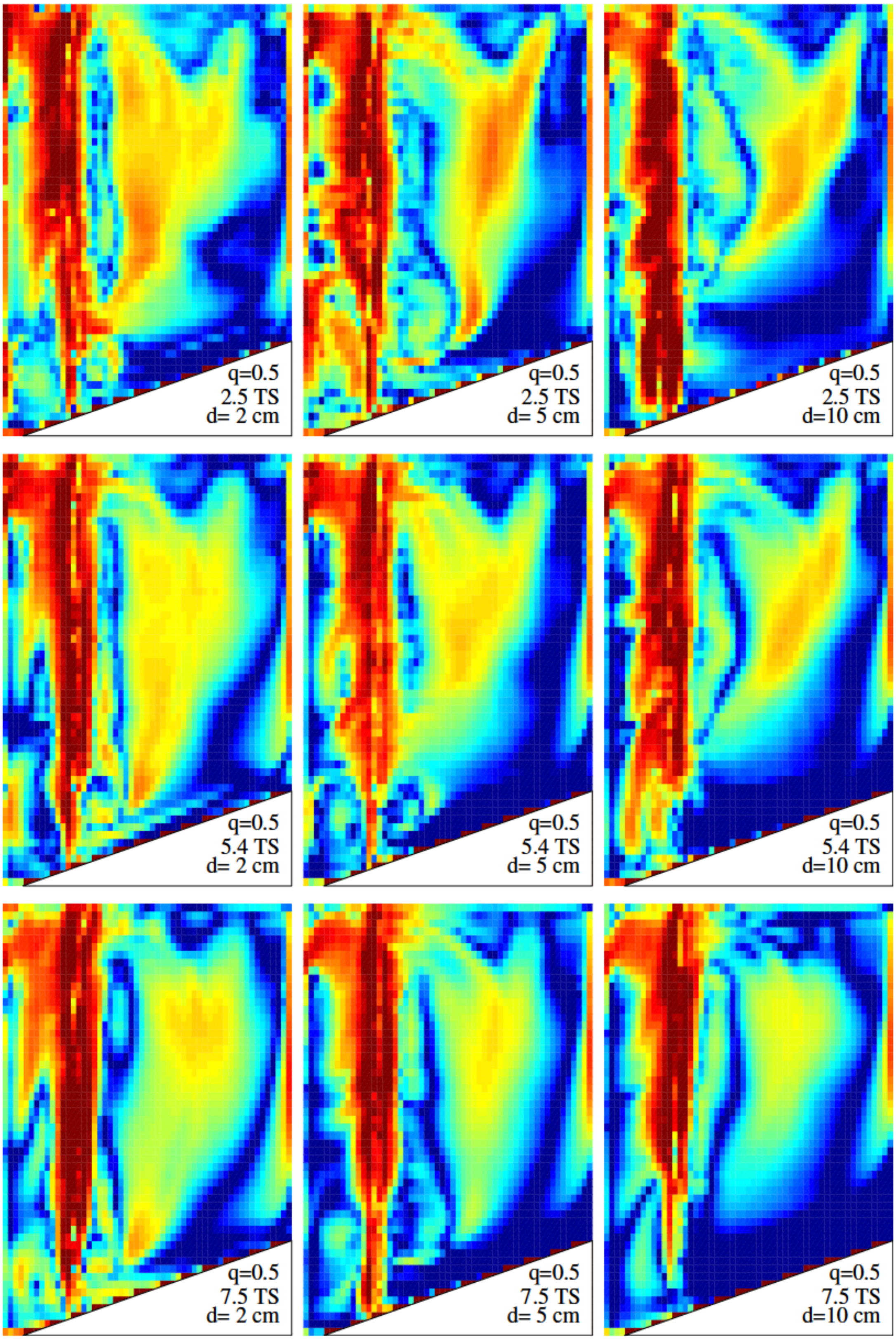

Figure 9.9 *Shear rate in logarithmic plot for* $q = 0.5$ *with* $\langle\dot{\gamma}\rangle \in \left(10^{-2}, 10^{0}\right)\ \mathrm{s}^{-1}$.

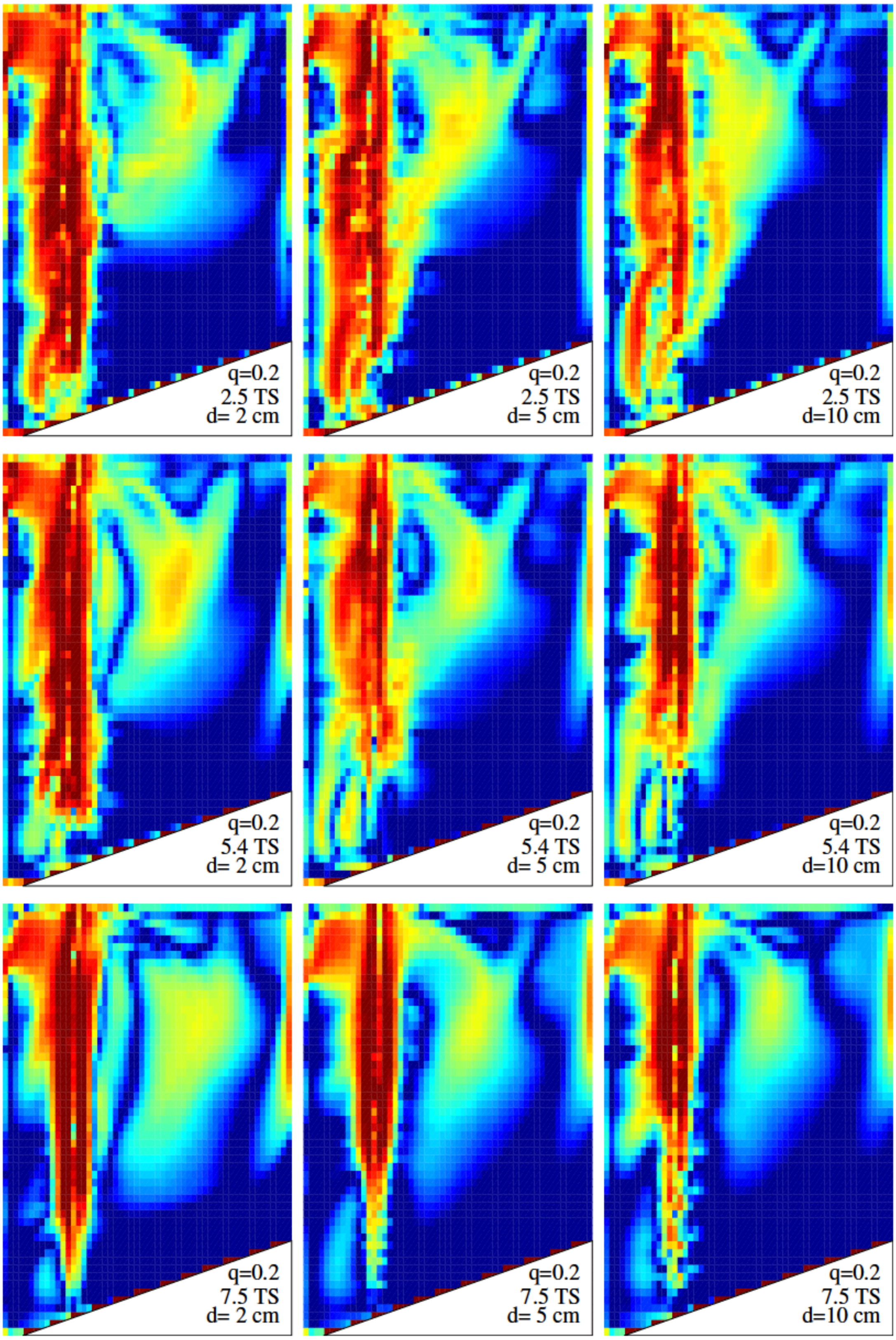

Figure 9.10 *Shear rate in logarithmic plot for* $q = 0.2$ *with* $\langle\dot{\gamma}\rangle \in \left(10^{-2}, 10^{0}\right)\ \mathrm{s}^{-1}$.

be fruitful. In Figures 9.8, 9.9 and 9.10, the shear rate magnitude field is depicted for different flow regimes. The average shear rate patterns follow the velocity field and the viscosity, with the pointwise value being higher where the velocity magnitude is higher, and the viscosity is lower. Another crucial observation is that, with ehe exclusion of the zone surrounding the bubble column, the average shear rate was found to be much lower than the minimum values suggested by Tchobanoglous et al. (2010). This is in agreement with Bridgeman (2012).

The observations from both the conclusions of Bridgeman (2012) and the analysis of Figures 9.8, 9.9 and 9.10 suggest that the mixing power input of an anaerobic digester can be lowered without affecting the average shear rate significantly. In order to verify this statement, the average shear rate $\langle\dot{\gamma}\rangle$ was plotted against q for different TS and bubble diameters (Figure 9.11). The general trend shows a growth for all the TS and bubble diameters, with a slower growth at $q \geq 0.7$. Also the numerical values of $\langle\dot{\gamma}\rangle$ are comparable for all the runs. Nevertheless, there are some differences depending both on total solids and bubble size. For a bubble diameter of 2 cm, for instance, $\langle\dot{\gamma}\rangle$ grows up to $q = 0.25$, then decreases slightly and finally increases above $q = 0.5$, with a slower growth for $q \geq 0.7$. This behaviour is reproduced by the 6 cm and 10 cm bubble size runs, with the difference that the decrease occurs for values of q between 0.5 and 0.7; conversely, the decrease does not occur for 7.5% TS.

Following Bridgeman (2012), an analysis was also undertaken by dividing the com-

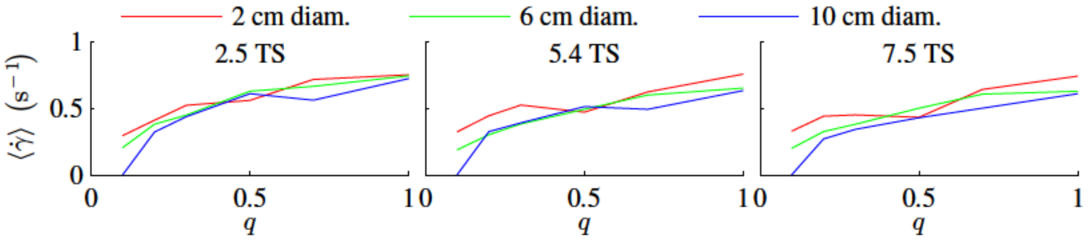

Figure 9.11 *Average shear rate against the power input for different values of TS and d.*

putational domain into zones of high or low mixing intensity. However, in this case, the subdivision was based on the proportions of different shear rate intervals, rather than on velocity magnitude. Four shear rate intervals were defined: $\langle\dot{\gamma}\rangle < 0.01$ s^{-1} (very low), $0.01 \leq \langle\dot{\gamma}\rangle < 0.1$ s^{-1} (low), $0.1 \leq \langle\dot{\gamma}\rangle < 1$ s^{-1} (medium), $\langle\dot{\gamma}\rangle > 1$ s^{-1} (high). The results are shown in Figure 9.12. The magnitude and behaviour of the shear rate relative volumes are similar for all the TS irrespective of bubble diameter, and in particular: (*i*) the relative volume with very low shear rate is initially high (approximately 0.5), but drops quickly to assume low values at $q = 0.3$—0.7; (*ii*) low shear rate relative volume is approximately constant with a value of around 0.5; (*iii*) the medium shear rate relative volume shows a growing trend up to $q = 0.5$—0.7 and then is approximately constant; (*iv*) the high shear rate relative volume is always negligible, with a weak tendency to increase proportionally with q; (*v*) most of the volume is occupied by very low shear rate up to $q \simeq 0.2$; very low, low and average shear rates equally occupy the domain for q from 0.2 to 0.5—0.7; and for q greater than 0.5—0.7 most of the volume is equally occupied by low and average shear rates.

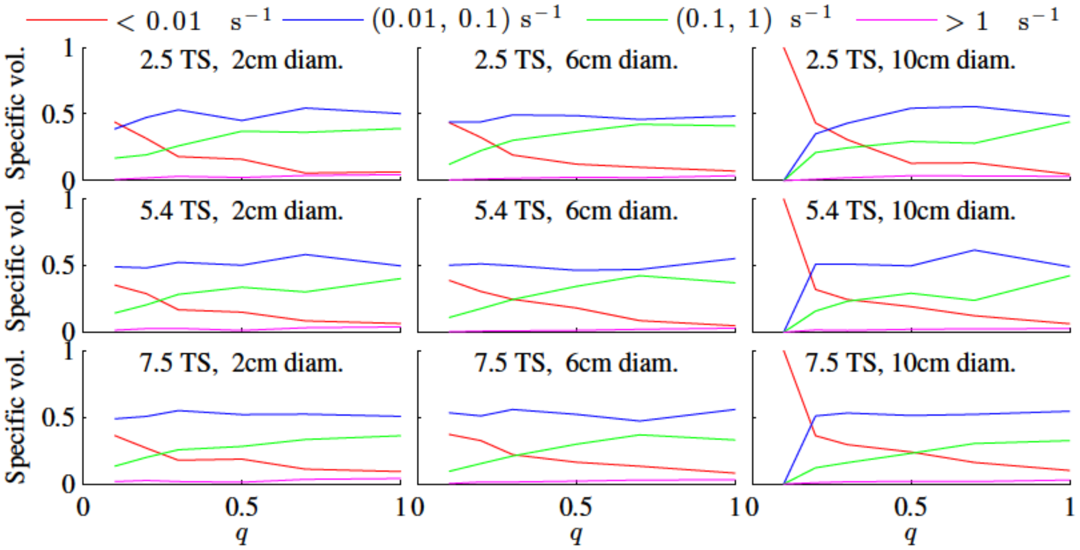

Figure 9.12 *Specific volume of the shear rate intervals against flow rate for different values of TS and d.*

As the high shear rate relative volume is negligible, the effectiveness of mixing is expected to depend on the mutual balance of very low, low and average shear rate relative volume. This implies that good quality mixing occurs when the average shear relative volume is high and very low shear relative volume is low. Considering the results shown in Figure 9.12, this condition can be considered to be verified for $q \geq 0.5$.

Considering the value of $Q_{\max}$ and the geometrical characteristics of the full-scale digester as in Table 5.2, according with Equation 5.1, the value of the total power per volume unit corresponding to $q = 0.5$ is around $1\ \mathrm{W\,m^{-3}}$.

9.5 Switching Between Nozzles Series

The issue described in Section 9.3 about the low-viscosity flow patterns can be mitigated by amending the geometry of the digester. Specifically, this can be accomplished quite simply, for instance, by arranging a second series of nozzles at a different distance from the tank symmetry axis. Biogas can be injected alternately from the original or the additional nozzles series, at constant intervals. As a result, the low viscosity flow patterns that arise when injecting biogas through the original nozzles series will be destroyed when biogas is injected via the new nozzles series.

This hypothesis was tested by performing an additional series of simulations, in which the gas injection through the original nozzles series was switched to a new series placed at a distance $R'_{\mathrm{noz}} = 5.49$ m from the tank axis. A value of $q = 0.5$ was chosen, in line with the conclusions on minimum mixing power per volume unit outlined in Section 8.5. As regards the bubble size, in Section 8.5 it was shown that the outcome of the simulations does not depend on bubble size incisively; on the other hand, the GCI test performed in Section 9.1 shows that the simulations conducted with smaller bubble sizes may become unaffordable. For these reasons, $d = 10$ mm was chosen as the bubble size for all the simulations.During the simulations, the nozzles injecting biogas were switched every minute, for a total time

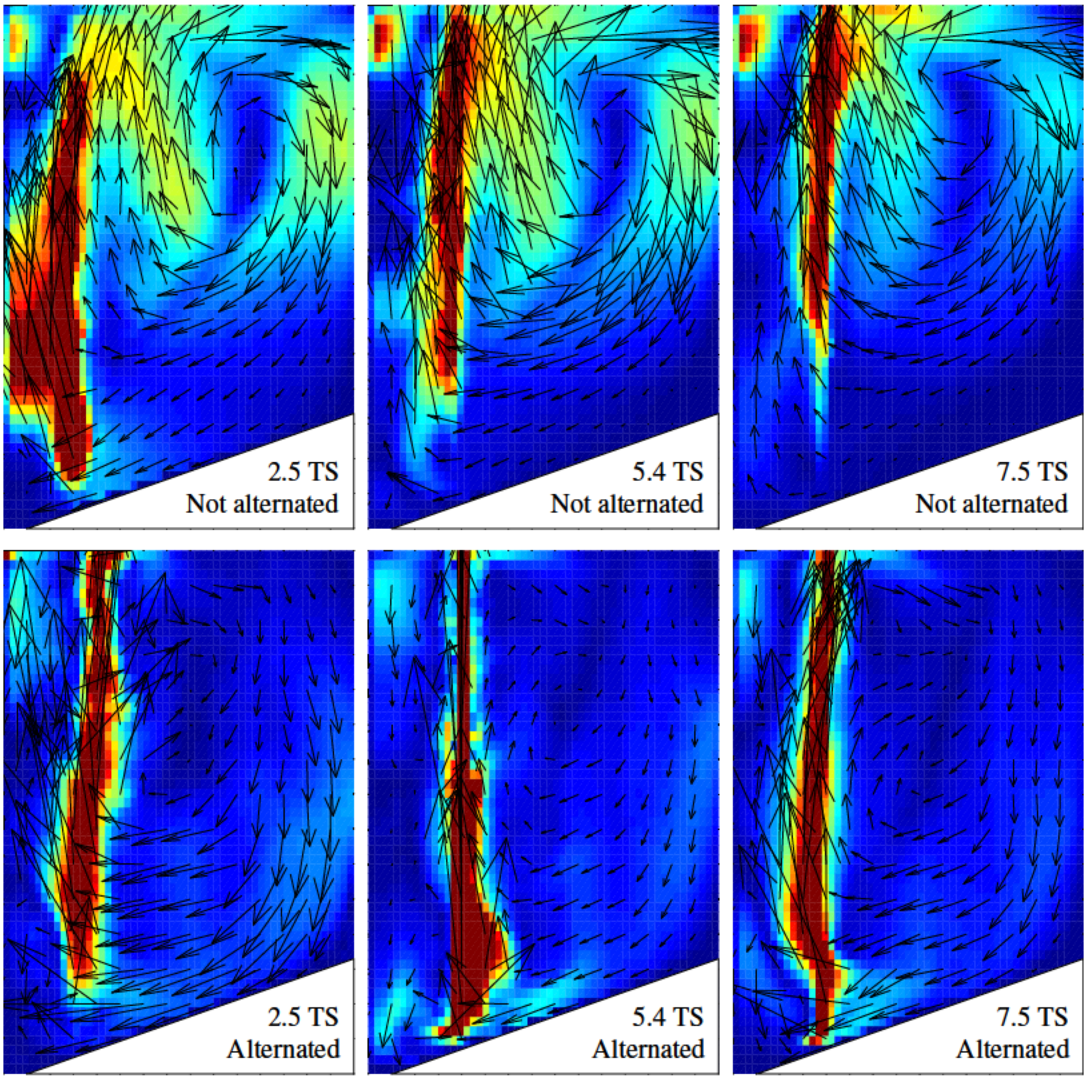

Figure 9.13 *Flow patterns for* $q = 0.5$ *with* $|\mathbf{u}| \in (0\,, 0.5)\ \mathrm{m\,s^{-1}}$ after 5 minutes. Nozzles switched every minute.

span of 5 minutes, in order to reproduce the effect of frequent switchings.

The effect of frequent switchings is depicted in Figure 9.13 (for the flow patterns), Figure 9.14 (viscosity patterns), and Figure 9.15 (shear rate magnitude patterns). The low-viscosity corridor corresponding to the descending vortex branch is absent when the nozzles are switched. However, the rapid switching of the nozzles leads to a deterioration of the mixing quality, the velocity and shear rate magnitude becoming substantially lower

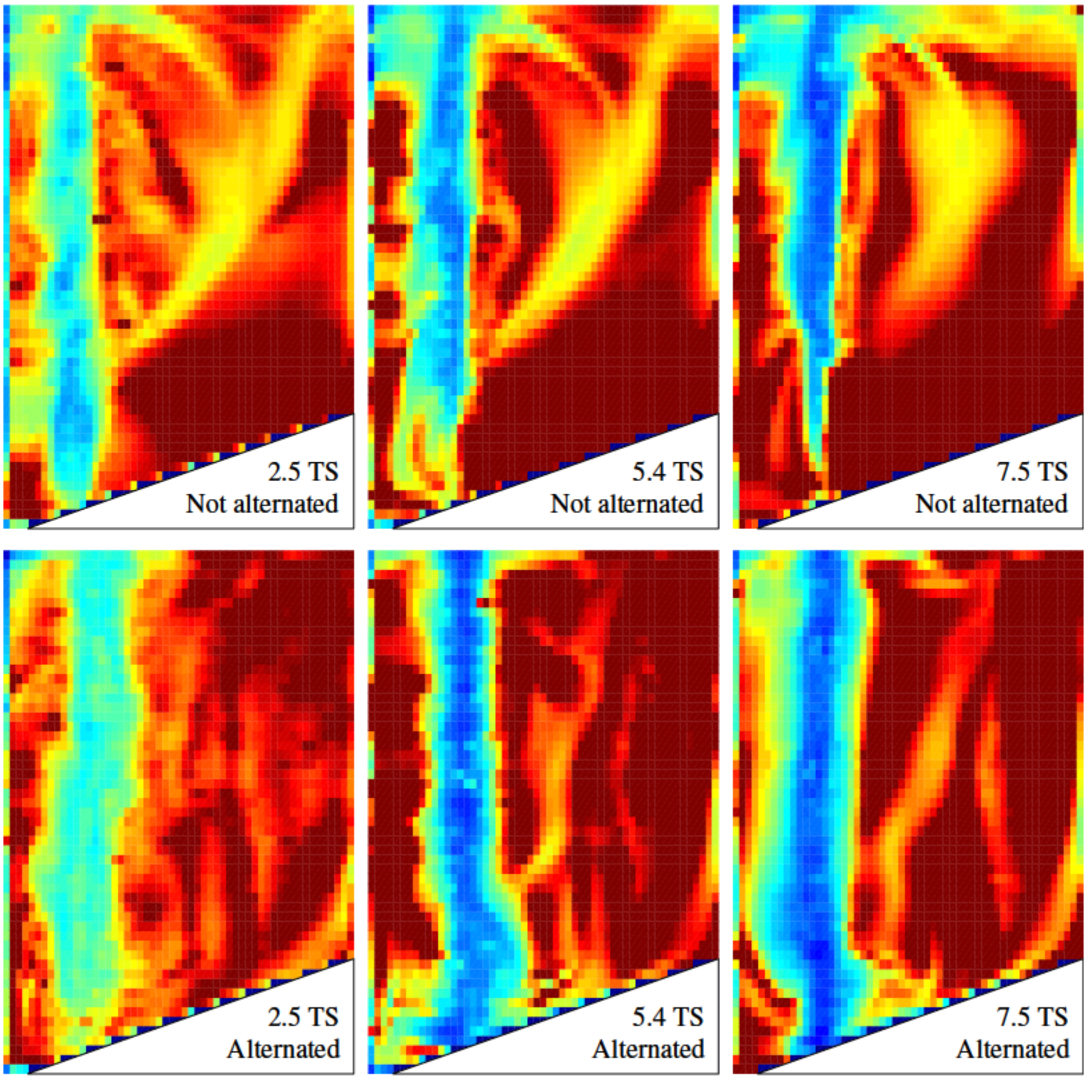

Figure 9.14 *Viscosity for* $q = 0.5$ *with* $\mu \in (0\,,0.1)$ *Pa s for the 2.5 TS runs,* $(0\,,0.6)$ *Pa s for the 5.4 TS runs,* $(0\,,2.0)$ *Pa s for the 7.5 TS runs* after 5 minutes. Nozzles switched every minute.

everywhere apart from the around the bubble column. This can be attributed to the fact that the system needs a non-zero time in order to develop flow patterns as the ones described in Sections 9.2 and 9.3. The time interval of one minute is evidently too short for the system to develop significant flow patterns. In general, however, this analysis cannot provide an answer on whether the mixing is improved or hindered when the injection is switched between the two nozzles series, and therefore a further investigation is necessary.

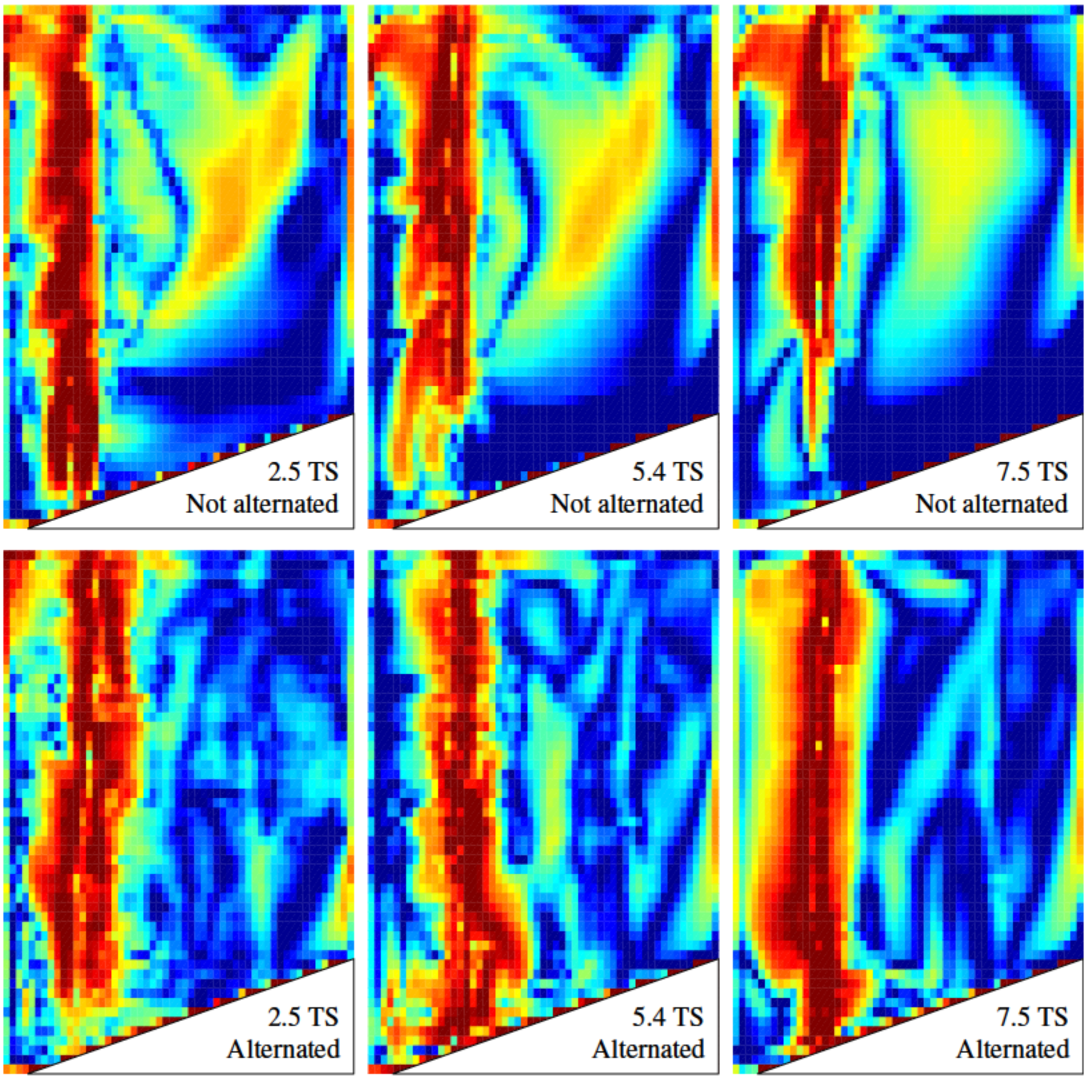

Figure 9.15 *Shear rate in logarithmic plot for* $q = 0.5$ *with* $\langle \dot{\gamma} \rangle \in \left(10^{-2}, 10^{0}\right)\ \mathrm{s}^{-1}$ after 5 minutes. Nozzles switched every minute.

A second analysis was performed in order to clarify the effectiveness of switching the biogas injection between two two nozzles series in terms of mixing. A non-diffusive tracer was defined, the concentration of which obeys to the follow equation:

$$\partial_t \chi + (\mathbf{u} \cdot \nabla)\, \chi = 0\,. \tag{9.1}$$

If, at the initial timestep, the tracer concentration is peaked in few spots inside the domain, a satisfactory level of mixing means that the concentration tends to become uniform through the whole domain. As the velocity flow patterns become less intense when total solids rises (Section 9.2), it is ito be expected that uniform concentration is more difficult to achieve in the 7.5% TS case. Therefore, it is reasonable to concentrate the attention on the 7.5% TS case. The setup described above consisting on switching the injecting nozzles every minute for a total time of five minutes was taken into consideration. In addition, another series of simulations was run, in which the nozzles were switched every five minutes, for a total time of fifteen minutes.

The results of both the setups are reported in Figure 9.16. The corresponding shear rate magnitude patterns are reported in Figure 9.17. The dimensionless concentration χ takes values between 0 and 1, the latter being the value at the four small squares at the start time. In the original (non-alternated) setup, the tracer is pushed down from its initial position and starts diffusing near the bottom of the tank. Then, it migrates towards the bubble column and is eventually spread through the upper parts of the domain. At that point, the diffusion tends to become more and more uniform through the whole domain due to the vortex. Higher values of χ on the sloping bottom of the tank indicate the existence of a stagnating zone just above the bottom of the tank. This is in agreement with Figures 9.2, 9.3 and 9.4, as the flow patterns are less intensive in the zone above the bottom of the tank.

When the nozzles are switched every minute, the tracer becomes much better distributed through the domain. This is in spite of the fact that switching the injection nozzles every minute brings to an attenuation of the velocity flow patterns, as indicated in Figure 9.13. This suggests that swiftly-changing yet not fully-developed flow patterns are more effective than fully-developed flow patterns for the purpose of mixing. Interestingly, the one-minute alterneted setup, which presents better mixing as explained above, also displays average shear rate patterns that are less intensive than the non alternated setup (Figure 9.17). This suggests that the average shear rate may not be the sole determinant parameter to classify

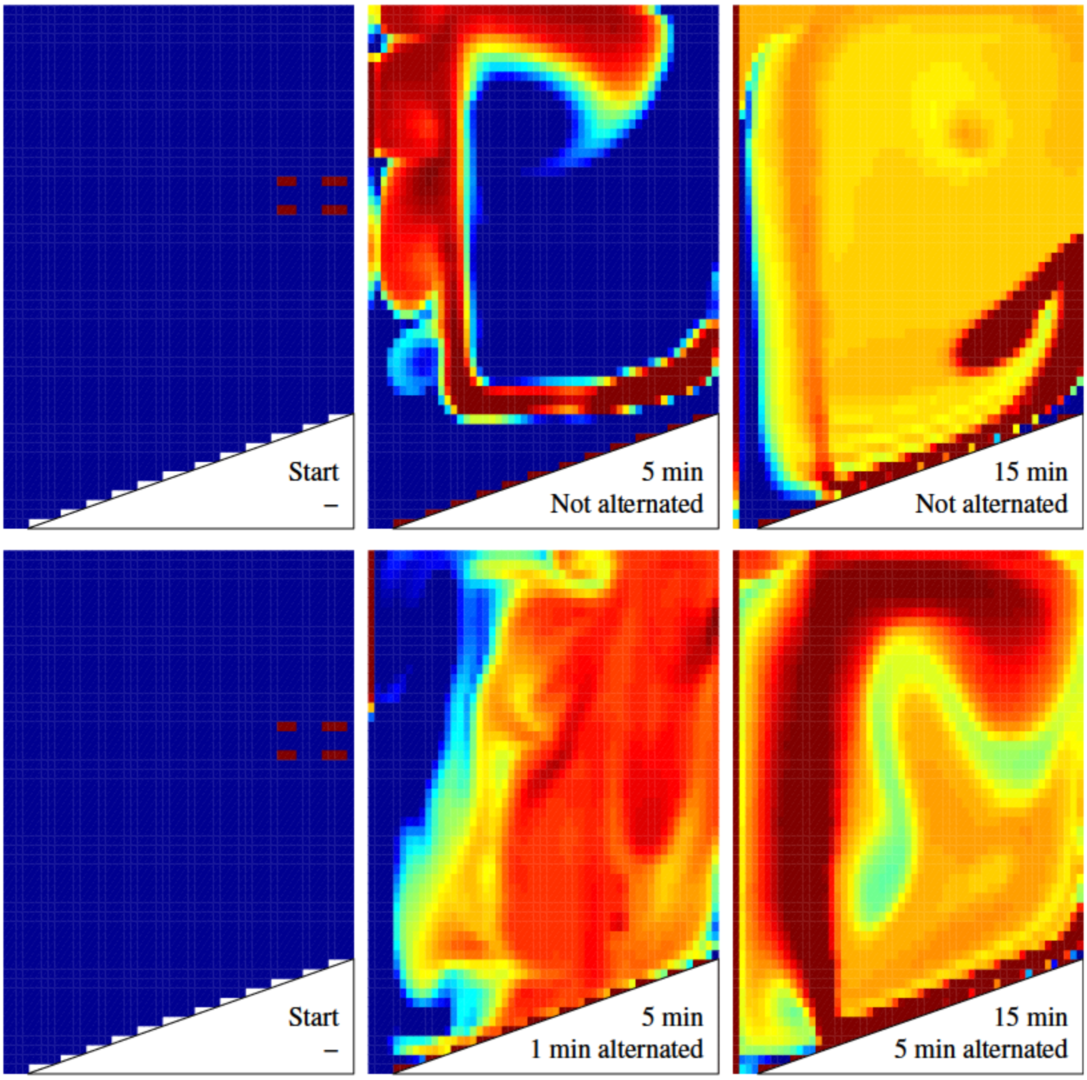

Figure 9.16 *Tracer concentration* χ *for* $q = 0.5$ *and 7.5% TS. Logarithmic plot with* $\chi \in \left(10^{-6}, 10^{-3}\right)$

the mixing quality.

Under a regime in which the nozzles are switched every five minutes, the advantages over the non-alternated setup are less clear. This is partially due to the fact that there is more time for the non-alternated simulation to achieve a quite uniform tracer distribution. In comparison with the non-alternated setup, the runs with switchings every five minutes do not display the zone of higher concentration at the lower external part of the tank; however,

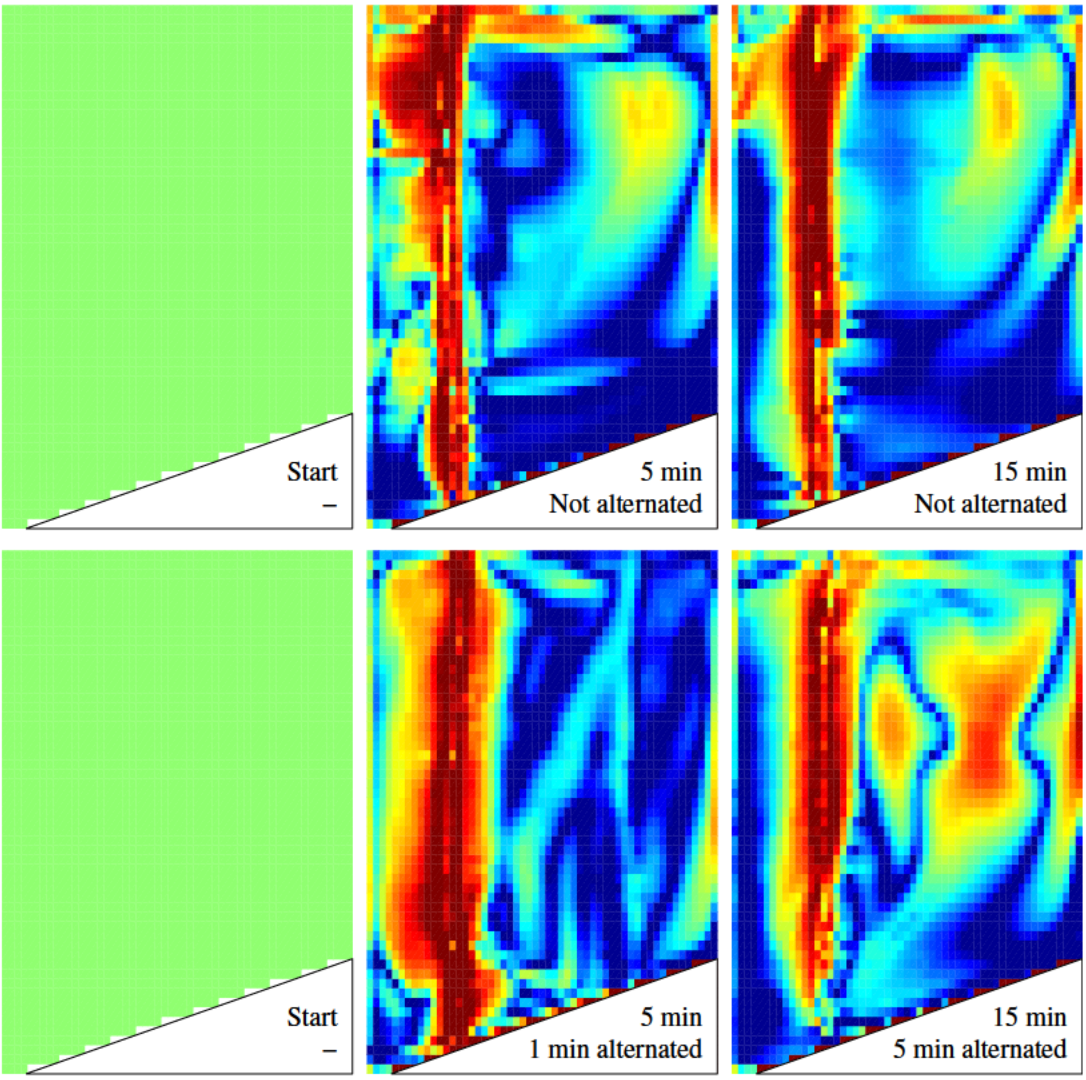

Figure 9.17 *Shear rate for* $q = 0.5$ *and 7.5% TS. Logarithmic plot with* $\langle\dot{\gamma}\rangle \in \left(10^{-2}, 10^{0}\right)$

it is not clear whether this corresponds to better mixing. Contrarily to the one-minute alternated case, the five-minutes alternated setup displays shear rate magnitude patterns that slightly are more intensive if compared to the non alternated setup.

By comparing the diffusion in the non-mixed case, the case in which the nozzles are alternated every minute, and the case with alternations every five minutes, it can be concluded that the frequent sweep flow pattern changes typical of the one minute-alternation setup produce better mixing, despite the attenuation of the flow patterns themselves. This appears to be particularly true in the short period (in the case taken into examination in this work, five minutes). It is therefore reasonable to postulate that, for a given input mixing power, sweeply changing flow patterns can achieve the same level of mixing of constant or slowly-variating flow patterns, but in less time. This means that sweeply-changing flow patterns should allow a reduction of the overall mixing time, thus saving energy.

10

Discussion

“As for me, all I know is that I know nothing.”

Socrates (399 BCE).
Apology

THE IMPORTANCE OF anaerobic digestion and renewable energy recovery in the wastewater industry is clear (Chapters 1 and 2), and the importance of mixing in that is widely recognised (Section 2.3). Work to move the state of the art in mixing design from empiricism to science has been reported in the literature, and CFD (Chapter 3) has been shown to be an invaluable tool in this regard, together with more conventional experimental work (Chapter 2). The progress is indeed noticeable, but much has still to be done to improve gas mixing. This lack of knowledge is principally due to the fact that the CFD work has been focussed on the easier task of modelling mechanical and recirculated mixing, and the difficulty of performing investigations and validations on a full-scale setup (Sections 2.5 and 3.7).

The purpose of the work undertaken in this thesis was to provide practical recommendations to improve mixing in a full-scale gas-mixed anaerobic digester, the definition of improved mixing adopted here being: same (or better) biogas yield, for a lower mixing energy input (Chapter 4). This has been done via a combined experimental direction and computational approach. The computational model was developed (Chapter 7), validated against the experimental results (Chapter 8) and applied to a full-scale design (Chapter 9). The elements of novelty and the key findings of this approach are discussed in Section 10.2

and 10.3 respectively, but before, the underlying assumptions of the model are reported in Section 10.1. The full-scale simulations facilitated the development of recommendations to enhance the performance of the design (Section 10.4).

10.1 Assumptions

In the development of the model, a number of assumptions were made and each of these assumptions are summarised and discussed below.

10.1.1 Multiphase Dynamics

Sludge is a complex mixture of water, biogas, flocculant and sedimenting debris, both organic and inert. The dimensions of such debris varies from molecules to sand and grit of approximately one millimetre. The dimension of the debris can grow up to some centimetres, if silage or food waste are added as in the case of agricultural digesters. In addition, gas bubbles are present in gas mixing.

Given the level of complexity, some simplifying assumptions were necessary for modelling. First, no information on scum or other floating matter is available from the industrial digesters used for full-scale modelling, and therefore flocculation was ignored for the sake of simplicity. Sedimentation in the digesters is known to take place over a timeframe of years. As the retention times do not exceed the time scale of one month, it appeared to be reasonable to ignore sedimentation. Finally, sludge in water industry is produced in settling basins, but wastewater is screened before entering these basins; therefore, it is reasonable to assume that the larger debris are removed, and only fragments of the order of one millimetre are present. As the computational mesh size was much larger and the trajectories of the single debris were of no interest in the analysis, it was natural to consider sludge as a single phase. The biogas bubbles constituted an obvious exception, as it was their motion that generated the sludge flow patterns.

These consideration can be synthesized in the points below.

MD1. Flocculation was ignored.

MD2. Sedimentation was ignored.

MD3. Sludge was considered as a two-phase fluid. A dispersed phase modelled the gas bubble, and a single continuous phase represented all the other components of sludge Throughout the work reported here, the term “sludge” implicitly identified the single continuous phase without the gas bubbles.

10.1.2 Continuous Phase

In Section 10.1.1, it was discussed that all the components of sludge (apart from the gas bubbles) could be approximated as a single, continuum phase. Given the predominance of water in the relative volume ratios, sludge was modelled as an incompressible fluid obeying the Navier-Stokes equations. In summary:

CP1. Sludge was modelled as an incompressible fluid (see Chapter 3 and Section 3.1 for details);

CP2. Sludge obeyed the Navier-Stokes Equations 3.1 and 3.2 (see Section 3.1 for details).

10.1.3 Sludge Rheology

The complex nature of sludge gives rise to a complex sludge rheology. In the work described here, the simplifying assumption of power-law viscosity was taken, and time-dependent behaviour was neglected:

SR1. Sludge obeyed the power-law model described in Equation 3.9 and the following discussion. The power-law index and consistency coefficient, as well as the intervals of validity, are reported in Table 5.1.

SR2. Thixotropic behaviour was ignored.

10.1.4 Dispersed Phase

The assumptions on the dispersed phase (gas bubbles) are described in detail in Section 7.1. In summary:

DP1. The dispersed phase was modelled as an ensemble of Lagrangian particles, each one obeying the Newton's second law (Equation 7.2);

DP2. bubble-bubble interactions were neglected, and a two-way coupling was adopted;

DP3. effects on fluid motion due to deformations of the bubble surface were neglected, and bubbles were considered as spherical;

DP4. bubbles were considered to be pointwise.

10.2 Elements of Novelty

Throughout the work described here, several elements of novelty have been introduced. The most relevant is the development of a novel Euler-Lagrange model for gas mixing in anaerobic digestion (Section 10.2.1). However, additional novelty is to be found in the process of experimental validation (Sections 10.2.2 and 10.2.3), and in the analysis of the full-scale data (Sections 10.2.4 and 10.2.5).

10.2.1 Euler-Lagrange Model

The most relevant element of novelty in the work reported here is the introduction of the first Euler-Lagrangian model to reproduce gas mixing in anaerobic digestion. It is clear that only a genuine two-phase model can reproduce the flow patterns accurately and reliably (Section 3.8), and the advantages of a Lagrangian model have been discussed (Section 7.1).

However, the scarcity of work on the topic, as well as the total absence of Euler-Lagrange modelling has been reported (Section 3.8). Consequently, the development of the model described in this thesis represents an important advance compared to the existing literature, and provides a new, effective tool of investigation for gas mixing in anaerobic digestion.

10.2.2 Laboratory-Scale Validation

The importance of validating a CFD model is well-recognized and has been described in Section 5.2. However, the difficulties of performing full-scale validations are well-known (Section 3.7). For this reason, rather than producing a genuine validation of a full-scale case, previous work offered laboratory-scale validation as a proof of the concept of the modelling approach. This is the approach followed by Wu (2010a). As explained in Section 5.2, validation of a scaled laboratory-scale case cannot be considered as a full-scale validation: correctly reproducing the flow patterns in a laboratory setup through dimensionless scaling is not sufficient as other issues, arising from the numerical nature of the problem, cannot be scaled. Such issues include the interaction between bubble size, number and behaviour, and meshing constraints. Nevertheless, a laboratory-scale case reproducing some of the most relevant characteristics of the full-scale setup is desirable in order to produce a more credible proof of concept.

In this respect, the two approaches of dimensionless scaling on one side, and reproducing the physical values of viscosity and input mixing power per unit of volume on the other, were discussed in Section 5.2. The latter was chosen due to the more credible reproduction of the bubble-mesh interaction and the possibility of testing the novel modelling approach under greater stress.

This approach towards robust laboratory-scale validation constitutes an advance in CFD modelling. Previous work, such as Wu (2010a), did not consider the problem at all; rather, performed laboratory-scale tests on systems which were completely different form the full-scale case of interest. Other authors, such as Karim et al. (2004, 2005b), adopted a simplistic approach which consisted of merely conforming to directives (U.S. EPA, 1979), without investigating their relevance to the real world.

For the future, no further laboratory-scale validations involving the reproduction of physical quantities appear to be useful, as the laboratory-scale validation described here already tested the modelling approach under the most adverse circumstances from a numerical point of view. Conversely, the application of the dimensionless scaling approach will be desirable to further confirm the robustness of the model. In this respect, a pilot-size validation (tank volume of $\sim 1\ \mathrm{m}^3$) will help covering the research gap in pilot-scale experiments for anaerobic digestion.

10.2.3 PEPT and Comparison with PIV

The experimental work presented an element of novelty as for the first time the PEPT technique was used to measure the flow patterns in unconfined gas mixing for anaerobic digestion. Karim et al. (2004) had already applied a radiative tracer technique (the CARPT, see Section 3.8) to gas mixing in anaerobic digestion, but their analysis was limited to confined mixing. It was not possible to solve the issue of occasional absence of tracer passages through certain areas by increasing the experiment time such as in Karim et al. (2004). Rather, the novel approach of comparing the data of a tracer technique (the PEPT) with the results of an imaging technique (the PIV), was proposed. This approach allowed the limitations of one technique to be compensated for by the strengths of the other, and constituted a novel approach compared to Karim et al. (2004).

10.2.4 Shear Rate Magnitude and Input Mixing Power

In the work described here, an analysis of the shear rate was performed. Other authors, such as Wu (2010b,c); Craig et al. (2013), performed similar investigations, but the work described here provides the first example of shear rate being used as an indicator to determine the mixing efficiency in terms of mixing power, unlike previous works, e.g. Wu (2010b,c); Craig et al. (2013), that limited their analyses to comparing the different setups of the impellers.

A novel approach to determine the optimum input mixing power was introduced in Section 9.4. The approach followed was to divide the domain into zones depending on the relative shear rate magnitude, and to compare the relative volumes of the zones. The optimum input mixing power was determined by a comparison between the relative volumes of very low, low and average shear rate magnitude.

10.2.5 Viscosity Patterns

A further element of novelty in the full-scale analysis consists of the study of the viscosity patterns (section 9.3). The non-Newtonian behaviour of sludge has been an object of investigation of previous work, but this is the first time that it has been accounted for in the context of of enhancing mixing, and it is the first time that apparent viscosity plots have been provided. Wu and Chen (2008) showed that simulations performed with Newtonian and non-Newtonian fluids give rise to totally different flow patterns and underlined the importance of reproducing the sludge rheology, but did not present a strategy to improve mixing.

The introduction of an analysis based on low-viscosity corridors, together with the strategy of switching between nozzles series, follows the idea, carried on in this thesis, of broadening the analysis of mixing to parameters which are not directly referred to the flow patterns and the average shear rate. This approach is justified by the presence of further layers of complexity due to the non-Newtonian nature of sludge. As the level of complexity increases, it is natural to introduce different kinds of analysis: therefore, it is fruitful to support the analysis of the flow patterns with a study of the apparent viscosity and the low-viscosity corridors, and a description of the diffusion of a passive tracer.

10.3 Key Findings

The work reported here produced a number of finding concerning mixing in a full-scale digester. Such findings can be listed as follows.

1. An ideal value for input mixing power was provided.
2. The criterion for optimum mixing power of of 50-80 s^{-1} suggested by Tchobanoglous et al. (2010) should be reconsidered.
3. The existence of low-viscosity, short-circuited flow corridors was demonstrated.
4. A mitigation strategy to mitigate the detrimental effect of the aforementioned low-viscosity corridors on mixing was developed.

The first two findings are discussed in Section 10.3.1; the latter two in Section 10.3.2.

10.3.1 Input Mixing Power and Criterion for Mixing

The novel shear rate analysis described in Section 9.4 provided for the first time an ideal value for the input mixing power. Such value was found to be around 1 s^{-1}. This value was found to be much less than both the values suggested by Tchobanoglous et al. (2010) and the values found in the laboratory-scale setups described in this (Chapter 8) and other work (Bridgeman, 2012; Sindall et al., 2013), and nevertheless the simulations reproduced a working digester.

In conclusion, both in laboratory and in full, industrial-scale digesters, the flow patterns are characterized by average shear rates which are much lower than the values recommended by Tchobanoglous et al. (2010), and nevertheless this fact does not hinder the biogas production. This is in line with the conclusions of Bridgeman (2012); Sindall et al.

(2013); in addition, it was found that the typical average shear rate values inside a full-scale digester are an order of magnitude smaller than the values in a laboratory-scale setup. Therefore, the criterion for a proper mixing suggested by Tchobanoglous et al. (2010) should be reconsidered.

10.3.2 Low-Viscosity Corridors and Mitigating Strategy

The analysis of the viscosity patterns (Section 9.3) evidenced the existence of low-viscosity, short-circuited flow corridors for the first time. Their detrimental effect on mixing was described in Section 9.5, and a strategy aimed at mitigating it was introduced.

The mitigation strategy consisted of switching biogas injection between two nozzles series. As reported in Section 2.4, the literature has already compared alternated with continuous mixing. However, the concept of switching the biogas injection between two nozzles series as presented here differs from the alternate mixing studied in the literature previously, because the former is compatible with both alternate and continuous mixing. For instance, it is possible to switch between each nozzle series every five minutes with no dead time, thus achieving continuous mixing. Alternatively, it is possible to switch between the nozzles series every five minutes for an overall time of twenty minutes, and then cease injection for forty minutes, thus achieving an alternated mixing with twenty minutes of mixing and forty minutes of non-mixing.

A first analysis based on the investigation of shear rate patterns did not produce clear results. This fact showed that the analysis of shear rate alone is not sufficient to provide a clear description of mixing under complex rheologic properties. It is for this reason that the passive, non-diffusive tracer was defined. Further investigation confirmed that rapid switching has a positive effect on the mixing quality. It is less clear whether such positive effect remains when the switching time is longer (five minutes), but it is reasonable to assert that switching between nozzles series can have a positive effect also when the period is of five minutes—at least, to achieve comparable levels of mixing in less time.

10.4 Recommendations to Enhance Performance of a Gas-Mixed Digester

Writing a series of recommendations addresses the knowledge gap described in Section 2.5, in a practical and immediately usable way. Furthermore, due to the relevance of the subject in terms of potential economic saving and reduced carbon footprint (e.g., Chapter 1), it is worthwhile to address the topic in terms that are immediately usable as design parameters.

These recommendations were produced from a specific industrial digester, and therefore they are specific for that setup. However, it is reasonable to suppose that it is possible to produce similar prescriptions for any specifc design. Hence, the recommendations given here for a specific design can be interpreted as a basics upon which to create specific recommendation for any different design.

- Gas input power around $1\ \mathrm{W\,m^{-3}}$. As discussed in Section 9.4, the distribution of average shear rate values is noticeably affected if the gas input power falls below such value, but represents only a marginal increase of input power.

- Switch biogas injection between two different nozzle series at regular time intervals. As discussed in Section 9.5, the mixing quality benefitted undoubtedly from one-minute switching, while the benefit was less clear in five-minutes switching. A conservative estimate suggests switching biogas injection at least every 3 minutes.

11

Conclusions

> *"All is impermanent."*
>
> Shakyamuni Buddha (c. 563-483 BCE).
>
> Sutta Nipata

The first Euler-Lagrangian model for gas mixing in anaerobic digestion was developed and implemented in Chapter 7 and then validated (Chapter 8) against the outcome of PIV and PEPT experiments (Chapter 6). The model was proved to be robust and affordable even in the most adverse circumstances—that is, bubble sizes not negligible when compared with cells size. Care must be adopted in choosing the appropriate mesh resolution. On one hand, a larger cell number is required when simulating larger gas flow rates or less dense solutions. On the other hand, too refined meshes (e.g. when mesh size becomes smaller than bubble size) can give rise to unfaithful results. Consequently, when using this model, a preliminary grid-independence test should be performed in order to find a balance between the two aspects described above.

Laboratory-scale digesters introduced in the previous literature produce input mixing energy values significantly higher than the typical values of full-scale digester, and therefore cannot faithfully reproduce the dynamics of a real plant (Section **??**). The design criteria for laboratory-scale digesters should be changed accordingly. A new design criterion in which input mixing power of a full-scale plant is implemented leads to comparable average shear rate. This criterion was applied in this work, as described in Section 5.2. As a consequence, the laboratory-scale experimental apparatus described in this study was able to reproduce the full-scale average flow rate values.

VISCOSITY FLOW patterns were observed and described in Section 9.3, and the detrimental effect on mixing was discussed. A mitigation strategy, consisting in switching biogas injection between two different nozzle series a regular time interval, was formulated and discussed in Section 9.5. It was shown that such strategy manages to improve the quality of mixing, with shorter time intervals being more effective than larger ones. It was suggested a time interval of 3 minutes or less should be implemented.

A BALANCE BETWEEN medium and very low shear rates led to the conclusion that input mixing power in the full-scale digester described in Section 5.2 and Table 5.2 can be reduced down to 1 $\mathrm{W\,m^{-3}}$ without detrimental effects in terms of mixing efficiency.

THE CRITERION FOR a good mixing defined in the classical literature and consisting of a minimum average shear rate of 50-80 s^{-1} was already called into question by more recent work. In this thesis, it was shown that such criterion is not appropriate to describe a good mixing. Instead, a more thorough analysis, which better reflects the complexity of a flow with shear rates of different orders of magnitude coexisting together, was applied. Such analysis comprised an analysis of the viscosity flow patterns, the subdivision of the computational domain into zones depending on both the particular geometry taken into consideration and the order of magnitude of the shear rate, and the simulation of the spreading of a scalar passive tracer. All these techniques proved to be successful in describing the flow more accurately and in classifying the effectiveness of mixing.

IN CONCLUSION, it was shown that CFD is an effective and reliable tool to describe the flow patterns in a full-scale digester and give indication on how to improve its efficiency based on recommendations that can be immediately applied to industrial design and run. Such recommendations consist of defining two parameters—the gas input power and the injection switching period—and define an ideal value for them. In order to give a precise picture of a given digester, the CFD work should be performed with the specific desig taken into consideration, but the values of mixing input power and switching period given in this thesis can be used both as a starting point and as a matter of comparison.

12

Recommendations for Further Work

Chekov: "Course heading, Captain?"

Kirk: "Second star to the right and straight on till morning."

Star Treck VI (inspired by Peter Pan)

BUBBLE DIAMETER is an input parameter of the theoretical model presented in this work, as explained in Sections 7.2 and 7.6. Moreover, it was showed in Chapter 9 that the flow patterns depend on bubble size. However, the issue of measuring the bubble size in a real digester has not yet been addressed in the literature. This problem was dealt with by performing simulations with diverse bubble sizes, and it was showed in Chapter 9 that its impact was marginal. Therefore, the recommendations for mixing efficiency hold irrespective of the bubble size. However, it is possible that the results may have been improved if a distribution of bubble diameters was provided. For this reason, experimental studies aimed at measuring the bubble diameter in a gas-mixed anaerobic digester are desirable. This may be realised, for instance, by placing a camera inside an industrial digester, one or two metres above a nozzle. The camera should be appropriately protected by the sludge by placing it inside a sealed, transparent container. A small LED lamp should provide the necessary source of light. However, careful planning would be required because the instalment of this device would require the closing-down of a plant, and work would be necessary to instal the camera with a protective container together with a power cable.

STRICTLY SPEAKING, the CFD model reported here is validated only against systems of the dimension of the experimental rig used, that is $4\ \ell$. Even though the model performed well enough to be considered for full-scale application, further research may seek to validate it against a larger experimental apparatus (say of about $1\ \mathrm{m}^3$ volume) in order to provide a higher level of confidence to the model.

ONLY ONE GEOMETRY for the full-scale simulations was tested in the present work. A much more complete analysis would be obtained by optimizing the average shear rate over a set of geometric variables, e.g. volume, inclination of the bottom, height over external diameter ratio, internal over external diameter ratio. Further research work may be performed in this direction.

SOME ARGUMENTS presented in this thesis suggest that the average shear rate and a good mixing may be decoupled under certain cirumstances—that is, mixing quality may be improved and at the same time the average shear rate magnitude may decrease. For instance, the one-minute switched mixing setup showed a better mixing degree and lower value of the shear rate magnitude if compared with the non-switched setup (Section 9.5, and in particular, Figures 9.16 and 9.17). Furthermore, the generally low values of the shear rate magnitude field reported in Chapter 9 may suggest that, for a full-scale anaerobic digester, good mixing does not mean turbulent mixing. However, further research is necessary to confirm these statements. In particular, no analysis has been carried out in this thesis on the average shear rate immediately after switching the nozzles. And as regards the turbulent mixing, it must be considered that it is far from trivial to define a degree of turbulence for a given digester setup: as many different orders of magnitude of shear rate and velocity magnitude coexist at the same time it would not be appropriate to define a global turbulence parameter such as the Reynolds number. Instead, an analysis of the turbulence intensity field, defined as $I(\mathbf{x}) \equiv \tilde{\mathbf{u}}(\mathbf{x}) \,/\, \langle \mathbf{u} \rangle(\mathbf{x})$, should be necessary.

COUPLING THE FLUID mechanics with a computational model aimed at reproducing the biochemical reaction chain of the anaerobic digestion would give a much clear and direct connection between input mixing energy and output biogas yield. This attempt has been realized only in Wu (2012b), and for the sole case of impeller-driven mixing. Similarly, the model introduced in this work may be successfully coupled with a biochemical model such as the one described in Rosen et al. (2006).

THE FIRST TASK of a CFD-biochemistry coupled model should be to give a deeper insight in the roles of diffusion and laminar advection in full-scale nutrients spreading. First, a series of simulations with no mixing and different tank volumes may be run in order to estimate the maximum volume at which no significant decrease in biogas yield is observed. This volume could be recognized as the maximum volume at which the sole diffusion is enough to provide a satisfactory nutrients spreading and therefore satisfactory conditions for anaerobic digestion. Then, the same procedure may be repeated with the introduction of mixing at a fixed input mixing energy. The aim will be once again to identify the maximum tank volume at which no significant drop in biogas production is observed. Such a volume can be identified as the maximum volume at which diffusion together with the chosen input mixing energy can provide satisfactory conditions with anaerobic digestion. The final aim of this study should be to provide a relationship between maximum volume for satisfactory anaerobic digestion and input mixing energy.

Bibliography

Achkari-Begdouri, A. and Goodrich, P. R. (1992). Rheological properties of dairy cattle manure. *Bioresource technology*, 40:149–156, ISSN 0960-8524, doi:10.1016/j.biortech.2004.06.020.

Agler, M. T., Aydinkaya, Z., Cummings, T. A., Beers, A. R., and Angenent, L. T. (2010). Anaerobic digestion of brewery primary sludge to enhance bioenergy generation: A comparison between low- and high-rate solids treatment and different temperatures. *Bioresource Technology*, 101(15):5842–5851, ISBN 0960-8524, ISSN 09608524, doi:10.1016/j.biortech.2010.03.023.

Ahring, B., Alatriste-Mondragon, F., Westermann, P., and Mah, R. (1991). Effects of cations on Methanosarcina thermophila TM-1 growing on moderate concentrations of acetate: production of single cells. *Applied Microbiology and Biotechnology*, 35(5), ISSN 0175-7598, doi:10.1007/BF00169638.

Allen, D. G. and Robinson, C. W. (1990). Measurement of Rheological Filamentous Fermentation Properties Broths. *Chemical Engineering Science*, 45(1):37–48.

Amanullah, A., Buckland, B. C., and Nienow, A. W. (2003). Mixing in the fermentation and cell culture industries. In Paul, E. L., Atiemo-Obeng, V. A., and Kresta, S. M., editors, *Handbook of industrial mixing*, chapter 18. John Wiley & Sons, Inc., Hoboken, NJ, USA, ISBN 0471269190, doi:10.1002/0471451452.ch18.

Andersson, B., Andersson, R., Håkansson, L., Mortensen, M., Defence, N., Sudiyo, R., and van Wachem, B. (2012). *Computational Fluid Dynamics for Engineers*. Cambridge University Press, ISBN 9781139093590.

ANSYS (2012). *ANSYS FLUENT 14.5 Theory Guide*. ANSYS, Inc.

Appels, L., Baeyens, J., Degrève, J., and Dewil, R. (2008). Principles and potential of the anaerobic digestion of waste-activated sludge. ISBN 0360-1285, ISSN 03601285, doi:10.1016/j.pecs.2008.06.002.

Arrhenius, S. (1889). *Über die Dissociationswärme und den Einfluss der Temperatur auf den Dissociationsgrad der Elektrolyte*. Wilhelm Engelmann, Leipzig.

Auty, D. and Marquet, R. (2009). Digester Mixing - Industry Overview. Technical report.

Barnes, H. A. (1997). Thixotropy - A review. *Journal of non_Newtonian fluid mechanics*, 70(97):1–33, ISSN 03770257, doi:10.1016/S0377-0257(97)00004-9.

Baudez, J. C., Slatter, P., and Eshtiaghi, N. (2013). The rheological behaviour of anaerobic digested sludge. *Chemical Engineering Journal*, 215-216(17):182–187, ISBN 1385-8947, ISSN 13858947, doi:10.1016/j.cej.2012.10.099.

Brade, C. E. and Noone, G. P. (1981). Anaerobic sludge digestion: Need it be expensive? Making more of existing resources. ISSN 0043129X.

Bridgeman, J. (2012). Computational fluid dynamics modelling of sewage sludge mixing in an anaerobic digester. *Advances in Engineering Software*, 44(1):54–62, ISSN 09659978, doi:10.1016/j.advengsoft.2011.05.037.

Bugay, S., Escudié, R., and Liné, A. (2002). Experimental analysis of hydrodynamics in axially agitated tank. *AIChE Journal*, 48(3):463–475, ISSN 00011541, doi:10.1002/aic.690480306.

Cabirol, N., Barragán, E. J., Durán, A., and Noyola, A. (2003). Effect of aluminium and sulphate on anaerobic digestion of sludge from wastewater enhanced primary treatment. *Water science and technology : a journal of the International Association on Water*

Pollution Research, 48(6):235–240, ISBN 0273-1223 (Print)\r0273-1223 (Linking), ISSN 0273-1223.

Camp, T. R. and Stein, P. C. (1943). Velocity gradients and internal work in fluid motion. *Journal of the Boston Society of Civil Engineering*, 85:218–237.

Casson, N. (1959). A flow equation for pigment-oil suspensions of the printing ink type. In Mills, C. C., editor, *Rheology of Disperse Systems*, chapter 5, pages 84–104. Pergamon Press, Oxford.

Celik, I. B., Ghia, U., Roache, P. J., Freitas, C. J., Coleman, H., and Raad, P. E. (2008). Procedure for Estimation and Reporting of Uncertainty Due to Discretization in CFD Applications. *Journal of Fluids Engineering*, 130(7):078001, ISSN 00982202, doi:10.1115/1.2960953.

Chae, K. J., Jang, A., Yim, S. K., and Kim, I. S. (2008). The effects of digestion temperature and temperature shock on the biogas yields from the mesophilic anaerobic digestion of swine manure. *Bioresource Technology*, 99(1):1–6, ISBN 09608524, ISSN 09608524, doi:10.1016/j.biortech.2006.11.063.

Chen, Y., Cheng, J. J., and Creamer, K. S. (2008). Inhibition of anaerobic digestion process: A review. *Bioresource Technology*, 99(10):4044–4064, ISBN 0960-8524 (Print)\n0960-8524 (Linking), ISSN 09608524, doi:10.1016/j.biortech.2007.01.057.

Cholette, A. and Cloutier, L. (1959). Mixing efficiency determinations for continuous flow systems. *The Canadian Journal of Chemical Engineering*, 37(3):105–112, ISSN 00084034, doi:10.1002/cjce.5450370305.

Clark, M. M. (1985). Critique of Camp and Stein's RMS velocity gradient. *Journal of Environmental Engineering*, I(6):741–754.

Conklin, A., Stensel, H. D., and Ferguson, J. (2006). Growth kinetics and competition between Methanosarcina and Methanosaeta in mesophilic anaerobic digestion. *Water environment research : a research publication of the Water Environment Federation*, 78(5):486–496, ISBN 1061-4303, ISSN 1061-4303, doi:10.2175/106143006X95393.

Coufort, C., Bouyer, D., and Liné, A. (2005). Flocculation related to local hydrodynamics in a Taylor-Couette reactor and in a jar. *Chemical Engineering Science*, 60(8-9):2179–2192, ISBN 0009-2509, ISSN 00092509, doi:10.1016/j.ces.2004.10.038.

Craig, K. J., Nieuwoudt, M. N., and Niemand, L. J. (2013). CFD simulation of anaerobic digester with variable sewage sludge rheology. *Water Research*, 47(13):4485–4497, ISBN 1879-2448 (Electronic) 0043-1354 (Linking), ISSN 00431354, doi:10.1016/j.watres.2013.05.011.

Daly, B. J. and Harlow, F. H. (1970). Transport Equations in Turbulence. *Physics of Fluids*, 13(11):2634–2649, ISSN 00319171, doi:10.1063/1.1692845.

De Bok, F. A. M., Plugge, C. M., and Stams, A. J. M. (2004). Interspecies electron transfer in methanogenic propionate degrading consortia. *Water Research*, 38(6):1368–1375, ISBN 0043-1354, ISSN 00431354, doi:10.1016/j.watres.2003.11.028.

Deen, N. G., van Sint Annaland, M., and Kuipers, J. A. M. (2004). Multi-scale modeling of dispersed gas-liquid two-phase flow. *Chemical Engineering Science*, 59(8-9):1853–1861, ISBN 0009-2509, ISSN 00092509, doi:10.1016/j.ces.2004.01.038.

Dewsbury, K., Karamanev, D., and Margaritis, a. (1999). Hydrodynamic characteristics of free rise of light solid particles and gas bubbles in non-Newtonian liquids. *Chemical Engineering Science*, 54(21):4825–4830, ISSN 00092509, doi:10.1016/S0009-2509(99)00200-6.

Eshtiaghi, N., Yap, S. D., Markis, F., Baudez, J. C., and Slatter, P. (2012). Clear model fluids to emulate the rheological properties of thickened digested sludge. *Water Research*, 46(9):3014–3022, ISSN 00431354, doi:10.1016/j.watres.2012.03.003.

Fan, X., Parker, D. J., and Smith, M. (2006). Labelling a single particle for positron emission particle tracking using direct activation and ion-exchange techniques. *Nuclear Instruments and Methods in Physics Research Section A: Accelerators, Spectrometers, Detectors and Associated Equipment*, 562(1):345–350, ISSN 01689002, doi:10.1016/j.nima.2006.03.015.

Frisch, U. (1995). *Turbulence*. Cambridge University Press.

Gerardi, M. H. (2003). *The microbiology of anaerobic digesters*. Wiley, ISBN 3175723993, ISSN 03043894, doi:10.1002/0471468967.

Gibson, M. M. and Launder, B. E. (1978). Ground effects on pressure fluctuations in the atmospheric boundary layer. *Journal of Fluid Mechanics*, 86:491–511, ISSN 0022-1120, doi:10.1017/S0022112078001251.

Gómez, X., Cuetos, M. J., Cara, J., Morán, a., and García, a. I. (2006). Anaerobic co-digestion of primary sludge and the fruit and vegetable fraction of the municipal solid wastes. Conditions for mixing and evaluation of the organic loading rate. *Renewable Energy*, 31(12):2017–2024, ISBN 0960-1481, ISSN 09601481, doi:10.1016/j.renene.2005.09.029.

Greenshields, C. J. (2015a). OpenFOAM Programmer's Guide. Technical Report May, OpenFOAM Foundation Ltd.

Greenshields, C. J. (2015b). OpenFOAM User Guide. Technical Report May, OpenFOAM Foundation Ltd.

Guibaud, G., Dollet, P., Tixier, N., Dagot, C., and Baudu, M. (2004). Characterisation of the evolution of activated sludges using rheological measurements. *Process Biochemistry*, 39(11):1803–1810, ISSN 00329592, doi:10.1016/j.procbio.2003.09.002.

Hanjalic, K. and Launder, B. E. (1972). A Reynolds stress model of turbulence and its application to thin shear flows. ISBN 9054101504, ISSN 0022-1120, doi:10.1017/S002211207200268X.

Hoffmann, R. A., Garcia, M. L., Veskivar, M., Karim, K., Al-Dahhan, M. H., and Angenent, L. T. (2008a). Effect of shear on performance and microbial ecology of continuously stirred anaerobic digesters treating animal manure. *Biotechnology and Bioengineering*, 100(1):38–48, ISBN 0006-3592, ISSN 00063592, doi:10.1002/bit.21730.

Hoffmann, R. A., Garcia, M. L., Vesvikar, M. S., Karim, K., Al-Dahhan, M. H., and Angenent, L. T. (2008b). Effect of shear on performance and microbial ecology of continuously stirred anaerobic digesters treating animal manure. *Biotechnology and Bioengineering*, 100(1):38–48, ISBN 0006-3592, ISSN 00063592, doi:10.1002/bit.21730.

Jackson-Moss, C. A. and Duncan, J. R. (1991). The effect of aluminium on Anaerobic digestion. *Biotechnology Letters*, 13(2):143–148, ISSN 0141-5492, doi:10.1007/BF01030466.

Jackson-Moss, C. A., Duncan, J. R., and Cooper, D. R. (1989). The effect of calcium on anaerobic digestion. *Biotechnology Letters*, 11(3):219–224, ISSN 0141-5492, doi:10.1007/BF01026064.

Janssen, P. H. (2003). Selective enrichment and purification of cultures of Methanosaeta spp. *Journal of Microbiological Methods*, 52(2):239–244, ISBN 0167-7012, ISSN 01677012, doi:10.1016/S0167-7012(02)00181-1.

Jones, W. and Launder, B. (1972). The prediction of laminarization with a two-equation model of turbulence. *International Journal of Heat and Mass Transfer*, 15(2):301–314, ISSN 00179310, doi:10.1016/0017-9310(72)90076-2.

Joshi, J., Elias, C., and Patole, M. (1996). Role of hydrodynamic shear in the cultivation of animal, plant and microbial cells. ISSN 09230467, doi:10.1016/0923-0467(95)03062-X.

Kaparaju, P., Buendia, I., Ellegaard, L., and Angelidakia, I. (2008). Effects of mixing on methane production during thermophilic anaerobic digestion of manure: Lab-scale and pilot-scale studies. *Bioresource Technology*, 99(11):4919–4928, ISBN 0960-8524, ISSN 09608524, doi:10.1016/j.biortech.2007.09.015.

Karim, K., Hoffmann, R. A., Klasson, K. T., and Al-Dahhan, M. H. (2005a). Anaerobic digestion of animal waste: Effect of mode of mixing. *Water Research*, 39(15):3597–3606, ISBN 0043-1354, ISSN 00431354, doi:10.1016/j.watres.2005.06.019.

Karim, K., Hoffmann, R. A., Klasson, K. T., and Al-Dahhan, M. H. (2005b). Anaerobic digestion of animal waste: Waste strength versus impact of mixing. *Bioresource Technology*, 96(16):1771–1781, ISSN 09608524, doi:10.1016/j.biortech.2005.01.020.

Karim, K., Klasson, K. T., Hoffmann, R. A., Drescher, S. R., DePaoli, D. W., and Al-Dahhan, M. H. (2005c). Anaerobic digestion of animal waste: Effect of mixing. *Bioresource Technology*, 96(14):1607–1612, ISBN 0960-8524, ISSN 09608524, doi:10.1016/j.biortech.2004.12.021.

Karim, K., Thoma, G. J., and Al-Dahhan, M. H. (2007). Gas-lift digester configuration effects on mixing effectiveness. *Water Research*, 41(14):3051–3060, ISSN 00431354, doi:10.1016/j.watres.2007.03.042.

Karim, K., Varma, R., Vesvikar, M. S., and Al-Dahhan, M. H. (2004). Flow pattern visualization of a simulated digester. *Water Research*, 38(17):3659–3670, ISSN 00431354, doi:10.1016/j.watres.2004.06.009.

Kennedy, P. K. and Zheng, R. (2013). *Flow Analysis of Injection Molds*. Hanser, ISBN 978-1-56990-512-8, doi:10.3139/9781569905227.

Kim, J., Moin, P., and Moser, R. (1987). Turbulence statistics in fully developed channel flow at low Reynolds number. *Journal of Fluid Mechanics*, 177:133–166, ISSN 0022-1120, doi:10.1017/S0022112087000892.

Kolmogorov, A. N. (1991a). Dissipation of energy in the locally isotropic turbulence. *Proceedings of the Royal Society of London, A*, 434:15–17.

Kolmogorov, A. N. (1991b). The equations of turbulent motion in an incompressible fluid. In Tikhomirov, V. M., editor, *Selected works of Andrej N. Kolmogorov Volume 1: Mathematics and Mechanics*. Springer, ISBN 978-94-010-5347-1, doi:10.1007/978-94-011-3030-1.

Kolmogorov, A. N. (1991c). The local structure of turbulence in incompressible viscous fluid with very large Reynolds numbers. *Proceedings of the Royal Society of London, A*, 434:9–13.

Kugelman, I. J. and Chin, K. K. (1971). Toxicity, synergism, and antagonism in anaerobic waste treatment processes. In Pohland, F. G., editor, *Anaerobic biological treatment processes*, volume 105 of *Advances in Chemistry*, chapter 5, pages 55–90. American Chemical Society, Washington, D. C., ISBN 0-8412-0131-5, doi:10.1021/ba-1971-0105.

Kulkarni, A. and Patwardhan, A. (2014). CFD modeling of gas entrainment in stirred tank systems. *Chemical Engineering Research and Design*, 92(7):1227–1248, ISSN 02638762, doi:10.1016/j.cherd.2013.10.025.

Kundu, P. K. and Cohen, I. M. (2008). *Fluid mechanics*. Academic Press, ISBN 0121782514, doi:2001086884.

Landau, L. D. and Lifshitz, E. M. (1987). *Course of Theoretical Physics vol. 6: Fluid Mechanics*. Pergamon Press.

Launder, B. E. (1990). Phenomenological modelling: Present.... and future? In Lumley, J. L., editor, *Whither Turbulence? Turbulence at the Crossroads*, pages 439–485, Berlin. Springer, ISBN 978-3-540-52535-6, doi:10.1007/3-540-52535-1.

Launder, B. E., Reece, G. J., and Rodi, W. (1975). Progress in the development of a Reynolds-stress turbulence closure. ISBN 1750-6859, ISSN 0022-1120, doi:10.1017/S0022112075001814.

Launder, B. E. and Reynolds, W. C. (1983). Asymptotic near-wall stress dissipation rates in a turbulent flow. *Physics of Fluids*, 26(5):1157, ISSN 00319171, doi:10.1063/1.864274.

Leadbeater, T. W., Parker, D. J., and Gargiuli, J. (2012). Positron imaging systems for studying particulate, granular and multiphase flows. *Particuology*, 10(2):146–153, ISSN 16742001, doi:10.1016/j.partic.2011.09.006.

Lien, F. and Leschziner, M. (1994). Assessment of turbulence-transport models including non-linear rng eddy-viscosity formulation and second-moment closure for flow over a backward-facing step. *Computers & Fluids*, 23(8):983–1004, ISSN 00457930, doi:10.1016/0045-7930(94)90001-9.

Lin, H., Zhang, M., Wang, F., Meng, F., Liao, B. Q., Hong, H., Chen, J., and Gao, W. (2014). A critical review of extracellular polymeric substances (EPSs) in membrane bioreactors: Characteristics, roles in membrane fouling and control strategies. ISSN 18733123, doi:10.1016/j.memsci.2014.02.034.

McCarty, P. L. and Kugelman, I. J. (1964). Ion effects in anaerobic digestion. Technical report 33. Technical report, Stanford University, Dept. of Civil Engineering.

McMahon, K. D., Stroot, P. G., Mackie, R. I., and Raskin, L. (2001). Anaerobic codigestion of municipal solid waste and biosolids under various mixing conditions-II: Microbial population dynamics. *Water Research*, 35(7):1817–1827, ISBN 0043-1354 (Print)\r0043-1354 (Linking), ISSN 00431354, doi:10.1016/S0043-1354(00)00438-3.

Menter, F. R. (1994). Two-equation eddy-viscosity turbulence models for engineering applications. *AIAA Journal*, 32(8):1598–1605, ISSN 0001-1452, doi:10.2514/3.12149.

Meroney, R. N. and Colorado, P. E. (2009). CFD simulation of mechanical draft tube mixing in anaerobic digester tanks. *Water Research*, 43(4):1040–1050, ISSN 00431354, doi:10.1016/j.watres.2008.11.035.

Miyamoto, K. (1997). Renewable biological systems for alternative sustainable energy production (FAO Agricultural Services Bulletin - 128). Technical report, Osaka University, Osaka, Japan, ISBN 92-5-104059-1.

Moeller, G. and Torres, L. G. (1997). Rheological characterization of primary and secondary sludges treated by both aerobic and anaerobic digestion. *Bioresource Technology*, 61(3):207–211, ISBN 0960-8524, ISSN 09608524, doi:10.1016/S0960-8524(97)00061-8.

Monteiro, P. S. (1997). The influence of the anaerobic digestion process on the sewage sludges rheological behaviour. *Sludge Rheology Selected Proceedings of the International Workshop on the Rheology of Sludges Sludge Management International Specialized Conference on Sludge Management*, 36(11):61–67, ISSN 0273-1223, doi:10.1016/S0273-1223(97)00670-7.

Mori, M., Isaac, J., Seyssiecq, I., and Roche, N. (2008). Effect of measuring geometries and of exocellular polymeric substances on the rheological behaviour of sewage sludge. *Chemical Engineering Research and Design*, 86(6):554–559, ISSN 02638762, doi:10.1016/j.cherd.2007.10.013.

Naot, D., Shavit, A., and WolfshteinM. (1970). Interaction between components of the turbulent velocity correlation tensor due to pressure fluctuations. *Israel Journal of Technology*, 8:259–269.

Ni, S., Woese, C. R., Aldrich, H. C., and Boone, D. R. (1994). Transfer of Methanolobus siciliae to the genus Methanosarcina, naming it Methanosarcina siciliae, and emendation of the genus Methanosarcina. *International journal of systematic bacteriology*, 44(2):357–359, ISSN 0020-7713, doi:10.1099/00207713-44-2-357.

Ong, H. K., Greenfield, P. F., and Pullammanappallil, P. C. (2002). Effect of mixing on biomethanation of cattle-manure slurry. *Environmental Technology*, 23:1081–1090.

Owen, W. F. (1982). Anaerobic Treatment Processes. In *Energy in wastewater treatment*. Prentice-Hall, Inc., Englewood Cliffs, NJ.

Parker, D. J., Broadbent, C., Fowles, P., Hawkesworth, M., and McNeil, P. (1993). Positron emission particle tracking - a technique for studying flow within engineering equipment. *Nuclear Instruments and Methods in Physics Research Section A: Accelerators, Spectrometers, Detectors and Associated Equipment*, 326(3):592–607, ISSN 01689002, doi:10.1016/0168-9002(93)90864-E.

Parker, D. J., Forster, R., Fowles, P., and Takhar, P. (2002). Positron emission particle tracking using the new Birmingham positron camera. *Nuclear Instruments and Methods in Physics Research Section A: Accelerators, Spectrometers, Detectors and Associated Equipment*, 477(1-3):540–545, ISSN 01689002, doi:10.1016/S0168-9002(01)01919-2.

Patel, G. B. and Roth, L. A. (1977). Effect of sodium chloride on growth and methane production of methanogens. *Canadian journal of microbiology*, 23(7):893–897, ISSN 0008-4166, doi:10.1139/m77-131.

Pevere, A., Guibaud, G., Goin, E., van Hullebusch, E., and Lens, P. (2009). Effects of physico-chemical factors on the viscosity evolution of anaerobic granular sludge. *Biochemical Engineering Journal*, 43(3):231–238, ISSN 1369703X, doi:10.1016/j.bej.2008.10.003.

Pinho, F. and Whitelaw, J. (1990). Flow of non-newtonian fluids in a pipe. *Journal of Non-Newtonian Fluid Mechanics*, 34(2):129–144, ISSN 03770257, doi:10.1016/0377-0257(90)80015-R.

Pope, S. B. (2000). *Turbulent Flows*. Cambridge University Press, ISBN 978-0521598866.

Prandtl, L. (1925). Bericht über die Entstehlung der Turbulenz. *Zeitschrift für Angewandte Mathematik*, 5:136–139.

Raffel, M., Willert, C. E., Wereley, S. T., and Kompenhans, J. (2007). *Particle Image Velocimetry: A practical guide*. Springer, Berlin, Heidelberg, New York, ISBN 978-3-540-72307-3.

Rajeshwari, K., Balakrishnan, M., Kansal, a., Lata, K., and Kishore, V. (2000). State-of-the-art of anaerobic digestion technology for industrial wastewater treatment. *Renewable and Sustainable Energy Reviews*, 4(2):135–156, ISBN 1364-0321, ISSN 13640321, doi:10.1016/S1364-0321(99)00014-3.

Reynolds, O. (1886). On the Theory of Lubrication and Its Application to Mr. Beauchamp Tower's Experiments, Including an Experimental Determination of the Viscosity of Olive Oil. *Philosophical Transactions of the Royal Society of London*, 177:157–234, ISSN 0261-0523, doi:10.1098/rstl.1886.0005.

Richardson, L. F. (1922). *Weather prediction by numerical process*. Cambridge University Press, Cambridge.

Roache, P. J. (1994). Perspective: a method for unifor reporting of grid refinement studies. *Journal of Fluids Engineering*, 116:405–413.

Roache, P. J. (1998). Verification of codes and calculations. *AIAA Journal*, 36(5):696–702, ISBN 0001-1452, ISSN 0001-1452, doi:10.2514/3.13882.

Rosen, C., Vrecko, D., Gernaey, K. V., Pons, M. N., and Jeppsson, U. (2006). Implementing ADM1 for plant-wide benchmark simulations in Matlab/Simulink. *Water Science and Technology*, 54(4):11–19, ISBN 1843395789, ISSN 02731223, doi:10.2166/wst.2006.521.

Rotta, J. (1951). Statistische Theorie nichthomogener Turbulenz. *Zeitschrift für Physik*, 129(6):547–572, ISSN 14346001, doi:10.1007/BF01330059.

Schink, B. and Stams, A. J. M. (2006). Syntrophism among Prokaryotes. In Dworkin, M., editor, *The Prokaryotes*, volume 2, pages 309–335. Springer, ISBN 978-0-387-25492-0, doi:10.1007/0-387-30742-7_11.

Schmidt, J. E. and Ahring, B. K. (1993). Effects of magnesium on thermophilic acetate-degrading granules in upflow anaerobic sludge blanket (UASB) reactors. *Enzyme and Microbial Technology*, 15(4):304–310, ISBN 0141-0229, ISSN 01410229, doi:10.1016/0141-0229(93)90155-U.

Schmidt, J. E. and Ahring, B. K. (1995). Interspecies electron transfer during propionate and butyrate degradation in mesophilic, granular sludge. *Applied and Environmental Microbiology*, 61(7):2765–2767, ISBN 0099-2240, ISSN 00992240.

Schmidt, J. E. and Ahring, B. K. (1999). Immobilization patterns and dynamics of acetate-utilizing methanogens immobilized in sterile granular sludge in upflow anaerobic sludge blanket reactors. *Applied and Environmental Microbiology*, 65(3):1050–1054, ISSN 00992240.

Shih, T.-H., Liou, W. W., Shabbir, A., Yang, Z., and Zhu, J. (1995). A new k-epsilon eddy viscosity model for high reynolds number turbulent flows. *Computers & Fluids*, 24(3):227–238, ISSN 00457930, doi:10.1016/0045-7930(94)00032-T.

Sindall, R. C. (2014). *Increasing the efficiency of anaerobic waste digesters by optimising flow patterns to enhance biogas production*. PhD thesis, University of Birmingham.

Sindall, R. C., Bridgeman, J., and Carliell-Marquet, C. (2013). Velocity gradient as a tool to characterise the link between mixing and biogas production in anaerobic waste digesters. *Water Science and Technology*, 67(12):2800–2806, ISBN http://www.iwaponline.com/wst/06712/wst067122800.htm, ISSN 02731223, doi:10.2166/wst.2013.206.

Stroot, P. G., McMahon, K. D., Mackie, R. I., and Raskin, L. (2001). Anaerobic codigestion of municipal solid waste and biosolids under various mixing conditions-I. digester performance. *Water Research*, 35(7):1804–1816, ISBN 0043-1354 (Print)\r0043-1354 (Linking), ISSN 00431354, doi:10.1016/S0043-1354(00)00439-5.

Succi, S. (2001). The Lattice Boltzmann Equation for Fluid for Fluid Dynamics and Beyond. ISBN 978-0-19-850398-9, ISSN 03701573, doi:10.1016/0370-1573(92)90090-M.

Sungkorn, R., Derksen, J. J., and Khinast, J. G. (2011). Modeling of turbulent gas-liquid bubbly flows using stochastic Lagrangian model and lattice-Boltzmann scheme. *Chemical Engineering Science*, 66(12):2745–2757, ISBN 0009-2509, ISSN 00092509, doi:10.1016/j.ces.2011.03.032.

Sungkorn, R., Derksen, J. J., and Khinast, J. G. (2012). Modeling of aerated stirred tanks with shear-thinning power law liquids. *International Journal of Heat and Fluid Flow*, 36:153–166, ISBN 0142-727X, ISSN 0142727X, doi:10.1016/j.ijheatfluidflow.2012.04.006.

Tchobanoglous, G., Burton, Franklin, L., and Stensel, H. D. (2010). *Wastewater Engineering*. Metcalf & Eddy, Inc, ISBN 7-302-05857-1.

Terashima, M., Goel, R., Komatsu, K., Yasui, H., Takahashi, H., Li, Y. Y., and Noike, T. (2009). CFD simulation of mixing in anaerobic digesters. *Bioresource Technology*, 100(7):2228–2233, ISBN 0960-8524, ISSN 09608524, doi:10.1016/j.biortech.2008.07.069.

Tomiyama, A., Tamai, H., Zun, I., and Hosokawa, S. (2002). Transverse migration of single bubbles in simple shear flows. *Chemical Engineering Science*, 57(11):1849–1858, ISSN 00092509, doi:10.1016/S0009-2509(02)00085-4.

U.S. EPA (1979). Process Design Manual for Sludge Treatment and Disposal. Technical report, U.S. Environmental Protection Agency, Cincinnati, OH.

van Haandel, A. and van der Lubbe, J. (2007). *Handbook of Biological Waste Water Treatment: Design and optimisation of activated sludge systems*. Quist Publishing, Leidschendam, The Netherlands.

van Wachem, B. G. M. and Almstedt, A. E. (2003). Methods for multiphase computational fluid dynamics. *Chemical Engineering Journal*, 96(1-3):81–98, ISBN 1385-8947, ISSN 13858947, doi:10.1016/j.cej.2003.08.025.

Vavilin, V. A. and Angelidaki, I. (2005). Anaerobic degradation of solid material: Importance of initiation centers for methanogenesis, mixing intensity, and 2D distributed model. *Biotechnology and Bioengineering*, 89(1):113–122, ISBN 1097-0290, ISSN 00063592, doi:10.1002/bit.20323.

Versteeg, H. K. and Malalasekera, W. (1995). *An introduction to Computational Fluid Dynamics*. Longman Scientific & Technical, ISBN 0-582-21884-5.

Vesvikar, M. S. and Al-Dahhan, M. H. (2005). Flow pattern visualization in a mimic anaerobic digester using CFD. *Biotechnology and Bioengineering*, 89(6):719–732, ISSN 00063592, doi:10.1002/bit.20388.

Ward, A. J., Hobbs, P. J., Holliman, P. J., and Jones, D. L. (2008). Optimisation of the anaerobic digestion of agricultural resources. *Bioresource Technology*, 99(17):7928–7940, ISBN 0960-8524, ISSN 09608524, doi:10.1016/j.biortech.2008.02.044.

WaterUK (2012). Sustainability Indicators 2010-2011. Technical report, Water UK, London.

Whitaker, S. (1976). *Elementary heat transfer analysis*. Pergamon, ISBN -.

Wilcox, D. C. (2006). *Turbulence Modeling for CFD*. DCW Industries, Inc., ISBN 1-928729-08-8.

Williams, M. L., Landel, R. F., and Ferry, J. D. (1955). The Temperature Dependence of Relaxation Mechanisms in Amorphous Polymers and Other Glass-forming Liquids. *Journal of the American Chemical Society*, 77(14):3701–3707, ISSN 0002-7863, doi:10.1021/ja01619a008.

Wolf-Gladrow, D. (2005). *Lattice-Gas Cellular Automata and Lattice Boltzmann Models*. Springer.

Wu, B. (2010a). CFD simulation of gas and non-Newtonian fluid two-phase flow in anaerobic digesters. *Water Research*, 44(13):3861–3874, ISSN 00431354, doi:10.1016/j.watres.2010.04.043.

Wu, B. (2010b). CFD simulation of mixing in egg-shaped anaerobic digesters. *Water Research*, 44(5):1507–1519, ISSN 00431354, doi:10.1016/j.watres.2009.10.040.

Wu, B. (2010c). Computational fluid dynamics investigation of turbulence models for non-newtonian fluid flow in anaerobic digesters. *Environmental science & technology*, 44(23):8989–8995, ISSN 1520-5851, doi:10.1021/es1010016.

Wu, B. (2011). CFD investigation of turbulence models for mechanical agitation of non-Newtonian fluids in anaerobic digesters. *Water Research*, 45(5):2082–2094, ISSN 00431354, doi:10.1016/j.watres.2010.12.020.

Wu, B. (2012a). CFD simulation of mixing for high-solids anaerobic digestion. *Biotechnology and Bioengineering*, 109(8):2116–2126, ISSN 00063592, doi:10.1002/bit.24482.

Wu, B. (2012b). Integration of mixing, heat transfer, and biochemical reaction kinetics in anaerobic methane fermentation. *Biotechnology and Bioengineering*, 109(11):2864–2874, ISBN 0006-3592, ISSN 00063592, doi:10.1002/bit.24551.

Wu, B. (2012c). Large eddy simulation of mechanical mixing in anaerobic digesters. *Biotechnology and Bioengineering*, 109(3):804–812, ISSN 00063592, doi:10.1002/bit.24345.

Wu, B. (2014). CFD simulation of gas mixing in anaerobic digesters. *Computers and Electronics in Agriculture*, 109:278–286, ISSN 01681699, doi:10.1016/j.compag.2014.10.007.

Wu, B. and Chen, S. (2008). CFD simulation of non-Newtonian fluid flow in anaerobic digesters. *Biotechnology and Bioengineering*, 99(3):700–711, ISSN 00063592, doi:10.1002/bit.21613.

Yang, F., Bick, A., Shandalov, S., Brenner, A., and Oron, G. (2009). Yield stress and rheological characteristics of activated sludge in an airlift membrane bioreactor. *Journal of Membrane Science*, 334(1-2):83–90, ISBN 0376-7388, ISSN 03767388, doi:10.1016/j.memsci.2009.02.022.

Zickefoose, C. and Hayes, R. B. J. (1976). Operations Manual - Anaerobic Sludge Digestion. Technical report, U.S. Environmental Protection Agency, Washington, D. C.

A

Derivation of the Navier-Stokes Equations

A DERIVATION OF the Navier-Stokes equations (Equations 3.1 and 3.2) is given. As reported at the begin of Section 3.1, the general framework is the description of the fluid as a continuum. The assumptions are conservation of mass, Galilean invariance and isotropy in the local rest frame. Other additional hypotheses are introduced later on.

A.1 Reynolds Transport Theorem

The Reynolds transport theorem is an important tool to derive the Navier-Stokes equations. It provides a description of the substantial derivative of a quantity integrated inside a Lagrangian fluid particle in terms of the variation of that quantity inside the particle volume and its flux through the particle surface. A beautiful description is reported in Whitaker (1976). Here a brief synthesis with few modifications is reported.

Theorem. *Let $\xi(\mathbf{x}\,,t)$ be a tensorial field defined in a domain $\Omega(t)$. Then the total derivative of the integral of ξ over Ω can be espressed as:*

$$\frac{\mathrm{d}}{\mathrm{d}t}\int_{\Omega(t)} \xi \ \mathrm{d}V = \int_{\Omega(t)} \partial_t \xi \ \mathrm{d}V + \int_{\partial\Omega(t)} \xi \left(\mathbf{v} \cdot \mathrm{d}\mathbf{A}\right) \ , \tag{A.1}$$

where $\mathbf{v}(\mathbf{x},\ t)$ is the velocity of the border $\partial\Omega$.

Proof: By definition of time derivative we have:

$$\frac{\mathrm{d}}{\mathrm{d}t}\int_{\Omega(t)} \xi \ \mathrm{d}V = \lim_{\delta t \to 0} \frac{\int_{\Omega(t+\delta t)} \xi(t+\delta t) \ \mathrm{d}V - \int_{\Omega(t)} \xi(t) \ \mathrm{d}V}{\delta t} \ . \tag{A.2}$$

The volume $\Omega(t+\delta t)$ is equal to $\Omega(t)$ plus the volume where Ω expands into, minus the volume from where Ω retires:

$$\Omega(t+\delta t) = \Omega(t) \cup \delta\Omega_+ \setminus \delta\Omega_- \ . \tag{A.3}$$

The integral over $\Omega(t+\delta t)$ in Equation A.2 can be written as:

$$\begin{aligned} \int_{\Omega(t+\delta t)} \xi(t+\delta t)\ \mathrm{d}V = & \int_{\Omega(t)} \xi(t+\delta t)\ \mathrm{d}V \\ & + \int_{\delta\Omega_+} \xi(t+\delta t)\ \mathrm{d}V_+ - \int_{\delta\Omega_-} \xi(t+\delta t)\ \mathrm{d}V_- \ . \end{aligned} \tag{A.4}$$

Thus, Equation A.2 becomes:

$$\begin{aligned} \frac{\mathrm{d}}{\mathrm{d}t} \int_{\Omega(t)} \xi\ \mathrm{d}V = & \lim_{\delta t \to 0} \frac{\int_{\Omega(t)} [\xi(t+\delta t) - \xi(t)]\ \mathrm{d}V}{\delta t} \\ & + \lim_{\delta t \to 0} \frac{\int_{\delta\Omega_+} \xi(t+\delta t)\ \mathrm{d}V_+ - \int_{\delta\Omega_-} \xi(t+\delta t)\ \mathrm{d}V_-}{\delta t} \ . \end{aligned} \tag{A.5}$$

The first term in the right member of Equation A.5, the quantities $\xi(t+\delta t)$ and $\xi(t)$ are evalued at the same point of time. Therefore, the term assumes the form of $\int_{\Omega(t)} \partial_t \xi\ \mathrm{d}V$. Moreover, the volume elements $\mathrm{d}V_+$ and $\mathrm{d}V_-$ can be expressed on terms of the respective elements of surface at the time $t+\delta t$:

$$\begin{aligned} \mathrm{d}V_+ &= \ \ \delta t\, \mathbf{v} \cdot \mathrm{d}\mathbf{A}_+ \\ \mathrm{d}V_- &= -\delta t\, \mathbf{v} \cdot \mathrm{d}\mathbf{A}_- \ . \end{aligned} \tag{A.6}$$

Thus the volume integrals in the second term of Equation A.5 can be converted into area integrals and the equation becomes:

$$\begin{aligned}\frac{\mathrm{d}}{\mathrm{d}t}\int_{\Omega(t)} \xi \;\mathrm{d}V = &\int_{\Omega(t)} \partial_t \xi \;\mathrm{d}V \\ &+ \lim_{\delta t\to 0} \frac{\delta t \int_{\partial\Omega_+} \xi(t+\delta t)\,(\mathbf{v}\cdot \mathrm{d}\mathbf{A}_+) + \delta t \int_{\partial\Omega_-} \xi(t+\delta t)\,(\mathbf{v}\cdot \mathrm{d}\mathbf{A}_-)}{\delta t}\;.\end{aligned} \tag{A.7}$$

As we have $\partial\Omega_+ + \partial\Omega_- \equiv \partial\Omega(t+\delta t)$, Equation A.7 becomes:

$$\frac{\mathrm{d}}{\mathrm{d}t}\int_{\Omega(t)} \xi \;\mathrm{d}V = \int_{\Omega(t)} \partial_t \xi \;\mathrm{d}V + \lim_{\delta t\to 0}\int_{\partial\Omega(t+\delta t)} \xi(t+\delta t)\,(\mathbf{v}\cdot \mathrm{d}\mathbf{A})\;. \tag{A.8}$$

The argument of the limit at the second member of Equation A.8 can be regarded as a function that associates a time to the result of the integral:

$$f: \quad \tau \longmapsto \int_{\partial\Omega(\tau)} \xi(\tau)\,(\mathbf{v}\cdot \mathrm{d}\mathbf{A})\;. \tag{A.9}$$

If the evolution of Ω takes place continuously, we have:

$$\int_{\partial\Omega(t+\delta t)} \xi(t+\delta t)\,(\mathbf{v}\cdot \mathrm{d}\mathbf{A}) \approx f(t) + \left.\frac{\mathrm{d}f}{\mathrm{d}t}\right|_t \delta t\;. \tag{A.10}$$

Thus follows that:

$$\lim_{\delta t\to 0}\int_{\partial\Omega(t+\delta t)} \xi(t+\delta t)\,(\mathbf{v}\cdot \mathrm{d}\mathbf{A}) = \int_{\partial\Omega(t)} \xi(t)\,(\mathbf{v}\cdot \mathrm{d}\mathbf{A}) \tag{A.11}$$

and therefore the thesis.

□

If the domain Ω represents a Lagrangian fluid particle, then the velocity $\mathbf{v}$ in Equation A.1 is equal to the fluid velocity $\mathbf{u}$ and the total derivative becomes the substantial derivative:

$$\frac{\mathrm{D}}{\mathrm{D}t}\int_{\Omega(t)}\xi\,\mathrm{d}V=\int_{\Omega(t)}\partial_t\xi\,\mathrm{d}V+\int_{\partial\Omega(t)}\xi\,(\mathbf{u}\cdot\mathrm{d}\mathbf{A})\ . \tag{A.12}$$

A.2 Continuity Equation

An equation can be derived from conservation of mass. The variation of mass inside a Lagrangian flow particle of volume Ω must be zero:

$$\frac{\mathrm{D}}{\mathrm{D}t}M\equiv\frac{\mathrm{D}}{\mathrm{D}t}\int_{\Omega}\rho\,\mathrm{d}V=0\ . \tag{A.13}$$

Using the result of the Reynolds transport theorem Equation A.12 we have:

$$\frac{\mathrm{D}}{\mathrm{D}t}\int_{\Omega}\rho\,\mathrm{d}V=\int_{\Omega}\partial_t\rho\,\mathrm{d}V+\int_{\partial\Omega}\rho\mathbf{u}\cdot\mathrm{d}\mathbf{A}\ . \tag{A.14}$$

The last term at the second member of Equation A.14 above can be rewritten as an integral over volume by Gauss theorem. Then we have:

$$\int_{\Omega}\left[\partial_t\rho+\nabla\cdot(\rho\mathbf{u})\right]\,\mathrm{d}V=0\ . \tag{A.15}$$

As Equation A.15 must hold for every volume Ω; it turns out that the integrand must be identically zero:

$$\partial_t\rho+\nabla\cdot(\rho\mathbf{u})=0\ . \tag{A.16}$$

Equation A.16 represents the conservation of mass in the most general form. An additional hypothesis consists of requiring incompressibility, that is constant density. This holds well with liquids but not for gases. Thus, Equation A.16 becomes:

$$\nabla\cdot\mathbf{u}=0\ . \tag{A.17}$$

A.3 Momentum Equations

A set of three equations can be derived by applying Newton's law to a Lagrangian particle: the variation of momentum equates the resultant of the forces acting on the particle. The latter can be split into a surface and body term. The surface term depends on the forces acting on the surface of the particle, while the volume term takes into account the forces acting on the volume.

$$\frac{\mathrm{D}}{\mathrm{D}t}\left(M\mathbf{U}\right) = \mathbf{F}_{\mathrm{A}} + \mathbf{F}_{\mathrm{V}} \ . \tag{A.18}$$

Equation A.18 can be expressed in terms of integrated quantities over the particle volume Ω and surface $\partial\Omega$:

$$\frac{\mathrm{D}}{\mathrm{D}t}\int_{\Omega}\rho\mathbf{u}\,\mathrm{d}V = \int_{\partial\Omega}\sigma\cdot\mathrm{d}\mathbf{A} + \int_{\Omega}\mathbf{b}\,\mathrm{d}V \ . \tag{A.19}$$

Applying the result of the Reynolds transport theorem Equation A.12 to the fist member of Equation A.19 we have:

$$\begin{aligned}\frac{\mathrm{D}}{\mathrm{D}t}\int_{\Omega}\rho\mathbf{u}\,\mathrm{d}V &= \int_{\Omega}\partial_t\left(\rho\mathbf{u}\right)\,\mathrm{d}V + \int_{\partial\Omega}\rho\mathbf{u}\otimes\mathbf{u}\cdot\mathrm{d}\mathbf{A}\\ &= \int_{\Omega}\partial_t\left(\rho\mathbf{u}\right)\,\mathrm{d}V + \int_{\Omega}\nabla\cdot\left(\rho\mathbf{u}\otimes\mathbf{u}\right)\,\mathrm{d}V \ ,\end{aligned} \tag{A.20}$$

where the Gauss theorem was applied to the second member on the right side. Substituting Equation A.20 into Equation A.19, applying the Gauss theorem to the surface forces terms and considering that the equivalence must hold for every control volume Ω, we have:

$$\partial_t\left(\rho\mathbf{u}\right) + \nabla\cdot\left(\rho\mathbf{u}\otimes\mathbf{u}\right) = \nabla\cdot\sigma + \mathbf{b} \ . \tag{A.21}$$

The stress tensor σ can be decomposed into its diagonal and a non-diagonal parts. The former represents the stresses normal to the particle surface, and the latter the shear stresses. Due to the isotropy assumption, the normal stresses tensor can assume only the form $-p\,\delta_{ij}$. Thus:

$$\sigma_{ij} = -p\,\delta_{ij} + \tau_{ij}\ . \tag{A.22}$$

The p in Equation A.22 can be interpreted as the pressure. Then we have:

$$\partial_t\left(\rho\mathbf{u}\right) + \nabla\cdot\left(\rho\mathbf{u}\otimes\mathbf{u}\right) = -\nabla p + \nabla\cdot\tau + \mathbf{b}\ . \tag{A.23}$$

The body force $\mathbf{b}$ can be splitted into the gravitational contribution ρg and all the other non-gravitational contributions $\bar{\mathbf{b}}$. When the addictional hypothesis of constant density is enforced, the gravitational term can be written as $\nabla\left(\rho\mathrm{g}\cdot\mathbf{x}\right)$ and then absorbed by a redefinition of the pressure as $p \longrightarrow p - \rho\mathrm{g}\cdot\mathbf{x}$. Thus, Equation A.23 becomes:

$$\rho\,\partial_t\mathbf{u} + \rho\nabla\cdot\left(\mathbf{u}\otimes\mathbf{u}\right) = -\nabla p + \nabla\cdot\tau + \bar{\mathbf{b}}\ . \tag{A.24}$$

Finally, an expression for the shear stress tensor τ must be provided. The shear forces acting on the particle at a given moment depend only on the other particles surrounding it, and therefore τ can depend only on the velocity field. In principle, τ may be composed by any combination of spatial derivatives of $\mathbf{u}$ that form a second rank tensor; it cannot contain terms in powers of $\mathbf{u}$ otherwise Galilean invariance would be violated. The Newtonian fluid hypothesis consists of neglecting all the non-linear terms and the terms containing derivatives of order higher than 1; therefore, only the terms proportional to $\partial_i u_j$ are taken into account. Also, the shear stresses must vanish when the fluid rotates with constant angular velocity, and this is only possible if τ is symmetric (Landau and Lifshitz, 1987). Therefore we have:

$$\tau = \mu\left(\partial_i u_j + \partial_j u_i\right)\ . \tag{A.25}$$

The constant of proportionality μ can be interpreted as the dynamic viscosity.

B

A Description of the k-ε Model

THE SIMPLEST two-equations turbulence model is the standard k-ε model. This model was introduced by Jones and Launder (1972). The model makes use of the Boussinesq hypothesis (Equation 3.46) and assumes that the flow is fully turbulent. The turbulent viscosity is specified as:

$$\nu_{\mathrm{T}} = C_\mu \frac{k^2}{\varepsilon} \ . \tag{B.1}$$

The equation for k can be obtained from Equation 3.30:

$$\partial_t k + \langle \mathbf{u} \rangle \cdot \nabla k = -\nabla \cdot \mathbf{T} + \mathcal{S}_k + \mathcal{P} - \varepsilon \ , \tag{B.2}$$

where $\mathcal{S}_k$ is a source term, and $\mathcal{P}$ the Reynolds tensor turbulent kinetic energy production term defined as:

$$\mathcal{P} = \frac{1}{\rho} R_{ij}\, \partial_i \langle u_j \rangle \ . \tag{B.3}$$

Easy manipulation, together with the turbulent viscosity hypothesis 3.46, leads to:

$$\mathcal{P} = \frac{\nu_{\mathrm{T}}}{2} \langle \dot{\gamma}_{ij} \rangle \langle \dot{\gamma}_{ij} \rangle \ . \tag{B.4}$$

The term $\mathbf{T}$ in Equation B.2 is defined as:

$$\mathbf{T} \equiv \frac{1}{2} \langle \tilde{u}_i \tilde{u}_j \tilde{u}_j \rangle + \frac{1}{\rho} \langle \tilde{u}_i \tilde{p} \rangle - 2\nu \left\langle \tilde{u}_j \dot{\tilde{\gamma}}_{ij} \right\rangle \ , \tag{B.5}$$

where $\nu \equiv \mu/\rho$ is the kinematic viscosity. The term above is modelled with a gradient-diffusion hypothesis:

$$\mathbf{T} = -\left(\nu + \frac{\nu_{\mathrm{T}}}{\sigma_k}\right)\nabla k\ . \tag{B.6}$$

The equation for ε is mostly empirical and takes the form:

$$\partial_t \varepsilon + \langle \mathbf{u} \rangle \cdot \nabla \varepsilon = \nabla \cdot \left[\left(\nu + \frac{\nu_{\mathrm{T}}}{\sigma_\varepsilon}\right)\nabla \varepsilon\right] + \mathcal{S}_\varepsilon + C_{\varepsilon 1}\frac{\mathcal{P}\varepsilon}{k} - C_{\varepsilon 2}\frac{\varepsilon^2}{k}\ , \tag{B.7}$$

where $\mathcal{S}_\varepsilon$ is a source term. The constants in Equation B.1, B.6 and B.7 are:

$$C_\mu = 0.09\,, \quad C_{\varepsilon 1} = 1.44\,, \quad C_{\varepsilon 2} = 1.92\,, \quad \sigma_k = 1.0\,, \quad \sigma_\varepsilon = 1.3\,. \tag{B.8}$$

C

Reynolds Stress Models

IN THE REYNOLDS stress models, all the six independent components of the Reynolds stress tensor, plus one scalar involving dissipation (e.g. ε) are directly solved. Thus, the turbulent viscosity assumption (Equation 3.46) is not considered. An equation for the Reynolds stress components can be worked out by manipulating the Reynolds equations 3.30:

$$(\partial_t + \langle u_k \rangle \partial_k) \langle \tilde{u}_i \tilde{u}_j \rangle + \partial_k T_{kij} = \mathcal{P}_{ij} + \mathcal{R}_{ij} - \varepsilon_{ij} \ , \tag{C.1}$$

where the production tensor $\mathcal{P}$ is defined as:

$$\mathcal{P}_{ij} \equiv - \langle \tilde{u}_i \tilde{u}_k \rangle \ \partial_k \langle u_j \rangle - \langle \tilde{u}_j \tilde{u}_k \rangle \ \partial_k \langle u_i \rangle \ , \tag{C.2}$$

the dissipation tensor ε as:

$$\varepsilon_{ij} \equiv 2\nu \ \langle \partial_k \tilde{u}_i \, \partial_k \tilde{u}_j \rangle \ , \tag{C.3}$$

the pressure–shear rate tensor $\mathcal{R}$ as:

$$\mathcal{R}_{ij} \equiv -\frac{1}{\rho} \left\langle \tilde{p} \, \dot{\tilde{\gamma}}_{ij} \right\rangle \tag{C.4}$$

and the Reynolds stress transport tensor as:

$$T \equiv T^{(u)} + T^{(p)} + T^{(\nu)} \ , \tag{C.5}$$

where:

$$T^{(u)}_{kij} \equiv \langle \tilde{u}_k \tilde{u}_i \tilde{u}_j \rangle \ , \tag{C.6}$$

$$T^{(p)}_{kij} \equiv \frac{1}{\rho} \langle \tilde{u}_i \, \tilde{p} \rangle \, \delta_{jk} + \frac{1}{\rho} \langle \tilde{u}_j \, \tilde{p} \rangle \, \delta_{ik} \ , \tag{C.7}$$

$$T^{(\nu)}_{kij} \equiv -\nu \, \partial_k \langle \tilde{u}_i \tilde{u}_i \rangle \ . \tag{C.8}$$

Equations C.6, C.7 and C.8 define the components of the Reynolds stress transport due to turbulent, pressure and viscous diffusion transport respectively. The tensors ε, $\mathcal{P}$, $\mathcal{R}$ and T need modelling.

C.1 Dissipation Term

As a consequence of Kolmogorov's local isotropy hypothesis, the dissipation tensor can be reduced to a scalar:

$$\varepsilon_{ij} = \frac{2}{3} \varepsilon \, \delta_{ij} \ . \tag{C.9}$$

The scalar ε in Equation C.9 can be modelled empirically as in the k-ε model, reproducing Equation B.7 and B.1, with the coefficients of Equations B.8. Alternatively, Hanjalic and Launder (1972) proposed a model with an anisotropic diffusivity:

$$\partial_t \varepsilon + \langle \mathbf{u} \rangle \cdot \nabla \varepsilon = \nabla \cdot \left(C_\varepsilon \frac{k}{\varepsilon} \langle \tilde{u}_i \tilde{u}_j \rangle \, \nabla \varepsilon \right) + \mathcal{S}_\varepsilon + C_{\varepsilon 1} \frac{\mathcal{P} \varepsilon}{k} - C_{\varepsilon 2} \frac{\varepsilon^2}{k} \ , \tag{C.10}$$

with $C_\varepsilon = 1.8$ and the other parameters as in Equation B.8.

C.2 Pressure-Shear of Rate Term

The pressure–shear rate tensor can be split in three terms. By applying the Reynolds decomposition Equation 3.27 to the Poisson equation for the pressure (Equation 3.7), one obtains:

$$\frac{1}{\rho}\,\nabla^2\tilde{p} = -2\,\partial_j\langle u_i\rangle\,\partial_i\tilde{u}_j - \partial_i\partial_j\left(\tilde{u}_i\tilde{u}_j - \langle\tilde{u}_i\tilde{u}_j\rangle\right)\ . \tag{C.11}$$

The fluctuating pressure can be decomposed into three terms, originating from rapid variations (that is, when the time scale of the main motion is larger than the turbulent time scale, or $\langle|\dot{\gamma}|\rangle^{-1} \gg k/\varepsilon$), slow variations ($\langle|\dot{\gamma}|\rangle^{-1} \lesssim k/\varepsilon$), and a harmonic contribution (Pope, 2000), respectively satisfying the following equations:

$$\frac{1}{\rho}\,\nabla^2 p^{(\mathrm{r})} = -2\,\partial_j\langle u_i\rangle\,\partial_i\tilde{u}_j\ , \tag{C.12}$$

$$\frac{1}{\rho}\,\nabla^2 p^{(\mathrm{s})} = -\partial_i\partial_j\left(\tilde{u}_i\tilde{u}_j - \langle\tilde{u}_i\tilde{u}_j\rangle\right)\ , \tag{C.13}$$

$$\nabla^2 p^{(\mathrm{h})} = 0\ . \tag{C.14}$$

Each term of the fluctuating pressure gives rise to an analogous term of the pressure–rate of strain tensor, namely $\mathcal{R}^{(\mathrm{r})}$, $\mathcal{R}^{(\mathrm{s})}$ and $\mathcal{R}^{(\mathrm{h})}$. The harmonic term is important only near the walls, and can be consequently neglected in the bulk (Pope, 2000).

Rotta (1951) analysed the slow varying term of the pressure–rate of strain tensor in the case of decaying homogeneous turbulence (zero production and transport), and introduced the following modelization:

$$\mathcal{R}^{(\mathrm{s})}_{ij} = -C_{\mathrm{R}}\,\frac{\varepsilon}{k}\left(\langle\tilde{u}_i\tilde{u}_j\rangle - \frac{2}{3}\delta_{ij}\right)\ . \tag{C.15}$$

Launder (1990) suggests $C_{\mathrm{R}} = 1.8$. The model above predicts a linear return to isotropy after the onset of anisotropic turbulence and for this reason is called “return to isotropy”. However, it was observed that the return to isotropy is not linear, and therefore many non-linear model were introduced in place of the Rotta’s model (Pope, 2000).

For the rapid varying term, an exact spectral analysis was carried out by Naot et al. (1970) in the case of homogeneous turbulence (zero transport). The conclusion was that, at the initial time, the rapid variating term of the pressure–rate of strain tensor acts to counteract the anisotropic turbulence production:

$$\mathcal{R}_{ij}^{(\mathrm{r})} = -C_2 \left(\mathcal{P}_{ij} - \frac{2}{3} \mathcal{P} \, \delta_{ij} \right) \;, \tag{C.16}$$

where $\mathcal{P} \equiv \frac{1}{2} \mathcal{P}_{ii}$. The term expressed in Equation C.16 is called "isotropization of production".

C.3 Transport Term

Of the transport tensor, the viscous transport contribution is negligible except near the wall (Pope, 2000). The other two terms can be modelled altogether as an anisotropic diffusion term (Daly and Harlow, 1970):

$$T_{kij}^{(u)} + T_{kij}^{(p)} = -C_s \, \frac{k}{\varepsilon} \, \langle \tilde{u}_k \tilde{u}_\ell \rangle \; \partial_\ell \, \langle \tilde{u}_i \tilde{u}_j \rangle \;. \tag{C.17}$$

Launder (1990) suggests $C_s = 0.23$. However, it has been reported (ANSYS, 2012) that Equation C.17 can lead to numerical instability, and therefore another approach is to simplify the problem by using an isotropic diffusivity (Lien and Leschziner, 1994):

$$T_{kij}^{(u)} + T_{kij}^{(p)} = - \left(\frac{\nu_{\mathrm{T}}}{\sigma_{\mathrm{R}}} + \nu \right) \partial_\ell \, \langle \tilde{u}_i \tilde{u}_j \rangle \;, \tag{C.18}$$

where ν_{T} is obtained from Equation B.1 and $\sigma_{\mathrm{R}} = 0.82$.

The model composed of Equation C.1, together with the modelizations expressed in Equations C.9, C.10, C.15, C.16 and C.17 constitute the Launder-Reece-Rodi model (Launder et al., 1975).

C.4 Near-Wall Region

In the near-wall region, the quantities mostly affected are the dissipation tensor ε and the pressure-rate of strain tensor $\mathcal{R}$ (Pope, 2000). According with Launder and Reynolds (1983), a non-isotropic component ε^* for the dissipation tensor depending on the versor normal to the wall $\mathbf{n}$:

$$\varepsilon_{ij}^* \equiv \frac{\varepsilon}{k} \frac{\langle \tilde{u}_i \tilde{u}_j \rangle + n_j n_\ell \langle \tilde{u}_\ell \tilde{u}_i \rangle + n_i n_\ell \langle \tilde{u}_\ell \tilde{u}_j \rangle + \delta_{ij} n_\ell n_m \langle u_\ell u_m \rangle}{1 + \frac{5}{2} n_\ell n_m \langle \tilde{u}_\ell \tilde{u}_m \rangle / k} \tag{C.19}$$

is to be added to the dissipation tensor via a blending function f depending on the Reynolds number:

$$\varepsilon_{ij} = f \varepsilon_{ij}^* + (1 - f) \frac{2}{3} \epsilon \delta_{ij} \; . \tag{C.20}$$

As regards the role of the fluctuating pressure, Pope (2000) showed that the harmonic term is negligible, and remaining terms can be interpreted as wall reflection. Gibson and Launder (1978) accounted for wall reflection by adding an additional pressure-rate of strain term:

$$\mathcal{R}_{ij}^{(\mathrm{w})} \equiv C_{\mathrm{w}} \frac{\varepsilon}{k} \frac{L}{y} \left(n_\ell n_m \delta_{ij} \langle \tilde{u}_\ell \tilde{u}_m \rangle - \frac{3}{2} n_j n_\ell \langle \tilde{u}_i \tilde{u}_\ell \rangle - \frac{3}{2} n_i n_\ell \langle \tilde{u}_j \tilde{u}_\ell \rangle \right) \; , \tag{C.21}$$

where $C_{\mathrm{w}} = 1/5$, $L = k^{3/2}/\varepsilon$ and y is the distance from the wall.

D

Implementation of the Multiphase Model

THE COMPUTATIONAL MODEL described in Chapter 7 was implemented with the OpenFOAM toolbox. In particular, the version 2.3.0 of the software was used. In Section D.1, a short description of OpenFOAM is reported; then, the specific code used in this work and the modifications preformed on the basic version are described in Section D.2 as regards the libraries, and in Section E.2 for the solver.

D.1 OpenFOAM

OpenFOAM (for ”Open source Field Operation And Manipulation”) is a C++ toolbox for the simulation of a wide range of fluid mechanics problem. The code is released as free and open source software under the GNU General Public License. It is managed, maintained and distributed by The OpenFOAM Foundation Ltd. (Greenshields, 2015b).

OpenFOAM is first and foremost a C++ library, used primarily to create executables, known as applications. The structure of teh OpenFOAM toolbox is sketched in Figure D.1. The applications fall into two categories: solvers, that are each designed to solve a specific

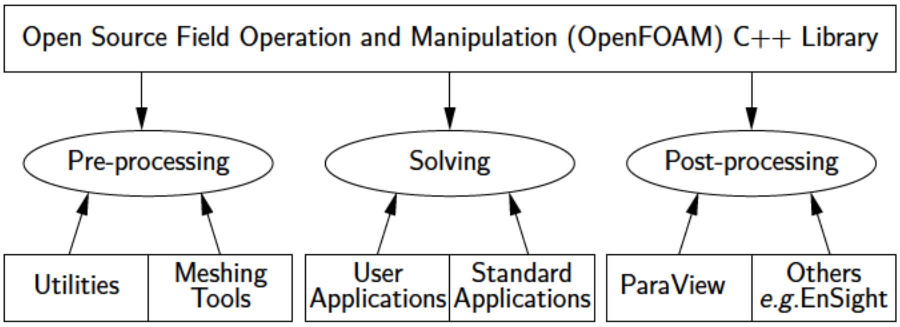

Figure D.1 *Overview of OpenFOAM structure. Greenshields (2015b).*

problem in continuum mechanics; and utilities, that are designed to perform tasks that involve data manipulation (Greenshields, 2015b). Being open source, OpenFOAM users can create new solvers, utilities and libraries by modifying the standard source code set, depending on their particular needs.

OpenFOAM makes use of C++ inheritance and overloading to introduce a syntax to write equations in a universal way, without the need to implement details such as discretization schemes, or implicit/explicit algorithms. For instance, in the following example (from Greenshields 2015a), the equation:

$$\partial_t \phi = \kappa \nabla^2 \phi$$

can be solved with an Euler implicit method by using the `fvm` class to discretise the terms implicitly:

```
solve(fvm::ddt(phi) == kappa*fvm::laplacian(phi))
```

The equation above can also be solved with an explicit method using the `fvc` class:

```
solve(fvc::ddt(phi) == kappa*fvc::laplacian(phi))
```

The advantage of this approach consist of the fact that the user can concentrate on the equation alone without the need of implementing all the algorithms for discretization and solving.

Figure D.2 depicts the most interesting parts of the OpenFOAM directory tree for the general user. The `OpenFOAM-<version>` directory contains all the files released within the base distribution and should never be modified. The user-created files are normally contained in `<Username>-<version>`. The source codes of the executables are contained in the `applications` folders, and are divided into `utilities` and

```
OpenFOAM
 |__OpenFOAM-<version> ............................ Distribution folder
 |   |__applications ................................. Base applications
 |   |   |__solvers
 |   |   |   |__...
 |   |   |__utilities
 |   |       |__...
 |   |__platforms .................................... Base executables
 |   |   |__...
 |   |__src ............................................. Base libraries
 |   |   |__...
 |   |__tutorials ................................... Examples of cases
 |       |__...
 |__<Username>-<version> ................................. User folder
     |__applications ......................... User-defined applications
     |   |__...
     |__platforms ............................. User-defined executables
     |   |__...
     |__run .................................. Cases created by the user
     |   |__...
     |   |__<dir1>
     |   |   |__<case_a>
     |   |   |__<case_b>
     |   |   |__...
     |   |__<case_1>
     |   |__<case_2>
     |__src .................................... User-defined libraries
         |__...
```

Figure D.2 *OpenFOAM relevant directory tree.*

`solvers`. The former involve data manipulation, while le latter solve a specific fluid mechanics problem, ad are the programs that are launched when a given simulation is run. All the classes definitions and implementations are contained in the `src` folders. The library files can be included in the applications directly, or can be compiled into dynamic library binaries `.dylib` files that are located in `OpenFOAM-<version>/platforms`. Each simulation is managed by the files comprised inside a “case” directory created by the user. All the cases are contained—and eventually arranged within a directory tree—inside the `run` directory. In general, the first step to create a new case is to choose and modify an example case taken from a wide collection located in the `tutorials` folder. All the binaries (both executables and dynamic libraries) that are part of the standard distribution are stored in `OpenFOAM-<version>/platforms`. The binaries resulting from the compilation of the user-defined code, conversely, is generally stored in `<Username>-<version>/platforms`.

D.2 User-Defined Libraries Employed in the Simulations

The `lagrangian` libraries contain a wide set of classes to describe Lagrangian modelling. A portion of the `lagrangian` directory tree is depicted in Figure D.3. The two most relevant libraries are the `basics` and `intermediate`, that are also compiled as binary dynamic libraries as `liblagrangian.dylib` and `liblagrangianIntermediate.dylib` respectively. Among the other things, the `basic` library contains the `particle` and `Cloud` classes that provide the basic structure to describe a single particle and a particles cloud respectively.

The `intermediate` library contains subclasses that extend the `particle` and the

```
lagrangian
|__ ...
|__ basis
|   |__ Cloud ............................... Basic particles cloud framework
|   |__ particle ............................ Basic single particle framework
|   |__ ...
|__ intermediate
    |__ clouds ............................................ Cloud subclasses
    |__ parcels ........................................ particle subclasses
    |__ ...
    |__ submodels ........................................ Physical models
        |__ ...
        |__ Kinematic .............. Models that affect the motion of the bubbles
            |__ ...
            |__ ParticleForces ............. External forces acting on particles
```

Figure D.3 *Portion of the* `lagrangian` *directory tree.*

`Cloud` classes, placed in `intermediate/parcels` and `intermediate/clouds` respectively. It also contains other things and, among the others, the `submodels` classes. This folder contains all the models that describe the physics affecting the behaviour of the bubbles. All the models affecting the kinematic of the particles are placed in the `Kinematic` folder and, among them, the model that describe the external forces acting on a particle are stored in the `ParticleForces` folder.

The drag models are stored in the `ParticleForces/Drag` directory; however, the Dewsbury model (Dewsbury et al., 1999) introduced in Section 7.2 is not included in the set. The model was added in the set of available models in the following way. The folder `OpenFOAM-<version>/src/lagrangian` was copied as `<Username>-<version>/src/myForcesLagrangian`. Then, the class for the Dewsbuty model `myDewsburyDragForce` was implemented in the new files `myDewsburyDragForce.C` and `myDewsburyDragForce.H`, which were placed into the directory `ParticleForces/Drag`. The files are reported in Sections E.1.2 and E.1.1 respectively. Finally, the libraries contained in `myForcesLagrangian/intermediate`. were compiled and the relative dynamic library was avaible as `libmyForcesLagrangianIntermediate.dylib`.

D.3 User-Defined Solver Employed in the Simulations

The `DPMFoam` solver was used as a starting point to create the solver used in the simulations. According with the version 2.3.0 release notes, `DPMFoam` "includes the effect of the particulate volume fraction on the continuous phase, suitable for dense particle flow simulation". In addition, it is designed to allow the `fixedFluxPressure` boundary condition for the pressure field. This boundary condition adjusts the pressure gradient so that the boundary flux matches the velocity boundary condition.

`DPMFoam` has been designed for systems in which the motion of the particles is of interest, while the flow patterns of the fluid phase is not relevant, as in the case of a fluidized bed. For this reason, `DPMFoam` is not expected to be reliable in reproducing fluid phase flow patterns—and in fact, it failed to reprodice the correct velocity profile of a laminar, fully developed, Newtonian, single phase flow through a circular, horizontal pipe with transverse gravitational field. As explained in Section 7.1, in the work presented here, the flow patterns were of primary interest, while the particles motion was not relevant, and therefore a modification of the solver was necessary.

For the motivation explained above, and also for the need of including the user-modified Lagrangian libraries described in Section D.2, `DPMFoam` was used as a base to implement a user-modified solver which was called `myParcelFoam`. (*i*) The first change to `DPMFoam` was to remove the effect of the particle volume fraction, thus returning to the basic formulation of the Euler-Lagrangian model reported in literature and described in Section 3.5.1. (*ii*) `DPMFoam` solves a version of the Navier-Stokes equations in which the gravity term is treated explicitly (Equation A.23), rather than the more common version in which the gravity is absorbed by redefining the pressure (Equation A.24). This is due to the fact that the pressure field without the redefinition is required to reproduce the buoyancy force acting on the particles. However, this complicates the algorithm for solving the continuum phase velocity and pressure fields, and therefore the following adjustment was introduced in stead: the pressure field was switched to the version without absorbed gravity before updating the particles velocities and positions; and the pressure field was switched to the version with absorbed gravity before updating the continuous phase. The `myParcelFoam` relevant source code is reported in Section E.2. Finally, `myParcelFoam` was compiled in a way that the user-modified Lagrangian dynamic library `libmyForcesLagrangianIntermediate.dylib` was linked to the solver's binary.

For the simulations with the passive tracer described in Section 9.5, a modification of `myParcelFoam`, called `myParcelTracerFoam`, was used. The `myParcelTracerFoam` source code is the same of `myParcelFoam`, with the following modifications: (*i*) a new source file, called `YiEqn.H`, solving Equation 9.1, is introduced (Section E.2.5). (*ii*) In the source file `myParcelFoam.C` (Section E.2.1), line 115 is uncommented. (*iii*) In the source file `createFields.H` (Section E.2.2), lines from 1 to 13 are uncommented.

E

User-Modified Source Code

E.1 Lagrangian Library

E.1.1 MyDewsburyDragForce.H

```
#ifndef MyDewsburyDragForce_H
#define MyDewsburyDragForce_H

#include ”ParticleForce.H”

// * * * * * * * * * * * * * * * * * * * * * * * * * * * * * * * * * * * * * //

namespace Foam
{
/*---------------------------------------------------------------------------*\
                     Class MyDewsburyDragForce Declaration
\*---------------------------------------------------------------------------*/

template<class CloudType>
class MyDewsburyDragForce
:
    public ParticleForce<CloudType>
{
    // Private Member Functions

        //- Drag coefficient multiplied by Reynolds number
        scalar CdRe(const scalar Re) const;
```

```


public:

    //- Runtime type information
    TypeName("myDewsburyDrag");


    // Constructors

        //- Construct from mesh
        MyDewsburyDragForce
        (
            CloudType& owner,
            const fvMesh& mesh,
            const dictionary& dict
        );

        //- Construct copy
        MyDewsburyDragForce(const MyDewsburyDragForce<CloudType>& df);

        //- Construct and return a clone
        virtual autoPtr<ParticleForce<CloudType> > clone() const
        {
            return autoPtr<ParticleForce<CloudType> >
            (
                new MyDewsburyDragForce<CloudType>(*this)
            );
        }


    //- Destructor
```

```
    virtual ~MyDewsburyDragForce();


    // Member Functions

        // Evaluation

            //- Calculate the coupled force
            virtual forceSuSp calcCoupled
            (
                const typename CloudType::parcelType& p,
                const scalar dt,
                const scalar mass,
                const scalar Re,
                const scalar muc
            ) const;
};


// * * * * * * * * * * * * * * * * * * * * * * * * * * * * * * * * * * * * * //

} // End namespace Foam

// * * * * * * * * * * * * * * * * * * * * * * * * * * * * * * * * * * * * * //

#ifdef NoRepository
#   include ”MyDewsburyDragForce.C”
#endif

// * * * * * * * * * * * * * * * * * * * * * * * * * * * * * * * * * * * * * //

#endif
```

```

// ************************************************************************* //
```

E.1.2 MyDewsburyDragForce.C

```
#include "MyDewsburyDragForce.H"

// * * * * * * * * * * * * * Private Member Functions * * * * * * * * * * * //

template<class CloudType>
Foam::scalar Foam::MyDewsburyDragForce<CloudType>::CdRe(const scalar Re) const
{
    if (Re > 195.0)
    {
        return 0.95*Re;
    }
    else
    {
        return 16.0*(1.0 + 0.173*pow(Re, 0.657))
             + 0.413*pow(Re, 2.09)/(16300 + pow(Re, 1.09));
    }
}


// * * * * * * * * * * * * * * * * Constructors * * * * * * * * * * * * * * //

template<class CloudType>
Foam::MyDewsburyDragForce<CloudType>::MyDewsburyDragForce
(
    CloudType& owner,
```

```
    const fvMesh& mesh,
    const dictionary& dict
)
:
    ParticleForce<CloudType>(owner, mesh, dict, typeName, false)
{}


template<class CloudType>
Foam::MyDewsburyDragForce<CloudType>::MyDewsburyDragForce
(
    const MyDewsburyDragForce<CloudType>& df
)
:
    ParticleForce<CloudType>(df)
{}


// * * * * * * * * * * * * * * * * Destructor * * * * * * * * * * * * * * * //

template<class CloudType>
Foam::MyDewsburyDragForce<CloudType>::~MyDewsburyDragForce()
{}


// * * * * * * * * * * * * * * * Member Functions * * * * * * * * * * * * * //

template<class CloudType>
Foam::forceSuSp Foam::MyDewsburyDragForce<CloudType>::calcCoupled
(
```

```
    const typename CloudType::parcelType& p,
    const scalar dt,
    const scalar mass,
    const scalar Re,
    const scalar muc
) const
{
    forceSuSp value(vector::zero, 0.0);

    value.Sp() = mass*0.75*muc*CdRe(Re)/(p.rho()*sqr(p.d()));

    return value;
}


// ************************************************************************* //
```

E.2 Solver

E.2.1 myParcelFoam.C

```
/*---------------------------------------------------------------------------*\
  =========                 |
  \\      /  F ield         | OpenFOAM: The Open Source CFD Toolbox
   \\    /   O peration     |
    \\  /    A nd           | Copyright (C) 2013-2014 OpenFOAM Foundation
     \\/     M anipulation  |
-------------------------------------------------------------------------------
License
    This file is part of OpenFOAM.

    OpenFOAM is free software: you can redistribute it and/or modify it
```

```
    under the terms of the GNU General Public License as published by
    the Free Software Foundation, either version 3 of the License, or
    (at your option) any later version.

    OpenFOAM is distributed in the hope that it will be useful, but WITHOUT
    ANY WARRANTY; without even the implied warranty of MERCHANTABILITY or
    FITNESS FOR A PARTICULAR PURPOSE.  See the GNU General Public License
    for more details.

    You should have received a copy of the GNU General Public License
    along with OpenFOAM.  If not, see <http://www.gnu.org/licenses/>.

Application
    myParcelFoam

Description
    Transient solver for the coupled transport of a single kinematic particle
    cloud.

\*---------------------------------------------------------------------------*/

#include ”fvCFD.H”
#include ”MULES.H”
#include ”subCycle.H”
#include ”interfaceProperties.H”
#include ”incompressibleTwoPhaseMixture.H”
#include ”singlePhaseTransportModel.H”
 #include ”turbulenceModel.H”
#include ”pimpleControl.H”
#include ”fvIOoptionList.H”
#include ”fixedFluxPressureFvPatchScalarField.H”

```

```
#ifdef MPPIC
    #include "basicKinematicMPPICCloud.H"
    #define basicKinematicTypeCloud basicKinematicMPPICCloud
#else
    #include "basicKinematicCollidingCloud.H"
    #define basicKinematicTypeCloud basicKinematicCollidingCloud
#endif

int main(int argc, char *argv[])
{
    argList::addOption
    (
        "cloudName",
        "name",
        "specify␣alternative␣cloud␣name.␣default␣is␣'kinematicCloud'"
    );

    #include "setRootCase.H"
    #include "createTime.H"
    #include "createMesh.H"
    #include "readGravitationalAcceleration.H"
    #include "createFields.H"
    #include "initContinuityErrs.H"

    pimpleControl pimple(mesh);

    Info<< "\nStarting␣time␣loop\n" << endl;

    while (runTime.run())
    {
        #include "readTimeControls.H"
        #include "CourantNo.H"
```

```
    #include "alphaCourantNo.H"
    #include "setDeltaT.H"

    runTime++;

    Info<< "Time␣=␣" << runTime.timeName() << nl << endl;

    continuousPhaseTransport.correct();
    muc = rhoc*continuousPhaseTransport.nu();

    Info<< "Evolving␣" << kinematicCloud.name() << endl;
    kinematicCloud.evolve();

    // Gravity correction.
    // Now p includes gravity.
    p = p - rhoc*gh;

    interface.correct();

    // Update continuous phase volume fraction field

    // --- Pressure-velocity PIMPLE corrector loop
    while (pimple.loop())
    {
        #include "UcEqn.H"

        // --- PISO loop
        while (pimple.correct())
        {
            #include "pEqn.H"
        }

```

```
            if (pimple.turbCorr())
            {
                continuousPhaseTurbulence->correct();
            }
        }

        // Update the scalar field.
//          #include ”YiEqn.H”

        // Gravity correction.
        // Now p does not include gravity.
        p = p + rhoc*gh;

        runTime.write();

        Info<< ”ExecutionTime␣=␣” << runTime.elapsedCpuTime() << ”␣s”
            << ”␣␣ClockTime␣=␣” << runTime.elapsedClockTime() << ”␣s”
            << nl << endl;
    }

    Info<< ”End\n” << endl;

    return 0;
}


// ************************************************************************* //
```

E.2.2 createFields.H

```
//      Info<< ”Reading field Yi\n” << endl;
//      volScalarField Yi
```

```
//    (
//        IOobject
//        (
//            "Yi",
//            runTime.timeName(),
//            mesh,
//            IOobject::MUST_READ,
//            IOobject::AUTO_WRITE
//        ),
//        mesh
//    );

    Info<< "Reading␣field␣Uc\n" << endl;
    volVectorField Uc
    (
        IOobject
        (
            "Uc",
            runTime.timeName(),
            mesh,
            IOobject::MUST_READ,
            IOobject::AUTO_WRITE
        ),
        mesh
    );

    Info<< "Reading␣field␣p\n" << endl;
    volScalarField p
    (
        IOobject
        (
            "p",
```

```
            runTime.timeName(),
            mesh,
            IOobject::MUST_READ,
            IOobject::AUTO_WRITE
        ),
        mesh
    );

    Info<< ”Building␣accessory␣gh␣fields\n” << endl;
    volScalarField gh(”gh”, g & mesh.C());
    surfaceScalarField ghf(”ghf”, g & mesh.Cf());


    Info<< ”Reading/calculating␣continuous-phase␣face␣flux␣field␣phic\n”
        << endl;
    surfaceScalarField phic
    (
        IOobject
        (
            ”phi”,
            runTime.timeName(),
            mesh,
            IOobject::READ_IF_PRESENT,
            IOobject::AUTO_WRITE
        ),
        linearInterpolate(Uc) & mesh.Sf()
    );

    Info<< ”\nReading␣transportProperties\n” << endl;
    incompressibleTwoPhaseMixture continuousPhaseTransport(Uc, phic);

    Info << ”Creating␣field␣alphac\n” << endl;
```

```
volScalarField& alphac(continuousPhaseTransport.alpha1());

Info << "Creating␣density␣field␣rhoc\n" << endl;
const dimensionedScalar& rho1 = continuousPhaseTransport.rho1();
const dimensionedScalar& rho2 = continuousPhaseTransport.rho2();

volScalarField rhoc
(
    IOobject
    (
        "rho",
        runTime.timeName(),
        mesh,
        IOobject::READ_IF_PRESENT
    ),
    alphac*rho1 + (scalar(1) - alphac)*rho2,
    alphac.boundaryField().types()
);
rhoc.oldTime();



label pRefCell = 0;
scalar pRefValue = 0.0;
setRefCell(p, mesh.solutionDict().subDict("PIMPLE"), pRefCell, pRefValue);


Info << "Creating␣effective␣viscosity␣field␣muc\n" << endl;
volScalarField muc
(
    IOobject
    (
```

```
            ”mu”,
            runTime.timeName(),
            mesh,
            IOobject::NO_READ,
            IOobject::AUTO_WRITE
        ),
        rhoc*continuousPhaseTransport.nu()
    );


    word kinematicCloudName(”kinematicCloud”);
    args.optionReadIfPresent(”cloudName”, kinematicCloudName);

    Info<< ”Constructing␣kinematicCloud␣” << kinematicCloudName << endl;
    basicKinematicTypeCloud kinematicCloud
    (
        kinematicCloudName,
        rhoc,
        Uc,
        muc,
        g
    );

    surfaceScalarField rhocf(”rhocf”, fvc::interpolate(rhoc));

    // Mass flux
    // Initialisation does not matter because rhoPhi is reset after the
    // alpha1 solution before it is used in the U equation.
    surfaceScalarField rhoPhic
    (
        IOobject
        (
```

```
            "rho*phi",
            runTime.timeName(),
            mesh,
            IOobject::NO_READ,
            IOobject::NO_WRITE
        ),
        rho1*phic
    );

    // Construct interface from alpha1 distribution
    Info<< "Creating␣interface␣model\n" << endl;
    interfaceProperties interface(alphac, Uc, continuousPhaseTransport);


    // Construct incompressible turbulence model
    Info<< "Creating␣turbulence␣model\n" << endl;
    autoPtr<incompressible::turbulenceModel> continuousPhaseTurbulence
    (
        incompressible::turbulenceModel::New(Uc, phic, continuousPhaseTransport)
    );
```

E.2.3 pEqn.H

```
{
    volVectorField HbyA("HbyA", Uc);
    HbyA = rAUc*UcEqn.H();

    surfaceScalarField phiHbyA
    (
        "phiHbyA",
        (
            (fvc::interpolate(HbyA) & mesh.Sf())
```

```
            + rhocf*rAUcf*fvc::ddtCorr(Uc, phic)
        )
    );

    // Update the fixedFluxPressure BCs to ensure flux consistency
    setSnGrad<fixedFluxPressureFvPatchScalarField>
    (
        p.boundaryField(),
        (
            phiHbyA.boundaryField()
            - (mesh.Sf().boundaryField() & Uc.boundaryField())
        )/(mesh.magSf().boundaryField()*rAUcf.boundaryField())
    );

    // Non-orthogonal pressure corrector loop
    while (pimple.correctNonOrthogonal())
    {
        fvScalarMatrix pEqn
        (
            fvm::laplacian(rhocf*rAUcf, p)
          ==
            fvc::div(rhocf*phiHbyA)
        );

        pEqn.setReference(pRefCell, pRefValue);

        pEqn.solve(mesh.solver(p.select(pimple.finalInnerIter())));

        if (pimple.finalNonOrthogonalIter())
        {
            phic = phiHbyA - pEqn.flux()/rhocf;

```

```
            p.relax();

            Uc = HbyA
              − rAUc∗fvc::reconstruct((pEqn.flux()/rhocf)/rAUcf);
            Uc.correctBoundaryConditions();
        }
    }
}

#include ”continuityErrs.H”
```

E.2.4 UcEqn.H

```
fvVectorMatrix UcEqn
(
    fvm::ddt(rhoc, Uc)
  + fvm::div(rhoPhic, Uc)
  + continuousPhaseTurbulence−>divDevRhoReff(rhoc, Uc)
 ==
    kinematicCloud.SU(Uc)
);
UcEqn.relax();

volScalarField rAUc(1.0/UcEqn.A());
surfaceScalarField rAUcf(”Dp”, fvc::interpolate(rAUc));


if (pimple.momentumPredictor())
{
    solve
    (
        UcEqn
```

```
        ==
            fvc::reconstruct
            (
//                  phicForces/rAUcf
                - fvc::snGrad(p)*mesh.magSf()
                + fvc::interpolate(interface.sigmaK())*fvc::snGrad(alphac)
                    * mesh.magSf()
            )
        );
}
```

E.2.5 YiEqn.H

```
fvScalarMatrix YiEqn
(
    fvm::ddt(rhoc, Yi)
  + fvm::div(rhoPhic, Yi)
  - fvm::laplacian(continuousPhaseTurbulence->nuEff()*rhoc, Yi)
);

YiEqn.relax();

//YiEqn.solve(mesh.solver("Yi"));
solve(YiEqn);
```

F

Publications Resulting from This Work